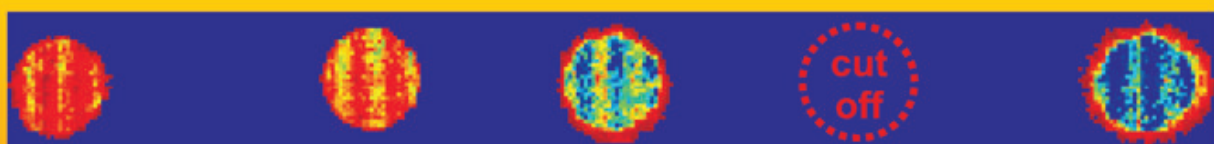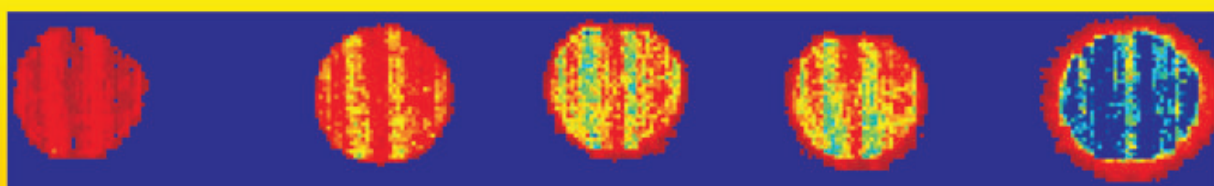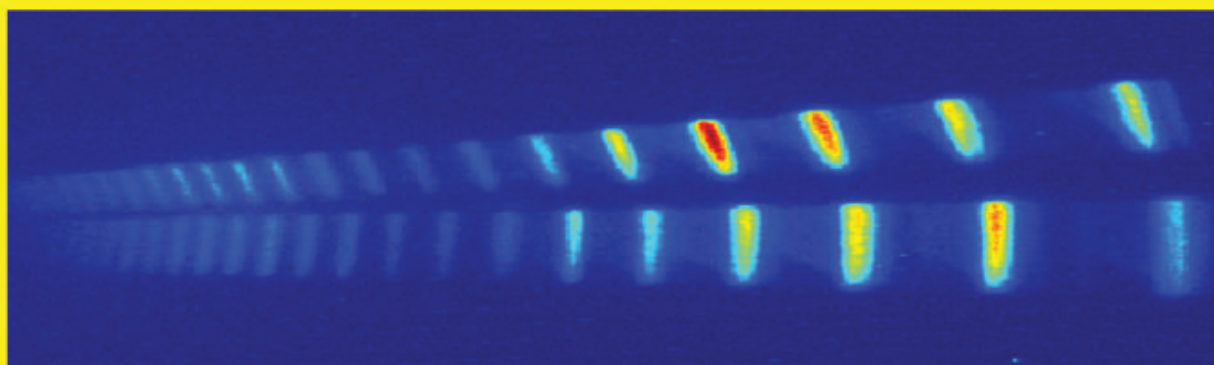Ulrich Hilmar Wagner

Sub-Picosecond Laser Plasma Experiments on Dielectric Solids

Ultrafast Ionisation and Observation of Megagauss Magnetic Fields

cut off

Cuvillier Verlag Göttingen

Sub-Picosecond Laser Plasma Experiments on Dielectric Solids: Ultrafast Ionisation and Observation of Megagauss Magnetic Fields

D i s s e r t a t i o n

zur Erlangung des akademischen Grades

doctor rerum naturalium (Dr. rer. nat.)

vorgelegt dem Rat der Physikalisch-Astronomischen Fakultät

der Friedrich-Schiller-Universität Jena

von Diplom-Physiker Ulrich Hilmar Wagner

geboren am 28.11.1972 in Eschwege

Zusammenfassung

Die Wechselwirkung eines intensiven sub-pikosekunden Laserpulses (10^{15}–10^{20} W/cm²) mit Materie umfasst eine Vielzahl unterschiedlicher Wechselwirkungen. Die vorwiegend experimentelle Arbeit konzentriert sich auf die ultraschnelle Ionisation und die Beobachtung von magnetischen Feldern im Megagauss Bereich:

Ultraschnelle Ionisation: Die ansteigende Flanke eines intensiven Laserpulses verursacht ein schnelles Anwachsen der Elektronendichte, so dass die kritische Elektronendichte rasch überschritten wird und eine zunächst transparente Glasplatte undurchsichtig wird. Im Rahmen dieser Arbeit wird ein theoretisches Modell dieser Wechselwirkung basierend auf der optischen Feldionisation (OFI) entwickelt. Die Computersimulationen zeigen, dass die Transmission eines mit einem 60 fs Laserpuls der Wellenlänge 800 nm erzeugten Plasmas in weniger als 10 fs um viele Größenordnungen abnimmt. Das schnelle Abnehmen der Transmission wird hauptsächlich durch die Absorption des einfallenden Laserstrahls und nicht durch die anwachsende Reflexion hervorgerufen. Um diese theoretischen Ergebnisse zu überprüfen, wurde ein Pump–Probe-Experiment mit einem Titan-Saphir-Laser (800 nm, 1 mJ) am Institut für Optik und Quantelektronik der Friedrich-Schiller-Universität in Jena durchgeführt. In diesem Experiment wurde mit 60 fs und 120 fs Laserpulsen, die auf eine Intensität von 10^{15} W/m² fokussiert wurden, ein Plasma erzeugt. Ein kleiner Teil dieser Pulse wurde als Probepuls benutzt, um die Zeit–Frequenz-Funktion der Plasmatransmission zu messen. Durch Vergleichen der Momente dieser Zeit–Frequenz-Funktionen mit den entsprechenden Momenten, die anhand von FROG-Messungen berechnet wurden, konnten die theoretischen Vorhersagen bestätigt werden, so dass dieser Schalter in zukünftigen Experimenten auch zur Pulscharakterisierung von sehr kurzwelliger UV-Strahlung eingesetzt werden kann.

Magnetische Felder im Megagauss Bereich: Bei der Wechselwirkung eines sub-pikosekunden Laserpulses mit einem Plasma können starke magnetische Felder vor allem durch radialen Wärmetransport, durch pondermotorische Kräfte und durch Ströme schneller Elektronen entstehen. Plasmakinetische (PIC) Simulationen zeigen, dass die stärksten Felder azimutal im Bereich hoher Dichte lokalisiert sind und exponentiell mit steigender Laserintensität anwachsen. Für den Fall eines schrägen Lasereinfalls werden die stärksten Felder nur auf einer Seite des Plasmas erzeugt. Diese Felder können z.B. mittels der Grenzfrequenz für die außerordentliche Welle (x-wave cut-off), dem Faraday- und dem Cotton-Moutoneffekt gemessen werden. Das Prinzip dieses Messverfahrens beruht auf der polarisationsabhängigen Ausbreitung eines Probepulses durch ein magnetisiertes Plasma. Indem man Hohe Harmonische der Laserfundamentalen benutzt, die durch den intensiven Laserpuls im Inneren des Plasmas erzeugt werden, kann man die Schwierigkeiten vermeiden, die sich bei Anwendung eines externen Probepulses durch zu starke Brechung an dem Dichtegradienten des Plasmas ergeben. Die Experimente wurden mit dem CPA-Strahl des VULCAN-Lasers (1053 nm, 750 fs, 10^{20} W/cm²) am Rutherford-Appleton Laboratory in Großbritannien durchgeführt. Die magnetischen Felder wurden mit drei VIS / UV-Polarimetern und zwei VUV / XUV-Polarimetern untersucht. Beruhend auf der Beobachtung des X-Wave Cut-Off ergab sich eine magnetische Feldstärke von mindestens 350($\pm$60) MG. Die Gleichungen für den Cotton-Mouton-Effekt der fünften Harmonischen weisen bereits auf eine Mindestfeldstärke von über 400($\pm$50) MG hin. Die VUV / XUV-Polarimetrie gibt sogar deutliche Hinweise auf Felder größer als 700($\pm$100) MG. Bis zu einer Laserintensität von 10^{20} W/cm² konnten keine Anzeichen einer Sättigung der magnetischen Feldstärke gefunden werden. Außerdem wurden keine Felder in Richtung der Target-Normalen beobachtet. Alle diese experimentellen Ergebnisse stimmen gut mit den Ergebnissen der PIC-Simulationen überein.

Abstract

The interaction of an intensive sub-picosecond laser pulse (10^{15}–10^{20} W/cm²) with matter comprises many different phenomena. This mainly experimental work concentrates on the ultrafast ionisation of a dielectric solid and the observation of megagauss magnetic fields in laser produced plasmas:

Ultrafast Ionisation: The rapidly increasing electron density, caused by the leading edge of an intensive laser pulse, surpasses the critical electron density very quickly, so that an initially transparent glass plate becomes opaque. In this work a theoretical model of this interaction is developed on the basis of optical field ionisation (OFI). Computational simulations show, that the transmissivity reduces by several orders of magnitude in less than 10 fs for plasma producing laser pulses with 800 nm wavelength and 60 fs pulse-duration. This rapid decrease in transmissivity is mainly due to the absorption of the incident laser beam and not due to an increasing reflectivity. To verify these theoretical findings a pump-probe experiment was performed with a Titanium-Sapphire laser (800 nm, 1 mJ) at the Institute for Optics and Quantum-Electronics at the Friedrich-Schiller-Universität in Jena. In this experiment laser pulses with a duration of 60 fs and 120 fs have been focused to an intensity of approximately 10^{15} W/m² to produce a plasma. A small part of these pulses was used as a probe pulse to measure the time–frequency function of the plasma transmissivity. By comparing the momenta of these time–frequency functions with the respective momenta calculated from FROG measurements the theoretical predictions have been verified, so that this switch can also be applied for characterising UV-pulses with a very short wavelength in future experiments.

Megagauss Magnetic Fields: The sub-picosecond laser–plasma interaction can generate strong magnetic fields mainly due to radial thermal transport, pondermotorive forces and fast electron currents. Particle in cell (PIC) simulations were performed, showing that the strongest fields are azimuthal fields growing exponentially with increasing laser-intensity in the high density region of the plasma. In the case of oblique incidence the strongest fields are present at one side of the plasma only. These fields can be measured by means of the x-wave cut-off, the Faraday- and the Cotton-Mouton effect, i.e. the polarisation dependent propagation of a probe beam through the magnetised plasma. By using the high harmonics of the fundamental laser frequency, which are produced inside the plasma, one can overcome the difficulties resulting from the application of an external probe pulse due to its strong refraction at the density gradient of the plasma. The experiment was performed with the CPA-beam of VULCAN (1053 nm, 750 fs, 10^{20} W/cm²) at the Rutherford-Appleton Laboratory, UK. The magnetic fields were observed with three VIS / UV polarimeters and two VUV / XUV polarimeters. Based on the observation of x-wave cut-offs the peak magnetic field was at least 350($\pm$60) MG. Whilst the equations of the Cotton-Mouton effect for the 5^{th} harmonic already suggested fields above 400($\pm$50) MG, the VUV / XUV polarimetry gave strong indications of fields even beyond 700($\pm$100) MG. Up to 10^{20} W/cm² no saturation of the field strength was found and no magnetic field could be observed close to normal incidence. All these results correspond well with the PIC simulations.

Contents

Chapter 1

Introduction

Humans are familiar with plasmas since time immemorial: lightning, polar lights and flames are popular examples of them. Furthermore, even more than 99 % of the apparent universe is made up of plasma. But nevertheless it took until the 20$^{\text{th}}$ century until extensive research in this area began. This is due to the technical difficulties in performing experiments with a plasma and the mathematical complexity involved in theoretical studies. In particular even for a bottom-of-the-line plasma model one has to combine a fully developed theory of electrodynamics and classical mechanics within the framework of a many-particle-problem.

When W. Crookes noticed in 1879, that the properties of the medium in gas discharges are different from solid, liquid and gaseous materials, he called this the 'fourth state of matter' [36]. The important fact, that the charged particles in these discharges exhibits a collective behaviour due to the long ranging Coulomb forces, was already known by Lord Rayleigh in 1906 [133]. In 1929 L. Tonks and I. Langmuir [177] recognised that this state of matter can be considered as a carrier for e.g. fast-electrons, molecules and ions of gas impurities (similar to blood carrying around its various corpuscles). Thus they called this state of matter a 'plasma' [113], originating from the Greek word $\pi\lambda\alpha\sigma\mu\alpha$, meaning mouldable substance. Nevertheless plasma-physics remained a small and unimportant field in physics, until countries like Great Britain, France, the U.S.S.R. and the USA started patronising it for their political interests in nuclear weapons and power-plants at the beginning of the 1950s [18]. In particular the energy crisis in 1973 boosted the efforts in building a controlled thermonuclear fusion reactor, leading to many large scale magnetic confined fusion (MCF) experiments, like the very successful 'Joint European Torus' (JET), which started in 1983 [76]. The next step is the 'International Thermonuclear fusion Reactor', which shall demonstrate the feasibility of a commercial fusion reactor [76]. Despite these huge scale experiments plasma-physics has nowadays become indispensable even in many fields of applied physics like material science, semiconductor technology and physical chemistry.

A new field within plasma physics arose shortly after the construction of the first Laser by Maiman in 1960 [100]. As soon as people learned how to build more intense lasers with a pulse duration in the nanosecond region, scientists reported optical breakdowns in air and in solid materials [73], the first laser produced plasmas. Quite soon it was realised that lasers emitting nanosecond pulses with a pulse energy of several kilojoules are an ideal tool to study high density plasmas, the physics of nuclear weapons, thermonuclear fusion (Inertia Confinement Fusion (ICF)) and plasma instabilities [3, 35]. Consequently a number of huge nanosecond laser systems with several dozens of beams, each delivering a pulse energy beyond 1 kJ, have been built during the 1970s and 1980s: among the best

known systems are PHEBUS at Limeil (France), GEKKO at Osaka (Japan), NOVA and Shiva at Livermore (USA), OMEGA at Rochester (USA) and VULCAN at the Rutherford-Appleton-Laboratories (United Kingdom) [91].

A technical milestone in laser plasma physics was accomplished with the idea of chirped pulse amplification (CPA) [101, 125, 163, 164] in 1985 by Mourou's group and the development of the first turnkey short pulse oscillator by Sibbett and his group in 1990 [155]. Soon this short pulse oscillator and the CPA amplification scheme were put together to make up the first high-power 'Table Top Terawatt' (T^3) laser [83, 166]. In contrast to the abovementioned nanosecond lasers with pulse energies usually beyond several 10 kJ, these systems often emit pulses with not much more energy than a few joules. But their pulse duration can be more than three orders of magnitude shorter, so that their peak pulse intensity even surpass the peak intensity of the nanosecond systems. The basic principle of these systems is to stretch a femtosecond pulse generated in a Kerr mode-locked Titanium-Sapphire(Ti:Sa)-oscillator to several picoseconds. In general this pulse is amplified in a series of Ti:Sa-crystals, before it is recompressed again [12, 124]. Today these T^3-systems are widely used around the world, because they are quite cheap and rather easy to operate, so that it is convenient to perform experiments with them. Among the largest operational CPA-systems at present are the VULCAN petawatt beam-line at the Rutherford-Appleton-Laboratory (United Kingdom) and the LULI petawatt beam-line at the École Polytechnique (France) with a pulse energy up to 500 J and a pulse duration between 500–1000 fs [91].

These CPA-systems also enable a new fusion scheme, called the 'fast igniter' [118, 168]. In this scheme a small sphere, made of a deuterium–tritium mixture, is heated and compressed by nanosecond laser pulses shining onto it from all sides. Then a 100 ps laser pulse drills a hole into the coronal plasma. At stagnation an additional pulse (containing several 10 kJ in 10 ps) propagates through the hole into the interior, where it produces a vast amount of energetic electrons. These electrons finally ignite the plasma. Beyond this fusion scheme many new phenomena can be explored with these CPA-systems: at intensities below 10^{15} W/cm^2 pump–probe experiments are a class of highly interesting experiments for studying ultrafast transitions in matter. An example for this kind of experiments are time resolved studies of processes like non-thermal melting and the excitation and decay of phonons [47, 136, 152]. At intensities beyond 10^{16} W/cm^2 many phenomena related to the laser–plasma interaction can be studied [58, 59]. A few examples are the emission of high order harmonics from a solid surface [13, 116, 175, 176, 182, 183, 191] or the K-α emission, due to fast electrons [59, 160]. One mechanism accelerating the electrons are plasma-waves [86]. Beyond 10^{18} W/cm^2 significant amounts of fast particles with energies of several MeV [102] are produced. These particles initiate nuclear reactions, which can produce γ-rays [53, 117], or fission the nucleus, which is particularly useful for nuclear waste disposal [93, 145]. At laser intensities above 10^{21} W/cm^2 even more phenomena, like pair production, become experimentally accessible.

Most sub-picosecond experiments involving solid targets either concentrate on study-

ing phenomena below the plasma formation limit, or they study the laser–plasma interaction itself. In contrast to that the plasma formation process is only rarely studied [9, 60, 149, 181, 184]. This is not a serious shortcoming for metals, because they can be considered as a very cold plasma from the very beginning, due to their free electron gas. But this does not hold true for dielectric media, which initially cannot be described as a plasma. In this case the laser has to create a plasma by means of optical field ionisation at first. As this process has been rarely studied for solid materials up to today, the first part of this work concentrates on this topic. Probably the most interesting result is that the transition from an initially transparent dielectric solid to the plasma state can be used as an ultrafast switch, which allows pump–probe experiments with a temporal resolution at the order of 10 fs for radiation whose wavelengths range from the vacuum ultraviolet to the near infrared.

Soon after the initially dielectric surface is transformed to a plasma, the laser pulse starts interacting with this plasma. One phenomena occurring during this interaction is the generation of strong magnetic fields inside the plasma. Up to now only measurements of the magnetic field in the under-dense region have been performed [21, 22]. Knowledge about the fields in the over-dense region was only available through computational simulations [103, 129, 189], predicting azimuthal fields of several 100 MG. This shortcoming is addressed in the second part of this work. In this part an experiment is discussed, which observed for the first time azimuthal fields well above 400 MG. With further increasing laser intensities, these exciting results will not only be interesting from an academic point of view, but they will also be the key to studying strongly magnetised high density plasmas (such as those present at the surface of white dwarfs and neutron stars) in the laboratory for the first time.

Chapter 2
Ultrafast Ionisation and Optical Gating

2.1 Introduction

As already mentioned beforehand, only a few experiments [9, 60, 149, 181, 184] focus onto the formation of a solid density like plasma from a dielectric surface, i.e. the transition from a cold solid material to a hot high density plasma. In addition, despite a publication from P. Blanc [19], there are no detailed experimental studies of plasma formation at the surface of a solid on a timescale well below 100 fs to the best knowledge of the author. Furthermore computer codes, used to simulate laser plasma interactions at solid densities, require a pre-ionised initial state in general, because ionisation models are only implemented to a very limited extent [17, 44, 45, 86, 132]. An exception are specialised codes, such as those developed by Ruhl and Mulser [137]. Furthermore it is remarkable, that there are not much more detailed studies of this process within an ultrashort timeframe, because this process has been proposed to be used for pre-pulse removal from ultrashort laser pulses. This application is known under the term *plasma mirror* in the scientific literature [61, 77, 142, 170, 173, 181]. In addition it is rarely discussed, that the phase transition from the solid state to a high density plasma can be used as a transmission gate as well. In Michelmann et. al. [109, 110] this gate is applied to characterise a 248 nm, 500 fs pulse. In the theoretical part of [110] we briefly showed (a more elaborate discussion is given in [174]), that the response time of this gate is not much longer than 50 fs. Beyond these studies it is interesting to explore, if the plasma switch is also applicable to pulses well below 100 fs or if the measured pulse properties are influenced by the increasing electron density. In this case one can try to derive the plasma properties from the measured pulse properties. These studies are the main scope of the present chapter. In its first part this issue is approached from a theoretical point of view by developing a macroscopic model describing the optical properties during the plasma formation process at a dielectric surface [174]. Based on this model, not only the optical properties of the transmission gate are calculated, but also valuable insight into the feasibility of the plasma mirror for pulse cleaning on ultrashort timescales is obtained. The experimental part of this chapter concentrates on the transmission properties of the emerging plasma, which are finally compared to the theoretical findings.

Even if the time resolution of measuring instruments increased quite a lot during the last few decades, femtosecond time resolution is still achieved by measuring the correlation between two signals. A widespread class of these correlation measurements are *pump–probe experiments* [134], which have been used successfully during the last years to study ultrafast melting, changing absorption, reflectivity and transmission of transparent semiconductors and insulators (see, e.g. [9, 47, 136, 149, 152, 180]) on a

picosecond timescale. Even more recently, time-resolved x-ray reflectivity measurements have become a standard tool for studying phase transitions in solid state physics on time-scales below 1 ps [47].

In our experiment the main laser pulse is split into a strong *pump pulse*, producing the plasma, and a much weaker *probe pulse*. Both pulses are focused onto the same area of an initially transparent target. As the probe pulse can be delayed in time with respect to the pump pulse, one can measure the correlation between the probe pulse and the optical properties of the plasma, respectively. This correlation can be used either for studying the time-dependent optical properties of the plasma, if the properties of the probe pulse are known, or for measuring the properties of the probe pulse, if the time dependent optical properties of the plasma are known.

2.2   A Time-Dependent Model of Optical Plasma Properties

Concerning the plasma formation process one can distinguish two kinds of solid materials: metals and dielectrics [138]. The free electron gas present in a metallic solid is already a plasma with an electron temperature of some meV. Thus the electric field of the laser can directly interact with the free electrons of this plasma, leading to collisional absorption, also called inverse bremsstrahlung [73, 172]. This heats up the initially cold plasma and increases the electron density even further by collisional ionisation. On the other hand, in a dielectric solid there are practically no free electrons present, so that this mechanism does not work initially. Instead of this, optical field ionisation (OFI) [50] initiates the ionisation process. As soon as the increasing electron density surpasses the so called critical electron density n_{ec}, an initially transparent dielectric material becomes opaque at its surface. n_{ec} is given by

$$n_{ec} = \frac{\epsilon_0 m_e}{e^2} \, \omega_0^2 \tag{2.1}$$

with the dielectric constant ϵ_0 in vacuum, the electron charge e, the electron mass m_e and the angular frequency ω_0 of the laser field. A schematic overview of our macroscopic plasma model describing this transition process is shown in Figure 2.1.

2.2.1   The Ionisation Process

To obtain a more detailed understanding of OFI it is useful to introduce the so called Keldysh parameter $\Gamma := \sqrt{\frac{I_{ioni}}{2U_q}}$, whereby I_{ioni} is the ionisation potential and U_q is the quiver energy:

$$U_q := \frac{e^2}{4m_e} \sqrt{\frac{\mu_0}{\epsilon_0}} \, \frac{I_{pump}}{\omega_0^2} \tag{2.2}$$

with the laser intensity I_{pump}, the dielectric constant ϵ_0 and the magnetic permeability μ_0. Then one can distinguish three different domains of OFI: a low intensity domain with ionisation mainly due to multi-photon absorption ($\Gamma \gg 1$), a high intensity domain ($\Gamma \ll 1$) with tunnel ionisation and a transition region. In all three domains the OFI is described fairly accurately with the Ammosov-Delone-Krainov(ADK) theory [5], which
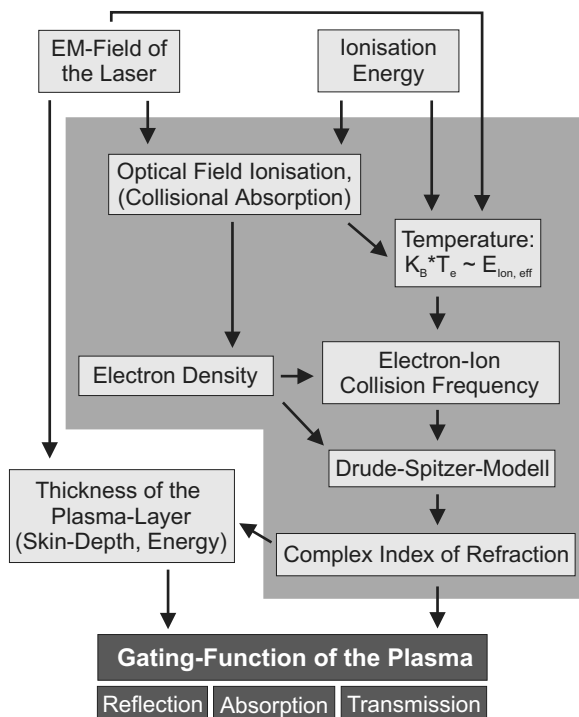
Figure 2.1: Physical model to calculate the time-dependent transmission properties of a plasma produced at an initially dielectric and transparent solid in the early phase of plasma formation.
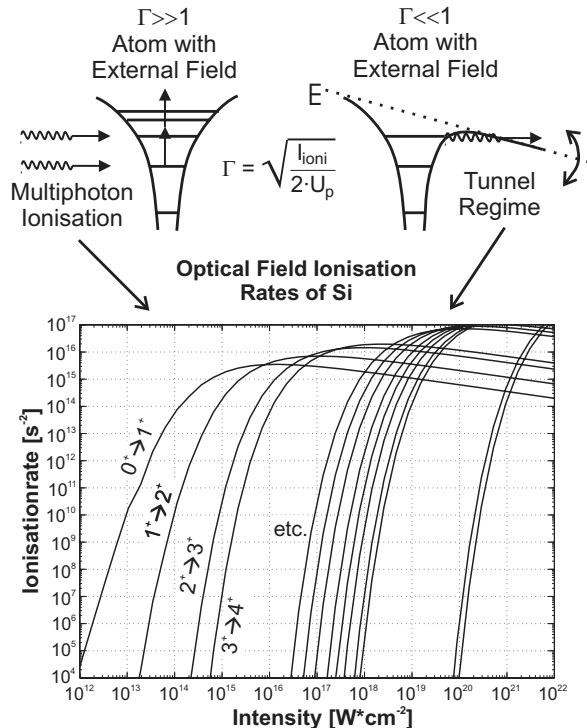
Figure 2.2: Optical field ionisation rates of Silicon from the multi-photon to the tunnel ionisation regime.

is an elaboration of the Keldysh theory [78], based on the Schrödinger equation and a scattering matrix approach. The latter theory is used in our plasma formation model (see Figure 2.1). In some cases this theory underestimates the ionisation rates as a comparison between calculated rates and experimental data shows [8, 50]. More serious are the restrictions of Keldysh's and similar theories [55] to a single atom. Extending these theories to a high density solid is a very extensive task, as one has to use a detailed quantum mechanical model of the solid. In the end, one would derive even higher ionisation rates, because the band structure of the solid almost always allows resonant absorption of photons [78]. Consequently this increases the rapidity of the switch even more. In summary, the Keldysh model is a fairly simple, but sufficiently sophisticated model to estimate lower boundaries for the ionisation rates during the plasma formation on the surface of a solid, if the ionisation potential, the incident laser frequency and intensity are known (see Figure 2.2). From these calculated rates, the time-dependent electron density n_e can be calculated easily by summing up the different transitions and taking the occupation of states into account (see Figure 2.3). It is noteworthy, that we obtained similar results, using the barrier suppression ionisation (BSI) model [7, 8].

The free electrons produced by OFI immediately gain a quiver energy up to U_q from the electric field of the laser, so that they can contribute to the ionisation rate by collisional ionisation. Consequently a binary encounter approximation of collisional ionisation, developed by Gryzinski [67], was included in the calculations. As can be seen from Figure 2.3, this only increases the electron density n_e significantly at times, when n_e is
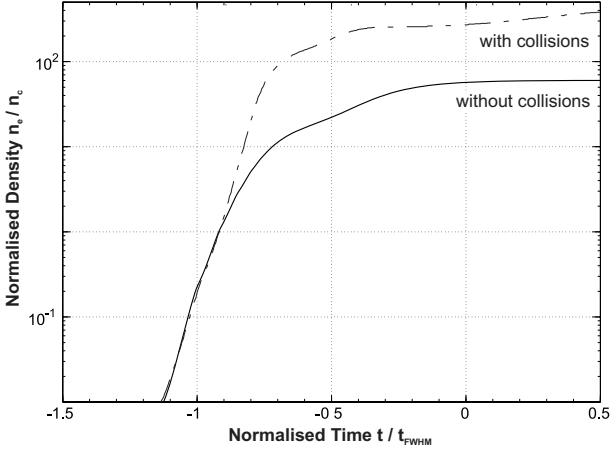
Figure 2.3: Time-dependent electron density with and without collisional ionisation. The time is normalised to t_{FWHM}, i.e. the FWHM of the pump pulse (800 nm, 60 fs, 10^{15} W/cm^2). Zero is at the peak intensity of the pump pulse.
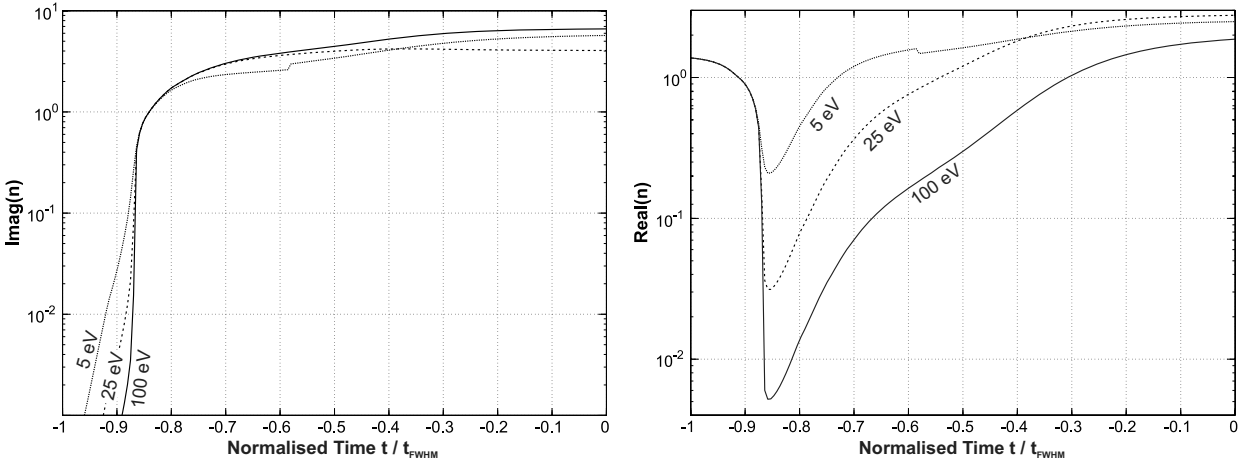
Figure 2.4: Complex index of refraction versus time for constant electron temperatures at the surface of a fused silica plate. The time is normalised to the FWHM of the pump pulse (800 nm, 60 fs, 10^{15} W/cm^2), zero is at the peak intensity of the pulse.

at least approximately as large as n_{ec}. A closer look shows that collisional ionisation slightly reduces the transition time and shifts the transition point (i.e. the time when $n_e(t)$ reaches n_{ec}) by a few femtoseconds. Thus, in summary, the transmission properties are not changed substantially by collisional ionisation.

2.2.2   The Time-Dependent Optical Properties

The next major step is to calculate the time-dependent optical properties of a thin plasma sheet, i.e. its complex index of refraction n. This can be accomplished using the Drude's model [24] of a metallic surface:

$$n^2 = \epsilon_\infty - \frac{1}{1+f^2}\frac{n_e}{n_{ec}} + i\frac{f}{1+f^2}\frac{n_e}{n_{ec}} \tag{2.3}$$

where ϵ_∞ is the dielectric function [187] at infinite frequency and f is a damping factor, equal to the electron–ion collision frequency normalised to the angular frequency ω_0 of the laser pulse. This damping factor can be estimated from Spitzer's theory [156]:

$$f = \frac{4\sqrt{2\pi}\,e^4}{(4\pi\epsilon_0)^2\sqrt{m_e}}\frac{n_e}{n_{ec}}\frac{Z_{eff}^2}{T_e^{3/2}}\frac{\ln\Lambda}{\omega_0} \tag{2.4}$$

In the last equation Z_{eff} is the average degree of ionisation, $\ln\Lambda$ is the Coulomb logarithm, m_e is the electron mass and T_e is the electron temperature. Because of the quickly

increasing ionisation the plasma is far from thermal equilibrium, thus, strictly speaking, a temperature is not defined. However, if the laser intensity is weak, then a reasonably good estimate of T_e is provided by the ionisation potential of the electrons, because one can argue that the electrons need a kinetic energy of the same order as the ionisation potential to prevent immediate recombination [114]. With increasing laser intensity the cycle averaged quiver energy [130], that the electrons gain in the oscillating laser field, becomes much larger than the ionisation potential, so that an estimate of T_e is given by the quiver energy. Note that the ADK theory limits the initial electron energy to 0.2 % of the quiver energy [5, 108]. Furthermore it works out that the temporal evolution of the transmission, derived from $\Im(n(t))$, depends only weakly on T_e (left plot in Figure 2.4). Note that this does not hold for the reflection, derived from $\Re(n(t))$ (right plot in Figure 2.4). Thus for modelling the transmission through the plasma a detailed knowledge of T_e is of minor importance, whilst it is important for calculating the reflection.

To calculate the transmissivity and reflectivity of the whole plasma, we consider a thin homogeneous plasma layer with a thickness dx first. The transmission through this layer is given by [24]:

$$T(t) = \exp\left(-\alpha(x, t)\, dx\right) \tag{2.5}$$

with the absorption coefficient $\alpha(t)$ and the speed of light c_0:

$$\alpha(t) = 2\frac{\omega_0}{c_0}\Im(n(t)) \tag{2.6}$$

On the other hand the reflectivity is given by Fresnel's equation [24], i.e. in the case of normal incidence:

$$R(t) = \frac{(\Re(n(t)) - 1)^2 + (\Im(n(t)))^2}{(\Re(n(t)) + 1)^2 + (\Im(n(t)))^2} \tag{2.7}$$

Hence the total transmission of the plasma layer is:

$$T_{tot}(t) \approx (1 - R(t))\, T(t) \tag{2.8}$$

The reciprocal of Eq. (2.6) is called the skin depth $l_{skin}(t)$ and is equivalent to the length over which the intensity of the radiation propagating through the plasma is absorbed by the free electron-gas to $^1/e$ of its initial value. This absorption mechanism is known as the skin effect, too.

In addition we define the ionisation depth:

$$l_{ioni}(t) := \frac{W_{n_e}(t)}{I_{pump}(t)} \tag{2.9}$$

where $W_{n_e}(t)$ is the power per volume, necessary to increase the ionisation according to the Keldysh ionisation rates, and $I_{pump}(t)$ is the pump pulse intensity. Thus $l_{ioni}(t)$ is an estimate of the plasma layer thickness, which can be ionised further, if the instantaneous power of the laser is fully consumed by the ionisation.

As shown in Figure 2.5 for early times $l_{ioni}(t)$ is much smaller than $l_{skin}(t)$, so that

the absorption of the probe pulse in the plasma can be neglected. In this case mainly the intensity of the pump pulse limits the thickness of the ionised plasma layer. If the plasma is almost opaque, then this situation starts turning upside down and $l_{ioni}(t) \gg l_{skin}(t)$ begins to hold. Now the thickness of the plasma layer with an increasing ionisation is determined by the skin depth. Consequently one can use the ionisation depth $l_{ioni}(t)$ and the skin depth $l_{skin}(t)$, whichever is smaller, to estimate the time dependent thickness of the plasma layer with rapidly growing ionisation. The ionisation process becomes more and more limited to a thinner layer at the target surface, because $l_{ioni}(t)$ and $l_{skin}(t)$ decrease with time. As one can neglect the hydrodynamic expansion of the plasma on these ultrashort time-scales, it is straight forward to derive an electron density profile along the axis of the incident laser beam. This profile has its peak density at the target surface and steeply falls off into the bulk. By numerical integration of Eq. (2.5) and Eq. (2.7) over this density profile one finally derives the reflectivity and transmissivity of the plasma.

2.2.3   Results and Validity of the Model

As already discussed in Subsection 2.2.1 on a longer time-scale collisional ionisation increases the ionisation rates considerable. Furthermore, even at very early times processes like multiple ionisation [46] and resonant multi-photon absorption [73] can increase the rates beyond the values calculated with the Keldysh theory. Anyway, all of them increase the rapidity of the switch even more and mainly advance the transition point by a few femtoseconds with respect to the pump pulse maximum. It is important to note, that other seemingly important processes can be neglected on time scales below hundred femtoseconds. Among them are the heating and ionisation of regions further away from the target surface, as this occurs on the longer time scale of the non-linear heat wave propagation. Using even an optimistic value of its propagation velocity of much more than 10^7 cm/s one easily calculates, that the duration for heating a depth of 1 μm requires at least several hundred femtoseconds. Also heating by highly energetic electrons [86] is of minor importance, because this requires higher laser intensities than the only moderate intensity of up to 10^{15} W/cm^2.

As shown in Figure 2.3 the electron density increases nearly exponentially with time, which is almost independent of the material used within the calculations. Thus the particular ionisation potentials of the material are of minor importance and the exponential increase is mainly determined by the laser pulse itself.

In Subsection 2.2.2 it was already discussed, that our model describes the reflectivity $R(t)$ less precisely than the transmissivity. Even worse for calculating $R(t)$ one has to derive the dielectric constant ϵ_∞ [187] included in $\Re(n(t))$ (see Eq. (2.3)) in addition. This constant is strongly dependent on the structure of matter, which changes drastically during the ionisation process. Thus our assumption, that ϵ_∞ is constant, is a rough description of the physical reality only. Nevertheless this coarse model gives valuable insight into the reflectivity of the plasma surface: initially there is a low but constant
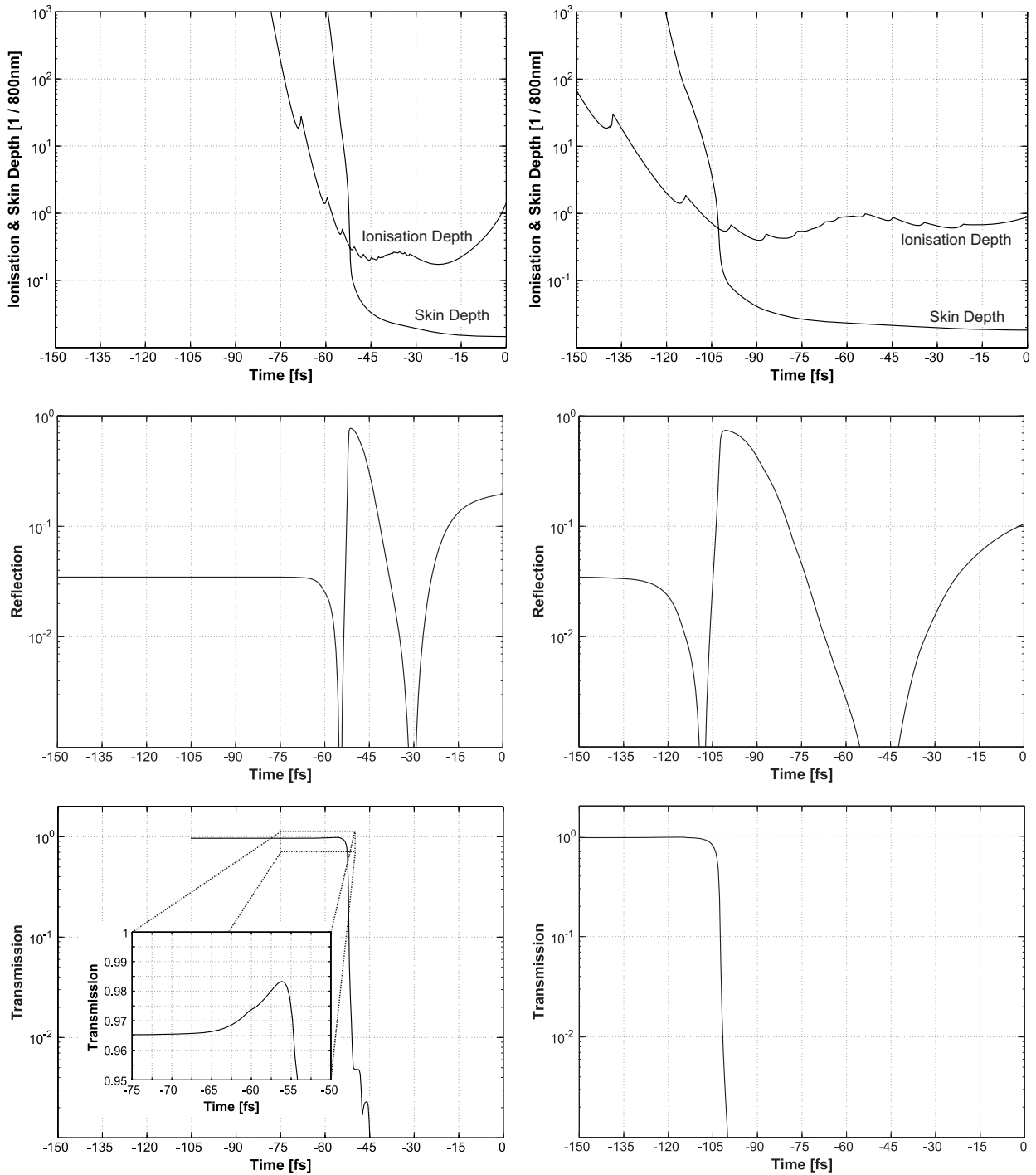
(a) 60 fs pulse, intensity: 10^{15} W/cm^2 (b) 140 fs pulse, intensity: $4 \cdot 10^{14}$ W/cm^2

Figure 2.5: Calculated time dependent ionisation depth, skin depth, reflectivity and transmissivity for a plasma produced with two different laser pulses ($\lambda = 800$ nm). The time zero is at the peak intensity of the pump pulse.

reflectivity, decreasing to zero, while the ionisation process is beginning. During the ionisation process the reflectivity increases again. After reaching a maximum it starts decreasing to zero once more, before it finally approaches a constant value at the end of the phase transition. This constant reflectivity is reached in a period longer than the duration of the laser pulse. This period and the final reflectivity, which is well below unity, depend on T_e (see Figure 2.4 and Figure 2.5). Hence it is questionable if the so called
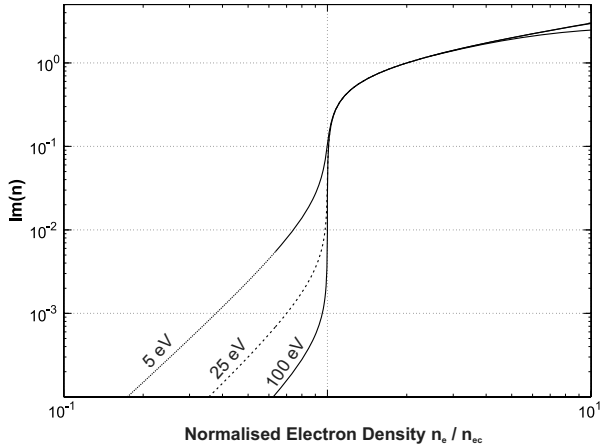
Figure 2.6: Imaginary part of the the refraction index, representing the absorption of laser radiation inside the plasma, versus the normalised electron density for different electron temperatures T_e. The electron density is normalised to the critical electron density of 800 nm radiation. For simplicity ϵ_∞ is set to unity.

plasma mirror is applicable for pulse cleaning on sub-hundred femtosecond time-scales.

The behaviour of the transmissivity $T(t)$ is much more simple: as shown in the lower plots of Figure 2.5, the transmission decreases by several orders of magnitude from a highly transparent state to an opaque one within a few femtoseconds. This fast decrease cannot be understood fully in terms of the approximately exponential increase of the electron density only. In addition one has to pay attention to a peculiarity of $\Im(n(t))$, as shown in Figure 2.6: if the normalised electron density n_{ec} is below unity, $\Im(n(t))$ is small, so that the absorption of radiation inside the plasma is negligible. As soon as n_{ec} becomes larger than unity, the absorption increases dramatically. This ultrafast change in the absorption is the reason for the rapidity of the gating process. As shown in Figure 2.6, the height of the step increases with increasing T_e. We found, that even if T_e is only a few electron volts, then the height of this step is still sufficient to assure an ultrafast transition. Furthermore the simulations reveal a response time in the order of a single oscillation of the pump pulse. In an experiment, which averages over several laser pulses, this is quite naturally a lower limit for the response time, as the phase of the fast oscillating carrier frequency of the laser pulse is not locked to the pulse envelope in general. In addition Keldysh's theory is not a fully time-dependent quantum mechanical ionisation model, so that the calculated ionisation rates may not be valid on the time-scale of the carrier frequency. An upper limit for the response time of the gating process is given by a simple energy consideration: if the ionisation depth is much smaller than the skin depth, then the plasma is transparent, while in the opposite case it is opaque. Thus the duration of the transition between these two extrema is an upper limit for the response time. As seen from the upper two plots in Figure 2.5 this is roughly ⅕ of the FWHM of the pump pulse. Consequently during an experiment one can expect a response time well below ⅕ of the pump pulse's FWHM, but larger than the theoretical limit of an oscillation period.

In the last paragraph only the absorption of the laser radiation inside the plasma was discussed. But for calculating the total transmission $T_{tot}(t)$ one has to pay attention to the reflectivity, too (compare Eq. (2.8)). Even, if one does not know the reflectivity precisely, one does not introduce a considerable error into the calculated transmissivity, because the reflectivity is only a few percent, while the plasma is transparent. Nevertheless as
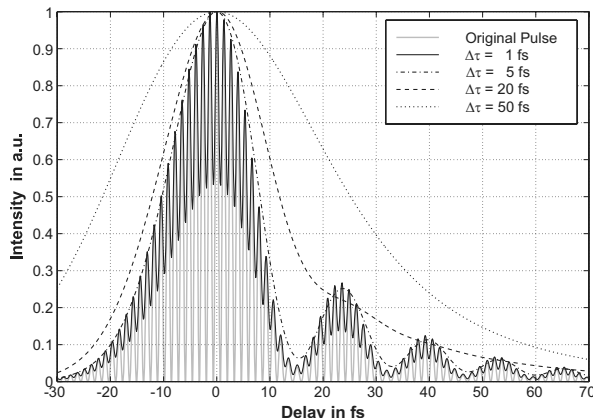
Figure 2.7: Simulated reconstruction of a strongly chirped optical pulse (800 nm, 18 fs). Before reconstruction the original pulse was convoluted with an error function of slope $\Delta\tau$ representing the gating function (compare Eq. (2.10)).

the reflectivity reduces to zero in the early phase of the plasma formation, while the absorption is still next to zero, one observes a few percent increase of the transmissivity (see inset of Figure 2.5(a)). This increase was measured in the experiment described in Section 2.4, too. With a peak pump pulse intensity of 10^{15} W/cm^2, $4 \cdot 10^{15}$ W/cm^2 and 60 fs, 140 fs, respectively, the parameters of the simulation shown in Figure 2.5 match the experimental conditions from Section 2.4.

2.3 Basics of Ultrafast Optical Gating

To verify the theoretical predictions from Section 2.2 one can perform a pump–probe experiment as proposed in Section 2.1 thus measuring the correlation function between the transmission properties of the plasma and the probe pulse. To re-obtain either the optical transmission properties of the plasma or the parameters of the probe pulse from the measured correlation function, it is vital to have a good understanding of the mathematical background behind these functions.

2.3.1 Basics of Pulsed Gating

The energy of a time-dependent optical signal, i.e. the probe pulse $s(t)$, can easily be measured with a time-integrating detector. On the other hand, it may be extremely difficult or even impossible to measure the fast vibrating electric field amplitude of the probe pulse itself. This obstacle can be overcome by putting a fast shutter in front of the time integrating detector. In our case this shutter is represented by the plasma, which is created with different delays τ with respect to the probe pulse. In the following we will call this application of the plasma the *plasma switch*. If its time-dependent transmission is given by $G(t)$ and the electric field of the probe pulse is $s(t)$ again, then one can measure their correlation:[§]

$$s_f(\tau) = \int_{-\infty}^{\infty} |s(t)\, G(t-\tau)|^2 \; dt \qquad (2.10)$$

Ideally $G(t)$ would be equal to a Dirac function, so that Eq. (2.10) reduces to $s_f(\tau) = s^2(\tau)$. This is experimentally difficult to realise, because two nearly instantaneous tran-

---

[§]In a more general case $G(t-\tau)$ and $s(t)$ are not a product, but $G(t-\tau)$ is a functional on $s(t)$: $G(t-\tau)\{s(t)\}$

sitions (one from closed to open and another one from opened to closed) are needed in a rapid series. More simple is a switch using a single transition, e.g. from open to closed. Ideally this transition is instantaneous, so that $G(-t)$ would equal the Heaviside function $H(-t)$ (see Eq. (A.25)). A good approximation of $H(t)$ is a time integrated Gauss function, also known as error function (see Eq. (A.24)), with a steep slope, i.e. short response time $\Delta\tau$. Our theoretical considerations in Subsection 2.2.3 show that the plasma switch is fast with a response time below $1/5$ of the duration of the pump pulse. Hence it is sensible to assume that the plasma switch is a good experimental approximation for an error function with a steep slope and thus for a step-like gating function.

As the temporal evolution of the signal $s(t)$ is measured by shifting the gating function across the signal, the temporal resolution is limited by the response time $\Delta\tau$ of the gating function. For resolving all details of the signal one would expect $\Delta\tau$ to be much shorter than the fastest variation of the signal (More precisely: the frequency $\frac{1}{\Delta\tau}$ is much larger than the highest frequency contained in the signal). Considering an optical or a VUV / XUV pulse for instance, this requires $\Delta\tau$ to be much smaller than 1 fs as shown for a pulse with a central wavelength of 800 nm and a pulse duration of 18 fs in Figure 2.7. In this case Eq. (2.10) reduces to $s_f(\tau) = \int_{-\infty}^{\tau} s^2(t)\,dt$ and $s^2(t)$ can be obtained by simply deriving $s_f(\tau)$. Unfortunately such fast switches do not exist so far. Another principal problem of these switches would be, that averaging over several pulses $s(t)$ can wipe out the fast oscillating carrier frequency easily, due to a small jitter of its absolute phase relative to its envelope among adjacent pulses. Consequently it is probably impossible with the plasma switch to measure the fast oscillating carrier frequency directly. For measuring the pulse envelope exclusively, a gate with $\Delta\tau < 10$ fs is sufficiently fast in the case of an 18 fs pulse (see Figure 2.7). This is longer than $1/5$ of the pulse duration, so that measuring the pulse envelope should be easily accomplished with the plasma switch (see Section 2.2). Furthermore, note, that if the gate is much slower than 20 fs, then one cannot even directly measure the envelope for pulses shorter than 100 fs.

2.3.2 Spectrally Resolved Pulsed Gating

Despite all these limitations it is possible with a more sophisticated approach to measure the properties of the fast oscillating carrier frequency. One may be tempted to obtain this information by measuring the energy spectrum of the pulse, but this only tells us which frequencies appear during the pulse and does not give us any information in which order these frequencies appear. For example, if the fast oscillating carrier frequency is either chirped from red to blue or from blue to red, then the energy spectra do not differ. The only way to distinguish between these two cases is a time-dependent Fourier analysis:

Instead of measuring the energy of the gated pulse as described by Eq. (2.10) one can put a spectrometer behind the gate, thus measuring the energy spectrum of the gated pulse, i.e. a time–frequency function:

$$s_f(\tau, \omega) := |\mathfrak{F}_{t\to\omega}\{s(t)\,G(t-\tau)\}|^2 \qquad (2.11)$$

with the Fourier transform $\mathfrak{F}_{t\to\omega}$ (see Appendix A.1). As the product $s(t)\,G(t-\tau)$ is a real function, the energy spectrum $s_f(\tau,\omega)$ is symmetric with respect to ω, i.e. $s_f(\tau,\omega) = s_f(\tau,-\omega)$, so that one can limit $s_f(\tau,\omega)$ to positive frequencies only, i.e. $s_f(\tau,\omega)|_{\omega<0} = 0$. This frequency limited spectrum is called the half range energy spectrum (see Appendix B.1.2). In many cases algebra is simplified even more by using the quasi half range energy spectrum $s_f^+(\tau,\omega)$ (see Appendix B.1.3), which is not exactly zero for $\omega < 0$, but can be considered to be zero at these points for all practical purpose. Due to this $s(t)$ and $G(t-\tau)$ become complex functions, which have to satisfy additional constraints given in Theorem B.3. As a reminder of this we shall write $s_c(t)$, $G_c(t-\tau)$ instead of $s(t)$ and $G(t-\tau)$ below. Furthermore in Appendix B.2 it is shown that these constraints are satisfied for all reasonable gating functions and all optical pulses, if written as complex functions.

Using the quasi half range signal and the identities from Appendix A.1 and A.2 one can rewrite Eq. (2.11) in a way which is more convenient for further discussion:

$$s_f^+(\tau,\omega) = \mathfrak{F}_{t\to\omega}\{F^+(\tau,t)\} \tag{2.12a}$$

$$F^+(\tau,t) := \bar{s}(\tau,t) *_\tau \bar{G}(\tau,t) \tag{2.12b}$$

$$\bar{s}(\tau,t) := s_c\left(\tau+\frac{t}{2}\right) s_c^*\left(\tau-\frac{t}{2}\right) \tag{2.12c}$$

$$\bar{G}(\tau,t) := G_c\left(-\tau+\frac{t}{2}\right) G_c^*\left(-\tau-\frac{t}{2}\right) \tag{2.12d}$$

It is important to note that Eq. (2.12b) and thus Eq. (2.12a) are completely symmetric concerning $\bar{s}(\tau,t)$ and $\bar{G}(\tau,t)$. Thus our two initial problems to calculate either the gating function, if the probe pulse properties are known, or to calculate the probe pulse properties, if the gating function is known, are completely identical from a mathematical point of view. Consequently one can limit the discussion to the latter case without any restrictions.

If $G(t) = H(-t)$ e.g., then the derivative

$$P_{PDF}(\tau,\omega) := \frac{\partial}{\partial\tau} s_f^+(\tau,\omega) \tag{2.13}$$

is called the Page distribution function (PDF): in 1951 C. Page argued [123], that in this case Eq. (2.12a) can be interpreted as a time running energy spectrum representing the total energy per frequency contained in the signal $s(t)$ up to the time τ. Thus the derivative given by Eq. (2.13) is the time-dependent change of frequency contents and can be considered as the instantaneous energy spectrum.

Obviously the Heaviside function is not the only possible gating function, so that one can construct different time-running energy spectra. Hence the question arises, how the various gating functions differ and if there is an outstanding one.

2.3.3 Time–Frequency Distribution Functions

A more fundamental study of these time-running energy spectra shows, that they are part of a set of joint time–frequency distribution function $P(\tau, \omega)$ [52, 123, 179]. Quite naturally one expects that these distribution functions hold two very fundamental constraints, called the Marginals:

$$\int_{-\infty}^{\infty} P(\tau, \omega) \, d\omega \;=\; |s_c(\tau)|^2 \tag{2.14}$$

$$\int_{-\infty}^{\infty} P(\tau, \omega) \, d\tau \;=\; |\widetilde{s}_c(\omega)|^2 \tag{2.15}$$

That is to say, by integrating out one variable, one either obtains the envelope or the energy spectrum of the pulse, respectively. Nevertheless it is still possible to construct an infinite number of these distribution functions with a bewildering manifoldness of properties, each dedicated to a different application, so that there is no generally outstanding one. A comprehensive review, explaining the properties of the most important time–frequency distribution functions, has been published by Cohen [33].

It was also noticed by Cohen [32] first, that all commonly used time–frequency distribution functions can be generated from a rewritten Eq. (2.12):

$$P(\tau, \omega) = \mathfrak{F}_{t \to \omega} \mathfrak{F}_{\theta \to \tau}^{-1} \mathfrak{F}_{u \to \theta} \left\{ \phi_{s_c}(\theta, t, \tau, \omega) \, s_c \left(u + \frac{t}{2} \right) s_c^* \left(u - \frac{t}{2} \right) \right\} \tag{2.16}$$

ϕ_{s_c} is called the kernel [30], where the index s_c denotes that the kernel can be a functional of the signal s_c. If the distribution function is time–frequency invariant (which applies for all well known distribution functions) then ϕ_{s_c} depends on θ and t only:

$$\phi_{s_c}(\theta, t) := \mathfrak{F}_{u \to \theta} \left\{ \frac{\partial}{\partial u} \left[G_{c,s_c} \left(-u + \frac{t}{2} \right) G_{c,s_c}^* \left(-u - \frac{t}{2} \right) \right] \right\} \tag{2.17}$$

Again in the case of the PDF:

$$\phi_{\text{PDF}}(\theta, t) := \frac{e^{i\theta|t|/2}}{\sqrt{2\pi}} \tag{2.18}$$

Separating the time–frequency distribution function into a signal dependent and a gating function dependent part has the huge advantage that the properties of the distribution function can be studied independently from the signal by studying the kernel. An even more modern approach goes one step further, using wavelet transforms and their intrinsic two dimensionality to avoid the issue of manyfold kernels [4, 65, 121].

From Eq. (2.16) an inversion formula is easily derived, if the kernel is not a functional of the signal $s_c(t)$:

$$M(t, \bar{t}) := s_c(t) \, s_c^*(\bar{t}) = \mathfrak{F}_{\theta \to (t+\bar{t})/2}^{-1} \mathfrak{F}_{\tau \to \theta} \mathfrak{F}_{\omega \to t - \bar{t}}^{-1} \left\{ \frac{P(\tau, \omega)}{\phi(\theta, t - \bar{t})} \right\} \tag{2.19}$$

If the kernel has only isolated zeros, then it is still possible to calculate $M(t, \bar{t})$ with steady continuation, as shown by Nutall [33]. By setting $\bar{t} = 0$ one can use this equation to calculate the original signal up to a constant phase from the measured time–frequency
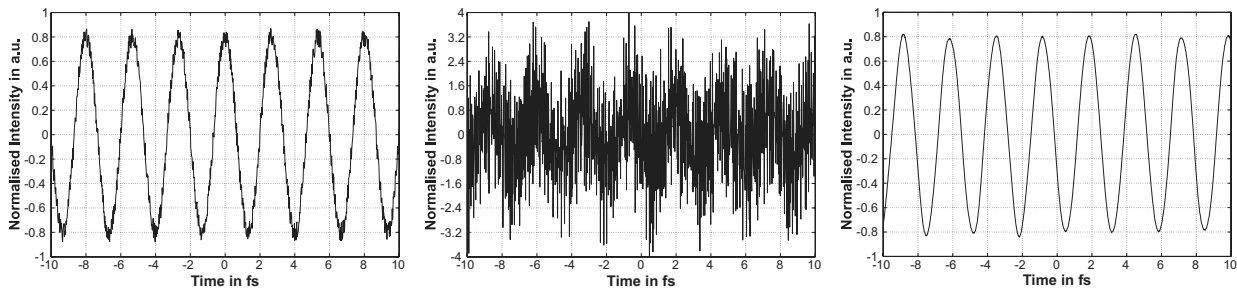
Figure 2.8: Derivative of a noisy signal: (left): original signal; (centre): direct derivative, i.e. differences between adjacent samples; (right): derivative with a digital differentiator filter.

distribution function. If one considers the case of a step-like gating function again, then Eq. (2.19) reduces to:

$$\widehat{s_f^+}(\tau, t) := \sqrt{2\pi} \, \frac{\partial}{\partial \tau} \, \mathfrak{F}_{\omega \to t}^{-1} \{s_f^+(\tau, \omega)\} \tag{2.20a}$$

$$M(t, \bar{t}) = s_c(t) \, s_c^*(\bar{t}) = \widehat{s_f^+}\left(t + \frac{|t - \bar{t}| - (t - \bar{t})}{2}, t - \bar{t}\right) \tag{2.20b}$$

The drawback of this seemingly simple method for deriving $s_c(t)$ from the measured $s_f^+(\tau, \omega)$ is, that all redundant information embodied in $M(t, \bar{t})|_{\bar{t} \neq 0}$ is neglected, leading to an unnecessary erroneous and noisy reconstruction of $s_c(t)$. This is even worse as the measured time–frequency function $s_f^+(\tau, \omega)$ contains some noise, which is dramatically increased by the derivative in Eq. (2.20a). This problem can be reduced by applying a digital differentiator filter [122] to the measured signal instead of calculating the derivative directly (see Figure 2.8). In our measurements the noise problem could not be overcome completely and due to the inherent frequency filter the measured signal could be altered significantly. Thus the direct reconstruction is not very feasible for most practical applications.

More promising is an alternative approach based on Eq. (2.11) again. Instead of calculating a reconstruction of $s_c(t)$ from the measured data, one assumes an arbitrary synthetic and noiseless signal $s_{c,a}(t)$, which is adapted in such a manner that its related time–frequency function (calculated with the help of Eq. (2.11)) fits the original measured data in a least-square sense. In many cases the signal $s_{c,a}(t)$ is subject to additional constraints, satisfying Maxwell's equations for optical signals and a limited spectral width etc., so that it is often possible to describe the signal by a mathematical model based on a few parameters. Hence only a few free parameters are involved in the fitting procedure, so that this approach is quite efficient. This is the main idea behind pulse reconstruction with frequency resolved optical gating (FROG) [178].

2.3.4 Signal Reconstruction using the First and Second Momentum

Despite these two approaches to re-obtain the original signal from the measured time–frequency function an even more simple method exists in the case of step-like gating functions. This approach is based on calculating the zeros and first conditional momentum of the time–frequency function. Using Eq. (2.12) and the equations tabulated in Appendix A.3.2, this calculation is straight forward.

The zeros momentum is given by:

$$M_{s_f^+}^{(0)}(\tau) := \int s_f^+(\tau, \omega) \, d\omega = \frac{1}{\sqrt{2\pi}} \iint F^+(\tau, t) \, e^{it\omega} \, dt \, d\omega \tag{2.21}$$

$$= \frac{1}{\sqrt{2\pi}} \int F^+(\tau, t) \int e^{it\omega} \, d\omega \, dt = \int F^+(\tau, t) \, \delta(t) \, dt = \bar{s}(\tau, 0) *_\tau \bar{G}(\tau, 0)$$

Calculating the first momentum results in:

$$M_{s_f^+}^{(1)}(\tau) := \int \omega \, s_f^+(\tau, \omega) \, d\omega = \frac{1}{\sqrt{2\pi}} \iint F^+(\tau, t) \, \omega \, e^{it\omega} \, dt \, d\omega \tag{2.22}$$

$$= \frac{1}{\sqrt{2\pi}} \int F^+(\tau, t) \int \omega e^{it\omega} \, d\omega \, dt = -i \int F^+(\tau, t) \left(\frac{\partial}{\partial t} \delta(t) \right) \, dt$$

$$= -i \int \left(\frac{\partial}{\partial t} F^+(\tau, t) \right) \delta(t) \, dt = -i \left[\frac{\partial}{\partial t} \left(\bar{s}(\tau, t) *_\tau \bar{G}(\tau, t) \right) \right]_{t=0}$$

$$= -i \left[\frac{\partial}{\partial t} \bar{s}(\tau, t) \right]_{t=0} *_\tau \bar{G}(\tau, 0)$$

To simplify the last two equations, note that the signal s_c is a function $\mathbb{R} \mapsto \mathbb{C}$. Hence one can write without any limitations $s_c(\bar{t}) := A(\bar{t}) \, e^{i\varphi(\bar{t})}$ with $A, \varphi : \mathbb{R} \mapsto \mathbb{R}$. With the definition of $\bar{s}(\tau, t)$ (see Eq. (2.12c)) one finds:

$$M_{s_f^+}^{(0)}(\tau) = A^2(\tau) *_\tau \bar{G}(\tau, 0) \tag{2.23a}$$

$$M_{s_f^+}^{(1)}(\tau) = \left(A^2(\tau) \, \varphi'(\tau) \right) *_\tau \bar{G}(\tau, 0) \tag{2.23b}$$

In the case of the PDF $G(\bar{t}) = H(-\bar{t})$, so that $\bar{G}(\tau, 0) = H(\tau)$. Then the zeros and first momentum are:

$$M_{s_f^+}^{(0)}(\tau) = \int s_f^+(\tau, \omega) \, d\omega = \int_{-\infty}^{\tau} A^2(t) \, dt \tag{2.24a}$$

$$M_{s_f^+}^{(1)}(\tau) = \int \omega \, s_f^+(\tau, \omega) \, d\omega = \int_{-\infty}^{\tau} A^2(t) \, \varphi'(t) \, dt \tag{2.24b}$$

The last two equations are the most important ones as they directly relate the measured quantity $s_f^+(\tau, \omega)$ with the envelope and phase of the original signal. These equations will be used to analyse the experimental data presented in the next section.

2.4   The Ultrafast Gating Experiment

Eventually we turn our attention to the experiment, which was performed to justify the theoretical predictions from Section 2.2. Before the measurements are presented and discussed the experimental setup and its alignment are explained.

2.4.1   Performing The Experiment

An overview of the experimental setup is given in Figure 2.9. One immediately recognises the typical pump–probe setup, where the laser pulse is split into a strong *pump pulse* and a much weaker *probe pulse*. In our particular setup the pump pulse is delayed with respect to the probe pulse.
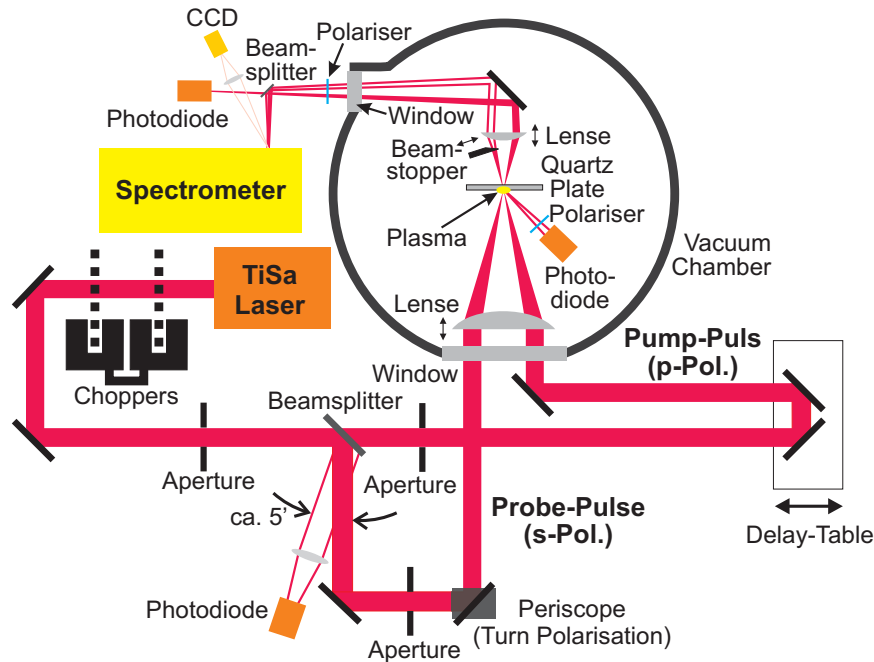
Figure 2.9: Setup of the ultrafast gating experiment

2.4.1.1 Experimental Setup

The Laser and Optical Chopper   The laser used throughout this experiment is a commercial 1 kHz, 1 mJ Ti:Sa laser [11] with a pulse duration of 60 fs, a central wavelength around 800 nm and a default beam diameter of a bit less than 10 mm. This laser is situated at the IOQ in Jena. During our experiment the repetition rate of the laser is reduced to a few Hertz, so that there is sufficient time between two adjacent laser pulses to move the target plate, on which the plasma spot is produced, to an area not affected by former laser pulses.

The reduction of the repetition rate is accomplished by putting two synchronised optical choppers into the optical path. The chopper plates are equipped with discs of roughly 150 mm diameter, each of which contains a single hole of 10 mm diameter close to the edge of the disc. Their minimal rotational speed is given by the constraint that the chopper plates must rotate for at least one hole diameter between two adjacent laser pulses. Using a series of two choppers, the laser's repetition rate can be chosen between less than 1 Hz and some 100 Hz.

The Beam-Splitter   Behind the optical choppers the laser beam is reflected from two alignment mirrors used to align its height and pointing. The correct alignment of the beam is determined by two apertures. The first one is positioned between the last alignment mirror and the beam-splitter, the second one is setup in the transmitted beam right behind the splitter. The beam-splitter itself consists of a 1 mm thick, slightly wedged fused silica plate, reflecting about 4 % of the beam from each of its two surfaces in somewhat different directions close to 45°. The transmitted pulse is the pump pulse, whilst the pulse reflected from the front surface is the probe pulse. The pulse reflected from the rear was originally focused onto a photodiode to control the incident energy of the laser throughout the experiment.

The Probe Pulse   Right after the probe pulse is reflected from the wedged beam-splitter, it passes through an alignment aperture. By closing this aperture one can reduce the beam's intensity inside the fused-silica plate so that its B-integral [2, 25] is still small after propagating through the target plate. Behind this aperture the polarisation of the probe pulse was rotated by 90° to be perpendicular to the polarisation of the pump pulse with the help of a periscope. After this periscope the beam passes through the 10 mm thick fused-silica entrance window of the target chamber before being focused onto the front surface of the target by an achromatic calcium-fluoride lens with $f = 250$ mm focal length.

The transmitted probe pulse is collected with a $f = 50$ mm fused-silica focusing lens. This lens is set up to produce an 80 times magnified image of the probe pulse's focal spot in a distance of 4 m away from the target surface. 25 cm behind this lens the pulse leaves the vacuum chamber through another 10 mm thick fused-silica window and passes a thin-film polariser. As the polarisation of the scattered light from the much stronger pump pulse is perpendicular to the polarisation of the probe pulse, this polariser reduces the impact of scattered light from the pump pulse on the measured probe pulse signal considerably.

20 cm in front of the image plane the probe pulse is split into two beams by a 1 mm thick glass plate. In the image planes of the two beams reflected from the front and rear surface of this plate a small photodiode (diameter less than 1 mm) is located for measuring the energy in the centre of the probe pulse. The diode is mounted onto a xy-translation stage, so that it can be easily centred on the image of the probe pulse. The tip of an optical fibre, surrounded with a white screen, is positioned in the image plane of the transmitted beam. The tip and the screen are both mounted onto a xy-translation stage, so that the tip can be aligned to the centre of the image. To simplify this alignment, the tip is observed with a CCD. The fibre itself is connected to an optical spectrometer with a resolution of $\lambda/\Delta\lambda$=1600. The spectrometer itself is equipped with a 12 bit CCD.

The Pump Pulse   This section describes the beam transmitted through the wedged beam-splitter, i.e. the pump pulse. Right after this beam-splitter the pump pulse passes the above mentioned alignment aperture before it is reflected back with a collateral shift from two mirrors mounted on a translation stage. This stage, also called the delay stage, has 35 mm range of motion and is driven by a stepper motor. The mirrors are aligned in such a way that the incident and reflected beam are exactly parallel. In addition, the direction of motion of the stage is also parallel to the beams. Hence changes in the pointing and lateral position of the back-reflected beam are minimised over the stage's range of motion. The path difference between the pump and probe pulse is chosen to be zero, if the delay stage is roughly centred between its two final positions. The unidirectional positioning accuracy of this stage has been increased to 160 nm per step, matching a time-delay of 1 fs.

After the delay stage another mirror right in front of the target chamber steers the

pump pulse through the entrance window and the focusing lens onto the target. With the help of this mirror it is possible to spatially overlap the pump and the probe pulse. Due to the small beam-diameter of the laser (less than 10 mm) the focal spot of the pump pulse has a diffraction limited FWHM of 25 µm. As the pump's energy is some 100 µJ on target, the average focused intensity is about 10^{15} W/cm^2.

Behind the target the remaining pump pulse is blocked with a knife-edge mounted onto a remote controlled translation stage. During the experiment the knife-edge blocks the transmitted pump pulse and most of its scattered light. But for alignment purposes it is moved out of the beam, so that the pump and probe pulse can be imaged onto the white screen around the tip of the optical fibre.

The Target The target is mounted on a remote controlled xyz-translation stage with a special target holder. With the help of this target holder it is possible to align the target precisely parallel to the xy-plane of the translation stage, so that one can move the target along this plane for several centimetres without changing its focal position by more than a few micrometers, which is much less than the focal depth (several 100 µm) of the laser pulses. With the help of the z-motion it is possible to align the front surface of the target precisely at the focal position. The x- and y-motions are controlled by a Labview [115] programme to move the focal spot over the target surface in a wriggled line, so that each laser pulse hits an unspoiled area of the surface.

The target itself consists of a 1 mm thick fused-silica glass plate. To check if the properties of the probe pulse are altered by non-linear interactions while propagating through the target plate, a control experiment was carried out. In this experiment the fused-silica plate was replaced with a 10 µm thick polyethylene foil, reducing the B-integral by approximately two orders of magnitude. Comparing the results of the two experiments no difference was found, so that one can rule out any non-linear effect influencing the probe pulse.

2.4.1.2 The Alignment Procedure

The alignment is carried out in two steps: a pre-alignment step, performed in air, and a precision alignment step, performed after the target chamber was evacuated.

Pre-Alignment At first the knife-edge is moved out off the pump pulse, the target is removed, all apertures are opened completely and ND-filters are placed in the pump and probe beam, so that one can use a microscope objective and a CCD to observe 40 times magnified images of the pump and probe beam's focal spots. Then the spatial overlap between the pump and probe pulse is aligned by turning the mirror, which is steering the pump pulse into the target chamber. Furthermore the lateral shift of these pulses against each other is checked over the whole 35 mm range of motion of the delay stage. This lateral shift is less than 50 µm. Thus this shift can be neglected for pulses shorter than a few ps as this corresponds to a translation range of less than 1 mm.

Finally the microscope objective, the CCD and the ND-filters are removed and the aperture in the probe beam is nearly fully closed to avoid producing a plasma with this

Pulse Type	Pulse FWHM T_H [fs]	Linear Chirp c_2 [fs^2]	Quadratic Chirp c_3 [fs^3]
Compressed	63	650	$2.7 \cdot 10^4$
Uncompressed	138	2400	$2.7 \cdot 10^4$

Table 2.1: Parameters of the two pulses used during the experiment right in front of the target: note that the chirps are given in the spectral domain, whilst the pulse-duration is in the temporal domain, of course. Thus the spectrum of the pulse is given by: $\widetilde{s^+}(\omega) = \exp\left(-\frac{T_H^2}{16\ln 2}(\omega - \omega_0)^2 + \sum_{j=2}^{\infty} i\frac{c_j}{j!}(\omega - \omega_0)^j\right)$ with the central frequency ω_0 of the laser pulse [162].

beam. The aperture in the pump beam is closed so much, that the air plasma, produced with the pump pulse, is just still visible. Then the probe pulse is used to observe the air plasma produced with the pump pulse: if the probe pulse is arriving in advance of the pump pulse, then it is not influenced by the raising air plasma; whilst, if it is delayed, strong diffraction patterns (several cm in diameter) can be observed with an infrared viewer on a white screen, located a few cm behind the target plane. Therewith one can determine the temporal overlap between the two pulses within 100 fs. Note that the electron density of the plasma produced in air is not sufficiently high to block the probe pulse, so that the plasma switch experiment cannot be carried out with an air plasma.

Precision Alignment   After installing the target again and evacuating the target chamber the final alignment is performed to correct for any misalignments due to evacuating the target chamber. At first all apertures are opened again and the focal position of the target is determined by moving the z-motion of the target and optimising the x-ray emission from the plasma produced with the pump pulse. This emission is measured with a silicon photodiode (Hamamatsu S1336 [69]).

Then the intensity of the pump pulse is lowered by putting ND-filters into the beam, so that this beam produces tiny burn marks on the target surface only. These burn marks are used to properly centre the probe pulse with respect to the plasma. This is accomplished by blocking the pump pulse with the knife-edge and observing the image of the probe pulse on the screen surrounding the tip of the optical fibre (see Figure 2.9). The burn marks can be seen as a dark spot in the probe beam's image.

To align the temporal overlap between the two pulses all ND-filters and the knife edge are removed and all apertures are nearly completely closed. The aperture of the probe pulse remains a bit more open to compensate for this beam being roughly 30 times weaker than the pump pulse. Then the delay stage is moved, until an interference pattern between the two beams becomes clearly visible in the image on the above mentioned screen. Thus it is possible to determine the temporal overlap within a few 10 fs.

Finally all apertures are set to there initial diameters and the knife-edge is set up to block the pump pulse and its scattered light as much as possible without blocking the probe pulse.

2.4.2   Discussion of the Experimental Results

To demonstrate how the plasma switch is working in an experiment, a series of CCD images with different time delays between the pump and probe pulse is shown in Fig-
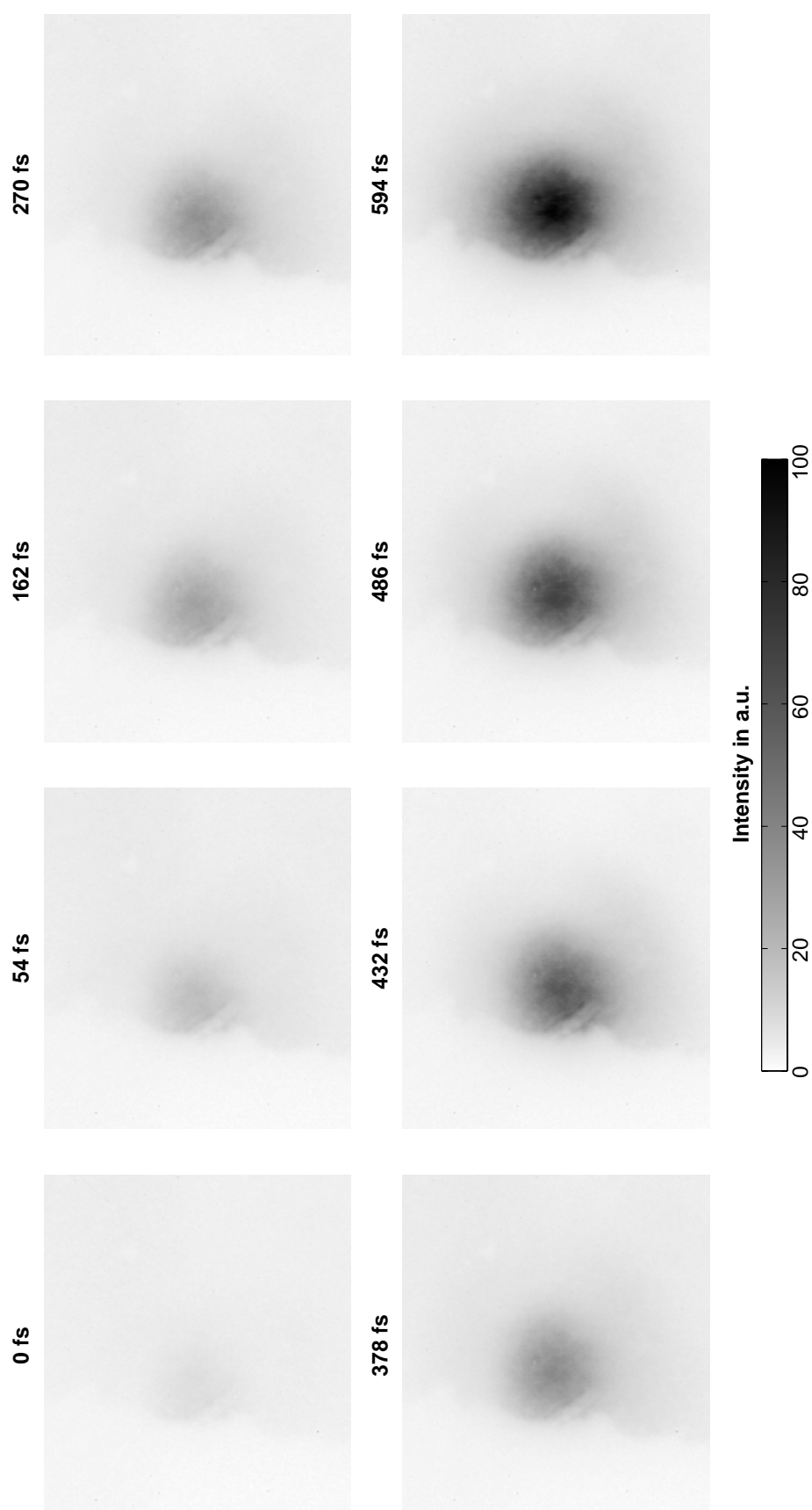
Figure 2.10: Time series of the plasma cutting off the probe pulse. Note, that this data set was obtained during a previous test experiment carried out with a 550 fs, 10 mJ, 248 nm KrF^*-laser.

(a) Compressed pulse (see Table 2.1)   (b) Uncompressed pulse (see Table 2.1)
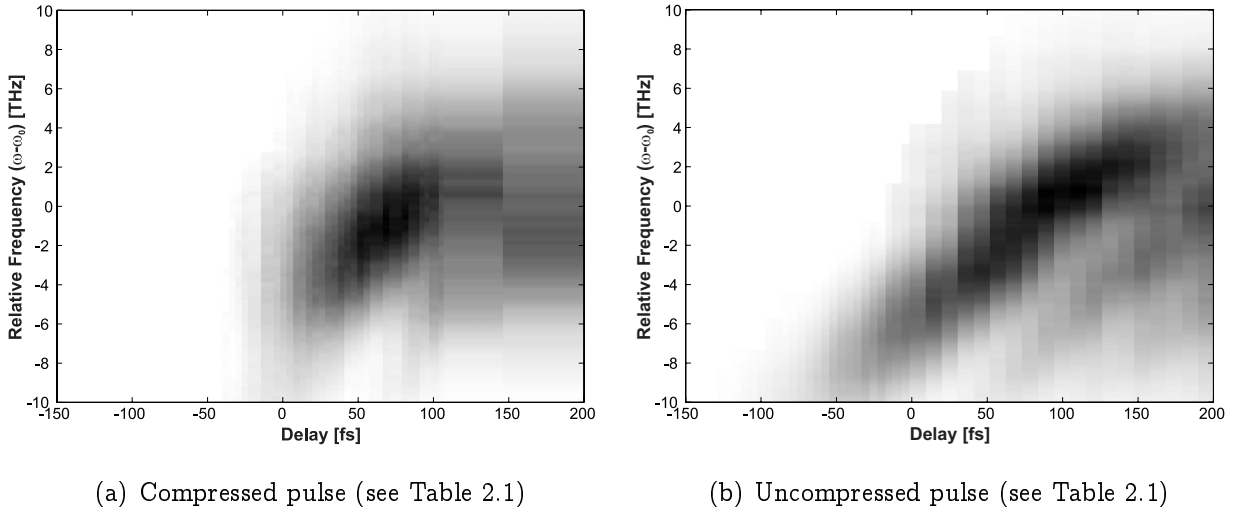
Figure 2.11: Two-dimensional time–frequency functions of the experimental data: the time delay τ between the pump and probe pulse is given by the abscissa, whilst the relative frequency $\omega - \omega_0$ of the energy spectra is given by the ordinate. ω_0 is the central frequency of the probe pulse.

(a) Compressed pulse (see Table 2.1)   (b) Uncompressed pulse (see Table 2.1)
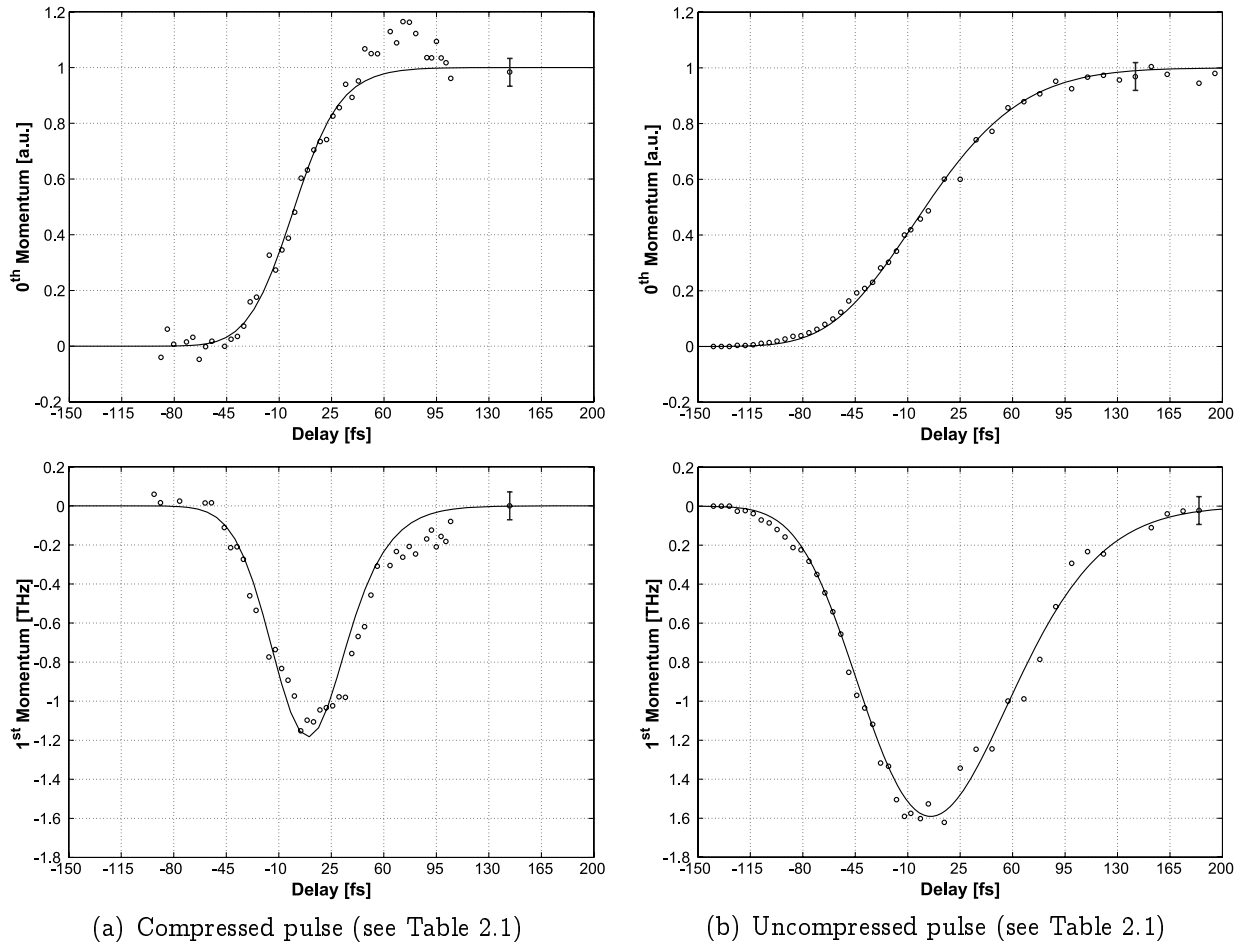
Figure 2.12: Zeroth and first conditional momentum of the time–frequency functions: the straight line represents the momenta calculated from the FROG measurement, whilst the open circles represent the momenta derived from the measured data shown above.

(a) Simulation: $\Delta\tau$=1 fs   (b) Measurement   (c) Simulation: $\Delta\tau$=40 fs
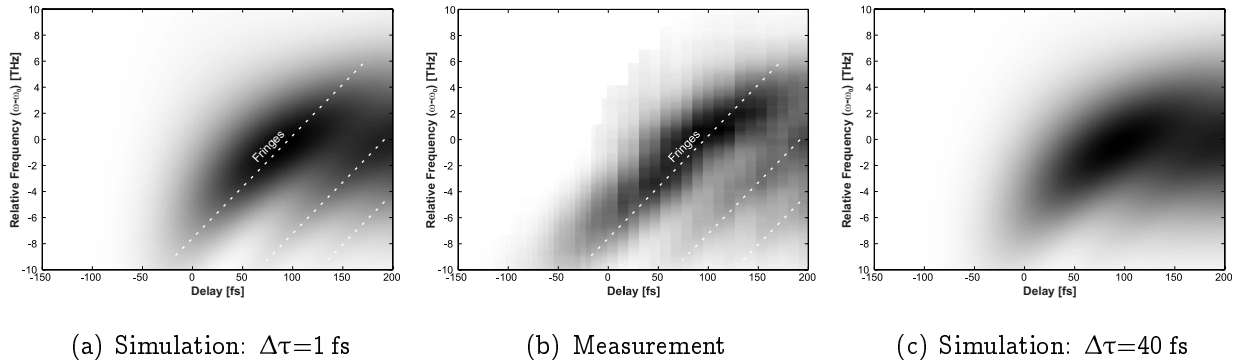
Figure 2.13: Comparison between the measured time–frequency function of the uncompressed pulse (see Table 2.1) and computer simulations based on the appropriate pulse parameters, but using different response times $\Delta\tau$ of the gating function. Figure 2.13(a) represents the ideal step function, showing a clearly visible fringe pattern that is blurred in Figure 2.13(c).

ure 2.10. It is clearly seen that with increasing delay time less of the probe-pulse is cut-off. Note, that this data set was obtained during a previous test experiment carried out with a 550 fs KrF*-laser. In contrast to that, the recent experiment is performed with two different Ti:Sa pulses: a *compressed* and an *uncompressed* one, generated by moving the compressor gratings. The two pulses were characterised with a standard FROG setup [43, 178] right behind the compressor gratings. Due to the huge bandwidth of these short fs-laser pulses the different frequency components of the pulse propagate with slightly different phase velocities through matter. Hence the initial pulse incures a group velocity dispersion [24, 43], while propagating from the laser through air and optical elements to the target. To account for this the appropriate pulse parameters at the target surface have been calculated from the values measured at the laser using the programm LAB II [89]. These calculated values are listed in Table 2.1. Furthermore it was assured, that the uncompressed pulse had a positive chirp, i.e. its carrier frequency increases with time. To measure the time–frequency function (see Subsection 2.3.2) of these pulses, the energy spectrum of the gated probe pulse was measured for different delays τ between the pump and probe pulse. For each delay 70 laser shots were accumulated to reduce energy fluctuations of the laser below 2.5 %. Other sources of error are the temporal jitter of the transition point and the wavelength calibration of the spectrometer. But overall the total error is not more than 5 %. The experimental results are shown in Figure 2.11 for the compressed and uncompressed pulse, respectively.

Frequency Shifts   If one plans to apply the plasma switch for characterising optical pulses, it is most important to find out how this switch influences the properties of the transmitted residual pulse. In any case an optical pulse propagating through a plasma with a changing electron density acquires a frequency shift [92]. During the plasma formation the electron density increases and the pulse is blue shifted, whilst it is red shifted in an expanding plasma with a decreasing electron density. If this effect starts influencing the transmitted residual pulse, then one expects that the increasing electron density during the plasma formation shifts the central frequency of the pulse to a higher frequency. Hence one would observe increasing central frequencies for decreasing delay times in the

time–frequency function, i.e. the time–frequency function would show a negative or at least reduced positive chirp. Nevertheless our compressed pulse still shows its originally small positive chirp, as can be seen in Figure 2.11(a). Consequently, one can already rule out a serious impact of frequency shifts onto the probe pulse. This is also an indication, that the ionisation process is so fast, that only a minor part of the probe-pulse is influenced by the ionisation process, i.e. the ionisation process is much faster than the FWHM of the pump-pulse.

The Response Time The ionisation model in Section 2.2 predicts, that a step function is a good approximation for the gating function on a time scale of the pump's FWHM. Thus the time–frequency functions in Figure 2.11 are supposed to be time–integrated PDFs (see Subsection 2.3.2) of the probe pulse. To justify this assumption experimentally, one can compare measured time–frequency functions with calculated ones. In Figure 2.13 this is shown for the uncompressed pulse. The time–frequency functions have been calculated by using Eq. (2.11) and are based on the pulse parameters given in Table 2.1. For modelling the gating function error, functions with a response time $\Delta\tau$ of 1 fs (Figure 2.13(a)) and 40 fs (Figure 2.13(c)), respectively, have been applied. The simulation with $\Delta\tau = 1$ fs shows distinct diagonal fringes, whilst these fringes are blurred in the simulation with $\Delta\tau = 40$ fs. As one can see these fringes in the measured time–frequency function Figure 2.13(b), the response time of the gating function in the experiment must be below 40 fs. This is at least 4 times faster than the FWHM of the laser pulse, agreeing with the prediction of our ionisation model from Section 2.2.

The Pulse Properties If the time–frequency functions in Figure 2.11 are time–integrated PDFs, then their zeros and first conditional momentum are related with the envelope and phase of the probe pulse by Eq. (2.24a) and Eq. (2.24b). In Figure 2.12 these momenta are shown: the open circles represent the momenta derived from the measurements, whilst the straight lines are the respective momenta calculated from the FROG measurements. By comparing these two curves it becomes evident that the FROG and plasma switch measurements agree well, despite a significant deviation in Figure 2.12(a) lasting from 40 fs to 100 fs. This deviation has also been predicted by our ionisation model (see Section 2.2) in terms of an increased transmissivity during the plasma formation process. Hence it is obvious that this experiment is not limited to the determination of the properties of an optical pulse, but that one can also determine the time-dependent optical properties of the plasma, if the characteristics of the probe pulse are known. The good agreement between the FROG and the plasma switch measurements shows that the gating function of the plasma switch is well approximated by a step function for optical pulses down to 60 fs. Furthermore note, that the agreement between the two measurements requires frequency shifts to be of minor importance.

2.5 Summary

In this chapter a macroscopic model (see Figure 2.1) of the plasma formation at an initially transparent dielectric solid was developed and implemented on a computer to

describe the reflectivity and transmissivity of a plasma produced with a sub-100 fs laser. The results derived with this model have been experimentally verified. In addition the ultrafast transition of the initially transparent medium to an opaque state was used to build an ultrafast switch.

The Computer Model   The computer simulations show that a transparent medium can be switched from a highly transparent state to an opaque one in less than $1/5$ of the FWHM of the pump pulse. The main reason for the ultrashort response time is a huge increase in the absorption of the probe pulse as soon as the electron density approaches the critical electron density (see Figure 2.6). Moreover this gating process is nearly independent of the electron temperature. This does not hold true for the plasma mirror; its gating properties strongly depend on the electron temperature (see Figure 2.4). In particular the final reflectivity can be far below 50 % and it lasts about the FWHM of the pump pulse until this final value is reached. Furthermore the reflectivity is a complicated function of time: decreasing at the beginning of the phase transition, approaching a maximum value during the transition, decreasing again and eventually slowly approaching its final value. Thus the simulations suggest that the plasma mirror is only partly applicable for removing pre-pulses from ultrashort laser pulses.

Mathematical Foundations   To learn how to analyse the experimental data, the mathematical basis of spectrally resolved pump–probe experiments was discussed briefly in Section 2.3. Furthermore an inversion formula Eq. (2.19) for deriving the time-dependent electric field of an optical pulse from the measured time–frequency distribution is presented. Also it works out that applying this equation is very difficult because of the derivative involved in calculating the distribution function from the respective time–frequency function. Instead of this, an alternative approach is given, that is based on calculating the zeros and first conditional momentum of the time–frequency function and then deriving the pulse properties.

Experimental Setup   The experimental setup shown in Figure 2.9 is a standard pump–probe setup. The part of the probe pulse, which is transmitted through the plasma, has been analysed with a spectrometer to measure the time–frequency function. To achieve a time resolution below 1 fs, a stepper motor driven translation table was equipped with a particular high resolution stepper motor. For future experiments the precision could be enhanced even more by using a closed loop translation stage. For pulses around 10 fs a piezo-actuator mounted on top of such a translation stage might be a good idea. During the experiment the pulse repetition rate of most ultrashort pulse-lasers has to be reduced, so that the target can be moved to a new unspoiled position between two adjacent pulses. This can be accomplished without any modifications inside the laser by putting a series of two synchronised optical choppers into the beam. Each chopper is equipped with a special, single-holed chopper-plate, so that the pulse repetition rate can be reduced by up to three orders of magnitude.
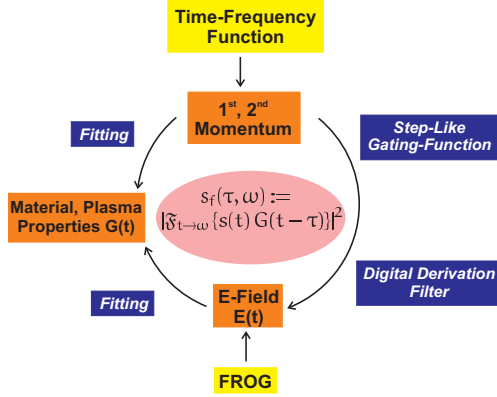
Figure 2.14: Relationship between the time–frequency function measured with the plasma switch, classical FROG measurements and the plasma properties: if the properties of the probe pulse are known, one can measure the time dependent optical properties of the plasma. On the other hand, if the time-dependent optical properties of the plasma are known, one can measure the properties of the probe pulse.

Experimental Results   In the experimental part of this chapter we focused on the ultrafast plasma switch and its feasibility to characterise sub-100 fs pulses. The experiment was performed with a 63 fs and a 138 fs laser pulse. The pulse properties were calculated from the measured time–frequency function by using the zeros and first momentum (see the right half of the circle in Figure 2.14 and Figure 2.12). These properties were compared with values measured with FROG. As both sets of data agree with one another, the assumption of a step like gating function is further justified afterwards. Furthermore we have been able to observe the theoretically predicted increase in transmission (see Figure 2.5(a)) during the plasma formation (see Figure 2.12(a)). Thus all theoretical predictions about the transmission properties have been experimentally verified and the transmission gate is very well applicable to characterise sub-100 fs pulses. On the other hand, if the pulse properties are known and one measures the time–frequency function, then one can calculate the optical properties of the plasma (see the left half of the circle in Figure 2.14). This is less interesting for pulses with a duration of 63 fs, as the transition is so fast, that it is still well approximated by a step function. But this is going to change for visible and NIR laser pulses below 20 fs. Then one can use this approach to study the ionisation process on a solid in even more detail.

Outlook   An advantage of the plasma switch in comparison to other gating processes is that it is applicable even in the VUV/XUV region. The only prerequisite is that the critical electron density associated with the wavelength of the probe pulse is lower than the maximum electron density inside the plasma. In addition, its response time is considerably faster than other gating techniques, such as third order Kerr shutters [43, 178]. In general the response time of a n-photon process is $2/n$ of the pump pulse's FWHM. Thus even a five photon process would lead to a response time of approximately $1/2$ of the pump pulse's FWHM for the Kerr gate in comparison to less than $1/5$ in the case of the plasma switch. Furthermore, in conjunction with well characterised extremely short laser pulses, one can also study the ionisation process in detail.

Chapter 3
DC Megagauss Azimuthal Magnetic Fields

3.1 Introduction

The last chapter focused on the plasma formation in dielectric media, i.e. the rapidly increasing electron density due to OFI. For these studies it is sufficient to consider laser intensities up to a few $10^{15}\,\mathrm{W/cm^2}$. If the laser intensity is increased further, then many other phenomena occur [59]. Most of these are primarily based on the strong interaction between free electrons, produced during the plasma formation, and the electromagnetic field of the laser pulse. An example is the an-harmonic oscillation of electrons, generating high harmonics of the laser fundamental [95, 96, 183]. This mechanism is relatively well understood in the case of solid targets [175] and the harmonic radiation was successfully used in this work to observe ultra-strong DC magnetic fields in high density laser produced plasmas for the first time.

The earliest observation of magnetic fields generated during the laser–plasma interaction was reported by Korobkin and Serov in 1966 [84]. They measured these fields by positioning a wire close to a gas breakdown produced with a nanosecond laser. The field strength was derived from the voltage inducted into this wire by the rising magnetic field (Langmuire probe). In 1971 Stampa et al. [158] carried out similar experiments, reporting magnetic fields around $1\,\mathrm{kG}$ and explained them in terms of thermoelectric currents associated with large temperature gradients. The great disadvantage of these Langmuire probes is, that they can sample only the area surrounding the laser plasma interaction and not the plasma itself, because the probes would be destroyed during the interaction. Thus, for measuring fields in the interaction area itself, one has to use optical probes. In 1975 Stampa et al. [159] reported on the measurement of multi-megagauss magnetic fields in a plane solid target experiment (focused laser intensity $10^{15}\,\mathrm{W/cm^2}$) using Faraday rotation of a linear polarised probe laser pulse. The first measurement of magnetic fields utilising the Zeeman splitting was carried out by McLean et al. in 1984 [107]. All of these experiments were performed with laser pulses having a pulse duration of several $100\,\mathrm{ps}$ to several nanoseconds. The main force driving these experiments was inertial confinement fusion (ICF) research [71, 97], because the magnetic fields can have a significant impact on the pellet compression process and on the ignition properties [157].

With the appearance of multi-terawatt fs-lasers around 1990, people started discussing DC magnetic fields in fs-laser produced plasmas. One of the first theoretical papers about this subject published by Sudan et al. in 1993 [165] predicted fields beyond several $100\,\mathrm{MG}$. He explained the generation of these fields with the pondermotorive force of the laser pulse. In his 1997 paper Haines [68] suggested that the magnetic field strength may be limited to an upper value due to the finite plasma conductivity. The first multi-

dimensional computer simulations with particle in cell codes (PIC) to study these fields were performed by Wilks et al. [189] in 1992, Pukhov et al. [129] and Mason et al. [103] around 1997/98, predicting fields up to a few 100 MG in the high density region of the plasma. The first experimental observation of self generated magnetic fields in fs-laser produced plasmas was accomplished by propagating an external linear polarised probe laser through the plasma and measuring the Faraday effect [21, 22]. Borghesi et al. found two spatially separated toroidally magnetic fields caused by different mechanisms of field generation. Due to the external optical probe this experiment was limited to sampling the under-dense areas of the plasma, so that the observable field strength was limited to a few megagauss (see Subsection 3.2.2). The observation of magnetic fields beyond 100 MG, generated in the high density region of the plasma, was reported for the first time in 2002 by our research team [171]. This chapter discusses this experiment in detail and the results obtained. Furthermore, it goes beyond the 2002 publication by presenting studies of the magnetic field with the help of VUV / XUV harmonics.

The first major part of this chapter gives a short introduction into the theory of magnetic field generation and presents PIC simulations matching the experimental conditions. These simulations are particularly useful in planning the experiment, because they give an estimate of the expected magnetic field strength and its location. Following this, the main idea of the experiment is explained and it is shown that high harmonics, generated inside the plasma, are an ideal, intrinsic source of electromagnetic radiation to observe the azimuthal DC magnetic fields. The next part shows how to measure the magnetic field strength in a plasma applying the cut-off of the extraordinary wave and the Cotton-Mouton effect, which are completely independent of each other from an experimental point of view. Then the experimental setup is explained. In addition to the general setup, the VIS / UV§ polarimeters and VUV / XUV♯ polarimeters, their calibration and the data analysis procedure are explained extensively. Finally the experimental results are presented and discussed.

3.2 Megagauss DC Magnetic Fields in Sub-Picosecond Laser Produced Plasmas

3.2.1 Mechanisms for DC Magnetic Field Generation

As a plasma is a macroscopic, many-particle system consisting of freely moving neutral, positive and negative charged particles, it is obvious that these particles can produce currents inside the plasma. Due to the Maxwell's equations Eq. (C.1) these currents are linked with a magnetic field. Any magnetic field applies the so called Lorentz force on the moving charged particles, thus influencing their orbits. An example of this is the well-known Pinch effect [148]. Not only self-generated magnetic fields can influence the motion of these particles, but also external fields, which are indispensable for plasma inclusion in Tokamaks and Stellerators [147].

---

§VIS / UV: Visible and ultraviolet radiation
♯VUV / XUV: Vacuum ultraviolet and extreme ultraviolet

(a) Thermoelectric Field   (b) Pondermotorive Field
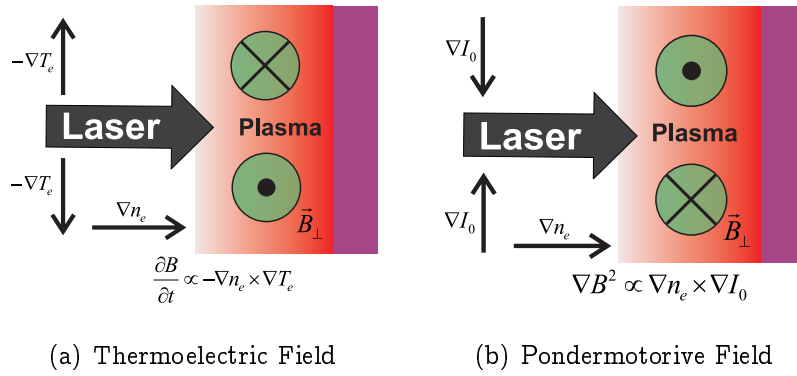
Figure 3.1: Orientation of the azimuthal magnetic fields

In laser produced plasma experiments the magnetic fields intrinsically grow, due to intrinsic gradients in the temporal and spatial profile of the laser pulse. On a sub-picosecond timescale one can neglect most forces pushing the ions, because they are more than three orders of magnitude heavier than the electrons, so that their response to these forces is much slower. Note, this does not mean that the ions do not move, as e.g. pressure gradients cannot be neglected. This reduces the number of mechanisms generating magnetic fields in a fs-laser produced plasma to at least three different main processes [58]:

Radial Thermal Transport   Referring to Stampa [158] non-parallel gradients of electron temperature T_e and density n_e give rise to a so called thermoelectric magnetic field:

$$\frac{\partial \vec{B}}{\partial t} = -\frac{\vec{\nabla} n_e \times \vec{\nabla} T_e}{e \, n_e} \tag{3.1}$$

Close to the original target surface $\vec{\nabla} n_e$ is perpendicular to this surface, because n_e naturally decreases with increasing distance from the target. On the other hand $\vec{\nabla} T_e$ is parallel, because T_e increases with increasing laser intensity and the radial spatial profile of the laser focus is roughly Gaussian. Thus, assuming cylindrical symmetry, the generated magnetic field is azimuthal with a direction as shown in Figure 3.1(a). Generally it takes a few picoseconds for $\vec{\nabla} n_e$ to build up. Hence this field reaches its maximum of some hundred megagauss (for a laser intensity about 10^{19} W/cm^2) a few picoseconds after the laser pulse maximum. Note that this field even exists in the under-dense plasma in front of the target, but with much lower strength. This can lead to the pinching of the plasma, altering its hydrodynamic expansion [16].

Pondermotorive Forces   It is well-known that a laser pulse with a gradient in its time-averaged spatial intensity pushes away the electrons along its propagation path. The underlying force is called the pondermotorive force [86, 172]:

$$\vec{F}_p := -\vec{\nabla} U_p := -\frac{e^2}{4 m_e \omega_0^2} \vec{\nabla} \vec{E}^2 \tag{3.2}$$

with the electron mass m_e, the electron charge e, the central laser frequency ω_0 and the electric field $\vec{E}$ of the laser pulse. In contrast to the electrons, the ions remain at rest on a sub-picosecond timescale, due to their much higher inertia. This results in

charge separation, building up electric fields, opposing the pushing. Finally a steady state is reached [189]. But if the laser intensity increases with time, i.e. if there is an increasing pondermotorive force, then the electrons are not only pushed away, but they are accelerated by the laser pulse itself, so that they acquire a velocity. Consequently the pondermotorive force is driving a current through the plasma resulting in magnetic field generation. The field strength is [165]:

$$\vec{\nabla}\vec{B}^2 \approx \vec{\nabla}n_e \times \vec{\nabla}I_0 \qquad (3.3)$$

As already discussed above $\vec{\nabla}n_e$ is perpendicular to the original target surface. On the other hand $\vec{\nabla}I_0$ is parallel to the surface and points to the principal axis of the incident laser, because of the laser's radial intensity profile. Assuming cylindrical symmetry once more the generated magnetic field is again azimuthal, located in the high density region of the plasma and spread over one skin depth. But in contrast to the thermoelectric field its direction is reversed (compare Figure 3.1(b)). As the field depends on the pondermotorive force, it is present during the laser plasma interaction only. Furthermore it was shown that these fields can be close to 1 GG (for a laser intensity about 10^{19} W/cm^2) [103, 165, 189].

Fast Electron Currents   A third mechanism for magnetic field generation comes from currents of fast electrons generated by collective absorption mechanisms independently of the pondermotorive force. These currents can be directed along the target surface [27, 57, 137] and into the bulk [129]. But, as they are generated by the laser pulse, they are only present during the laser–plasma interaction. Like all currents, they produce a magnetic field quite naturally. Due to return currents, balancing the flux of fast electrons, the magnetic field strength is much lower than in the case of pondermotorively generated fields. For a laser intensity of about 10^{19} W/cm^2 Pukhov et al. found fields not above 100 MG in their PIC simulations. Because of their low field strength, these fields are less relevant for our experimental studies.

3.2.2   PIC Simulations of Mega-Gauss DC Magnetic Fields

Before experimentally studying the magnetic field in a laser produced plasma it is useful to have a rough understanding about its location and its possible strength for the given laser parameters and target geometry. This understanding can be obtained by performing particle in cell (PIC) [17, 86] simulations to model the experiment. In a PIC simulation a plasma is modelled with a huge number of charged particles. These particles are moved around by the electromagnetic forces from the incident laser pulse and the self-generated electric and magnetic fields. As a simplification, collisions between the particles are neglected, although more advanced versions have begun to include collisions.

Such simulations have been carried out with the OSIRIS framework [64, 70, 112], a two to three dimensional collisionless PIC code for parallel computing developed at the University of California and Los Angeles (UCLA). To simulate the present experiment, periodic boundary constraints were chosen in the transverse direction and open boundary constraints in the longitudinal direction. The transition from vacuum to plasma was given

(a) Azimuthal Magnetic Field (B$_3$)   (b) Electron Density
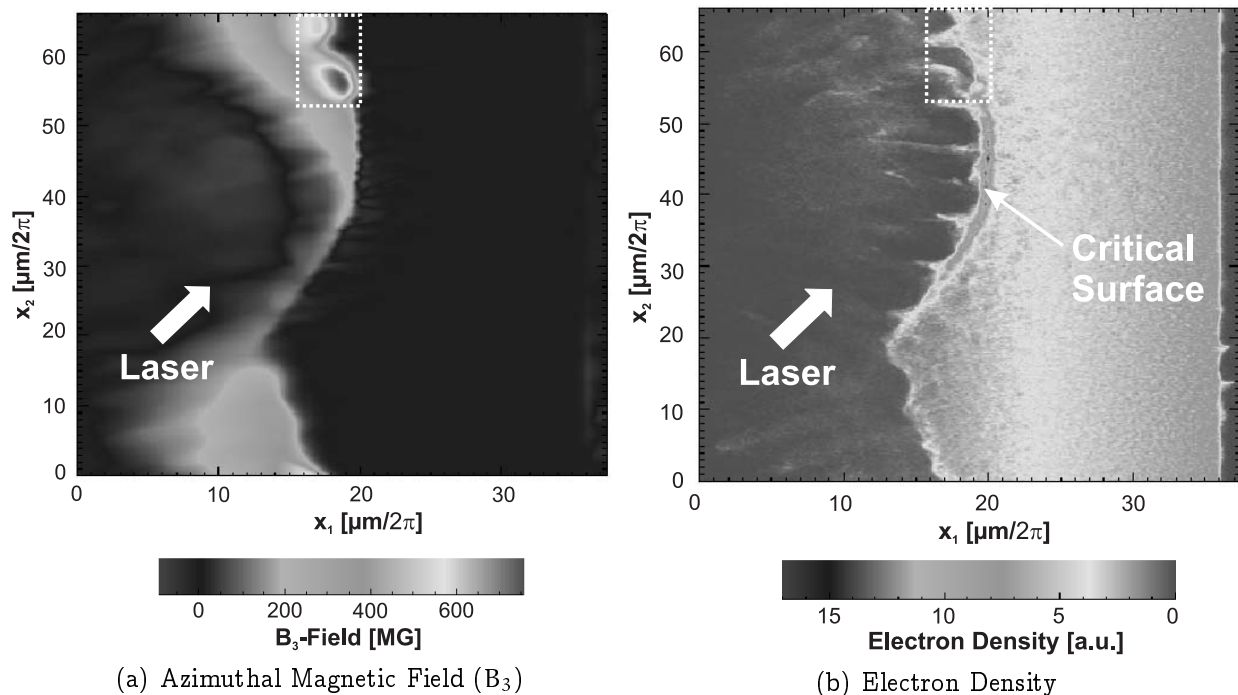
Figure 3.2: OSIRIS PIC simulation of the VULCAN magnetic field experiment [171] (p-polarised laser incident at 45°, wavelength 1053 nm, constant intensity of 10^{19} W/cm^2 throughout the whole simulation and a spatial Gaussian profile, plasma density 20 times over-critical with a step-like density profile). The plots show the situation 80 fs after the simulation started. The white box frames the area with the strongest magnetic field.

by a step-like density profile. To keep computing time on a reasonable level, the spatial resolution was set to 122 cells per laser wavelength and the duration of the simulation was limited to a few hundred femtoseconds. For the same reason, the plasma density was limited to 20 times over-critical and 20 million particles were used. The p-polarised laser beam with a wavelength of 1053 nm and with a spatial Gaussian profile was switched on at the beginning of the simulation and had a constant intensity of 10^{19} W/cm^2. Its angle of incidence was 45° with respect to the target normal. To increase the precision of the simulation, the movement of the ions was also included. As usual for PIC simulations, a fully ionised hydrogen plasma was assumed.

If the laser was switched on at the begin of the simulation, then it lasted some 10 fs until the magnetic fields had built up. After this time the field strength stayed fairly constant throughout the remaining time of the simulation. Thus the maps in Figure 3.2 show the magnetic field distribution and the electron density 80 fs after the laser pulse was switched on.

In Figure 3.2(a) the B$_3$ component of the magnetic field is plotted. This component is perpendicular to the target normal and the incident laser beam. The B$_1$ (parallel to the target normal) and B$_2$ (perpendicular to B$_1$ and B$_3$) field components have been found to be less than $^1/_{10}$ of the B$_3$ component. Hence they are not shown, as they are of minor importance. The maximal B$_3$ field strength in this simulation is 750 MG (see the boxed area in Figure 3.2(a)). This peak magnetic field is located in a small high density area outside the focal spot. If one splits Figure 3.2(a) into a lower and an upper half-plane

along the target normal through the centre of the focal spot, then this field is found in the half-plane opposite to the half-plane including the incident laser beam. Thus it seems as if the incident laser pulse compresses the magnetic field to a strong but very localised one, whilst the field in the other half-plane is much weaker, but expanded over a larger area. This is a very important result, namely, that one has to observe the magnetic field in the half-plane along the target normal not containing the incident beam in order to measure the strongest fields in the plasma. Furthermore, note that the magnetic field strength in the focal spot can be neglected in comparison to this field. However it is important to note that hybrid fluid models are more appropriate for calculating the magnetic field in the high density areas than the collisionless PIC codes.

In the electron density map, shown in Figure 3.2(b), one clearly sees the curvature of the critical density surface produced by the pondermotorive force of the laser pulse. The ripples of this surface and the flares of electrons emitted from it are due to the strong non-linear interaction of the laser with the electrons in this area. These strong an-harmonic oscillations of the surface produce bright high order harmonic emission eventually.

In a real experiment pre-pulses of the laser and a pedestal on a nanosecond timescale can produce an extensive pre-plasma with a long density gradient. Thus the density profile in an experiment will be somewhat different from the assumed step-like profile used in the simulations. In time, the leading edge of the laser pulse pushes away the electrons along the incident path of the laser due to the pondermotorive force, so that eventually a steep density gradient is produced again. In Subsection 3.3.2 it is discussed, that bright and localised emission of harmonics from a near solid density plasma requires a steep density gradient. Furthermore in Subsection 3.3.1 it is shown that for successfully measuring strong magnetic fields with our experimental setup this kind of harmonic emission is a prerequisite.

3.3   The Basic Idea of the Experiment

3.3.1   Observing Magnetic Fields in Near Solid Density Plasmas

As already mentioned in Section 3.1, the strength and the sign of the magnetic field can be measured with the help of an electromagnetic probe beam propagating through the magnetised plasma. In Section 3.4 we shall see that two completely independent methods exist to measure the magnetic field. The first method is only dependent on the wavelength of the electromagnetic probe beam. The second one requires that the probe's initial state of polarisation is known, in addition. Furthermore a polarimeter is needed to measure its final state of polarisation. The polarimeters, used throughout this experiment, are described in Subsection 3.5.2.

In Figure 3.3(a) the experimental setup on principle is shown for the case of a visible external probe beam. The probe is diffracted at the steep density gradients at the edges of the plasma so that it cannot penetrate into the high density region of the plasma, where the strongest magnetic fields are present. Thus the probe is not affected by these fields and consequently they cannot be measured with this kind of probe. To overcome
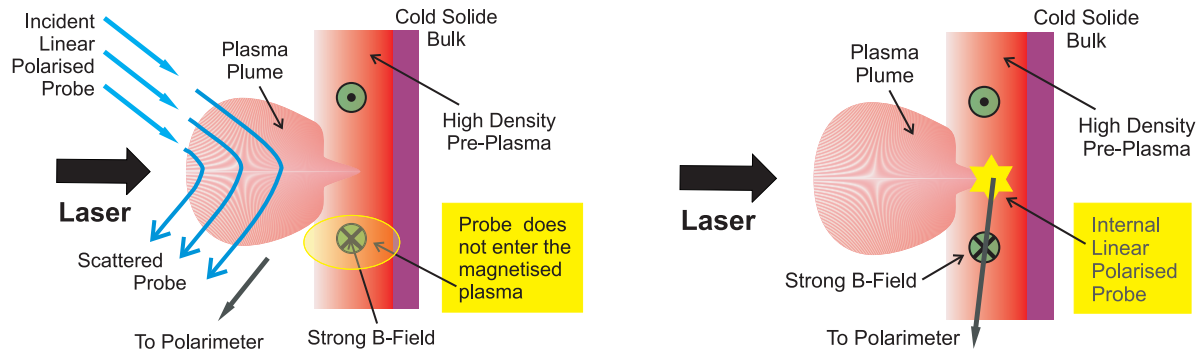
(a) Refraction of an external, visible probe beam at the steep density gradient of the plasma. Note that the probe beam does not enter the high density region, where the ultra-strong magnetic fields are present.

(b) Plasma with an internal point-like source of radiation. If the ultra-strong magnetic fields are in the line of sight from the radiation source to the polarimeter, then they can be observed.

Figure 3.3: Schematic layout of experiments measuring the magnetic field strength with an external and an internal probe beam, respectively.

this problem one has to reduce the refraction of the probe. This can be achieved by using x-rays, which propagate through the densest areas of the plasma. But present x-ray sources and optics still need further development to deliver sufficiently intense, polarised, monochromatic and sub-picosecond x-ray pulses, coincident to the magnetic field producing laser-pulse and a high spatial resolution at the same time in single shot operations.

An alternative approach is shown in Figure 3.3(b): instead of using an external source of electromagnetic radiation the source is located inside the plasma itself. If one can measure any radiation emitted from that source and if the strongly magnetised area of the plasma is in the line of sight from that source to the polarimeter, then the observed radiation can be influenced by the magnetic field. In summary, the use of an internal source instead of an external one is an important reason why we succeeded in observing magnetic fields close to a gigagauss. Of course, this source must meet some prerequisites: One obvious requirement of this source is that sufficient radiation to perform a measurement is emitted in the direction given by the line of sight from the centre of the source to the localised strong magnetic field. A second condition is that the source has to be a point-like source. Otherwise there is always a chance to have a direct line of sight from the polarimeter to a considerable part of the source bypassing the localised strongly magnetised area, so that one only measures an averaged value for the field, which can be much lower than the peak field strength. This geometrical constraint on the source size is clarified in Figure 3.4(a). Thirdly, the wavelength of the electromagnetic radiation has to be adequately short so that it can propagate through the magnetised high density regions. Two other advantages of using short wavelength radiation are that simplifying approximations for calculating the magnetic field strength (see Subsection 3.4.5) hold and that with decreasing wavelength the calculated magnetic field strength is less dependent on a precise knowledge of the electron density (compare Figure 3.8). Finally, to calculate the magnetic field by means of Müller matrices (see Subsection 3.4.6) the initial
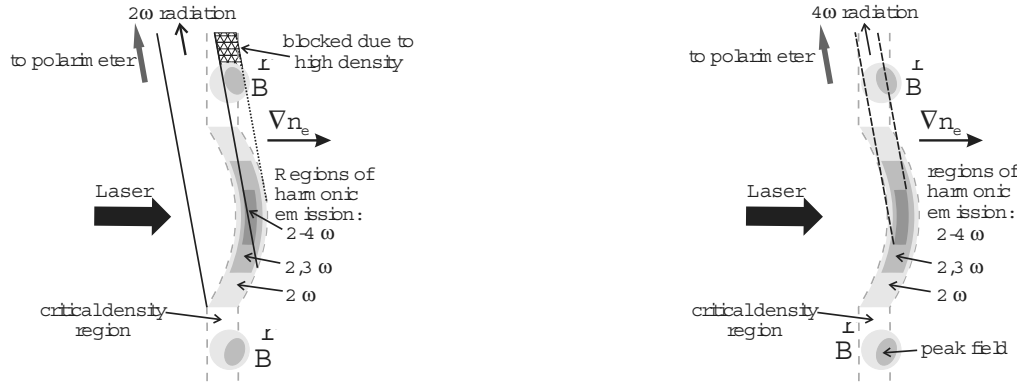
(a) 2nd.-harmonic: Because of the high density in the strongly magnetised area, the 2nd harmonic cannot propagate through this area. But due to its large emission area most of the radiation propagates through areas with lower magnetic fields.

(b) 4th.-harmonic: This harmonic observes the strong magnetic field almost exclusively, because its emission region is sufficiently small and it can propagate through the high density region, where the strong field is present, due to its shorter wavelength.

Figure 3.4: Emission regions of different harmonics and possible obstacles observing ultra-large DC magnetic fields: note that *all* harmonics are also produced in the centre of the laser–plasma interaction and that only the diameter of the emission area decreases with increasing harmonic order. The criterion, if a harmonic can propagate through a region with a certain density, is given by the critical electron density (see Eq. (2.1)).

polarisation state of the radiation has to be known. Ideally this state is linear polarised.

3.3.2   High Harmonics as a Source for Observing Magnetic Fields

The most obvious sources of electromagnetic radiation in a plasma produced at a solid are the atomic line and continuum emission. But these sources expand over a huge volume of the plasma, so that they are not point-like at all and, in addition, they are unpolarised in general. High harmonics, on the other hand, are an alternative and promising source of radiation as can be seen from some basic theoretical considerations.

3.3.2.1   Theoretical considerations

A simple and phenomenological, but intuitive model, to explain high harmonic radiation from a plasma produced at a solid surface is the 'moving mirror' model proposed by Bulanov et al. [28] in 1994. An elaborate introduction is given by von der Linde et al. [183] and Lichters [95]: in this model an electromagnetic wave with a central frequency ω_0 interacts with the electrons inside the plasma, whilst the ions remain at rest, because they are three orders of magnitude heavier than the electrons, and thus their interaction with the electromagnetic wave is much weaker. For a near solid density plasma with a steep density gradient this interaction is limited to a thin surface layer given by the skin depth (this is the reciprocal of Eq. (2.6)). This layer begins to move back and forth normal to the target surface with an angular frequency $2\omega_0$ due to the pondermotorive force (see Eq. (3.2)[§]). In addition to this oscillation all electrons in this surface layer perform an oscillation with ω in the direction of the electric field $\vec{E}$. If the incident laser beam is p-polarised, then $\vec{E}$ has a component normal to this surface. Consequently this layer moves back and forth with both frequencies $2\omega_0$ and ω_0. On the other hand, in

---

[§]$\vec{F}_p \propto \vec{\nabla}\vec{E}^2 \propto \vec{\nabla} \sin^2(\omega_0 t - \vec{k}\cdot\vec{x}) \propto \vec{\nabla}\sin(2\omega_0 t - \vec{k}\cdot\vec{x})$

Laser	s-pol. harmonics	p-pol. harmonics
s-pol. fundamental	odd	weak, even
p-pol. fundamental	forbidden	even and odd

Table 3.1: Polarisation selection rules for harmonic generation [183].

the case of a s-polarised laser beam, this layer oscillates back and forth exclusively with $2\omega_0$, because $\vec{E}$ is now parallel to the surface. This consideration leads to the polarisation selection rules for harmonic generation [183]: in the case of an incident p-polarised laser-beam even and odd p-polarised harmonics are produced, whilst s-polarised harmonics are forbidden. For an incident s-polarised beam mainly s-polarised odd harmonics are produced. But as soon as the electron motion becomes relativistic, weak p-polarised even harmonics are also generated (see Table 3.1). A rigid derivation of these selection rules is given by Lichters et al. [95, 96]. Furthermore Lichters compares the theoretical results, derived from the moving mirror model and a cold relativistic plasma fluid model, with PIC simulations and found them in good agreement.

In addition to the polarisation selection rules one can also derive the intensities of the produced harmonics [183]. This calculation shows that the intensity of a certain harmonic increases with increasing laser intensity and that the intensity of the generated harmonics decreases with increasing harmonic order for a constant laser intensity. Hence one can conclude that for a laser pulse with a spatial Gaussian profile the spatial profile of the harmonic emission region is centred around the laser pulse maximum and that the FWHM of the emission area decreases with increasing harmonic order (see Figure 3.4). It is important to mention, that these basic considerations need considerable amendments, if the laser intensity increases and the plasma surface becomes rippled due to spatial and temporal non-linearities [175, 185].

A further extension of this simple model is the inclusion of a density profile as discussed in [54, 175, 176]. In a plasma with a density profile the harmonics are generated in the vicinity of the critical density surface, i.e. the surface where the electron density matches the critical electron density (see Eq. (2.1)). The actual location of this surface depends on the temporal and spatial profile of the laser pulse. If the oscillation of the electrons in the electric field of the laser becomes relativistic, then the position of this surface is shifted to a region with a higher density and the relativistic kinetic leads to the generation of particular high harmonics. This relativistically altered critical density can be calculated by multiplying the original nonrelativistic value with the relativistic γ-factor [58]:

$$n_{ec_{rel}} := n_{ec}\,\gamma = n_{ec}\,\sqrt{1 + \frac{e^2}{4\pi^2\epsilon_0 m_e^2 c^5}\,I\lambda^2} \qquad (3.4)$$

3.3.2.2 Experimental Findings

In a real experiment pre-pulses of the laser and a nanosecond pedestal due to the amplified spontaneous emission can produce an extensive pre-plasma. In comparison to the main pulse the strongest pre-pulse was smaller than 10^{-6} for the CPA-beam of the VULCAN:Nd

glass laser (750 fs, 100 J, 1053 nm) [37–39]. As the focused intensity of this beam is up to 10^{20} W/cm^2, the pre-pulses and the pedestal still produce a considerable under-dense plasma with a scale length of several microns [140].

A pre-plasma reduces the intensities of the high harmonics emitted from the plasma drastically as reported by Zepf et al. [191]. Nevertheless Norreys et al. [116] reported bright high harmonic emission from a plasma produced with the Vulcan laser. They found conversion efficiencies of laser energy into harmonic radiation beyond 10^{-6} for harmonics with an order lower than 68. Recently Teubner et al. [175] measured conversion efficiencies above 10^{-4} for the 6th harmonic produced with a particular clean 395 nm fs-laser pulse (i.e the pre-pulses and the pedestal of this fs-laser pulse were below the plasma formation threshold). Furthermore, in the same paper Teubner et al. discussed modulations in the intensity scaling of the emitted harmonics versus harmonic order. They showed that these modulations vanish, if an extensive pre-plasma is present. Consequently one would not expect to measure these modulations with the CPA-beam of VULCAN, because of its extensive pre-plasma. Nevertheless Watts et al. [185] reported on finding these modulations in the harmonic spectra emitted from a plasma produced with VULCAN.

These seemingly contradicting experimental results can be explained, if one assumes mechanisms steepening the density profile at VULCAN again. Indeed at intensities beyond 10^{19} W/cm^2 the pondermotorive forces are so strong that significant steepening of the density profile [189] appears. This can also be seen clearly in the PIC simulation presented in Figure 3.2. In addition the pondermotorive forces push away the electrons along the path of the incident laser beam, thus forming a channel depleted of electrons. Due to the lacking electron density along this path, the magnetic fields do not alter the laser beam's state of polarisation significantly during its propagation (compare Eq. (3.28), Eq. (3.30)). Hence it is reasonable to assume that the harmonics are produced by a p-polarised laser pulse. Recalling the theoretical considerations from above, one can conclude that the emitted high harmonics are also p-polarised.

Nevertheless, one can question the validity of the polarisation selection rules, if the laser intensity is such high, that the critical density surface becomes rippled. Based on experiments carried out by von der Linde, Balcou, Tarasevitch et al. [13, 169, 182], this should happen if the laser parameters surpass I$\lambda^2 < 10^{17}$ Wμm^2/cm^2 (I: intensity, λ: wavelength). To examine the influence of a rippled critical density surface on the polarisation properties of the harmonics a glass target was sand-blasted and the roughened surface was irradiated with a laser pulse not much beyond 10^{17} W/cm^2 to avoid strong magnetic fields influencing the polarisation properties of the harmonics. The polarisation properties of the 3rd harmonic were measured with the experimental setup described in Subsection 3.5.2 and it was found that the radiation remained fully p-polarised in accordance with the polarisation selection rules.

Nevertheless, if I$\lambda^2 \gg 10^{17}$ Wμm^2/cm^2, then the critical density surface is not only rippled, but pondermotorive forces also lead to hole boring (compare the PIC simulations in Figure 3.2). Hence the critical density surface becomes curved and irregular, so that

the emission of high harmonics is no longer limited to the specular direction only [13, 169, 182]. Indeed, one can observe emission of harmonics into a solid angle of 2π as reported by Norreys et al. [116] using the VULCAN CPA-beam.

In the same paper Norreys et al. discussed measurements, showing, that the conversion efficiency decreases with increasing harmonic order and that the harmonic intensity increases for a particular harmonic with increasing laser intensity. Thus, as discussed from a theoretical point of view beforehand, it seems as if higher harmonics need higher intensities to be produced with a high photon flux. Due to the spatial profile of the laser focus one can conclude that the higher harmonics are produced in an area increasingly limited to the centre of the laser focus, so that the source area becomes more point-like for these harmonics. In addition, harmonics with a higher order can propagate through more dense regions of the plasma, because of their higher critical electron density (see Eq. (2.1)). As one expects stronger magnetic fields in areas with higher density (see Subsection 3.2.2), these particular high harmonics are even more suited for measuring stronger magnetic fields (see Figure 3.4).

3.3.2.3 Summarising Discussion

The experimental and theoretical considerations discussed above suggest that the harmonics produced with VULCAN's CPA-beam are generated around the principal axis of the incident laser beam close to the critical density surface in a pondermotorively steepened density profile. Even if these considerations do not hold exactly, the observed magnetic field strength is always a lower limit of the strongest fields present inside the plasma. Thus, in the worst case the observed fields are much lower than the peak magnetic field as will be discussed in Subsection 3.4.4 and in Subsection 3.4.6 extensively.

As most of the harmonics are produced in the temporal vicinity of the laser pulse maximum, we shall not be able to measure the thermoelectric magnetic field, which appears much later in time. But the pondermotorively generated magnetic field and the magnetic field due to currents of fast electrons are present in the temporal vicinity of the laser pulse maximum. In comparison to the pondermotorively generated field the field due to currents of fast electrons is more than one order of magnitude weaker (see Section 3.2), so that it can be neglected in comparison to the other field. Thus in this experiment, most likely the pondermotorively generated magnetic field is observed.

However, even if the mechanisms producing high harmonics at VULCAN are not completely understood so far and further research is needed for a complete understanding, high harmonics are an ideal and easy to use source for observing magnetic fields in laser produced plasmas, because they meet all prerequisites from Subsection 3.3.1. The theoretical considerations and experimental findings presented in the last two sections suggest that the high harmonics are initially p-polarised even for laser intensities well above 10^{17} W/cm^2. But measurements of the magnetic fields should not solely depend on an experimental scheme requiring a well defined initial polarisation state. Nevertheless such a scheme may give further valuable insight into the generation of harmonics and the
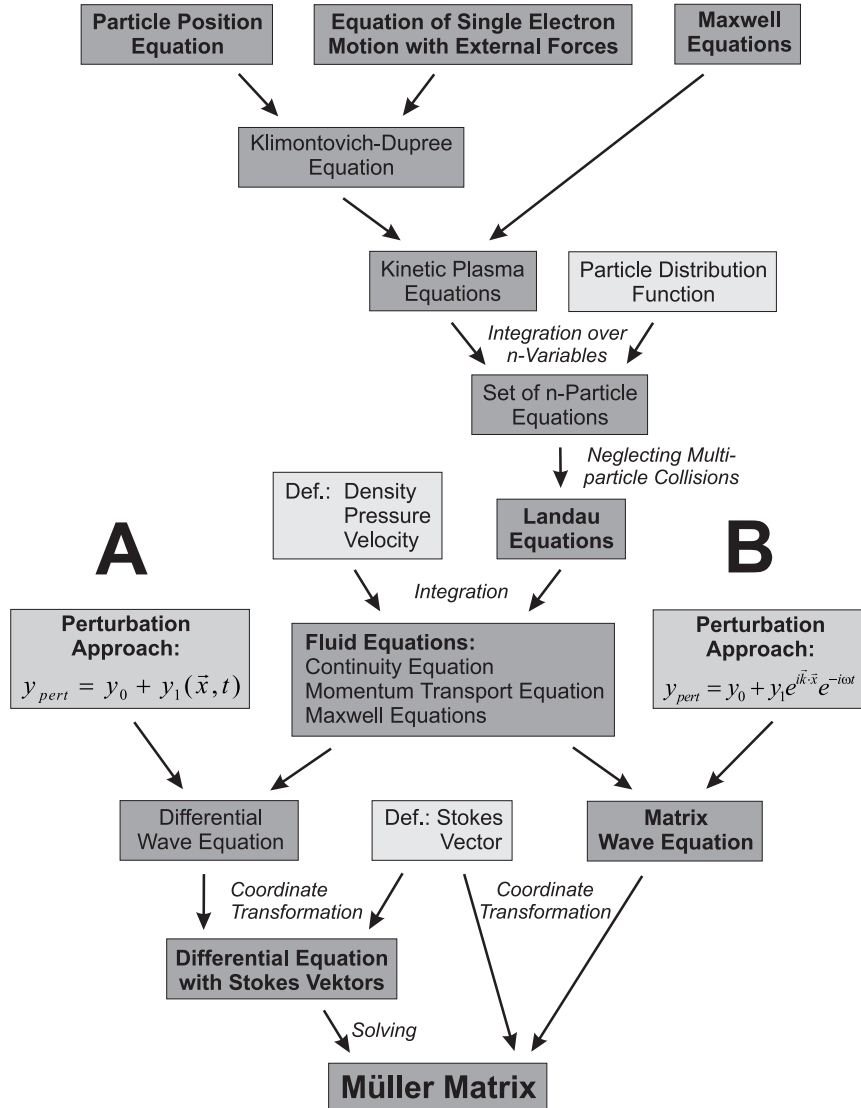
Figure 3.5: Physical model to derive the Müller matrix of a laser produced plasma. This matrix is used to calculate the magnetic field strength inside the plasma. The Figure shows two possibilities to derive this matrix: the differential equation (A) and the matrix (B) approach (see Appendix E.2 in addition).

magnetic fields present in a laser produced plasma, if there are independent additional methods to determine the magnetic field strength.

3.4 Observing Magnetic Fields in a Laser Produced Plasma

3.4.1 Electromagnetic Waves in a Magnetised Plasma

To measure the magnetic field strength with an electromagnetic wave, it is vital to obtain a quantitative understanding of the interaction between the electromagnetic wave and the magnetised plasma. A schematic sketch of a physical model describing this interaction is shown in Figure 3.5. A more detailed discussion of this model is given in Appendix E:

Starting with the particle position equation and the equation of motion of a single electron one can derive the Klimontovich–Dupree equation. The particle position equation is a time dependent function of space and velocity, which is always zero despite the points where a particle of a certain species can be found (see Eq. (E.1)). Supplementing the Klimontovich–Dupree equation with the Maxwell equations leads to a microscopic
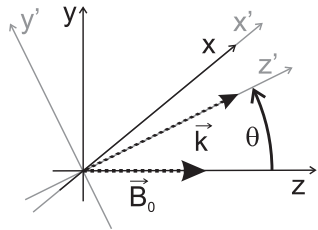
Figure 3.6: Direction of the magnetic field and of the electromagnetic wave propagating through the plasma in the coordinate system O and O$'$.

kinetic description of the plasma. The resulting equations can be reduced to a hierarchy of n-particle equations by averaging over a corresponding number of variables (see Eq. (E.4) to Eq. (E.6b)) and introducing n-particle distribution functions (see [85] or Appendix E.1). To close this infinite hierarchy of n-particle equations it is necessary to make assumptions on all particle distribution functions with n larger than an arbitrary integer. Assuming that all particle distribution functions with $n > 2$ are zero, one neglects all multi-particle collisions despite binary collisions, thus deriving the Landau equation. With the definition of the density, pressure and velocity it is straight forward to calculate the macroscopic fluid equations (see Eq. (E.6a), Eq. (E.6b), Eq. (E.11), Eq. (E.12)). In this fluid model the electrons and each ion species make up an independent fluid. But in general it is a good approximation to use only one ion-species with an averaged degree of ionisation. Thus one obtains the two fluid model.

With the so called cold plasma assumption the complexity of this model is reduced even more. This assumption requires, that

$$\sqrt{\frac{kT_e}{m_e}} \ll \frac{\omega}{k_\omega} \tag{3.5}$$

with the Boltzmann constant k, the electron temperature T_e, the electron mass m_e and the wave vector k_ω of the electromagnetic wave with frequency ω. This is in particular valid during the early phase of a laser produced plasma, because its thermal temperature T_e is only a few electron volts as briefly discussed in Subsection 2.2.2. In addition Krall [85] mentions, that this is generally a good assumption, if strong magnetic fields are present. Furthermore, if the magnetic field strength is below 3 GG and electromagnetic radiation used to measure the field strength has a wavelength below 360 nm, one can neglect the interaction between the electromagnetic wave and the ions, so that one has to take into account the electrons only.

The remaining equations can be solved with a perturbation approach. The mathematical details are given in Appendix E.2. With the most general perturbation approach (case A in Figure 3.5) one obtains a linear differential wave equation, which can be transformed to a differential equation based on Stokes parameters (see Eq. (E.25)). With the more specialised approach (case B in Figure 3.5) one derives a matrix wave equation, which is more easy to solve. Using a coordinate system O, in which the static magnetic field $\vec{B}_0$ is parallel to the z-axis and in which the propagation direction of the electromagnetic wave, given by $\vec{k}$, lies in the yz-plane (see Figure 3.6), one calculates:

$$\mathbf{A}\,\vec{E}_1 := \begin{pmatrix} n^2 - \epsilon_1 & i\epsilon_2 & 0 \\ -i\epsilon_2 & n^2 \cos^2\theta - \epsilon_1 & -n^2 \sin\theta\cos\theta \\ 0 & -n^2 \sin\theta\cos\theta & n^2 \sin^2\theta - \epsilon_3 \end{pmatrix} \begin{pmatrix} E_{1x} \\ E_{1y} \\ E_{1z} \end{pmatrix} = 0 \qquad (3.6a)$$

where θ is the angle between the z-axis and the propagation direction $\vec{k}$ of the electromagnetic wave. Furthermore the dielectric constants are given by:

$$\epsilon_1 = 1 - \frac{\omega_{pe}^2}{\omega^2 - \omega_{ce}^2} \quad (3.6b) \qquad \epsilon_2 = \frac{\omega_{ce}}{\omega} \frac{\omega_{pe}^2}{\omega^2 - \omega_{ce}^2} \quad (3.6c) \qquad \epsilon_3 = 1 - \frac{\omega_{pe}^2}{\omega^2} \quad (3.6d)$$

where $\omega_{ce} := \frac{q_e}{m_e}|\vec{B}_0|$ is the cyclotron frequency of the electrons, $\omega_{pe} := \sqrt{\frac{q_e^2 n_e}{\epsilon_0 m_e}}$ is the electron plasma frequency, $n := c_0 \frac{|\vec{k}|}{\omega}$ is the index of refraction and q_e is the elementary charge.

3.4.2 The Solution of the Wave Equation

To find the non-trivial solutions of the wave equation Eq. (3.6) the determinant of the Matrix $\mathbf{A}$ is required to be zero. Solving $\det(\mathbf{A}) = 0$ for n and using the identity $\epsilon_1^2 - \epsilon_2^2 = \epsilon_1\epsilon_3 - (\epsilon_3 - \epsilon_1)$ leads to the so called Appleton-Hartree equation, representing the dispersion relation:

$$\begin{aligned} n_{\pm}^2 &= 1 - \frac{\epsilon_3(1 - \epsilon_3)}{\epsilon_3 - \frac{1}{2}\frac{\epsilon_3 - \epsilon_1}{1 - \epsilon_1}\sin^2\theta \pm \sqrt{\left(\frac{1}{2}\frac{\epsilon_3 - \epsilon_1}{1 - \epsilon_1}\sin^2\theta\right)^2 + \frac{\epsilon_3 - \epsilon_1}{1 - \epsilon_1}\epsilon_3^2 \cos^2\theta}} \\ &= 1 - \frac{\frac{\omega_{pe}^2}{\omega^2}\left(1 - \frac{\omega_{pe}^2}{\omega^2}\right)}{\left(1 - \frac{\omega_{pe}^2}{\omega^2}\right) - \frac{1}{2}\frac{\omega_{ce}^2}{\omega^2}\sin^2\theta \pm \sqrt{\left(\frac{1}{2}\frac{\omega_{ce}^2}{\omega^2}\sin^2\theta\right)^2 + \left(1 - \frac{\omega_{pe}^2}{\omega^2}\right)^2 \frac{\omega_{ce}^2}{\omega^2}\cos^2\theta}} \end{aligned} \qquad (3.7)$$

Obviously the dispersion relation given by Eq. (3.7) splits into two branches: a branch with a low index of refraction n_+ in case of a plus sign in front of the root and a branch with a high index of refraction in case of a minus sign. These branches are also called the fast and the slow branch, respectively, because of the phase velocity of the associated waves. This difference in the phase velocity allows the measurement of the magnetic field strength inside the plasma (see the following sections).

As discussed in Appendix C.1 the fundamental solutions of a linear wave equation like Eq. (3.6a) are real time-harmonic vector waves with a propagation direction parallel to the local wave-vector $\vec{k}(\vec{r})$. Furthermore the electric field vectors of these fundamental solutions are always given by a linear combination of two linear independent vectors. By substituting $n_\pm$ into Eq. (3.6a) and solving the two emerging systems of linear equations one calculates the two characteristic vectors $\vec{E}_+$ and $\vec{E}_-$. Thus any electromagnetic wave propagating through a magnetised plasma can be written as:

$$\vec{E}_{in}(\vec{r}) = e_{in_+}\vec{E}_+(\vec{r}) + e_{in_-}\vec{E}_-(\vec{r}) \qquad (3.8)$$

with the parameters e_{in_+} and e_{in_-}.

The most fundamental feature of $\vec{E}_+$ and $\vec{E}_-$ is, that their polarisation properties do not alter while propagating through the magnetised plasma, if the plasma and the magnetic field are homogeneous. Thus their electric field vectors after a propagation distance Δz are:

$$\vec{E}_{1\pm}(\Delta z, t) = \vec{E}_\pm \, e^{i\Delta z \frac{n_\pm \, \omega}{c_0}} \, e^{i\omega t} \tag{3.9}$$

Hence the electric field of an arbitrary initial state of polarisation $\vec{E}_{in}$ after a propagation distance Δz is:

$$\vec{E}_{out}(\Delta z, t) = \left(e_{out_+}\vec{E}_+ + e_{out_-}\vec{E}_- \right) e^{i\omega t} = \left(e_{in_+}\vec{E}_+ e^{i\Delta z \frac{n_+ \omega}{c_0}} + e_{in_-}\vec{E}_- e^{i\Delta z \frac{n_- \omega}{c_0}} \right) e^{i\omega t} \tag{3.10}$$

This equation can easily be written as a 2×2-matrix equation in the coordinate system O (see Figure 3.6). After transforming this matrix to the coordinate system O', it is straight forward to rewrite the 2×2-matrix equation in terms of Stokes parameters (see Appendix E.2 and Appendix C.2.3):

$$\vec{S}_{out}(\Delta z) = \mathsf{M}_A(\vec{B}, \Delta z)\, \vec{S}_{in} \tag{3.11}$$

The explicit calculation of $\mathsf{M}_A(\vec{B}, \Delta z)$ is discussed in a publication by Segre [146]. The matrix $\mathsf{M}_A(\vec{B}, \Delta z)$ is also called the Müller matrix (see Appendix D.1) of a magnetised plasma. As the derivation is straight forward but lengthy, only the final result with respect to the coordinate system O' (see Figure 3.6) is given:

$$\mathsf{M}_A(\vec{B}, \Delta z) := \begin{pmatrix} 1 & 0 & 0 & 0 \\ 0 & \frac{\Omega_\parallel^2}{\Omega_0^2}\cos(\Omega_0\Delta z) + \frac{\Omega_\perp^2}{\Omega_0^2} & -\frac{\Omega_\parallel}{\Omega_0}\sin(\Omega_0\Delta z) & \frac{\Omega_\parallel\Omega_\perp}{\Omega_0^2}\left(1 - \cos(\Omega_0\Delta z)\right) \\ 0 & \frac{\Omega_\parallel}{\Omega_0}\sin(\Omega_0\Delta z) & \cos(\Omega_0\Delta z) & -\frac{\Omega_\perp}{\Omega_0}\sin(\Omega_0\Delta z) \\ 0 & \frac{\Omega_\parallel\Omega_\perp}{\Omega_0^2}\left(1 - \cos(\Omega_0\Delta z)\right) & \frac{\Omega_\perp}{\Omega_0}\sin(\Omega_0\Delta z) & 1 - \frac{\Omega_\perp^2}{\Omega_0^2}\left(1 - \cos(\Omega_0\Delta z)\right) \end{pmatrix} \tag{3.12a}$$

with:

$$V := \frac{\omega_{pe}^2}{(n_+ + n_-)c_0\,\omega^3\left[1 - \omega_{ce}^2\left(\frac{\sin^2\theta}{\omega^2 - \omega_{pe}^2} + \frac{\cos^2\theta}{\omega^2}\right)\right]} \tag{3.12b}$$

$$\Omega_\perp := V\frac{\omega_{ce}^2\omega^2}{\omega^2 - \omega_{pe}^2}\sin^2\theta \tag{3.12c} \qquad \Omega_\parallel := V\,2\omega_{ce}\omega\cos\theta \tag{3.12d}$$

$$\Omega_0 := \sqrt{\Omega_\perp^2 + \Omega_\parallel^2} = V2\omega_{ce}\omega\sqrt{\left(\frac{\omega_{ce}\omega}{2(\omega^2 - \omega_{pe}^2)}\sin^2\theta\right)^2 + \cos^2\theta} \tag{3.12e}$$

If the inhomogeneities in the plasma are not too large Eq. (3.12) remains valid, because one can use the WKB-approximation (see [74, 146]) and substitute e.g. $\Omega_0\Delta z$ with the integral along the path $\vec{r}(z)$, i.e. with $\int \Omega_0(\vec{r}(z)) \, \|\partial/\partial z\vec{r}(z)\| \, dz$. Thus one can limit all further discussion to thin homogeneous plasma layers, simplifying the notation.

3.4.3 The Dispersion Relation of the Faraday and Cotton-Mouton Effect

The fairly complex equations Eq. (3.7) and Eq. (3.12) are simplified considerably, if θ equals either $0°$ or $90°$. If θ equals $0°$, i.e. $\vec{B}_0 \parallel \vec{k}$, then the influence of the magnetised plasma on the electromagnetic wave is known as the Faraday effect. If θ equals $90°$, i.e. $\vec{B}_0 \perp \vec{k}$, then the interaction is called the Cotton-Mouton effect. The analogy to the Faraday effect is the circular anisotropy in an inhomogeneous optical medium and the analogy to the Cotton-Mouton effect is the linear anisotropy. If θ is neither $0°$ nor $90°$, one finds a mixture between the Faraday and the Cotton-Mouton effect, whereby one effect can become dominant over the other (see Subsection 3.4.5).

For now, we limit the discussion to the dispersion relation of the Faraday and Cotton-Mouton effect. The corresponding Müller matrices are presented later in Subsection 3.4.5.

3.4.3.1 The Faraday effect ($\vec{B}_0 \parallel \vec{k}$)

In this case the Appleton-Hartree equation Eq. (3.7) reduces to:

$$n_\pm^2 = \epsilon_1 \pm \epsilon_2 = 1 - \frac{\omega_{pe}^2}{\omega(\omega \pm \omega_{ce})} \tag{3.13}$$

and one calculates the characteristic vectors

$$\vec{E}_\pm = \vec{e}_x \mp i\,\vec{e}_y \tag{3.14}$$

where $\vec{e}_x$ and $\vec{e}_y$ are unit vectors in the x and y direction, respectively. The characteristic vectors $\vec{E}_\pm$ correspond to right and left circular polarised light. Because the Faraday effect is of minor importance for the experiment presented in this work (compare Subsection 3.2.2, Subsection 3.4.5), it is referred to [29, 85, 161] for a more detailed discussion.

3.4.3.2 The Cotton-Mouton effect ($\vec{B}_0 \perp \vec{k}$)

The dispersion relation of the Cotton-Mouton effect is more complicated. In this case the Appleton-Hartree equation reduces to:

$$n_+^2 = n_o^2 = \epsilon_3 = 1 - \frac{\omega_{pe}^2}{\omega^2} \tag{3.15a}$$

$$n_-^2 = n_e^2 = \frac{\epsilon_1^2 - \epsilon_2^2}{\epsilon_1} = \frac{(\omega^2 - \omega_1^2)(\omega^2 - \omega_2^2)}{\omega^2(\omega^2 - \omega_H^2)} = 1 - \frac{\omega_{pe}^2}{\omega^2}\frac{\omega^2 - \omega_{pe}^2}{\omega^2 - \omega_{pe}^2 - \omega_{ce}^2} \tag{3.15b}$$

with [85]::

$$\omega_1 = \frac{\omega_{ce}}{2}\left(\sqrt{1 + \frac{4\omega_{pe}^2}{\omega_{ce}^2}} - 1\right) \quad (3.16a) \qquad \omega_2 = \frac{\omega_{ce}}{2}\left(\sqrt{1 + \frac{4\omega_{pe}^2}{\omega_{ce}^2}} + 1\right) \quad (3.16b)$$

$$\omega_H = \sqrt{\omega_{pe}^2 + \omega_{ce}^2} \tag{3.16c}$$

ω_1 and ω_2 are called cut-off frequencies and ω_H is the upper hybrid frequency (see [29, 85, 161]). As the dispersion relation Eq. (3.15a) and the dispersion relation of an unmagnetised plasma are identical, Eq. (3.15a) is called the ordinary branch, whilst Eq. (3.15b) is called the extraordinary branch. Substituting these equations into Eq. (3.6a) gives the
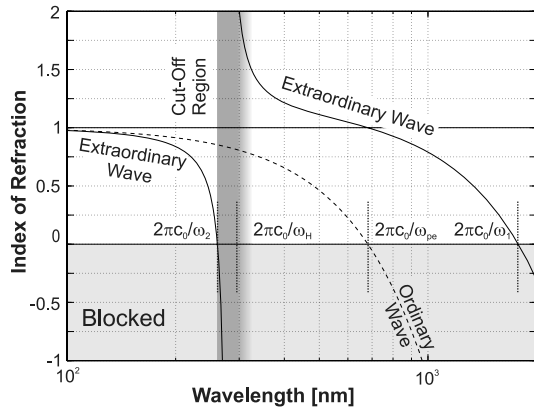
Figure 3.7: The dispersion relation of the Cotton-Mouton effect for optical frequencies. The situation shown here corresponds to the $4^{th}\omega$ cut-off in the experiment. I.e.: $n_{ec} = 2.4 \cdot 10^{21}$ cm^{-3}, $\left|\vec{B}_0\right| = 350$ MG. c_0 is the speed of light in vacuum.
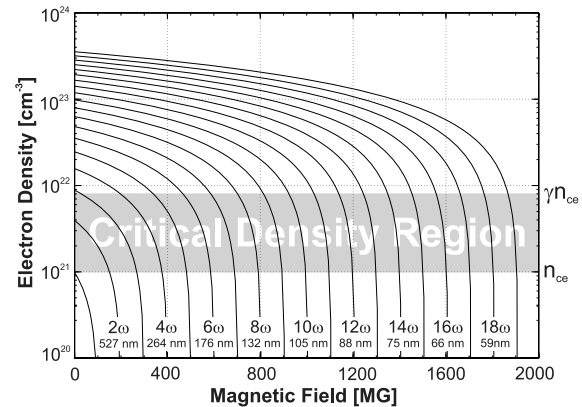
Figure 3.8: Cut-offs for the 1st to the 19th harmonic of 1053 nm radiation from VULCAN in terms of electron density and magnetic field (see Eq. (3.19)). The density range inside the magnetised areas of the plasma is coloured in gray.

characteristic vectors:

$$\vec{E}_+ = \vec{E}_o = \vec{e}_z \qquad (3.17a) \qquad \vec{E}_- = \vec{E}_e = \alpha\vec{e}_x + i\vec{e}_y \qquad (3.17b)$$

with

$$\alpha = \frac{E_x}{E_y} = \frac{\epsilon_1}{\epsilon_2} = \frac{\left(\omega^2 - \omega_{pe}^2 - \omega_{ce}^2\right)\omega}{\omega_{pe}^2 \omega_{ce}} \qquad (3.18)$$

As θ equals $90°$ in the Cotton-Mouton case, the ordinary and extraordinary wave (also called the o-wave and the x-wave, respectively) propagate in the y-direction (see Figure 3.6). With Eq. (3.17) it is obvious, that the o-wave ($\vec{E}_+$) is purely transverse. On the other hand the x-wave ($\vec{E}_-$) may have an additional longitudinal component. But this longitudinal component is solely imaginary. The ratio between the real transversal and the imaginary longitudinal component is given by Eq. (3.18).

The different branches of the dispersion relations Eq. (3.15a) and Eq. (3.15b) are shown in Figure 3.7 for optical frequencies. The ordinary branch is identical to the dispersion relation in an unmagnetised plasma, i.e. n_+ approaches unity for $\omega \to \infty$ and waves with frequencies below ω_{pe} are cut-off, i.e. they cannot propagate through the plasma.

The behaviour of the extraordinary branch is more complicated. But n_- approaches unity for $\omega \to \infty$ again, whilst a cut-off already appears at ω_2, well above ω_{pe}. ω_2 shifts to higher frequencies, if the magnetic field strength is increased. Unfortunately, there is still another branch, so that lower frequencies can propagate again. Its high frequency limit ω_H is a resonance, where the incident energy of the electromagnetic wave is consumed to stimulate strong oscillations of the electrons. At a frequency ω_1 well below ω_{pe} this branch is finally cut-off, too, so that no extraordinary polarised radiation with frequencies below ω_1 can propagate through the plasma.

In summary, extraordinary radiation with frequencies between $\omega_H - \delta$ and ω_2 is cut-off and cannot propagate through the plasma, whilst ordinary radiation can propagate. Thus the plasma acts like a linear polariser in this frequency range.

3.4.4   Observing Magnetic Fields with the X-Wave Cut-Off

In our experiment harmonic radiation (generated mainly around the critical density surface in the centre of the laser produced plasma and propagating through the magnetised areas of the plasma (see Subsection 3.3.1)) is used to observe the magnetic field strength: if the frequency of a particular harmonic is in the x-wave cut-off region, then the extraordinary component of this harmonic, i.e. its p-polarised part, is cut-off. As the harmonics are mainly p-polarised (see Subsection 3.3.2), the observed harmonic intensity decreases considerably if a cut-off appears. This intensity drop can be increased even further by putting a polariser, blocking the ordinary polarised radiation, in front of the detector. Using this setup the measured signal can vanish completely, if a cut-off appears (see Figure 3.19). Hence, even if the radiation is completely unpolarised, the cut-offs can be used to estimate a lower boundary of the magnetic field strength inside the plasma. This boundary can be calculated by solving Eq. (3.16b) for $\left|\vec{B}_0\right|$ and substituting ω_2 with ω_{Harm}:

$$\left|\vec{B}_0\right| \geq \frac{m_e}{e}\omega_{\mathrm{Harm}} - \frac{e}{\epsilon_0}\frac{n_e}{\omega_{\mathrm{Harm}}} \tag{3.19}$$

The only unknown quantity despite $\left|\vec{B}_0\right|$ in this equation is the electron density n_e in the magnetised area. Without knowing this density, Eq. (3.19) can be used to plot the lowest magnetic field strength necessary for an x-wave cut-off versus electron density, using the harmonic order as a parameter (see Figure 3.8). From this figure it is seen that one can determine a lower limit of the magnetic field strength with a reasonable error even if the electron density is known only within one order of magnitude as long as this density is not too high.

Another important conclusion can be drawn from the observation of a complete x-wave cut-off: in Subsection 3.4.5 it is shown that even at angles θ close to $90°$ the Faraday effect can be dominant over the Cotton-Mutton effect. Thus it is initially unclear, if the Faraday effect can be neglected in comparison to the Cotton-Mouton effect. If the Faraday effect is important, then the characteristic vectors of the plasma are no longer linear, but elliptically polarised (see Subsection 3.4.3). In this case one of the elliptically polarised characteristic vectors is cut-off, so that the polarisation state behind the magnetised area is elliptically polarised. In consequence it is impossible, that the measured signal behind a linear polariser vanishes completely. Hence, if this signal is fully extinguished, one has to conclude that the characteristic vectors are linear polarised and thus the interaction between the plasma and the electromagnetic wave is determined by the Cotton-Mouton effect exclusively.

To derive Eq. (3.19) it was assumed, that the cold plasma approximation holds, i.e. collisions are neglected and the temperature is approximated by zero (see Subsection 3.4.1). Consequently the influence of a finite temperature on the x-wave cut-offs needs further attention: it is well known that additional branches appear in the dispersion relation, mainly at harmonics of ω_{ce}, if the temperature is not zero [85, 161]. Hence

it might become impossible to observe the cut-offs. But even if they can be observed, it is still unclear, if the upper cut-off frequency ω_2 is shifted by the finite temperature. Recalling Eq. (3.5) and noticing that the index of refraction becomes zero at that frequency, it is obvious that the cold plasma approximation holds next to the cut-off frequencies and thus this frequency is not supposed to depend on temperature strongly.

Furthermore relativistic effects alter the upper cut-off frequency: if the motion of the electrons in the magnetised area becomes sufficiently fast, then the electron mass and density in all equations need to be multiplied by the relativistic γ-factor (see Eq. (3.4)). As can be seen from Eq. (3.19) easily, in this case even higher magnetic fields are required to cut-off a certain harmonic. Thus, by neglecting relativistic effects, one only underestimates the magnetic field strength inside the plasma.

In summary, observing the magnetic field strength with the x-wave cut-offs is a very robust method, always giving a lower boundary of the peak magnetic field strength.

3.4.5 The Müller Matrices of the Faraday and Cotton-Mouton Effect

Apart from the x-wave cut-offs another completely independent method to determine the magnetic field strength exists. It is even applicable when the field strength is too low to produce a cut-off. Its main disadvantage in comparison to the cut-offs is that one has to know the propagation length of the electromagnetic probe through the magnetised area and its initial state of polarisation in addition to the electron density in the magnetised region. This method is based on measuring components of the Müller matrix (see Eq. (3.12)) in a magnetised plasma. Before discussing, how to measure single components of the Müller matrix and how to derive the magnetic field strength, we shall have a closer look onto the Müller matrix of the Faraday and Cotton-Mouton effect:

3.4.5.1 The Faraday effect ($\theta := 0°$)
In this case $\Omega_\perp$ equals 0 and Eq. (3.12) reduces to:

$$
\mathsf{M_F}(\vec{B}) := \begin{pmatrix} 1 & 0 & 0 & 0 \\ 0 & \cos(\Omega_\parallel \Delta z) & -\sin(\Omega_\parallel \Delta z) & 0 \\ 0 & \sin(\Omega_\parallel \Delta z) & \cos(\Omega_\parallel \Delta z) & 0 \\ 0 & 0 & 0 & 1 \end{pmatrix}
\tag{3.20a}
$$

With the ordinary index of refraction $n_o := \sqrt{1 - \frac{\omega_{pe}^2}{\omega^2}}$ one sees, that $\Omega_\parallel$ holds:

$$
\Omega_\parallel = \frac{2\omega_{pe}^2 \omega_{ce}}{c_0 n_o \omega^2 \left(\sqrt{1 + \frac{\omega_{pe}^2 \omega_{ce}}{(\omega + \omega_{ce})(\omega^2 - \omega_{pe}^2)}} + \sqrt{1 - \frac{\omega_{pe}^2 \omega_{ce}}{(\omega - \omega_{ce})(\omega^2 - \omega_{pe}^2)}} \right) \left(1 - \frac{\omega_{ce}^2}{\omega^2} \right)}
$$
$$
\stackrel{\substack{\omega \gg \omega_{ce} \\ \omega \gg \omega_{pe}}}{\approx} \frac{\omega_{pe}^2 \omega_{ce}}{c_0} \frac{1}{\omega^2}
\tag{3.20b}
$$

Eq. (3.20) can be derived far more simply, if one remembers that the characteristic vectors of the Faraday effect are left (LCP) and right (RCP) circular polarised electromagnetic waves (see Eq. (3.14)). Consequently one can think of the Faraday effect in terms of a

circular anisotropy with a phase difference $\Delta\Phi$ between the RCP and LCP wave after a propagation distance Δz of:

$$\Delta\Phi = \frac{(n_+ - n_-)\omega\Delta z}{c_0} \tag{3.21}$$

Substituting $\Delta\Phi$ into the Müller matrix of a circular retarder Eq. (D.30) results in Eq. (3.20).

3.4.5.2 The Cotton-Mouton effect ($\theta := 90°$)

In this case $\Omega_\parallel$ equals 0 and Eq. (3.12) reduces to:

$$M_C(\vec{B}) := \begin{pmatrix} 1 & 0 & 0 & 0 \\ 0 & 1 & 0 & 0 \\ 0 & 0 & \cos(\Omega_\perp\Delta z) & -\sin(\Omega_\perp\Delta z) \\ 0 & 0 & \sin(\Omega_\perp\Delta z) & \cos(\Omega_\perp\Delta z) \end{pmatrix} \tag{3.22a}$$

With the ordinary index of refraction n_o one sees, that $\Omega_\perp$ holds:

$$\Omega_\perp = \frac{\omega_{pe}^2\omega_{ce}^2}{c_0 n_o \omega \left(1 + \sqrt{1 - \frac{\omega_{pe}^2\omega_{ce}^2}{(\omega^2-\omega_{pe}^2-\omega_{ce}^2)(\omega^2-\omega_{pe}^2)}}\right)(\omega^2 - \omega_{pe}^2 - \omega_{ce}^2)} \overset{\substack{\omega\gg\omega_{ce}\\ \omega\gg\omega_{pe}}}{\approx} \frac{\omega_{pe}^2\omega_{ce}^2}{2c_0}\frac{1}{\omega^3} \tag{3.22b}$$

Similar to the Faraday effect, Eq. (3.22) can be derived by noticing that the characteristic vectors of the Cotton-Mouton effect are the linear polarised states in the x- and y-direction (see Eq. (3.17)). Consequently one can think of the Cotton-Mouton effect in terms of a linear anisotropy with a phase difference $\Delta\Phi$ between the two characteristic waves after a propagation distance Δz. Substituting $\Delta\Phi$ into the Müller matrix of a linear retarder Eq. (D.16) results in Eq. (3.22).

3.4.5.3 Propagation close to perpendicular ($\theta := 90° - \hat{\theta}$; $\hat{\theta} \to 0$)

At a first glance one might think that the interaction between the magnetised plasma and the electromagnetic wave is always determined by the Cotton-Mouton effect, if the propagation direction is close to perpendicular. But at a closer look one quickly recognises that things are not so simple: in Eq. (3.12e) the term

$$\sqrt{(a\sin^2(90° - \hat{\theta})) + \cos^2(90° - \hat{\theta})} = \sqrt{(a\cos^2\hat{\theta})^2 + \sin^2\hat{\theta}} \quad \text{with} \quad a := \frac{1}{2}\frac{\omega_{ce}/\omega}{1 - \omega_{pe}^2/\omega^2}$$

is approximated either by a or by $\hat{\theta}$, depending on the ratio of $a/\hat{\theta}$:

The Faraday effect is dominant If $a \ll \hat{\theta} \ll 1$, then one can approximate the corresponding Müller matrix with:

$$\mathsf{M}_{F_{app}}(\vec{B}) := \tag{3.23a}$$

$$\begin{pmatrix} 1 & 0 & 0 & 0 \\ 0 & \left(1 - \frac{a^2}{\hat{\theta}^2}\right)\cos(\Omega_\parallel \Delta z) + \frac{a^2}{\hat{\theta}^2} & -\left(1 - \frac{a^2}{2\hat{\theta}^2}\right)\sin(\Omega_\parallel \Delta z) & \frac{a}{\hat{\theta}}(1 - \cos(\Omega_\parallel \Delta z)) \\ 0 & \left(1 - \frac{a^2}{2\hat{\theta}^2}\right)\sin(\Omega_\parallel \Delta z) & \cos(\Omega_\parallel \Delta z) & -\frac{a}{\hat{\theta}}\sin(\Omega_\parallel \Delta z) \\ 0 & \frac{a}{\hat{\theta}}(1 - \cos(\Omega_\parallel \Delta z)) & \frac{a}{\hat{\theta}}\sin(\Omega_\parallel \Delta z) & 1 - \frac{a^2}{\hat{\theta}^2}(1 - \cos(\Omega_\parallel \Delta z)) \end{pmatrix}$$

whereby:

$$\Omega_\parallel = \frac{\omega_{pe}^2 \omega_{ce} \sin\hat{\theta}}{c_0} \frac{1}{\omega^2} \tag{3.23b}$$

Comparing this result with the Müller matrix of the Faraday effect one notes, that Eq. (3.20a) is the zeros order approximation of Eq. (3.23a). Thus the Faraday effect is dominant in this case.

The Cotton-Mouton effect is dominant On the other hand, if $a \gg \hat{\theta}$, then one can approximate the corresponding Müller matrix with:

$$\mathsf{M}_{C_{app}}(\vec{B}) := \tag{3.24a}$$

$$\begin{pmatrix} 1 & 0 & 0 & 0 \\ 0 & \frac{\hat{\theta}^2}{a^2}\cos(\Omega_\perp \Delta z) + \left(1 - \frac{\hat{\theta}^2}{a^2}\right) & -\frac{\hat{\theta}}{a}\sin(\Omega_\perp \Delta z) & \frac{\hat{\theta}}{a}(1 - \cos(\Omega_\perp \Delta z)) \\ 0 & \frac{\hat{\theta}}{a}\sin(\Omega_\perp \Delta z) & \cos(\Omega_\perp \Delta z) & -\left(1 - \frac{\hat{\theta}^2}{2a^2}\right)\sin(\Omega_\perp \Delta z) \\ 0 & \frac{\hat{\theta}}{a}(1 - \cos(\Omega_\perp \Delta z)) & \left(1 - \frac{\hat{\theta}^2}{2a^2}\right)\sin(\Omega_\perp \Delta z) & 1 - \left(1 - \frac{\hat{\theta}^2}{a^2}\right)(1 - \cos(\Omega_\perp \Delta z)) \end{pmatrix}$$

whereby:

$$\Omega_\perp = \frac{\omega_{pe}^2 \omega_{ce}^2 \cos^2\hat{\theta}}{2c_0} \frac{1}{\omega^3} \tag{3.24b}$$

In analogy to the Faraday effect one notes, that Eq. (3.22a) is the zeros order approximation of Eq. (3.24a). Consequently the Cotton-Mouton effect is dominant now.

If the propagation is close to perpendicular, then it is unclear in the first instance, if the interaction between the electromagnetic wave and the magnetised plasma is determined by the Faraday or the Cotton-Mouton effect. Thus one has to find a possibility to determine which effect is the more important one in an experiment.

3.4.6 Observing Magnetic Fields with the Müller Matrix

To understand how one can distinguish between the Faraday and Cotton-Mouton case experimentally, how to measure components of the Müller matrix and finally derive the magnetic field strength, it is useful to understand, that an arbitrary set of Stokes parameters $\vec{S}_{in}$ can be written as (see also Appendix C and Appendix D):

$$\vec{S}_{in} = \vec{S}_{pol} + \vec{S}_{unpol} = I_{pol}\, \mathsf{M}_{rot}(45° - \alpha)\mathsf{M}_{2\eta}(0°)\, \vec{S}_{45°} + I_{unpol}\vec{S}_u \tag{3.25}$$

$\vec{S}_{45°}$ are the Stokes parameters of a linear polarised electromagnetic wave with an azimuth angle of 45° and an intensity of unity (see Eq. (C.8)). $\vec{S}_u$ are the Stokes parameters of a completely unpolarised wave with an intensity of unity (see Eq. (C.23)). $\mathsf{M}_{2\eta}(0°)$ is the Müller matrix of a wave plate with a linear anisotropy, introducing a phase-shift of 2η between the x- and y-component of the electromagnetic wave (see Eq. (D.16)). $\mathsf{M}_{\mathrm{rot}}(45° - \alpha)$ rotates the coordinate system by $45° - \alpha$. With the help of Eq. (C.5) and Eq. (C.13) one immediately recognises, that $\vec{S}_{\mathrm{pol}}$ are Stokes parameters with an intensity I_0, an ellipticity $\tan\eta$ and an azimuth angle α.

3.4.6.1 The General Case

Now consider the Cartesian coordinate system O' from Figure 3.6, which is also the coordinate system of $\mathsf{M}_A(\vec{B})$ from Eq. (3.12): let α be the azimuth angle of S_{in} in O' and let β be the angle between the x-axis of O' and the x-axis of the polarimeters (see Subsection 3.5.2), then the measured Stokes parameters $\vec{S}_{\mathrm{out}} := \mathsf{M}_{\mathrm{rot}}(\beta)\mathsf{M}_A(\vec{B})\vec{S}_{\mathrm{in}}$ are given by:

$$
\vec{S}_{\mathrm{out}}(\vec{B}) = \left[
\begin{pmatrix}
1 \\
\left(-\frac{\Omega_\parallel}{\Omega_0}\sin 2(\alpha - \beta)\cos 2\eta - \frac{\Omega_\perp}{\Omega_0}\sin 2\beta \sin 2\eta\right)\sin\Omega_0\Delta z \\
\left(+\frac{\Omega_\parallel}{\Omega_0}\cos 2(\alpha - \beta)\cos 2\eta - \frac{\Omega_\perp}{\Omega_0}\cos 2\beta \sin 2\eta\right)\sin\Omega_0\Delta z \\
\frac{\Omega_\perp}{\Omega_0}\sin 2\alpha \cos 2\eta \sin\Omega_0\Delta z
\end{pmatrix}
\right.
$$

$$
+ \begin{pmatrix}
0 \\
\left(\left(\sin 2\alpha\sin 2\beta + \frac{\Omega_\parallel^2}{\Omega_0^2}\cos 2\alpha\cos 2\beta\right)\cos 2\eta - \frac{\Omega_\parallel\Omega_\perp}{\Omega_0^2}\cos 2\beta\sin 2\eta\right)\cos\Omega_0\Delta z \\
\left(\left(\sin 2\alpha\cos 2\beta - \frac{\Omega_\parallel^2}{\Omega_0^2}\cos 2\alpha\sin 2\beta\right)\cos 2\eta + \frac{\Omega_\parallel\Omega_\perp}{\Omega_0^2}\sin 2\beta\sin 2\eta\right)\cos\Omega_0\Delta z \\
\left(\frac{\Omega_\perp^2}{\Omega_0^2}\sin 2\eta - \frac{\Omega_\parallel\Omega_\perp}{\Omega_0^2}\cos 2\alpha\cos 2\eta\right)\cos\Omega_0\Delta z
\end{pmatrix}
$$

$$
\left. + \begin{pmatrix}
0 \\
\left(+\frac{\Omega_\perp^2}{\Omega_0^2}\cos 2\alpha\cos 2\eta + \frac{\Omega_\parallel\Omega_\perp}{\Omega_0^2}\sin 2\eta\right)\cos 2\beta \\
\left(-\frac{\Omega_\perp^2}{\Omega_0^2}\cos 2\alpha\cos 2\eta - \frac{\Omega_\parallel\Omega_\perp}{\Omega_0^2}\sin 2\eta\right)\sin 2\beta \\
\frac{\Omega_\parallel\Omega_\perp}{\Omega_0^2}\cos 2\alpha\cos 2\eta + \left(1 - \frac{\Omega_\perp^2}{\Omega_0^2}\right)\sin 2\eta
\end{pmatrix}\right] I_{pol} + \begin{pmatrix} 1 \\ 0 \\ 0 \\ 0 \end{pmatrix} I_{unpol} \qquad (3.26)
$$

This equation is valid for an arbitrary electromagnetic wave propagating through a magnetised plasma. To calculate $\Omega_0(\vec{B})$ and to prevent ambiguity it is required that $\Omega_0(\vec{B})\Delta z < \pi$ holds. This means that the propagation length of the wave through the magnetised plasma may not be too large and that the field may not be too strong. Anyway, if this restriction does not hold for a certain electromagnetic wave, then it is possible to use an electromagnetic wave with a shorter wavelength, because $\Omega_0\Delta z$ decreases with decreasing wavelength (see Eq. (3.12)).

In general Eq. (3.26) is too complicated to be applied successfully for analysing experimental data. Luckily, this equation is simplified significantly if one can assume that either the Faraday or the Cotton-Mouton effect is dominant.

3.4.6.2 The Faraday Case

In this case the first order approximation of Eq. (3.26) with respect to $\hat{\theta} := 90° - \theta$ is given by:

$$\vec{S}_{\text{out}}(\vec{B}) = \begin{pmatrix} 1 \\ \cos(2(\alpha - \beta) + \Omega_{\parallel}\Delta z)\cos 2\eta \\ \sin(2(\alpha - \beta) + \Omega_{\parallel}\Delta z)\cos 2\eta \\ \frac{a}{\hat{\theta}}\left(\cos 2\alpha - \cos(2\alpha + \Omega_{\parallel}\Delta z)\right)\cos 2\eta + \sin 2\eta \end{pmatrix} I_{\text{pol}} + \begin{pmatrix} 1 \\ 0 \\ 0 \\ 0 \end{pmatrix} I_{\text{unpol}} \quad (3.27)$$

with $\Omega_{\parallel}$ from Eq. (3.23b).

It is seen immediately that this equation is simplified even more, if $\alpha = \beta$. In this case the magnetic field is most simply calculated using the ratio of the Stokes parameter S_3 and S_2. If $\Omega_{\parallel}\Delta z \ll \pi$ holds, then one finds:

$$\frac{S_3}{S_2} = \tan(2(\alpha - \beta) + \Omega_{\parallel}\Delta z) = \tan(\Omega_{\parallel}\Delta z) \approx \Omega_{\parallel}\Delta z = \frac{\omega_{pe}^2 \omega_{ce}\sin\hat{\theta}}{c_0}\frac{1}{\omega^2}\Delta z \propto \frac{|\vec{B}_0|}{\omega^2}n_e\Delta z$$
$$(3.28)$$

Consequently in the Faraday case, the measured values of $\Omega_{\parallel}\Delta z$ scale with the reciprocal square of the wavelength. Even if $\alpha = \beta$ does not hold, it is possible to calculate $\Omega_{\parallel}\Delta z$, if one can determine $\alpha - \beta$ from the geometry of the experimental setup.

3.4.6.3 The Cotton-Mouton Case

In this case the first order approximation of Eq. (3.26) with respect to $\hat{\theta} := 90° - \theta$ is given by:

$$\vec{S}_F(\vec{B}) = \left[\begin{pmatrix} 1 \\ \left(-\frac{\hat{\theta}}{a}\sin 2(\alpha - \beta)\sin\Omega_{\perp}\Delta z + \sin 2\alpha\sin 2\beta\cos\Omega_{\perp}\Delta z + \cos 2\alpha\cos 2\beta\right)\cos 2\eta \\ \left(+\frac{\hat{\theta}}{a}\cos 2(\alpha - \beta)\sin\Omega_{\perp}\Delta z + \sin 2\alpha\cos 2\beta\cos\Omega_{\perp}\Delta z - \cos 2\alpha\sin 2\beta\right)\cos 2\eta \\ \left(\frac{\hat{\theta}}{a}\cos 2\alpha(1 - \cos\Omega_{\perp}\Delta z) + \sin 2\alpha\sin\Omega_{\perp}\Delta z\right)\cos 2\eta \end{pmatrix} \right.$$
$$\left. + \begin{pmatrix} 0 \\ -\sin 2\beta\sin\Omega_{\perp}\Delta z\sin 2\eta \\ -\cos 2\beta\sin\Omega_{\perp}\Delta z\sin 2\eta \\ (1 + \cos\Omega_{\perp}\Delta z)\sin 2\eta \end{pmatrix} \right] I_{\text{pol}} + \begin{pmatrix} 1 \\ 0 \\ 0 \\ 0 \end{pmatrix} I_{\text{unpol}} \quad (3.29)$$

with $\Omega_{\perp}$ from Eq. (3.24b).

A very special case is $\alpha = 0$ combined with an incident linear polarised electromagnetic wave, i.e. $\eta = 0$. If $\hat{\theta}/a \approx 0$ holds in addition, then Eq. (3.29) is independent of the magnetic field, so that the measured Stokes parameters are not influenced by the Cotton-Mouton effect and one observes the Faraday effect only (see Eq. (3.27)).

Calculating the magnetic field strength from the measured Stokes parameters in the Cotton-Mouton case is more complicated than in the Faraday case. The equations can be simplified somewhat by setting $\alpha = \beta$ or $\beta = 0$. The easiest way to determine the field strength is to use the fourth Stokes parameter and to assume that $\Omega_{\perp}\Delta z \ll \pi$, $\hat{\theta}/a \approx 0$

and $\eta \approx 0$ hold:

$$\frac{S_3}{I_{pol}} \overset{\text{Eq. (C.21)}}{=} \frac{S_3}{\sqrt{S_1^2 + S_2^2 + S_3^2}} \approx \sin 2\alpha \cos 2\eta \sin \Omega_\perp \Delta z \approx \sin 2\alpha \cos 2\eta \ \Omega_\perp \Delta z \propto \Omega_\perp \Delta z$$

$$= \sin 2\alpha \frac{\omega_{pe}^2 \omega_{ce}^2 \cos^2 \hat\theta}{2c_0} \frac{1}{\omega^3} \Delta z \propto \sin 2\alpha \frac{|\vec{B}_0|^2}{\omega^3} n_e \Delta z \tag{3.30}$$

Now the measured values of $\Omega_\perp \Delta z$ scale with the reciprocal cube of the wavelength. To calculate the ellipticity angle η one can use the parameters S_1 or S_2.

If the prerequisites from above do not hold, then it is possible by least square fitting to calculate $\Omega_\perp \Delta z$, if at least any of the three quantities α, β and η is known. In general β is determined by the experimental setup, as the direction of the magnetic field is pretty much parallel to the surface of the target (see Subsection 3.2.2). α and η can be estimated from the observation of harmonic radiation at low laser intensities when the magnetic fields are still very weak. If estimates for all three quantities are known, then Eq. (3.29) is overdetermined and the size of the least square error is an indication of the validity of these assumptions.

3.4.6.4 The s^2/p^2-Ratio

If one is going to use radiation in the VUV / XUV range or radiation with an even shorter wavelength to determine the magnetic field strength (see Subsection 3.5.3), then additional difficulties arise. Despite the necessity to set up the polarimeter in vacuum and to find a suitable radiation detector for this wavelength range, the most challenging problem is to measure the complete set of Stokes parameters, because wave-plates for this wavelength range are practically unavailable. But it is sufficient to measure the s^2/p^2-ratio for observing the magnetic field, though this is a single quantity and one cannot check the assumptions made about α, β and η any more.

In the Faraday and Cotton-Mouton case one can write $S_0 = I_{pol} + I_{unpol}$ and $S_1 = (a\cos(\Delta\Omega) + b)I_{pol}$ with constants $\Delta\Omega, a, b \in \mathbb{R}$. Thus one derives the s^2/p^2-ratio:

$$\frac{I_s}{I_p} := \frac{E_s^2}{E_p^2} := \frac{< E_y E_y^* >}{< E_x E_x^* >} = \frac{S_0 - S_1}{S_0 + S_1} = \frac{1 - (a\cos(\Delta\Omega) + b)p}{1 + (a\cos(\Delta\Omega) + b)p}$$

$$\approx \frac{1 - (a+b)p}{1 + (a+b)p} + \frac{ap}{(1 + (a+b)p)^2} \Delta\Omega^2 \left(1 - \frac{1 - (5a-b)p}{12(1 + (a+b)p)} \Delta\Omega^2 + \mathcal{O}(4) \right) \tag{3.31}$$

whereby the righthand-side is the Taylor expansion of the lefthand-side and p is the degree of polarisation (see Eq. (C.24)).

The Faraday Effect In this case $a = \cos 2\eta$, $b = 0$ and $\Delta\Omega = 2(\alpha - \beta) + \Omega_\parallel \Delta z$ (see Eq. (3.27)) hold, so that with Eq. (3.23b) the s^2/p^2-ratio is:

$$\frac{I_s}{I_p} \approx \frac{1 - p\cos 2\eta}{1 + p\cos 2\eta} + \frac{p\cos 2\eta}{(1 + p\cos 2\eta)^2} (2(\alpha - \beta) + \Omega_\parallel \Delta z)^2 + \mathcal{O}(4)$$

$$\approx \frac{1 - p\cos 2\eta}{1 + p\cos 2\eta} + \frac{p\cos 2\eta}{(1 + p\cos 2\eta)^2} \left(\frac{\omega_{pe}^2 \omega_{ce} \sin\hat\theta}{c_0} \frac{1}{\omega^2} \Delta z + 2(\alpha - \beta) \right)^2 \tag{3.32}$$

This equation is simplified considerably, if $\alpha \approx \beta$, $\eta \approx 0$ and $p \approx 1$:

$$\frac{I_s}{I_p} \approx \frac{1}{2^2} \left(\frac{\omega_{pe}^2 \omega_{ce} \sin \hat{\theta}}{c_0} \frac{1}{\omega^2} \Delta z \right)^2 \propto \left(\sin \hat{\theta} \frac{|\vec{B}_0|}{\omega^2} n_e \Delta z \right)^2 \tag{3.33}$$

The Cotton-Mouton Effect In this case $a = \cos 2\eta \sin 2\alpha \sin 2\beta$, $b = \cos 2\eta \cos 2\alpha \cos 2\beta$ and $\Delta\Omega = \Omega_\perp \Delta z$ (see Eq. (3.29)) hold, so that with Eq. (3.24b) the s^2/p^2-ratio is:

$$\frac{I_s}{I_p} \approx \frac{1 - p \cos 2\eta \cos 2(\alpha - \beta)}{1 + p \cos 2\eta \cos 2(\alpha - \beta)} + \frac{p \cos 2\eta \sin 2\alpha \sin 2\beta}{(1 + p \cos 2\eta \cos 2(\alpha - \beta))^2} (\Omega_\perp \Delta z)^2 + \mathcal{O}(4) \tag{3.34}$$

$$\approx \frac{1 - p \cos 2\eta \cos 2(\alpha - \beta)}{1 + p \cos 2\eta \cos 2(\alpha - \beta)} + \frac{p \cos 2\eta \sin 2\alpha \sin 2\beta}{(1 + p \cos 2\eta \cos 2(\alpha - \beta))^2} \left(\frac{\omega_{pe}^2 \omega_{ce}^2 \cos^2 \hat{\theta}}{2c_0} \frac{1}{\omega^3} \Delta z \right)^2$$

This equation is simplified considerably, if $\alpha \approx \beta$, $\eta \approx 0$ and $p \approx 1$:

$$\frac{I_s}{I_p} \approx \left(\frac{\sin(\alpha + \beta)}{2} \right)^2 \left(\frac{\omega_{pe}^2 \omega_{ce}^2 \cos^2 \hat{\theta}}{2c_0} \frac{1}{\omega^3} \Delta z \right)^2 \propto \left(\sin(\alpha + \beta) \cos^2 \hat{\theta} \frac{|\vec{B}_0^2|}{\omega^3} n_e \Delta z \right)^2 \tag{3.35}$$

At the beginning of this section the question, how one can distinguish between the Faraday and Cotton-Mouton effect, was asked. Comparing Eq. (3.23b) with Eq. (3.24b) or respectively Eq. (3.33) with Eq. (3.35) one recognises that one can distinguish between the two effects by simply comparing how $\Omega_\parallel$ and $\Omega_\perp$ scale with the wavelength: in the Faraday case this scaling is $\propto \omega^{-2}$ and in the Cotton-Mouton case it is $\propto \omega^{-3}$.

3.5 The Experimental Setup for Producing and Observing Magnetic Fields

In this section the experimental setup for generating and measuring ultra-strong magnetic fields in a laser produced plasma is discussed in detail. This experiment was performed at the Rutherford-Appleton-Laboratory using the CPA-beam of VULCAN [37–39]. In the first subsection an overview of the whole experimental setup is given. The next subsection describes a polarimeter used for measuring the Stokes parameters of harmonic radiation with a wavelength longer than 200 nm. The final section explains the VUV / XUV polarimeter, used to measure the s^2/p^2-ratio of VUV / XUV harmonics. Furthermore in each of these two subsections the calibration of the respective polarimeter and the evaluation of the measured data are discussed.

3.5.1 The General Setup

A schematic overview of the experiment is shown in Figure 3.9: The CPA-beam of VULCAN was focused onto a glass target to produce the plasma. Then the harmonic radiation generated during the laser–plasma interaction was collected and analysed with polarimeters for the visible (VIS), UV and VUV / XUV range, so that one can calculate the magnetic field strength using the equations discussed in Subsection 3.4.4 and Subsection 3.4.6.
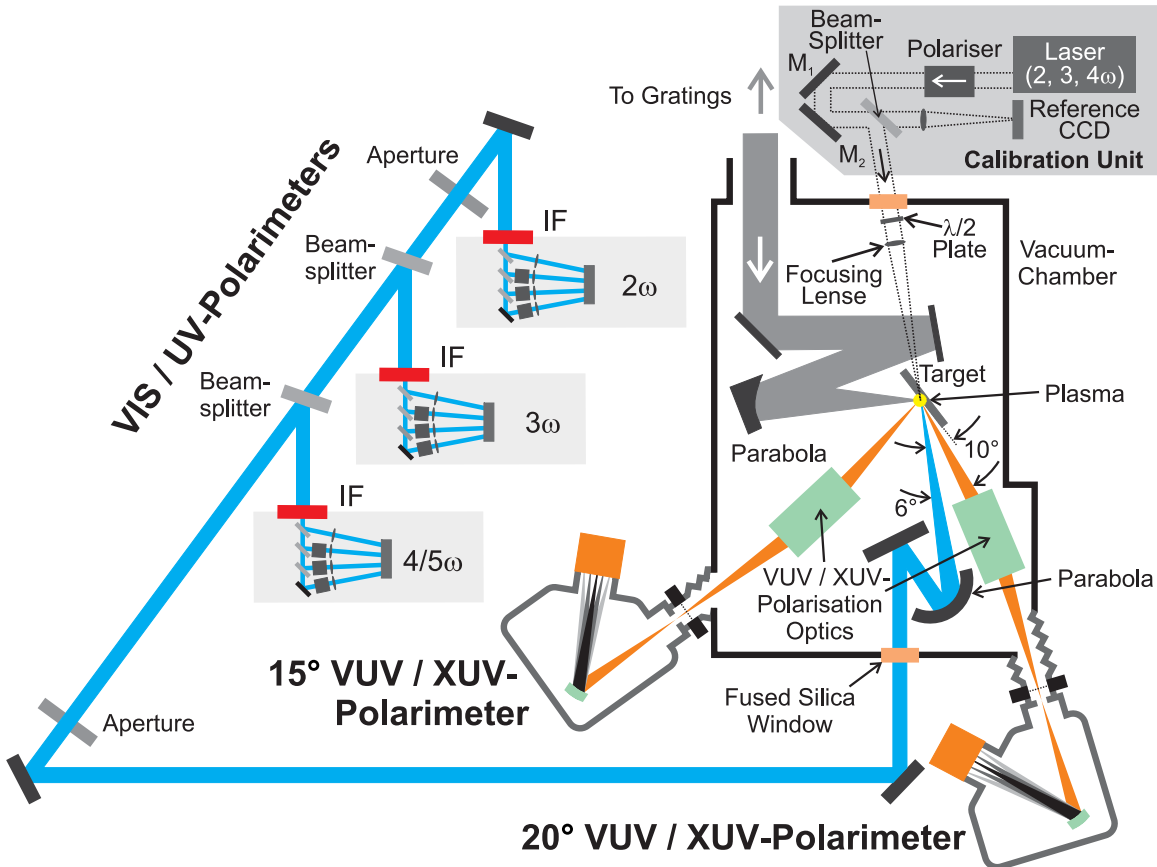
Figure 3.9: Setup of the experiment performed with the VULCAN CPA-beam to produce and measure ultra-strong magnetic fields in near solid density laser produced plasma.

3.5.1.1   The Optical Setup

The CPA-beam-line of VULCAN [39] is based on one of its nanosecond amplifier chains [37]. But instead of amplifying a nanosecond pulse a stretched fs-pulse is amplified and then re-compressed. This amplification scheme is called chirped pulse amplification (CPA) [163, 164].

The fs-seed pulse is produced in a commercial Kerr lens mode-locked Ti:Sa oscillator (Tsunami, Spectra-Physics [154]) pumped with an Argon ion laser. This oscillator produces 120 fs pulses at 80 MHz with a pulse energy of 5 nJ and a wavelength of 1053 nm[§]. After these pulses are stretched to more than 500 ps in a double pass-stretcher [12, 43, 125], a single pulse is selected from the continuous pulse train using two Pockel cells in series. This single pulse is pre-amplified in a chain of double-passed Nd:glass rod amplifiers, before it is seeded into one of the main VULCAN amplifier chains. Finally this pulse is re-compressed with a single-pass grating configuration. The second grating is already located in a vacuum chamber to prevent pulse distortion due to self-phase modulation in air. Right behind the second compressor-grating the CPA-beam of VULCAN has a rectangular beam diameter of about 20 cm × 11 cm and a pulse duration of 750 fs FWHM. By charging the capacitors, used for firing the flash lamps in the disc amplifiers, to different levels the energy of the laser pulse could be changed from 10 J up to the

---

[§]The generation of pulses with a wavelength of 1053 nm is less efficient than the generation of pulses at 800 nm, but necessary because the disc amplifiers operate at 1053 nm only

maximal value of 100 J on target. By not charging these capacitors at all a special low energy mode with roughly 1 J was available in addition. The intensity-ratio between the strongest pre-pulse and the main pulse was measured to be smaller than 10^{-6} by using a third order auto-correlator [37–39]. Furthermore, for alignment purposes a cw YLF-laser was available, propagating through the whole amplifier chain.

In the target chamber the laser beam is reflected by two mirrors, which can be used to change its lateral position and its pointing. Right after these mirrors the beam is focused with a $f/3$ parabolic mirror to a Gaussian spot of $\lesssim 10\,\mu m$ diameter FWHM, leading to a mean focused intensity of $\lesssim 10^{20}\,W/cm^2$ in the focal spot. During the experiment the diameter of the focal spot was checked regularly with a microscope objective coupled to a CCD, whilst the target chamber was evacuated. For checking the focal spot size the pulse energy was reduced to a few μJ. At the same time the precise alignment of the cw 1064 nm *alignment laser* to the short pulse beam was verified, too. In addition, for each shot the pulse energy, the pulse duration, the spectrum, the near and far field were measured, using a beam, leaking through one of the mirrors [39].

3.5.1.2 The Target

The targets are made of quadratic glass plates with a size of 1 cm and a thickness of 1.5 mm. They are glued to a post, which is clamped onto a goniometer table. This table is mounted on a rotation stage. Hence the target could be tilted and rotated with respect to the laser beam. Its alignment is performed by reducing the diameter of the alignment laser beam to approximately 1 mm. Then the target is aligned to precisely reflect the laser back and eventually it is rotated to a 35° angle of incidence. The final position of the reflected alignment laser is marked on the wall of the target chamber to simplify the alignment of succeeding targets.

To move the target surface precisely to the longitudinal position of the focus the rotation stage is mounted on a three axes motor-driven translation stage, so that the target could be positioned within 1 μm in all three dimensions of space. Furthermore a metallic cross-wire with 5 μm wide lines is evaporated onto the target surface. Hence one could easily align the target to the focal spot of the laser, whilst the target chamber is evacuated by moving the translation stage until the alignment laser, generally transmitted through the glass plate, is completely obscured by the centre of the cross-wire.

With this alignment scheme the target could be positioned within $\pm\,10\,\mu m$ of the the focal spot easily. After aligning the target surface to the focal spot of the laser the target is moved a few microns in the vertical direction to make sure, that the laser hits the plane glass surface and not the metallic cross-wire.

3.5.1.3 The Target Chamber

The steering mirrors, the focusing optics and the target mount are contained inside the target chamber. This chamber has a cylindrical shape with its axis of symmetry parallel to the floor. Its diameter is roughly 2 m and its depth is about 1 m. On each of its flat sides there is an access door with a diameter of approximately 1 m. On its curved side

there are rectangular access ports with about 90 cm × 35 cm around the whole chamber. Inside the chamber there is a table for setting up the experiment. This table is directly bolted to the floor and decoupled from the chamber by flexible vacuum feed-through, so that the alignment cannot change by evacuating the target chamber.

The chamber itself is connected to a pumping system, which evacuates it to a pressure of $\sim 10^{-3}$ mbar within 15 min. To avoid damaging the open multi-channel plates (MCP), which have been used for observing the VUV / XUV harmonics emitted from the laser produced plasma, a pressure lower than $\lesssim 10^{-6}$ mbar is needed in the target chamber itself. To reach this pressure a liquid nitrogen trap is mounted to the target chamber in addition. After the chamber has been pumped down to $\lesssim 10^{-3}$ mbar this trap is filled with liquid nitrogen, so that the pressure reduces to $\lesssim 10^{-6}$ mbar within a few minutes.

3.5.1.4 The Diagnostics

For measuring the magnetic field inside the plasma two different types of diagnostics are used: a chain of three VIS / UV polarimeters and two VUV / XUV polarimeters. Despite one VUV / XUV polarimeter, which is set up close to normal incidence, all other polarimeters are setup up as close to gracing incidence as possible at that side of the plasma, where the strong magnetic fields are present (compare Subsection 3.2.2).

The VIS / UV Polarimeters The harmonic radiation for the VIS / UV polarimeters is collected and collimated with a 60 cm, 16° off-axis parabola set up at a gracing incidence angle of $\lesssim 10°$ with respect to the target surface. The parabola and all mirrors reflecting the harmonic radiation are coated with an UV-enhanced Aluminium coating, each delivering a reflectivity of more than 90 % in a wavelength range from 200 nm − 500 nm. Right after the parabola and a first turning mirror the radiation emerges from the vacuum chamber through a window. To prevent any change of the polarisation state the angle of incidence to this window is normal and it is made of UV grade fused silica, which is a non crystalline, amorphous material with no intrinsic birefringence. With two UV-enhanced mirrors the radiation is steered through two alignment apertures, limiting the beam diameter to roughly 8 mm, onto the chain of polarimeters. The radiation for the first two UV polarimeters is split off from the collimated beam with UV-enhanced metallic ND-filters with an optical density of ND 2.0 for the first and ND 0.2 for the second beam-splitter.

Furthermore, in front of the polarimeters one to two bandpass interference filters are setup to select a certain harmonic. Their extinction ratio for radiation outside the bandpass is better than 10^6 per filter in a wavelength range from 180 nm − 1200 nm. It is shown experimentally that the extinction is sufficient to extinguish any signal on all channels of a polarimeter, if bandpass filters for two different harmonics are combined. Additionally, to prevent any change of the harmonic's polarisation state, the interference filters are set up normal to the incident radiation.

The first polarimeter in this chain is designed to operate on the fourth and fifth harmonic by changing the interference filter. The second polarimeter observes the second harmonic and the third polarimeter observes the third harmonic. Their design, their

calibration and the evaluation of the Stokes parameters are discussed in Subsection 3.5.2.

It is important to note that due to a more clearly presentation the angles of incidence onto the mirrors and beam-splitters in the schematic Figure 3.9 are much larger than they have been in the real setup. In reality all angles were kept well below 20° to minimise the difference in reflection and transmission properties between the s- and p-polarised component (see Subsection 3.5.2.2).

The VUV / XUV Polarimeters   As mentioned beforehand one of the VUV / XUV polarimeters is observing the plasma at a gracing incidence angle of approximately 6°, so that this polarimeter could observe harmonic radiation propagating through the most strongly magnetised regions of the plasma. The second VUV / XUV polarimeter is set up at a gracing incidence angle of roughly 80°, i.e. close to the target normal. Thus one could observe the magnetic field strength in two different directions. To measure the s^2/p^2-ratio (see Subsection 3.4.6) of the harmonic radiation a so called polarisation splitter, splitting the incident radiation in a s- and a p-polarised part, is setup in front of a cylindrical mirror. This mirror refocuses the two polarisations vertically separated onto the entrance slit of a VUV / XUV spectrometer (Acton Research, 502 VUV). The combination of the polarisation splitters and the cylindrical mirrors are represented by rectangular boxes in Figure 3.9, labelled *VUV / XUV Polarisation Optics*.

Self-evidently the whole VUV / XUV polarimeters are set up in vacuum, because radiation with a wavelength shorter than 180 nm cannot propagate through air. Due to the small entrance slits of the Acton spectrometers it is necessary to equip them with separate turbo molecular pumps to guarantee a pressure better than 10^{-6} mbar for safely operating the open multi-channel plates (MCP) [128]on a short-term[§]. To avoid ventilating and pumping down the open MCPs again and again a valve was put right in front of the entrance slits of the Acton spectrometers, separating them from the target chamber.

A detailed discussion of the VUV / XUV polarimeter design and the evaluation of the s^2/p^2-ratio is given in Subsection 3.5.3.

3.5.2   The VIS and UV Polarimeters

In Subsection 3.4.6 it was shown that the magnetic field strength inside a plasma can be determined by measuring the polarisation state of an electromagnetic wave in front and behind the magnetised plasma. As the polarisation state is most conveniently expressed in terms of Stokes parameters (see Appendix C), this section describes how to set up a polarimeter for measuring these parameters in a single-shot laser plasma experiment. Furthermore the calibration of this instrument and the evaluation of the measured data is discussed in detail.

3.5.2.1   Design of the Polarimeters

Measuring the Stokes Parameters   The first major issue, which needs to be addressed, is how to measure the Stokes parameters (Eq. (C.13)) of an electromagnetic wave. This

---

[§]For long-term operation of open MCPs a pressure better than 10^{-8} mbar is recommended.

can be accomplished by relating the Stokes parameters $\vec{S}$ to a series of pulse energy measurements as discussed in Born et. al. [24] (see also Eq. (C.11)). In contrast to this usual set of measurements we use a slightly different set of pulse energies measurements, which suits our experimental constraints better:

S_0 : This parameter is the only one which can be measured directly. Recalling the definition of the pulse energy measurement $I_E :\approx < \vec{E}(t) \cdot \vec{E}^*(t) >$ (see Eq. (C.9)) and the definition of the Stokes parameters Eq. (C.13), one immediately recognises, that the pulse energy $I_{E,0}$ holds:

$$I_{E,0} := \left(\vec{S}\right)_0 = S_0 \tag{3.36a}$$

Thus $I_{E,0}$ can be measured with a calorimeter, a photodiode or a CCD as in our experiment. Instead of measuring $I_{E,0}$ one could put a polariser set to 90° in this channel and measure $I_{E,s} := \left(M_{pol}(90°)\,\vec{S}\right)_0 = \frac{1}{2}\left(S_0 - S_1\right)$, alternatively.

S_1 : This parameter can be measured as a linear combination of S_1 and S_0 by putting an ideal linear polariser with its polarising axis set to 0° in front of the radiation detector. With the Müller matrix of this polariser Eq. (D.9a) and $a = 1$, $b = 0$ one finds that the measured energy equals:

$$I_{E,1} := \left(M_{pol}(0°)\,\vec{S}\right)_0 = \frac{1}{2}\left(S_0 + S_1\right) \tag{3.36b}$$

S_2 : This parameter can be measured as a linear combination of S_2 and S_0 by putting an ideal linear polariser with its polarising axis set to 45° in front of the radiation detector. With its Müller matrix Eq. (D.12) and $a = 1$, $b = 0$ one finds:

$$I_{E,2} := \left(M_{pol}(45°)\,\vec{S}\right)_0 = \frac{1}{2}\left(S_0 + S_2\right) \tag{3.36c}$$

S_3 : This parameter is more difficult to measure, as it cannot be measured by just putting a polariser in front of the radiation detector. But by putting a quarter wave-plate with its principal axis set to an angle of 45° (see Eq. (D.24)) into the beam, one can swap the Stokes parameters S_1 and S_3, so that the original parameter S_3 can be measured in the same manner as the parameter S_1[§]. Hence one finds:

$$I_{E,3} := \left(M_{pol}(0°)\,M_{\pm\pi/2}(45°)\,\vec{S}\right)_0 = \frac{1}{2}\left(S_0 \pm S_3\right)^{[\sharp]} \tag{3.36d}$$

[§]Alternatively, one could set the principal axis of the quarter wave-plate to 0° (see Eq. (D.23)), so that S_3 and S_2 are swapped and one can measure S_3 in the same manner as S_2, i.e. the polariser is set to 45° (see Eq. (D.12)). This configuration simplifies the calibration matrix Eq. (3.44) for non-ideal optical components a bit.

[♯]If the plus or the minus sign is valid depends on whether the optical axis of the wave-plate is the fast or the slow axis (See Appendix D.4).
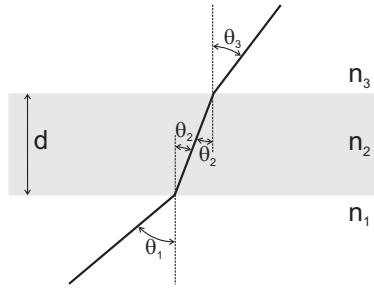
Figure 3.10: Electromagnetic wave propagating through the front surface of a beam-splitter.

Thus it is straight forward to calculate the Stokes parameters from the measured energies $I_{E,0}$, $I_{E,1}$, $I_{E,2}$, $I_{E,3}$ in the case of an ideal polarimeter:

$$S_0 = I_{E,0} \tag{3.37a}$$

$$S_1 = 2I_{E,1} - I_{E,0} \tag{3.37b}$$

$$S_2 = 2I_{E,2} - I_{E,0} \tag{3.37c}$$

$$S_3 = \pm(2I_{E,3} - I_{E,0}) \tag{3.37d}$$

Optical Properties of a Beam-Splitter Apart from polarisers and wave-plates mirrors and beam-splitters are key components for building a polarimeter. Unfortunately these important parts can alter the state of polarisation considerably, so that a closer understanding of their optical properties is needed. The beam-splitters, used throughout the experiment, are made of a thin metallic layer on a fused silica substrate. Thus, for modelling these beam-splitters, we consider the interaction of an electromagnetic wave with a thin metallic layer on an infinitely thick substrate first (compare Figure 3.10):
The reflection R, the transmission T and the phase changes δ_R, δ_T are given by [24]:

$$R := r\,r^* \qquad T := \frac{N_3 \cos\theta_3}{N_1 \cos\theta_1}\,t\,t^* \qquad \delta_R := \arg(r) \qquad \delta_T := \arg(t) \tag{3.38a}$$

with:

$$r := \frac{E_{0,R}}{E_{0,I}} = a_r\, \frac{\left((M)_{1,1} + (M)_{1,2}\,p_3\right)p_1 - \left((M)_{2,1} + (M)_{2,2}\,p_3\right)}{\left((M)_{1,1} + (M)_{1,2}\,p_3\right)p_1 + \left((M)_{2,1} + (M)_{2,2}\,p_3\right)} \tag{3.38b}$$

$$t := \frac{E_{0,T}}{E_{0,I}} = a_t\, \frac{2p_1}{\left((M)_{1,1} + (M)_{1,2}\,p_3\right)p_1 + \left((M)_{2,1} + (M)_{2,2}\,p_3\right)} \tag{3.38c}$$

whereby

$$p_j := \begin{cases} N_j \cos\theta_j \\ \frac{\cos\theta_j}{N_j} \end{cases} \qquad a_r := \begin{cases} e^{0i} \\ e^{\pi i} \end{cases} \qquad a_t := \begin{cases} 1 & \text{for s-polarisation} \\ \frac{N_1}{N_3} & \text{for p-polarisation} \end{cases}$$

$$N_j := \sqrt{\frac{\epsilon_{r,j}}{\mu_{r,j}}} \qquad \sin\Theta_{i+1} = \sin\Theta_i\,\frac{\tilde{n}_i}{\tilde{n}_{i+1}}$$

With the real refraction index n_j and the attenuation κ_j the complex refraction index is:

$$\tilde{n}_j := n_j + i\kappa_j = \sqrt{\epsilon_{r,j}\mu_{r,j}} \tag{3.38d}$$

In the above equations j denotes the layer as shown in Figure 3.10. $E_{0,I}$, $E_{0,R}$ and $E_{0,T}$
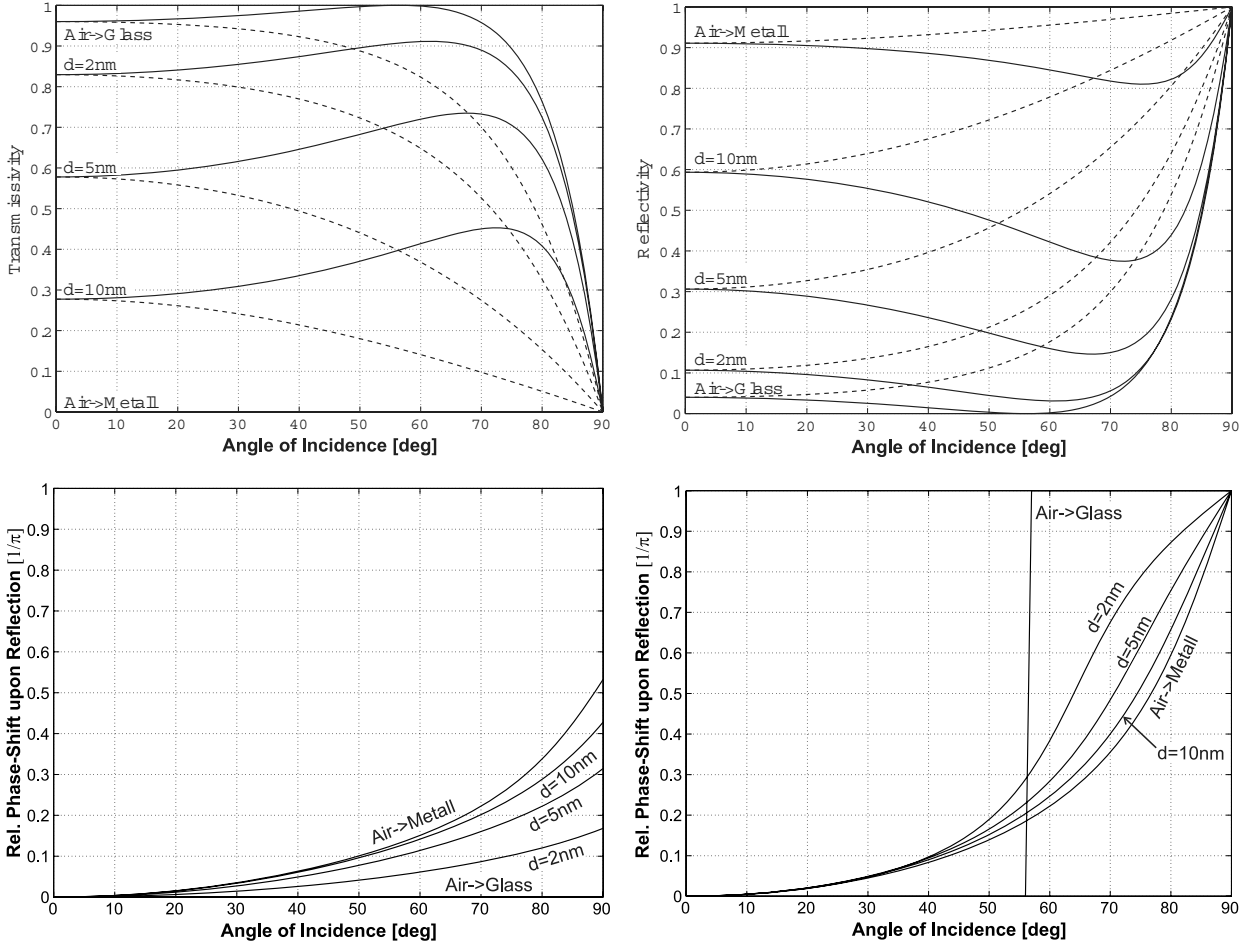
Figure 3.11: Reflectivity, transmissivity and the respective phase-shift between s- and p-polarisation at a thin metallic Al-layer ($n = 0.4$, $\kappa = 4$) on a fused silica substrate ($n = 1.5$) for radiation with a wavelength of 351 nm. The dashed line is for s-polarisation, whilst the continuous line is for p-polarisation.

are the amplitudes of the incident, reflected and transmitted electric field, respectively. $\epsilon_{r,j}$ is the dielectric constant and $\mu_{r,j}$ is the magnetic permeability of the respective layer. The characteristic matrix $\mathbf{M}$ of the metallic layer is given by [24]:

$$\mathbf{M} = \begin{pmatrix} \cos\left(\frac{2\pi}{\lambda_0}\tilde{n}_2 d \cos\theta_2\right) & -\frac{2}{p_2}\sin\left(\frac{2\pi}{\lambda_0}\tilde{n}_2 d \cos\theta_2\right) \\ -ip_2\sin\left(\frac{2\pi}{\lambda_0}\tilde{n}_2 d \cos\theta_2\right) & \cos\left(\frac{2\pi}{\lambda_0}\tilde{n}_2 d \cos\theta_2\right) \end{pmatrix} \tag{3.38e}$$

As the thickness of the beam-splitter's substrate is on the scale of some millimetres, whilst the coherence length of a sub-picosecond pulse is well below 0.5 mm, the reflection and transmission of the electromagnetic wave on the front and rear side are independent from each other. Thus the equations valid at the rear-side are obtained from Eq. (3.38) by setting $d=0$, so that the characteristic matrix reduces to the identity matrix and Eq. (3.38) describes a single boundary. The total reflectivity is basically the sum of the reflectivities at the front and rear-side, the total transmissivity is calculated by multiplying the transmissivities at both sides and the total phase change in transmission is the sum of both phase changes. Furthermore, if one chooses $d=0$ again and n_3 is the complex refraction index of a metal, then Eq. (3.38) describes the reflectivity of a metallic mirror.

Typical curves for the transmission and reflection of s- and p-polarised light with a

Figure 3.12: Schematic setup of a polarimeter for measuring the Stokes parameters. For a more clearly presentation the angles of incidence onto the mirrors and beam-splitters are drawn much larger in comparison to the real setup, where they have been kept close to normal.
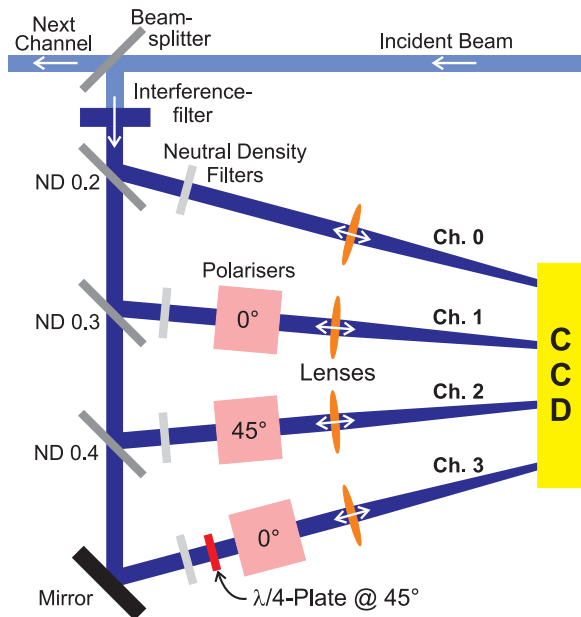
wavelength of 351 nm at a thin metallic Al-surface on an infinitely thick substrate are shown in Figure 3.11. It is seen clearly, that the mirrors and beam-splitters alter the state of polarisation drastically, if the angle of incidence θ becomes large. If θ is below 20°, which is still sufficient for a feasible setup, these changes remain fairly small even if other materials and wavelengths are used.

Experimental Setup With the considerations from the last two paragraphs it is straight forward to set up a polarimeter for measuring the Stokes parameters. Such an instrument is shown in Figure 3.12: right after the radiation of a particular harmonic is selected with an interference filter the beam is split into four beams (each making up a polarimeter channel) by using three UV-enhanced metallic neutral density filters (ND 0.2, ND 0.3, ND 0.4) and an UV-enhanced aluminium mirror. With regards to the last paragraph in the real setup all angles of incidence are kept well below 20°. Fused silica lenses with a focal length of 20 cm are employed to focus all channels to approximately 3 mm huge spots onto a CCD.

The polarimeters observing the second and third harmonic are equipped with UV-extended CCDs with a fused silica entrance window (Andor, DV 420-BU). The polarimeter for the fourth and fifth harmonic is fitted with a CCD coated with a CsI-layer on its sensitive detector surface in addition (Andor, DV 420-BU2). The CCDs have 1024×256 pixels and 16 bit A/D-converters [6]. To use the full dynamic range of the CCDs neutral density filters are put into each polarimeter channel to balance the signal strength. This is particularly important, because the Stokes parameters are given by small differences between the measured signals (see Eq. (3.37)).

The polarisers are installed in front of the focusing lenses in the second, third and fourth channel of each polarimeter. For the second and third harmonic two UV thin-film polarisers are used in series on each channel. For the fourth and fifth harmonic MgF-Rochon polarisers [72] with a separation angle between the ordinary and extraordinary beam of 2.6° and 5.1° are used.
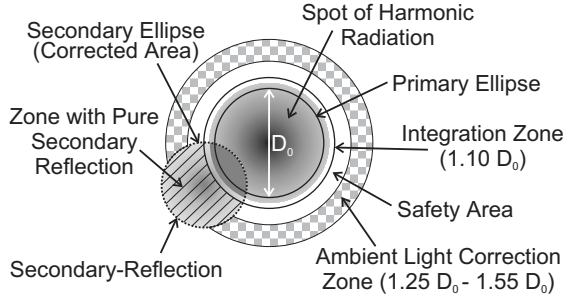
Figure 3.13: Schematic diagram of a spot with harmonic radiation observed with a CCD. In addition the different ellipses and zones used to analyse the acquired images are shown.

To align these polarisers the target is removed and the calibration laser (see Figure 3.9) is set to s-polarisation by turning the half wave-plate to 45° (see Appendix D.4.2). Then all polarisers are rotated until the observed signal is completely extinguished or reaches a minimum at least. After that the quarter wave-plate is installed in the fourth channel right in front of the polariser. To determine its axis it is rotated until the signal on the fourth channel vanishes again. Finally the polariser on the third and the wave-plate on the fourth channel are rotated by 45° to finish the setup.

In consequence all angles are aligned within ±1°, i.e. for a setup angle of 45° the alignment errors are smaller than 2 %. Hence this misalignment can be neglected in comparison to other sources of error and thus $\hat{\alpha}_n$ and $\bar{\beta}_n$ (see Subsection 3.5.2.2) in Table 3.2 are approximately zero. To avoid ambient light influencing the measurements a black cardboard cover is installed around each polarimeter.

Analysis of the CCD Images   The acquired CCD images have been analysed with a programme based on the numerical computing language Matlab [104]: at first an averaged dark-image, consisting of 10 single images, is calculated. Then this averaged dark-image is subtracted from all acquired images, so that any counts due to internal off-sets of the CCD are removed. The resulting image shall be called $P_D(x, y)$ with the pixel-row x and pixel-column y. For further analysis each spot belonging to a polarimeter channel is presented with a steep brightness curve on the screen, so that one can easily select four points at the edge of the particular spot. After that a *primary ellipse* passing through all four points (see Figure 3.13) is calculated. Then the same spot is plotted with a very flat brightness curve, so that *secondary reflections* from the entrance window in front of the CCD can be seen easily. Analogous to the primary ellipse one can determine a *secondary ellipse* for each secondary reflection.

After this last manual step ambient light by-passing the light protection cover, built around each polarimeter, is removed from the measured image as far as possible: this is accomplished by subtracting the *ambient light correction image* $P_A(x, y)$ from $P_D(x, y)$. For each polarimeter channel a different $P_A(x, y)$ is calculated from the respective *ambient light correction zone* A_A (see Figure 3.13). This zone includes all pixels in an area given by the primary ellipse magnified by 1.25 to 1.55, but excluding the pixels enclosed in any secondary ellipse. $P_A(x, y)$ is a plane given by the least square fit of $\{(x, y, P_A(x, y)) \in \mathbb{R}^3 | (x, y) \in A_A\}$ to the two-dimensional surface $\{(x, y, P_D(x, y)) \in \mathbb{R}^3 | (x, y) \in A_A\}$.

Eventually the image is corrected for secondary reflections: as the harmonic spots have steep edges and the number of counts per pixel inside the spots is pretty constant,

one can calculate an average number of counts per pixel for each secondary reflection by summing up all counts in the *zone with pure secondary reflection* and by dividing this value with the number of pixels in this area. This averaged number of counts is subtracted from all pixels inside the secondary ellipse.

Finally all points inside the integration zone, which equals the primary ellipse magnified by 1.1, are summed up, resulting in the measured signals $I_{E,k}$; $k \in \{0, 1, 2, 3\}$ (compare Eq. (3.36)).

3.5.2.2 Calibration of the Polarimeters

Calibration Matrix   Naturally the relation between the measured values $I_{E,k}$; $k \in \{0, 1, 2, 3\}$ and the true Stokes parameters $\vec{S}_{in}$ is given by a matrix M_{Cal} (see Eq. (D.1)):

$$\left(\vec{I}_E\right)_k := \sum_{l=0}^{3} \left(M_{Cal}\right)_{k,l} \left(\vec{S}_{in}\right)_l \tag{3.39}$$

In principle it is possible to determine all 16 elements of M_{Cal} experimentally and then inverting M_{Cal} to calculate $\vec{S}_{in}$ from the $I_{E,k}$. But this requires a very precise measurement of all matrix elements and a thorough study about the inversion properties of M_{Cal}. Hence it is advantageous to keep M_{Cal} as simple as possible, i.e. the diagonal matrix elements should be much larger than the outer-diagonal elements. To understand how this can be achieved, it is necessary to write M_{Cal} in terms of easy to measure optical properties. For this it is necessary to discuss the Müller matrices of each single optical component first:

Non-Ideal Mirrors   If an electromagnetic wave is reflected from a mirror at oblique incidence, then the reflectivity between the s- and p-polarised component differs and the two components acquire a mutual phase-shift as we have seen earlier already. The difference in reflectivity can be represented by the Müller matrix of a non-ideal linear polariser with the polarising axis set to $0°$ and reflection coefficients a, b of the electric field (see Eq. (D.9a)). Ideally a and b are close to unity. The phase-shift $\breve{\phi}$ can be represented by the Müller matrix of a wave-plate with a linear anisotropy and its principal axis set to $0°$ (see Eq. (D.16)). Thus the Müller matrix of a single mirror is given by:

$$M_M\left(\breve{a}, \breve{b}, \breve{\phi}\right) := M_{\breve{a}, \breve{b}}\left(0°\right) M_{\breve{\phi}}\left(0°\right) = M_{\breve{\phi}}\left(0°\right) M_{\breve{a}, \breve{b}}\left(0°\right) \tag{3.40}$$

Then the Müller matrix of a series of mirrors 1 to k with parallel and orthogonal reflection planes is given by:

$$\begin{aligned} M_M\left(\breve{a}, \breve{b}, \breve{\phi}\right) :=& M_M\left(\breve{a}_1 \cdots \breve{a}_k, \breve{b}_1 \cdots \breve{b}_k, \breve{\phi}_1 \cdots + \breve{\phi}_k\right) \\ :=& M_{\breve{a}_1, \breve{b}_1}\left(0°\right) M_{\breve{\phi}_1}\left(0°\right) \cdots M_{\breve{a}_k, \breve{b}_k}\left(0°\right) M_{\breve{\phi}_k}\left(0°\right) \end{aligned} \tag{3.41}$$

Furthermore, it is important to note, that the Müller matrix of an isotropic, non-depolarising material (i.e. any material that does not show birefringence and does not alter the degree of polarisation) is the identity matrix. Nevertheless, in the case of oblique incidence onto the surface of such a material an electromagnetic wave is split into a s- and a p-polarised component. Due to the discontinuity of the refraction index at this boundary the two components of the wave have a different transmission coefficient and

acquire a mutual phase-shift [24]. Thus the propagation of an electromagnetic wave through and the reflection at a plate made of such a material (e.g. fused silica windows, neutral density or interference filters) is described by Eq. (3.40), too.

Non-Ideal Wave-Plate In the case of an electromagnetic wave, propagating through a non-ideal wave-plate with a nominal phase-shift ϕ at a certain wavelength and its principal axis set to a nominal angle β with respect to the p-polarisation plane of the mirrors, the true phase-shift and angle are $\phi + \bar{\phi}$ and $\beta + \bar{\beta}$, respectively. In some cases one can compensate for the phase-mismatch $\bar{\phi}$ of the wave-plate by tilting the plate around its axis. But then, analogous to a glass plate, the transmission coefficients parallel and perpendicular to the wave-plate's axis become different. Thus the wave-plate's Müller matrix is given by (see Eq. (D.11a), Eq. (D.18)):

$$\mathsf{M}_W\big(\bar{a}, \bar{b}, \bar{\phi}, \bar{\beta}, \beta, \phi\big) := \mathsf{M}_{\bar{a},\bar{b}}\big(\beta + \bar{\beta}\big)\,\mathsf{M}_{\bar{\phi}}\big(\beta + \bar{\beta}\big)\,\mathsf{M}_{\phi}\big(\beta + \bar{\beta}\big) \tag{3.42}$$

where $\bar{a}$ and $\bar{b}$ are the transmission coefficients of the electric field.

Non-Ideal Linear Polariser The non-ideal polariser is discussed in Appendix D.3. Nevertheless some real polarisers like a Rochon polariser have a pretty long propagation length of the electromagnetic wave through a birefringent material, so that a mutual phase-shift between the ordinary and extraordinary wave can appear. Thus they are described as a combination of a wave-plate with a phase-shift $\hat{\phi}$ and a non-ideal polariser with the transmission coefficients $\hat{a}$, $\hat{b}$ of the electric field (see Eq. (D.11a), Eq. (D.18)):

$$\mathsf{M}_P\big(\hat{a}, \hat{b}, \hat{\phi}, \hat{\alpha}, \alpha\big) := \mathsf{M}_{\hat{\phi}}\big(\alpha + \hat{\alpha}\big)\,\mathsf{M}_{\hat{a},\hat{b}}\big(\alpha + \hat{\alpha}\big) \quad, \tag{3.43}$$

where α is the polariser axis with respect to the p-polarisation plane of the mirrors and $\hat{\alpha}$ is the alignment error.

A Single Polarimeter Channel With the Müller matrices of each optical component we can calculate the Müller matrix of a single polariser channel. If the initial set of Stokes parameters is given by $\vec{S}_{in}$, then the number of counts measured at the nth polarimeter channel of the mth polarimeter is given by:

$$\Big(\vec{I}^m_{E,Meas}\Big)_n := \Big(\mathsf{M}^m_{Cal}\Big)_{n,j}\Big(\vec{S}_{in}\Big)_j \tag{3.44}$$

$$= \Big(\mathsf{M}^m_P\big(\hat{a}^m_n, \hat{b}^m_n, \hat{\phi}^m_n, \hat{\alpha}^m_n, \alpha^m_n\big)\,\mathsf{M}^m_W\big(\bar{a}^m_n, \bar{b}^m_n, \bar{\phi}^m_n, \bar{\beta}^m_n, \beta^m_n, \phi^m_n\big)\,\mathsf{M}^m_M\big(\check{a}^m_n, \check{b}^m_n, \check{\phi}^m_n\big)\Big)_{0,j}\Big(\vec{S}_{in}\Big)_j$$

This general equation reduces to the equation of the nth polarimeter channel, if the respective values from Table 3.2 are substituted into it. The resulting matrix is called the calibration matrix of the mth-polarimeter.

Setup for the Experimental Calibration To determine and justify the values printed on a medium- or dark-gray background in Table 3.2 it is necessary to carry out an experimental calibration. The experimental setup is shown in Figure 3.9: a 150 mJ Nd-Yag laser with a pulse duration of 2 ns and a wavelength of 1064 nm [34] is frequency-multiplied with appropriate frequency-multiplying crystals and separator mirrors to produce the second third and fourth harmonic, normally generated inside the plasma. The energy

Channel	Parameters			Polarisers				Wave-Plates				Mirrors		
#	α_n	β_n	ϕ_n	$\hat{a}_n$	$\hat{b}_n$	$\hat{\phi}_n$	$\hat{\alpha}_n$	$\bar{a}_n$	$\bar{b}_n$	$\bar{\phi}_n$	$\bar{\beta}_n$	$\check{a}_n$	$\check{b}_n$	$\check{\phi}_n$
0	$0°$	$0°$	0	1	1	0	0	1	1	0	0	$\check{a}_0$	$\check{b}_0$	$\check{\phi}_0$
1	$0°$	$0°$	0	1	0	0	0	1	1	0	0	$\check{a}_1$	$\check{b}_1$	$\check{\phi}_1$
2	$45°$	$0°$	0	1	0	0	0	1	1	0	0	$\check{a}_2$	$\check{b}_2$	$\check{\phi}_2$
3	$0°$	$45°$	$\pm\pi/2$	1	0	0	0	$\bar{a}_3$	$\bar{b}_3$	$\bar{\phi}_3$	0	$\check{a}_3$	$\check{b}_3$	$\check{\phi}_3$

Table 3.2: Parameters of the VIS / UV polarimeters. On the lefthand-side of the vertical double line the parameters from Eq. (3.36) are given for each channel. Deviations from these values and further parameters are listed on the right hand side (compare Eq. (3.44)). The values shown on a gray background depend on the optical properties of the components and their precise alignment: light-gray: parameters cannot influence the measurement; medium-gray: parameters generally contribute to minor errors only; dark-gray: parameters can falsify the result considerably.

ratio between the p- and s-polarised component of the emitted radiation is roughly 10:1. To increase this ratio to more than 1000:1 a Rochon polariser is installed in front of the frequency-multiplying unit. Then most of the radiation is steered into the target chamber with a semi-transparent mirror. The transmitted minor part of the beam is focused onto an UV-enhanced Andor CCD and is used as a reference to measure the initial pulse energy $I_{0,Ref}$. With the mirrors M_1 and M_2 it is possible to align the beam precisely through the alignment apertures of the polarimeter. The beam, steered into the target chamber, propagates through a half wave-plate to adjust its plane of polarisation (see Appendix D.4.2). Behind this wave-plate the beam is focused with a fused silica lens f=60 cm to a spot at the position, where the laser produced plasma is supposed to be. The target has been removed from the target mount to avoid any interaction between the target plate and the calibration beam. Eventually, after being reflected from the parabola this beam is collimated again.

Experimental Calibration With the experimental setup discussed in the last paragraph one can study the optical properties of each component used to build the polarimeter, thus determining the parameters of Eq. (3.44). To become independent of the absolute value of laser energy deposited onto the CCDs the measured values $I_{E,k}$ are divided by $I_{E,Ref}$.

Polarisers To determine the quality of a linear polariser, one generally uses the extinction Ext, which is the ratio between the polarisers maximal and minimal transmissivity for linear polarised radiation, i.e. $Ext := \hat{a}^2/\hat{b}^2$ with $\hat{a}$, $\hat{b}$ from Eq. (3.43). The extinction of the Rochon polarisers used throughout the experiment is better than 400:1. Similar extinctions are reached with a series of two UV thin-film polarisers, applied for the second and third harmonic polarimeter. This extinction was independent from the angle of the half wave-plate's principal axis. Hence the ellipticity of the calibration beam behind the half wave-plate must be less than 0.05. During the calibration we found the extinction of all polarisers to be much better than 150:1 by just setting the polarisers to the appropriate angles, using the scales on the polariser mounts. Consequently one can write with Eq. (3.43):

$$M_P\left(\hat{a}, \hat{b}, \hat{\phi}, \hat{\alpha}, \alpha\right) = \hat{a}\, M_P\left(1, \hat{b}/\hat{a}, \hat{\phi}, \hat{\alpha}, \alpha\right) \approx \hat{a}\, M_P\left(1, 0, \hat{\phi}, \hat{\alpha}, \alpha\right) \qquad (3.45)$$

In the case of Rochon polarisers $\hat{a}$ was found to be about 0.95, whilst for a series of two thin-film polarisers $\hat{a}$ was as low as 0.20. Nevertheless if the polarisers are not removed during the calibration of the mirrors and if they are set to s- and p-polarisation respectively, then $\hat{a}$ can be incorporated into the s- and p-reflectivity of the mirror because of Eq. (3.44).

Wave-Plates   The wave-plate (Appendix D.4) can be treated analogous to a mirror with a phase-shift $\phi + \hat{\phi}$ and reflection coefficients $\bar{a}$ and $\bar{b}$ of the electric field. In the case of a wave-plate $\bar{a}$ is the transmission of the electric field through the plate parallel to the optical axis, i.e. the extraordinary wave. $\bar{b}$ is the transmission of the electric field perpendicular to the optical axis, i.e. the ordinary wave. Consequently the Müller matrix of the wave-plate M_W can be fully included into M_M from Eq. (3.44), if the wave-plate is set to an angle of ϕ=0°. But in our case ϕ equals 45° and similar to a polariser (see Eq. (3.45)) one can include only $\bar{a}$ into M_M. If the surfaces of the wave-plate are not covered with a dielectric anti-reflection coating, then with Eq. (3.38) the ratio $\bar{b}/\bar{a}$ for normal incidence is given by:

$$\frac{\bar{b}}{\bar{a}} = \left(\frac{N_e/N_{air} + 1}{N_o/N_{air} + 1}\right)^2 \frac{N_o}{N_e} \stackrel{\mu_r \approx 1}{\approx} \left(\frac{n_e + 1}{n_o + 1}\right)^2 \frac{n_o}{n_e} \quad , \tag{3.46}$$

whereby n_o and n_e are the ordinary and extraordinary index of refraction, respectively. During the calibration we found e.g. for 266 nm radiation that $\bar{a}$=.991($\pm$20) and $\bar{b}$=.946($\pm$20).

A more serious error in using wave-plates is the mismatch of the wavelength: if a wave-plate introduces a phase-shift ϕ_1 at a certain wavelength λ_1, but is used at a slightly different wavelength λ_2, then its phase-shift is ϕ_2. By using $\phi_j := 2\pi \frac{h}{\lambda_j} \Delta n_j$ with $\Delta n_j := (n_{e,j} - n_{o,j}); j \in \{1,2\}$ and the thickness h of the plate [24] one can easily calculate the phase difference:

$$\bar{\phi} := \phi_2 - \phi_1 = 2\pi \left(\frac{\Delta n_2}{\lambda_2} - \frac{\Delta n_1}{\lambda_1}\right) \frac{\phi_1 \lambda_1}{2\pi \Delta n_1} = \phi_1 \frac{\Delta n_2/\Delta n_1 \lambda_1 - \lambda_2}{\lambda_2} \approx \phi_1 \frac{\lambda_1 - \lambda_2}{\lambda_2} \tag{3.47}$$

For the 2nd, 3rd and 4th harmonic the nominal wavelength of the utilised quarter wave-plates does not differ from the respective central wavelength by more than 1 %. Only for the 5th harmonic the deviation was 5 %. Beyond these systematic deviations no additional non-ideal behaviour of the wave-plates is observed during the calibration, so that $\bar{\phi} \lesssim$ 0.005 π for the 2nd, 3rd and 4th harmonic and $\bar{\phi} \approx$0.025 π for the 5th harmonic.

Mirrors   The s- and p-polarised transmissivities of a series of non-ideal mirrors and beam-splitters are simply measured by setting the half wave-plate in Figure 3.9 to 45° (s-pol.) and 0° (p-pol.). As mentioned beforehand we also include $\hat{a}$ and $\bar{a}$ into the transmissivities of the mirrors by setting all polarisers and the quarter wave-plates to 90° and 0°, respectively. Then the total transmissivity is given by dividing $I_{E,k}$ with $I_{E,Ref}$. It is important to note, that, in contrast to the properties of the polarisers and wave-plates discussed in the last paragraphs, these values depend on the angles of incidence onto the optical components and thus have to be measured again after modifying the setup.
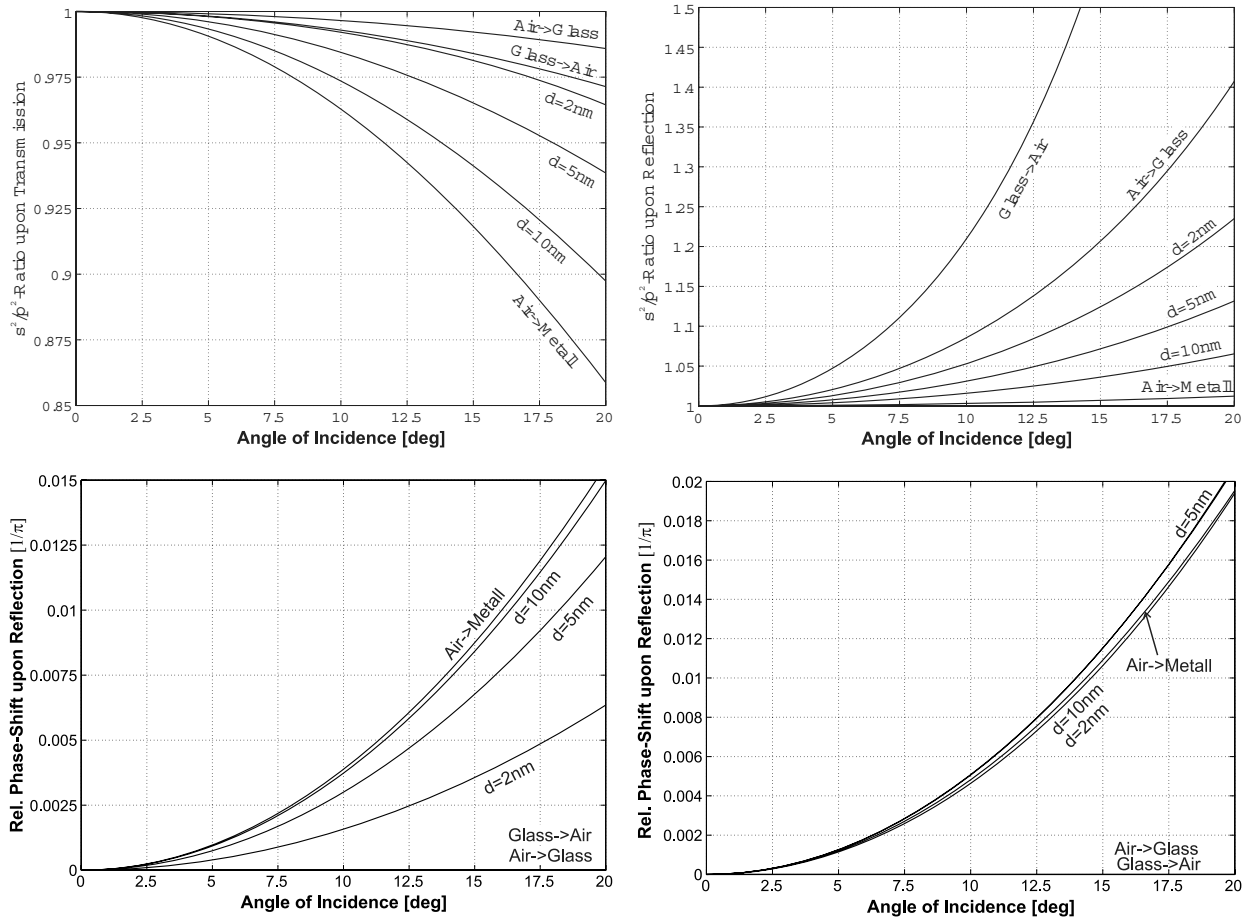
Figure 3.14: Enlargement of Figure 3.11 to estimate the optical properties of the mirrors and beam-splitters used to build the polarimeter.

In Figure 3.14 the angle dependent s^2/p^2-ratios (i.e. reflectivity and transmissivity of s-polarised light divided by the respective quantity for p-polarised light) are calculated for aluminium layers on fused silica substrates at a wavelength of 351 nm. Using these curves one can estimate the s^2/p^2-ratio for an arbitrary polarimeter channel. The estimated values for our experimental setup range from 0.7 to 1.4, which agrees with the measured s^2/p^2-ratios.

The phase difference $\check{\phi}_n$ introduced by the mirrors and beam-splitters can be neglected for the zeroth and first polarimeter channel, because the zeroth channel does not include any polariser, so that $I_{E,0}$ is independent of $\check{\phi}_0$, and the first channel is supposed to measure the p-polarised part of the radiation exclusively. Thus the influence of $\check{\phi}_1$ on the measurements is limited by the misalignment angle $\hat{\alpha}_1$ (see Eq. (3.43)). As this angle is less than $1°$, one can indeed neglect the influence of $\check{\phi}_1$. To measure $\check{\phi}_n$ for the the 2nd and 3rd polarimeter channel it is convenient to remove the quarter wave-plate at first. Then one can determine $\check{\phi}_n$ by setting the half wave-plate to roughly $45°$ and use the polarisers already installed right in front of the focusing lenses (see Figure 3.12). Hence one can measure the normalised angle dependent pulse energy $\frac{I_{E,n}(\alpha,0)}{I_{E,Ref}}$ by rotating the polariser (see Figure C.2 and Eq. (C.10)). From these measurements one can determine the normalised principal axes a'_n, b'_n of the polarisation ellipse and the transmission coefficient a_n, b_n of the electric field in the s- and p-direction. Using Eq. (C.6b) one

calculates:

$$\check{\phi}_n \approx \sin\check{\phi}_n = \frac{a'_n b'_n}{a_n b_n} \tag{3.48}$$

From Figure 3.14 it is seen that $\check{\phi}_3 - \check{\phi}_2 \lesssim 0.015\,\pi$, because the phase-shifts due to the reflection from the last beam-splitter in the chain are pretty much the same for both channels. Assuming one polarimeter channel with a series of 5 mirrors, 5 beam-splitters and $17°$ angle of incidence on average one estimates the total phase-shift to be less than $\check{\phi}_n \lesssim 0.12\,\pi$. Indeed we measured phase-shifts around $\check{\phi}_n \lesssim 0.041\,\pi$, which agrees with an average angle of incidence of $10°$.

Independently of these measurements it was verified that the vacuum window did not introduce any additional phase-shifts, even if the target chamber was pumped down.

Calculation of the Initial Stokes Parameters   To calculate the Stokes parameters from the measured values $I_{E,k}$ Eq. (3.44) is used. By substituting the values tabulated in Table 3.2 into M_{Cal} one obtains a simplified calibration matrix:

$$M_{Cal}^{45°} := \begin{pmatrix} \frac{\check{A}_0}{2} & \frac{\check{B}_0}{2} & 0 & 0 \\ \frac{\check{a}_1^2}{2} & \frac{\check{a}_1^2}{2} & 0 & 0 \\ \frac{\check{A}_2}{4} & \frac{\check{B}_2}{4} & \frac{\check{C}_2\cos\check{\phi}_2}{2} & -\frac{\check{C}_2\sin\check{\phi}_2}{2} \\ X_{30} & X_{31} & X_{32} & X_{33} \end{pmatrix} \tag{3.49a}$$

$$M_{Cal}^{0°} := \begin{pmatrix} \frac{\check{A}_0}{2} & \frac{\check{B}_0}{2} & 0 & 0 \\ \frac{\check{a}_1^2}{2} & \frac{\check{a}_1^2}{2} & 0 & 0 \\ \frac{\check{A}_2}{4} & \frac{\check{B}_2}{4} & \frac{\check{C}_2\cos\check{\phi}_2}{2} & -\frac{\check{C}_2\sin\check{\phi}_2}{2} \\ \frac{\check{A}_3}{4} & \frac{\check{B}_3}{4} & \frac{\check{C}_3\cos\Phi}{2} & -\frac{\check{C}_3\sin\Phi}{2} \end{pmatrix} \tag{3.49b}$$

with

$$X_{30} := \frac{\check{A}_3\bar{A}_3}{8} - \frac{\check{B}_3\bar{C}_3}{4}\sin\bar{\phi}_3 \qquad X_{31} := \frac{\check{B}_3\bar{A}_3}{8} - \frac{\check{A}_3\bar{C}_3}{4}\sin\bar{\phi}_3$$

$$X_{32} := \frac{\check{C}_3}{4}\left(\bar{B}_3\cos\check{\phi}_3 + \bar{C}_3\cos\bar{\phi}_3\sin\check{\phi}_3\right) \qquad X_{33} := -\frac{\check{C}_3}{4}\left(\bar{B}_3\sin\check{\phi}_3 - \bar{C}_3\cos\bar{\phi}_3\cos\check{\phi}_3\right)$$

and for all $\bar{A}_j, \check{A}_j, \bar{B}_j, \check{B}_j, \bar{C}_j, \check{C}_j, \; j \in \{0,1,2,3\}$ respectively:

$$A_j := a_j^2 + b_j^2 \qquad B_j := a_j^2 - b_j^2 \qquad C_j := a_j b_j \qquad \Phi := \check{\phi} + \hat{\phi} + \pi/2$$

The quantities $\bar{a}_3, \bar{b}_3, \bar{\phi}_3, \check{a}_n, \check{b}_n$ and $\check{\phi}_n$ have been calculated or measured as described above. $M_{Cal}^{45°}$ is the calibration matrix, if the wave-plate is set to an angle of $45°$. $M_{Cal}^{0°}$ is the matrix, if the wave-plate is set to angle of $0°$. In this case the transmission properties of the wave-plate are fully included in $\check{a}_3$ and $\check{b}_3$.

To avoid numerical instabilities a linear multidimensional fit was performed to calculate the Stokes parameters instead of inverting Eq. (3.49a). The calculated initial Stokes parameters are correct within a few percent. If the calibration matrix Eq. (3.49a) is reduced to Eq. (3.36) by setting the corresponding matrix elements to zero, the errors increase to approximately 15 %.

3.5.3   The VUV / XUV Polarimeters

As already mentioned beforehand for measuring magnetic fields well beyond 500 MG it is vital to use electromagnetic radiation with a shorter wavelength, namely VUV / XUV radiation. This subsection describes the design, setup and calibration of a VUV / XUV
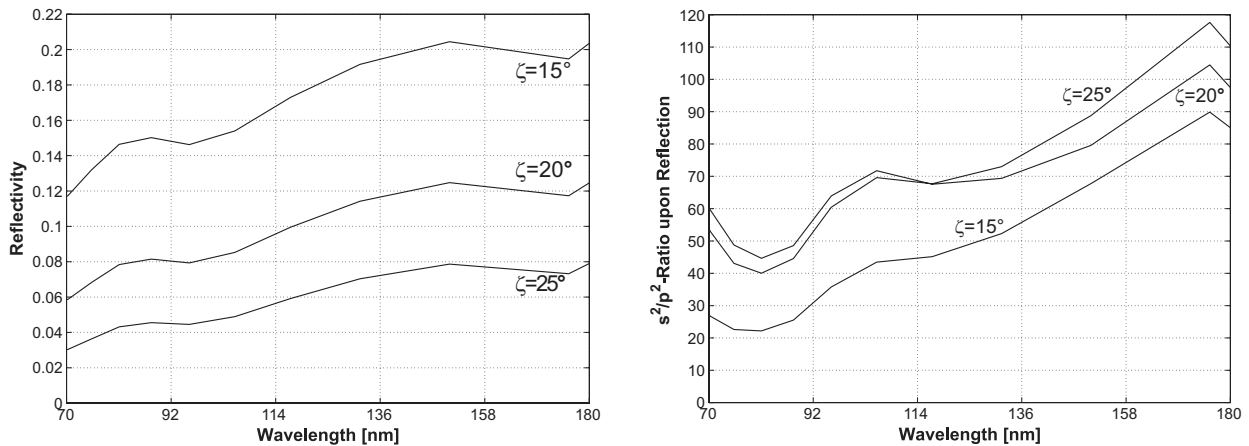
Figure 3.15: Reflectivity and Extinction versus wavelength, i.e. s^2/p^2-ratio, of the three mirror polarisation splitter (Figure 3.16) for different angles of gracing incidence ζ.

polarimeter, measuring the s^2/p^2-ratio. Furthermore it is explained, how the measured data have been analysed to determine the magnetic field strength with Eq. (3.34).

3.5.3.1 Design of the Polarimeter

Building a VUV / XUV polarimeter is even more challenging than building a VIS / UV polarimeter, because high quality VUV / XUV beam-splitters and wave-plates off are not available of the shelf. Hence one is dependent on using the reflection properties of solid, mostly metallic, surface to build such a polarimeter [48, 120].

Polarisation Splitter   If VUV / XUV radiation is reflected from a solid material, one observes similar angle of incidence dependent properties as with VIS / UV radiation. Thus the s^2/p^2-ratio of reflected VUV / XUV radiation shows a maximum at a certain angle of incidence, too. Hence a series of mirrors set up to this angle of incidence formes a good polariser [14]. Unfortunately this angle (measured as an angle of gracing incidence now, i.e. between the target surface and the incident beam) is considerably larger than $0°$ and the reflectivity decreases dramatically with an increasing angle of gracing incidence. In general, this becomes even worse, if the wavelength is reduced or the surface roughness is increased [111]. Our mirrors have been made of a gold coated glass substrate with a low surface roughness. By examining the gold surface with a high resolution electron microscope and by directly measuring the surface roughness with a profilometre we found, that the surface roughness is determined by gold clusters with a diameter of up to 20 nm.

To achieve a reasonable reflectivity we decided to use an angle of gracing incidence considerably smaller than the ideal polarising angle, thus reducing the extinction-ratio of the polariser. To compensate for this poor extinction-ratio we have been using a series of three mirrors as shown in the inset of Figure 3.16. The interplay between the reflectivity and the degree of polarisation is clarified in Figure 3.15: the smallest angle ($15°$) of gracing incidence onto the first mirror in this series of three mirrors gives the lowest extinction, but has a high reflectivity (up to 0.2), whilst the largest angle ($25°$) has the lowest reflectivity (lower than 0.08). A good compromise with a reasonable reflectivity and polarisation is an angle of $20°$.
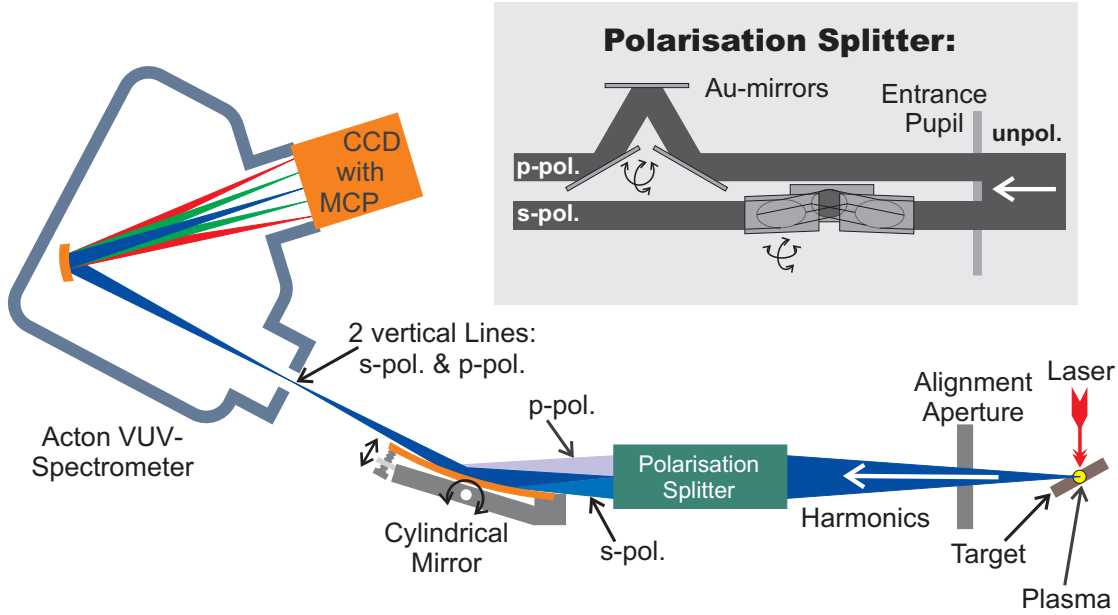
Figure 3.16: Schematic drawing of the VUV / XUV polarimeter. The inset shows the polarisation splitter.

It is worth to mention that the phase-shift acquired upon the reflection could be used to build a wave-plate in the VUV / XUV range. But due to the angle dependence of the phase-shift it is difficult to align this wave-plate to a particular phase-shift. Furthermore these wave-plates are far from ideal, as the s- and p-reflectivity differs considerably.

To avoid these additional complications our VUV / XUV polarimeter measures the s- and p-component of the incident electromagnetic wave only. This is accomplished with two sets of three mirrors installed in a closed compartment, called polarisation splitter. A schematic drawing of this splitter is shown in the inset of Figure 3.16. The plane of incidence of the first set of mirrors coincides with the p-polarisation plane of the laser and the incident plane of the second set coincides with the s-polarisation plane. Thus the first set mainly reflects s-polarised, whilst the second set mainly reflects p-polarised radiation.

Experimental Setup   In our experiment we have been using two VUV / XUV polarimeters, one observing the target with a gracing incidence angle of 6° and a second observing the target with a gracing incidence angle of 80°. The angle of gracing incidence onto the first mirrors of the former polarimeter is 20° and on the latter 15° (see Figure 3.9).

The schematic setup of a single VUV / XUV polarimeter is shown in Figure 3.16: the partially polarised harmonic radiation, generated inside the laser produced plasma, propagates through an alignment aperture with a diameter of 4 mm, located 215 mm away from the plasma. Right in front of the polarisation splitter the beam-diameter was sufficiently large to illuminate both entrance pupils ($\varnothing \approx 1.5$ mm) for the s- and p-polariser completely (see inset of Figure 3.16). By tilting the last mirror in each polariser set one can centre the beams onto a cylindrical mirror and align their direction against each other. The cylindrical mirror is made of a 100 mm long, 10 mm wide and 1.5 mm thick glass substrate with a low surface-roughness and a gold coating. Its curvature can
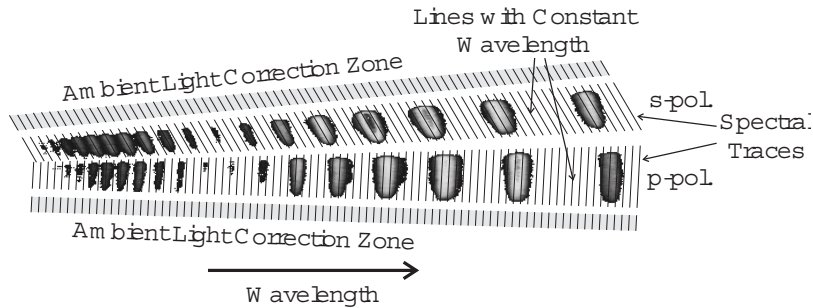
Figure 3.17: Measured s- and p-polarised spectral traces of the VUV / XUV harmonic emission.

be altered by adjusting a screw, pushing from behind at one end of the mirror, whilst the opposite end is fixed. The whole mirror can be rotated, so that one can change the angle of gracing incidence between $3°$ and $6°$. With these degrees of freedom it is possible to steer and focus the s- and p-polarised beams to two vertically separated lines onto the entrance slit of an Acton VUV 502 spectrometer [1]. To avoid the s^2/p^2-ratio to become dependent on the precise position of the two vertical lines on this entrance slit it is opened to a width of more than 3 mm during the experiment.

With the help of a 1200 lines/mm blazed spherical Iridium grating the spectra of the two beams are imaged into the image plane of the Acton spectrometer. The wavelength in the centre of this image plane can be determined by rotating the grating with a remote controlled stepper motor. The Acton spectrometer has been modified by substituting the exit slit with a special mount holding an open MCP [128]. The front surface of this MCP coincides with the image plane of the spectrometer. Due to the diameter of the MCP the spectral range is limited to approximately ± 40 nm around the central wavelength. The phosphore screen of the open MCP is coupled by a fibre-optic taper to an intensified 8 bit CCD with 768×288 pixels manufactured by Darkstar [127].

Analysis of the CCD Images   The acquired CCD images have been analysed with the help of a Matlab [104] programme. Again, the average over 10 dark images is calculated at first. Then this averaged dark image is subtracted from all acquired images, so that any counts due to internal off-sets of the CCD are removed. The resulting image shall be called $P_D(x, y)$ with the pixel-row x and pixel-column y.

For calculating the s- and p-polarised harmonic spectra the *spectral traces* have to be integrated along lines with constant wavelength. This is not completely straight forward, as these lines are not parallel to the pixel rows or columns of the CCD (see Figure 3.17). Thus the direction of these coordinate lines is calculated as an average over an arbitrary number of lines, selected interactively by the operator. Self-evidently, the operator draws these lines parallel to the tilted spectral lines. After that, two nearly horizontal lines determining the lower and upper integration boundary of a spectral trace have to be chosen. With this input a map-image $P_M(x, y)$ is calculated. In $P_M(x, y)$ all pixels outside the integration boundaries of the corresponding spectral trace are set to zero. All other pixels are related to an artificial wavelength number n_a. This number is given by the column number of the pixel closest to the intersection between the lower respectively upper integration boundary line and the constant wavelength line, passing through the

pixel under consideration. Then the counts of all pixels with the same n_a are summed up to define a preliminary spectral trace $S_{p_{\{s,p\}}}(n_a)$. In addition the function $N_{S\{s,p\}}(n_a)$, giving the total number of pixels belonging to n_a, is defined.

To correct for ambient light two nearly horizontal lines, limiting the *ambient light correction zone* above respectively below the spectral trace, have to be selected. Again a map-file is calculated by using the intersection between the constant wavelength line, passing through the pixel under consideration, and the lower respectively upper integration boundary of the spectral trace. Again all pixels outside the ambient light correction zone are set to zero in this map-file. Using this map-file the trace of ambient light $A_{p_{\{s,p\}}}(n_a)$ and the total number $N_{A\{s,p\}}(n_a)$ of pixels belonging to a certain n_a are calculated in analogy to $S_{p_{\{s,p\}}}(n_a)$ and $N_{S\{s,p\}}(n_a)$. Thus it is straight forward to calculate the ambient light corrected spectral trace:

$$S_{t_{\{s,p\}}}(n_a) := S_{p_{\{s,p\}}}(n_a) - \frac{N_{S\{s,p\}}(n_a)}{N_{A\{s,p\}}(n_a)} A_{p_{\{s,p\}}}(n_a) \tag{3.50}$$

As the wavelength in the centre of the image is known roughly, one can guess the harmonic order of the closest harmonic. Furthermore the wavelength difference between two successive harmonics is also known. Hence one can calculate a linear relation between the artificial wavelength number and the real spectral wavelength λ, easily. For further analysing the data it is more advantageous to plot the spectra versus $k_n := \frac{\lambda_0}{\lambda_n}$, i.e. the harmonic order, where λ_0 is the central wavelength of the laser. Then the abscissae of all harmonic maxima are next to integers. Hence these maxima are easily found by performing a maximum search around the appropriate integer values. Then a wavelength λ_r between this maximum and the next maximum on the righthand-side is determined by the wavelength next to λ_0 for which the number of counts falls below a certain percentage of the counts at the harmonic maximum. If no such λ_r is found, then the minimum between the two maxima is used as λ_r. Then the same procedure is performed at the lefthand-side of the maximum to determine (λ_l). After that the counts between λ_l and λ_r are summed up to the total number of counts for a certain harmonic. This analysis is performed for the s- and p-polarised trace, so that the measured s^2/p^2-ratio for every harmonic can be calculated. With the calibration Eq. (3.52), discussed in the next section, it is very simple to calculate the initial s^2/p^2-ratio right behind the plasma.

3.5.3.2 Calibration of the Polarimeter

In the VUV / XUV range it is even more necessary to calibrate the polarimeters, for measuring the s^2/p^2-ratio of the radiation, because in this wavelength range the optical components are in general even less ideal than in the VIS / UV range.

Calibration Equation   From Figure 3.16 it can be seen, that all components of the employed VUV / XUV polarimeter are reflective elements with the plane of incidence either in the s- or p-polarisation plane. Thus the relation between the incident Stokes parameters and the Stokes parameters in front of the detector is given by Eq. (3.41). Consequently the equation between the incident $I_{in,\{s,p\}}$ and the measured $I_{meas,\{s,p\}}$ s- and p-polarised pulse

energies can be written as:

$$\begin{pmatrix} I_{meas,s} \\ I_{meas,p} \end{pmatrix} := \begin{pmatrix} m_s\, s_s\, s_a & m_p\, s_p\, s_a \\ m_s\, p_s\, p_a & m_p\, p_p\, p_a \end{pmatrix} \begin{pmatrix} I_{in,s} \\ I_{in,p} \end{pmatrix} \tag{3.51}$$

with the reflectivities $m_{\{s,p\}}$ for the cylindrical mirror and the Acton grating in common, the reflectivities $s_{\{s,p\}}$ for the s-polarising mirror set of the polarisation splitter and $p_{\{s,p\}}$ for the p-polarising mirror set. All reflectivities are for s- and p-polarised light respectively. Whilst $m_{\{s,p\}}$, $s_{\{s,p\}}$ and $p_{\{s,p\}}$ depend on the optical properties of the reflective elements only, s_a and p_a are geometry factors, representing the area of the entrance pupil for the s- and p-polarised part of the beam, respectively. By using Eq. (3.51) it is easy to calculate the initial s^2/p^2-ratio in front of the polarisation splitter:

$$\left(s^2/p^2\right)_{in} = K\,\frac{\left(s^2/p^2\right)_{meas} - L}{1 - M\left(s^2/p^2\right)_{meas}} \tag{3.52a}$$

with:

$$K := \frac{1}{R}\frac{p_p}{s_s}\frac{m_p}{m_s} \qquad L := R\frac{s_p}{p_p} \qquad M := \frac{1}{R}\frac{p_s}{s_s} \qquad R := \frac{s_a}{p_a} \tag{3.52b}$$

If the optical properties of all gold mirrors are the same and the s- and p-polarising parts of the polarisation splitter are symmetric then

$$\frac{p_p}{s_s} \approx 1 \qquad\qquad \frac{s_p}{p_p} \approx \frac{p_s}{s_s} \qquad\qquad R \approx 1$$

These relations can be used to simplify Eq. (3.52). Ideally L and M should be close to zero, whilst K should be close to unity.

Experimental Setup The calibration was performed with a high harmonic laser plasma source located at the FORTH facility in Greek. The harmonics are produced in a gas-jet with a kHz-Ti:Sa laser delivering pulses with a pulse energy of a few mJ and a pulse duration below 100 fs. To rotate the polarisation plane of the incident laser beam a half wave-plate (Appendix D.4.2) is installed in front of the lens, which focuses the beam into the gas-jet. The remaining experimental setup is precisely the same as in Figure 3.16, only the solid target is replaced by the gas-jet and the VUV / XUV polarimeter are aligned along the axis of the incident laser beam.

A basic prerequisite for performing the calibration is, that the applied radiation must have a defined state of polarisation; ideally this is linear polarisation. Luckily the polarisation of gas harmonics is determined by the polarisation of the laser, i.e. if the laser is linear polarised, then the high harmonics are linear polarised too and both polarisation planes coincides. This was verified for the lower harmonics, i.e. harmonics with a wavelength larger than 150 nm, again by replacing the polarisation splitter with a Rochon polariser and the Darkstar CCD with an Andor CCD. If the polarising axis of the Rochon polariser was in the polarisation plane of the laser, one could observe the harmonic spectrum. If the polarising axis was perpendicular, then the harmonic spectrum vanished. This result was independent from the setup angle of the half wave-plate's axis.
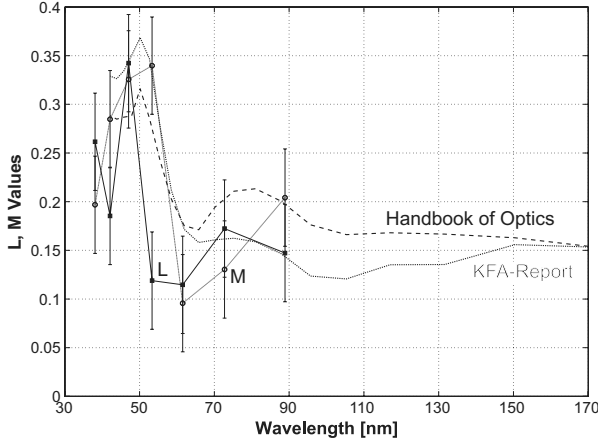
Figure 3.18: Measured L, M values from Eq. (3.52) in comparison to calculated values, based on two independent measurements of the complex refraction index of gold [98, 186].

Results   Calibrating the polarimeter means to determine the constants K, L, M from Eq. (3.52). This can be achieved by setting the axis of the half wave-plate to different angles $\alpha/2$ and measuring $(s^2/p^2)_{meas}(\alpha)$ versus α. In our case $(s^2/p^2)_{in}(\alpha) = \tan^2\alpha$, so that Eq. (3.52) can be written as:

$$(s^2/p^2)_{meas}(\alpha) = \frac{\tan^2\alpha + K\,L}{M\tan^2\alpha + K} \tag{3.53a}$$

By developing this function into a Taylor series one finds with $\Delta\alpha$ sufficiently small and c_i real constants:

$$(s^2/p^2)_{meas}(\,0° + \Delta\alpha) = L + c_1\Delta\alpha^2 + \mathcal{O}(4) \tag{3.53b}$$

$$(s^2/p^2)^{-1}_{meas}(90° + \Delta\alpha) = M + c_2\Delta\alpha^2 + \mathcal{O}(4) \tag{3.53c}$$

$$(s^2/p^2)^{-1}_{meas}(45° + \Delta\alpha) = \frac{M + K}{1 + K\,L} + c_3\Delta\alpha + c_4\Delta\alpha^2 + c_5\Delta\alpha^3 + \mathcal{O}(4) \tag{3.53d}$$

As can be seen from these equations L and M can be determined quite precisely, because they are the minimum of the respective curves, whilst K is more difficult to measure. Fortunately K is only a scaling constant in Eq. (3.52), so that it is of minor importance, if one is only interested in the relative changes of the s^2/p^2-ratio, i.e. the increase of the magnetic field. Indeed in our calibration experiment the values of K are subject to considerable errors. In contrast to that the M and L values can be determined more precisely. They are shown in Figure 3.18. In addition to our measurements calculated curves derived by using Eq. (3.38) are shown. The complex indices of refraction for gold is taken from two different references [98, 186], both based on measurements with synchrotron radiation. In comparison to the deviation between these calculated curves our measurements are in agreement with them. But it is rather obvious, that for future experiments a 16 bit detector should be used to have a larger dynamic range and that a calibration based on the well defined conditions at a synchrotron radiation source should be carried out in addition.

3.6   Experimental Results

As already discussed in Section 3.4 the magnetic field strength can be measured in two independent ways: either by means of x-wave cut-offs or by means of Müller matrices.
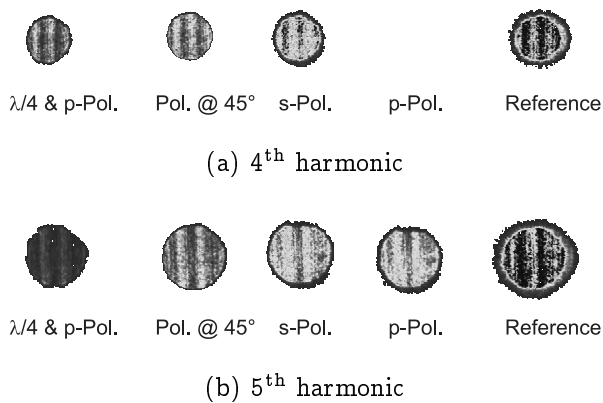
λ/4 & p-Pol.   Pol. @ 45°   s-Pol.   p-Pol.   Reference

(a) 4th harmonic

λ/4 & p-Pol.   Pol. @ 45°   s-Pol.   p-Pol.   Reference

(b) 5th harmonic

Figure 3.19: Typical CCD images showing the existence of a 4th harmonic cut-off of the extraordinary wave (i.e. p-polarisation), whilst the 5th harmonic is not cut-off. The focused intensity was approximately $1 \cdot 10^{20}$ W/cm^2.
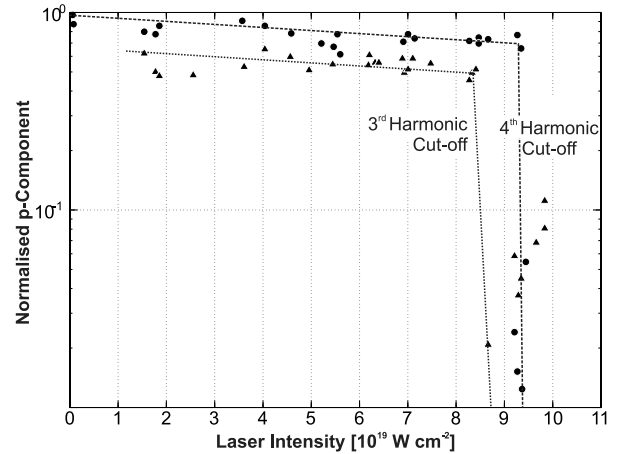

Figure 3.20: Ratio between the x-wave (p-polarisation) and total harmonic emission of the 3rd (triangles) and 4th (circles) harmonic for different pulse energies. The x-wave cut-offs are clearly visible at intensities greater than $8 \cdot 10^{19}$ W/cm^2.

To derive the field strength from the x-wave cut-offs only the electron-density has to be known within one order of magnitude, if the density is not too high. To derive the field strength from the elements of the Müller matrix the initial polarisation state of the electromagnetic wave in front of the magnetised plasma and its propagation distance through the magnetised area also have to be known.

In this subsection the experimental results of the magnetic field experiment performed with the CPA-beam of VULCAN are presented: at first the measurements of the field strength based on the x-wave cut-offs (see Subsection 3.4.4) are shown, then the observation of magnetic fields with the Müller matrix approach (see Subsection 3.4.6) is discussed. Finally VUV / XUV harmonic measurements are presented. These measurements are vital for measuring magnetic fields beyond 500 MG and for examining fields in the high density regions of the plasma.

3.6.1 Observation of Magnetic Fields by X-Wave Cut-Offs

Observing the magnetic field strength inside the plasma with the x-wave cut-off is a very striking experiment, because a quick look onto the data already reveals the field strength: in Figure 3.19 the p-polarised (i.e. extraordinarily polarised) spot of the 4th harmonic is gone, whilst the respective spot of the 5th harmonic is present. Thus with the help of Table 3.3 one can determine limits for the magnetic field strength immediately, if the electron density in the magnetised area along the propagation path of the harmonics is known. To determine this density additional considerations concerning the harmonic source geometry are necessary.

3.6.1.1 Influence of Electron Density and Source Geometry on the Observed Field Strength

As already discussed in Subsection 3.3.2 the leading edge of the main laser pulse immediately pushes away the free electrons of the pre-plasma along its path of incidence, so that a channel depleted of electrons is formed. Hence any magnetic fields present inside

Harmonics of		Cut-Off for $n_{ec}=8 \cdot 10^{21}$ cm^{-3} in MG	Cut-Off for $n_{ec}=4 \cdot 10^{21}$ cm^{-3} in MG	Cut-Off for $n_{ec}=1 \cdot 10^{21}$ cm^{-3} in MG	Cut-Off for $n_{ec}=1 \cdot 10^{20}$ cm^{-3} in MG
#	nm				
2	527		72	153	198
3	351	35	170	271	302
4	264	204	305	381	406
5	211	346	427	488	509
6	176	475	542	593	610
7	151	596	653	697	711
8	132	712	762	800	812
9	117	824	869	903	915
10	105	935	976	1006	1020
11	96	1044	1081	1108	1121
12	88	1152	1186	1211	1222
13	81	1259	1290	1313	1323
14	75	1365	1394	1415	1424
15	70	1470	1497	1518	1524
16	66	1575	1600	1619	1625
17	62	1680	1704	1721	1732
18	59	1784	1806	1824	1834
19	55	1888	1909	1925	1935

Table 3.3: Minimal magnetic field strength required to cut off the extraordinary wave of a certain harmonic at a given electron density. The values are calculated with Eq. (3.19).

this channel cannot alter the polarisation state of the incident main pulse seriously. Furthermore the pondermotorive forces, generated by the p-polarised main pulse, steepens the density gradient at the target surface again, even drilling a hole into the over-dense plasma (see Subsection 3.2.2), so that efficient harmonic generation can take place at the relativistically corrected critical electron density surface (see Subsection 3.3.2 and [191]).

The harmonic radiation, produced around to the bottom of this hole, might propagate through magnetised plasma areas at the side-walls of the hole with densities such high, that the harmonics are already cut off at a rather low magnetic field strength (Figure 3.8). But there is always some harmonic radiation produced in regions further away from the bottom of the hole and from the axis of the incident laser pulse, where the relativistically corrected electron density is much lower. Due to the electron density gradients pointing away from the centre of the laser–plasma interaction, the harmonics generated in these outer regions will not propagate through plasma areas with an electron density considerably higher than the density in their region of origin.

The peak intensity of the focused VULCAN laser pulse is about $1.5 \cdot 10^{20}$ W/cm^2, so that the relativistically corrected electron density (see Eq. (3.4)) varies from $n_{ec_{rel}} := 8 \cdot 10^{21}$ cm^{-3} ($\gamma \lesssim 8$) at the bottom of the hole to $n_{ec} := 1 \cdot 10^{21}$ cm^{-3} ($\gamma \approx 1$) in the periphery of the laser–plasma interaction. Consequently, one can only observe complete x-wave cut-offs, if the harmonics produced at n_{ec} are also cut-off. Hence an electron

density not much beyond n_{ec} is appropriate for a good estimate of the minimal magnetic field strength present inside the plasma (compare in addition Figure 3.8). To avoid overestimating the peak magnetic field strength all further considerations are based on an electron density of $n_e = 2 \cdot 10^{21}\,\mathrm{cm^{-3}}$. This is roughly the relativistically corrected critical electron density for $10^{19}\,\mathrm{W/cm^2}$. Furthermore, the error bars of the magnetic field strength cover a density range from $1 \cdot 10^{20}\,\mathrm{cm^{-3}}$ to $4 \cdot 10^{21}\,\mathrm{cm^{-3}}$.

Using Table 3.3, one immediately recognises, that the 4th harmonic cut-off requires a lower limit of the peak magnetic field of $350(\pm 60)\,\mathrm{MG}$. If the plasma should become relativistic in the magnetised region for any reason, then this value only underestimates the peak magnetic field strength (see Subsection 3.4.4). On the other hand so far no 5th harmonic cut-off has been observed. Thus the strongest magnetic field in the plasma could be lower than approximately $470(\pm 50)\,\mathrm{MG}$. But it is important to note that this upper limit is not totally conclusive, as there are several reasons why a cut-off cannot be observed: at first this might be due to the none-zero temperature inside the plasma (see end of Subsection 3.4.4). Another reason is that the magnetic fields can be very localised in comparison to the emission volume of the 5th harmonic, so that most of the radiation bypasses this area and the observed decrease in the p-polarised harmonic intensity becomes negligibly small. Even worse, the field may be exclusively present in a region with such a high electron density, that the 5th harmonic cannot propagate through this area and is not influenced by this field consequently.

3.6.1.2   Influence of the Laser Intensity on the Cut-Offs

To answer the question, at which laser intensity a certain harmonic is cut-off, the measured CCD images (compare Figure 3.19) have been analysed with the programme described in Subsection 3.5.2.1. Furthermore Eq. (3.49a) has been used to derive the Stokes parameters of the harmonics right behind the plasma. Eventually the p-polarised component of the harmonic emission normalised to the total harmonic emission, i.e. $0.5\,(1 + s_1/s_0)$ is plotted versus the average focal laser intensity in Figure 3.20 for the 3rd and 4th harmonic. It is clearly seen that the 3rd harmonic is already cut-off at $8.5 \cdot 10^{19}\,\mathrm{W/cm^2}$, whilst the 4th harmonic is cut of at intensities above $9.5 \cdot 10^{19}\,\mathrm{W/cm^2}$ only. This is in agreement with theoretical considerations stating that the magnetic field strength should increase with increasing laser intensity (see Section 3.1 and [68]). If the intensity is increased further, then the normalised p-component in Figure 3.20 starts growing again, because the volume emitting a particular harmonic increases too, so that a part of the harmonic radiation can bypass the magnetised plasma now (see Figure 3.4). This is particularly bad in the case of the 2nd harmonic, which is emitted from a volume so large that the cut-off is never complete in general. The gentle decrease of the normalised p-component of the 3rd and 4th harmonic for intensities below $8.5 \cdot 10^{19}\,\mathrm{W/cm^2}$ in Figure 3.19 is due to the increasing Cotton-Mouton effect (see Subsection 3.4.3): with increasing laser intensity the ellipticity of the harmonic radiation increases, i.e. their s-polarised component grows whilst their p-polarised component decreases.

3.6.1.3 Complete Cut-Offs and Magnetic Field Properties

As already mentioned above, we observed complete x-wave cut-offs in our experiments. From the observation of these complete cut-offs important conclusions about the properties of the magnetic field can be drawn:

- In Subsection 3.4.2 it is shown (see in addition Appendix E.2), that the two characteristic vectors of an electromagnetic wave propagating through a magnetised plasma become elliptically polarised as soon as the magnetic field has a component parallel to the propagation direction. In this case a cut-off would allow only one elliptically polarised characteristic vector to propagate through the magnetised plasma, so that the polarisation state behind the plasma is always elliptically polarised. Hence the signal behind a linear polariser can never vanish completely. As we have observed complete cut-offs, the characteristic vectors have to be linear polarised. Consequently the magnetic field is perpendicular to the propagation direction of the electromagnetic wave, i.e. one can neglect the Faraday effect in comparison to the Cotton-Mouton effect.

- If the harmonics already have an ordinary component with respect to the magnetic field in front of the magnetised plasma, then the signal $I_{E,0}$ on the zeroth polariser channel cannot vanish even in the case of a complete cut-off. As $I_{E,0}$ never became zero in our experiments, the initial harmonic polarisation always had an ordinary component. Thus $I_{E,1}$ can only vanish, if the respective polariser is aligned perpendicular to this ordinary component. Consequently the axis of the first polarimeter channel and hence the whole polarimeter is aligned perpendicular to the polarisation direction of the ordinary wave, i.e perpendicular to the magnetic field. Consequently β from Eq. (3.29) (i.e. the angle between the polarisation direction of the x-wave and the polarimeter axis) is approximately zero.

- Recalling that the target is aligned in such a manner, that its normal vector is parallel to the p-polarisation plane of the polarimeter and that the magnetic field is perpendicular to this plane (see last item), it is clear, that the magnetic field is also parallel to the target surface. This agrees with the theoretical prediction from Subsection 3.2.2, showing that the magnetic field strength normal to the target is less than 10 % of the azimuthal field strength.

- Depolarisation due to density gradients, i.e. a gradient of the refractive index [94, 126] along the propagation path of the harmonics, can alter their polarisation state too. In general this polarisation mechanism leads to elliptically polarised harmonics. Hence one cannot observe a complete cut-off if this effect is large behind the x-wave cut-off region of the plasma. In addition the density gradients are pointing away from the centre of the laser plasma interaction, so that the propagation direction of the harmonics is rather parallel to these gradients and thus the depolarisation effect is reduced even more. This consideration is also true for the incident laser beam where this effect is particularly small, due to the reduced electron density along its path of incidence. It is also noteworthy that the depolarisation decreases with decreasing wavelength.

3.6.2 The Müller Matrix Approach

If one cannot observe the x-wave cut-offs, then the magnetic field strength can be determined with the Müller matrix approach. But applying this method some pre-conditions have to be met.

3.6.2.1 Pre-Conditions

At first it is vital to know the polarisation state of the laser harmonics before they enter the highly magnetised plasma region. Already in Subsection 3.3.2 theoretical considerations have been made, showing that the harmonic radiation is supposed to have the same polarisation state as the laser, i.e. in the present experiment the harmonics should be linear polarised. Experimentally verifying this theoretical predictions is not straight forward, because one can only measure the harmonic radiation after its propagation through the plasma, i.e. when it is already influenced by magnetic fields and possibly further effects. But, if one reduces the pulse energy of VULCAN to roughly 1 J, then the magnetic field strength reduces considerably in comparison to full energy shots as shown by PIC simulations similar to Subsection 3.2.2. Thus the observed polarisation state of the harmonics should not differ much from the original polarisation state. The influence of these relatively weak magnetic fields onto the polarisation of the harmonics can be reduced even more, if higher order harmonics are used, because the Cotton-Mouton effect scales with ω^{-3} (see Subsection 3.4.5). For the 4th harmonic the ellipticity was already less than $0.028\,\pi$ and the azimuth angle (i.e. the rotation of the major principle axis of the harmonics against the p-polarisation plane of the polarimeter) was $15(3)°$. The degree of polarisation was over $90\,\%$. Similar results, independent from the laser pulse energy, were obtained by measuring the polarisation state of harmonics, propagating along a line of sight from the centre of the laser–plasma interaction in a direction close to the target normal. This agrees with the PIC simulations in Figure 3.2, predicting only weak magnetic fields along this line of sight even for high laser intensities.

Despite magnetic fields, the polarisation state of the harmonic radiation can also be altered by depolarisation due to density gradients. As already discussed in Subsection 3.6.1.3 this effect is presumably small and can be neglected, so that in summary all measurements and theoretical considerations support the assumption of initially linear polarised harmonics.

Another open, but important question is the extension of the magnetised plasma volume. As spatially resolved measurements of the magnetic field distribution inside a laser produced plasma are still under way [62], one has to estimate the propagation length of the harmonics through the strongly magnetised areas of the plasma. Optical probing of the under-dense pre-plasma region [117] suggests to assume a density scale length of 1 µm. This is also supported by the extension of the magnetised region in the PIC simulation in Subsection 3.2.2.

Before discussing the experimental results, the parameters necessary for calculating the field strength, using the equations given in Subsection 3.4.6, are briefly summarised again:
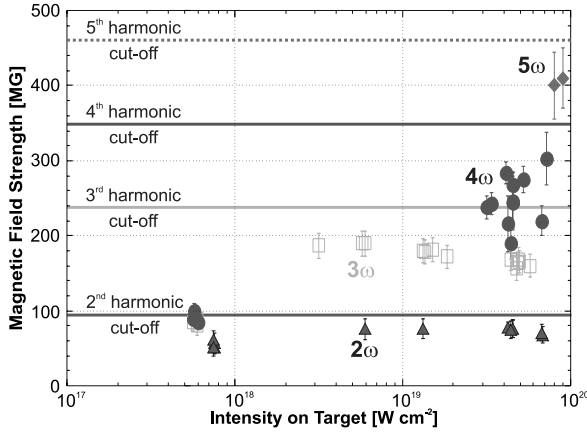
Figure 3.21: Magnetic field strength calculated from the measurement of Stokes parameters for various harmonics (initially linear polarised; azimuth angle 15(5)°; angle between the magnetic field and the polarimeter axis $\approx 0(3)°$; electron density $2 \cdot 10^{21}$ cm^{-3}; propagation length 1 µm).

Angle of Magnetic Field: In Subsection 3.6.1.3 it was discussed, that due to the alignment of the target and the existence of complete cut-offs, the angle between the p-polarisation plane of the polarimeter and the magnetic field must be approximately zero, i.e. $\beta \approx 0(3)°$.

Initial Polarisation State: The harmonics' initial state of polarisation has been found to be linear polarised, with an azimuth angle of $15(3)°$ relative to the polarimeter axis, thus $\alpha - \beta \approx \alpha \approx 15(3)°$.

Electron Density: Coming back to the discussion about the appropriate electron density in the magnetised plasma region form above, we again assume that $n_e = 2 \cdot 10^{21}$ cm^{-3}.

Propagation Length: So far one is limited to estimate the propagation length from computational simulations and measurements of the plasma scale length. These simulations and measurements suggest a scale lenght of $\Delta z \approx 1$ µm.

The precision of the measurements will increase if future experiments lead to a better knowledge of the appropriate electron density in the magnetised volume and the extension of this volume. Nevertheless relative measurements of the magnetic field strength, i.e. the comparison between the field strength derived from different harmonics, do not depend on these parameters, as they mutually cancel each other in this case. Hence relative magnetic field measurements are already a very powerful tool to study magnetic fields in laser produced plasmas.

3.6.2.2   Observation of Magnetic Fields with VIS / UV Polarimetry

With the polarimeters described in Subsection 3.5.2 the VIS / UV harmonics, i.e. the 2nd to the 5th harmonic, have been studied. To derive the Stokes parameters behind the plasma from the data acquired with these polarimeters the calibration equation Eq. (3.49a) has been used. The particularities of the polarimeter calibration and the image analysis procedure are explained in Subsection 3.5.2. By knowing the Stokes parameters behind the plasma one can derive the magnetic field strength with Eq. (3.29), if one pays attention to the pre-requisites discussed in Subsection 3.6.2.1. The outcome of this calculation is shown in Figure 3.21 for the different harmonics. The error bars mainly include the calibration errors of the polarimeters whilst systematic errors like wrong assumptions about the estimated parameters in Eq. (3.29) are not included.

At first one recognises that the observed magnetic field strength increases with increasing harmonic order. This can be most easily understood if one remembers that the strongest magnetic fields in the PIC simulations (see Subsection 3.2.2) are observed in areas with a high density and that probably the low order harmonics cannot propagate through these high density areas (compare Figure 3.4(a)). In addition this can also be a geometric effect: as higher intensities are needed to produce higher order harmonics more efficiently (see Subsection 3.3.2), the source size of the higher order harmonics is smaller than the source size of the lower order harmonics, due to the approximately Gaussian spatial profile of the laser pulse. Thus the line of sight from the polarimeter to the emission region of a harmonic with a rather high order may pass through the highly magnetised area exclusively, whilst the line of sight for a harmonics with a lower order may partially bypass the highly magnetised area, so that one observes a lower averaged magnetic field strength.

At a second glance one recognises that the magnetic field strength derived with the Müller matrix approach does not reach the value at which the respective x-wave cut-off appears. This could be due to assuming wrong values for the electron density or the extension of the magnetised plasma region. However the field strength calculated with the Müller matrix approach does not differ much from the values calculated with the cut-offs. Hence the assumptions about the parameters from Subsection 3.6.2.1 seem to be realistic. In addition, even if the assumptions about these parameters should be wrong, then this still does not explain why the field strength already becomes constant for intensities well below the x-wave cut-off intensity (compare Figure 3.20). The main reasons for this constant field strength are less obvious, because they are related to the derivation of Eq. (3.29) and its succeeding equations: for deriving these equations it is required that $\Omega_\perp \Delta z \ll \pi$. Furthermore one often uses an approximation of $\Omega_\perp$ instead of the exact expression Eq. (3.22b) for simplicity. This does not hold any more, if the magnetic field strength approaches the cut-off strength. Hence the derived magnetic field strength already saturates for intensities well below the cut-off intensity and does not reach the field strength calculated from the respective x-wave cut-off. On the other hand, if the magnetic field strength is well below the respective cut-off level and the laser intensity is low, so that the source size does not become too large, then one expects to observe the same field strength for different harmonics. In fact this is observed for the 3$^{\text{rd}}$ and 4$^{\text{th}}$ harmonic at intensities below 10^{18} W/cm^2 (see Figure 3.21). In contrast to that, the field strength calculated from the 2$^{\text{nd}}$ harmonic is even lower, because it is very easily generated in a huge plasma volume, so that it mainly propagates through weakly to unmagnetised plasma areas.

An even closer look shows that the field strength observed with the 2$^{\text{nd}}$ and 3$^{\text{rd}}$ harmonic begins to decrease again shortly before the laser intensity reaches the cut-off level. This can be understood if one realises, that the magnetic field strength is mainly calculated from the Stokes parameter S_3 (see Eq. (3.30)) and that this parameter represents the ellipticity (see Eq. (C.5)). If there are already some regions inside the

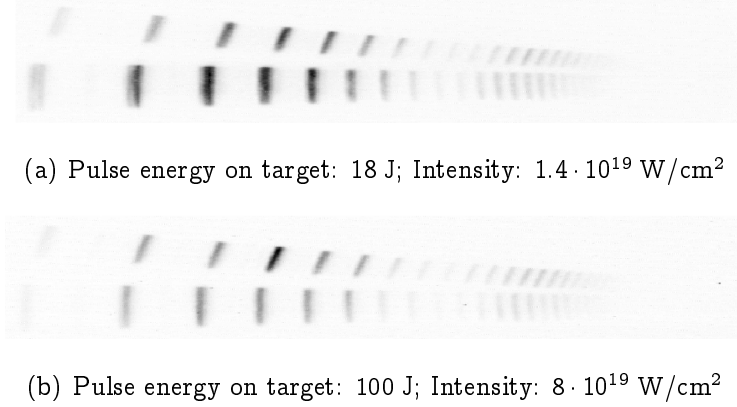(a) Pulse energy on target: 18 J; Intensity: $1.4 \cdot 10^{19}$ W/cm^2

Figure 3.22: The originally acquired spectral traces for a low and a high energy shot. The high energy shot clearly shows an increase of the s-polarised component in comparison to the low energy shot.

(b) Pulse energy on target: 100 J; Intensity: $8 \cdot 10^{19}$ W/cm^2

plasma, where the field strength necessary for producing a cut-off is surpassed, then only the s-polarised part of the harmonic radiation is transmitted through these areas. This linear polarised part reduces the mean ellipticity of the total emission, eventually leading to a lower observable field strength. In contrast to that, the geometric effect from Subsection 3.6.1.2 (i.e. that with increasing laser intensity the source size becomes larger and can surpass the size of the plasma region in which the magnetic fields produces a cut-off) can lead to an increased ellipticity again. However these values are not plotted in Figure 3.21 anymore.

An important conclusion drawn from these studies is, that all values of the magnetic field strength calculated with the Müller matrix approach are a lower boundary of the field strength derived from the respective cut-off. Hence the Müller matrix approach gives reasonable lower boundaries of the peak magnetic field strength inside the plasma, if the necessary parameters are chosen carefully.Applying this approach to the Stokes parameters observed for the 5$^{\text{th}}$ harmonic shows that the peak magnetic field is presumably above 400($\pm$50) MG, which agrees well with the results derived from the x-wave cut-offs in Subsection 3.6.1.1.

3.6.2.3   Observation of Magnetic Fields with VUV / XUV Polarimetry

Recalling that our experimental studies suggest that the observed magnetic field strength increases with increasing harmonic order, VUV / XUV harmonics will presumably discover even stronger magnetic fields. Thus during our experiment two VUV / XUV polarimeters have been employed to study the magnetic fields by observing the VUV / XUV harmonics. One polarimeter was looking onto the plasma at an angle of gracing incidence of 4°, whilst the second was observing the plasma in a direction close to normal, i.e. at 80° with respect to the target surface (see Figure 3.9). These polarimeters are described in detail in Subsection 3.5.3. In Figure 3.22 typical CCD-images acquired with the gracing incidence polarimeter are shown for a low (18 J) and a high (100 J) energy shot. These spectral traces have been analysed with the Matlab programme described in Subsection 3.5.3 to derive the measured $^{s^2}/_{p^2}$-ratio. The initial $^{s^2}/_{p^2}$-ratio right behind the plasma has been calculated by using the calibration equation Eq. (3.49a) and the reflectivity data of a gold surface from [186] (see Figure 3.18). This ratio can be used to derive the magnetic field strength (see Subsection 3.4.6.4), because the cyclotron fre-
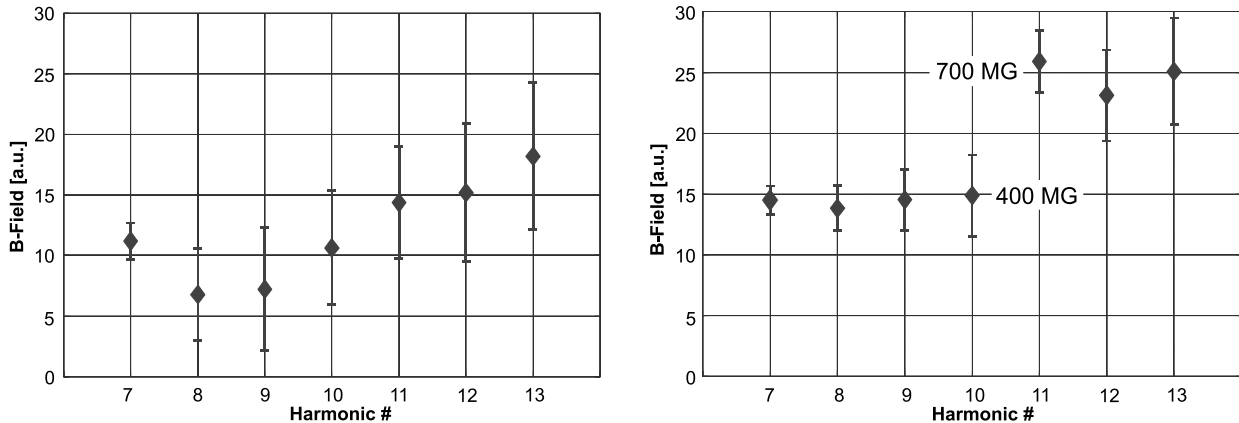
(a) Pulse energy: 18 J; Intensity: $1.4 \cdot 10^{19}$ W/cm^2 (b) Pulse energy: 100 J; Intensity: $8 \cdot 10^{19}$ W/cm^2

Figure 3.23: Magnetic field strength measured with VUV XUV polarimetry for a low and a high energy shot. The observation angle of the polarimeter was approximately 4° with respect to the target surface.

quency ω_{ce} (see Eq. (3.6)) is much smaller than the vibration frequency of sufficiently high VUV / XUV harmonics.

In Figure 3.23 the value for the magnetic field strength is calculated for a low and a high energy shot from the measured $^{s^2}/_{p^2}$-ratio, assuming that the Cotton-Mouton effect dominates the interaction between the harmonic radiation and the magnetic field, i.e. Eq. (3.35) is valid. Within the experimental errors, growing with increasing harmonic order and being mainly caused by the 8 bit dynamic range of the Darkstar CCDs, the calculated value for the magnetic field strength can be considered constant at roughly 10 a.u. for the low energy shot. This is completely different for the high energy shot, where we observe a jump of the calculated field strength value from 14.5 a.u. to 25 a.u. between the 10th and 11th harmonic. From the 7th to the 10th and from the 11th to the 13th harmonic the calculated field strength remains constant. It is important to mention, that between the low and high energy shot only the target was replaced and the laser energy was increased, so that any changes due to the alignment can be ruled out and one can compare the two plots directly. In addition, for some high energy shots this jump appeared between the 9th and 10th harmonic, so that it cannot be due to the optical properties of the polarimeter. Furthermore the second polarimeter (set to an angle of 80° with respect to the target surface) has never observed any difference between low and high energy shots for any harmonic. Hence this phenomena must be caused by a physical process related to the laser–plasma interaction, depending on the focused laser intensity and the angle of observation.

The PIC simulations in Subsection 3.2.2 predict azimuthal magnetic fields, which depend on the focused laser intensity and should be observable with a gracing incidence polarimeter only. These predictions agree well with our experimental findings. Furthermore an azimuthal magnetic field in conjunction with our experimental setup requires that mainly the Cotton-Mouton effect alters the polarisation state of the harmonics. As already discussed in Subsection 3.4.6.4 the Cotton-Mouton effect scales with ω^{-3} (see Eq. (3.35)), whilst the Faraday effect scales with ω^{-2} (see Eq. (3.33)). Hence magnetic

field values calculated form the s^2/p^2-ratio, by assuming the dominance of the Cotton-Mouton effect and thus using Eq. (3.35), should only remain constant for several different harmonics if this assumption holds. Indeed this agrees with Figure 3.23, where the the magnetic field values remain constant from the 7th to the 10th and from the 11th to the 13th harmonic.

In Figure 3.23 the magnetic field strength value, given in arbitrary units, increases between the 10th and the 11th harmonic by a factor of $\approx$1.75. This is a strong indication of a peak magnetic field beyond 700($\pm$100) MG inside the plasma: From the x-wave cut-off we know that the peak magnetic field is greater than 350($\pm$60) MG. Measurements performed with the 5th harmonic, based on the Müller matrix approach, even suggests fields beyond 400($\pm$50) MG. Thus it is reasonable to assume that the 7th to the 10th harmonic are also influenced by a magnetic field of at least 400($\pm$50) MG. Consequently the 11th to the 13th harmonic must be influenced by a field of at least 700($\pm$100) MG. It is important to note that the increase of the magnetic field strength derived from its height does not depend on the electron density n_e and the propagation length Δz in Eq. (3.35), because we are comparing the polarisation properties of two successive harmonics, which propagate along similar paths as discussed in the next paragraph. Furthermore a field strength of 700($\pm$100) MG could give raise to a cut-off of the 8th harmonic, but to observe this cut-off, the extinction-ratio of the polarisation splitters (see Figure 3.15) has to be increased even more.

Finally, it is interesting to note that the critical electron density for the 11th harmonic is $n_{ec} = 1.1 \cdot 10^{23}$ cm^{-3}, so that this harmonic can penetrate through very dense areas of the plasma and one can observe magnetic fields from the interior of the target and not only from areas close to the target surface. This cannot explain the jump between the 10th and 11th harmonic completely, as the difference in the critical electron density between these two harmonics is only 4 %. Consequently a more likely explanation is the difference in source size, as already discussed above (see e.g. Subsection 3.3.2). For a more detailed understanding of this exciting discovery further studies and an improved VUV / XUV polarimeter are indispensable.

3.7 Summary

In this chapter the generation and observation of magnetic fields in sub-picosecond laser produced plasmas were discussed. There are three main sources for the generation of magnetic fields in sub-picosecond laser produced plasmas: radial thermal transport, pondermotorive forces and fast electron currents.

As the field due to radial thermal transport needs several picoseconds to build up, it is presumably still rather weak during the direct laser–plasma interaction (i.e. at times when the high harmonic radiation is produced). Hence, most likely, we have been observing the pondermotorively generated field, because it is much stronger than the field due to fast electron currents. Its strength was studied with three different experimental techniques: cut-offs, VIS / UV polarimetry and VUV / XUV polarimetry. We observed a field strength

of about 400($\pm$50) MG and found strong indications of fields up to 700($\pm$100) MG.

PIC Simulations   To get more insight into the location and strength of the magnetic field inside the plasma PIC simulations have been performed with the programme OSIRIS [64, 70, 112] from the University of California at Los Angeles (UCLA). For normal incidence of the laser beam the strongest magnetic field lines had an azimuthal shape. But in the case of oblique incidence, this field was compressed to an even higher field strength in the half plane along the target normal not containing the incident beam. In the half plane containing the incident beam, the field was much lower but expanded over a larger region. This important result clarifies that the strong magnetic fields could be observed from one side of the plasma only. Furthermore, these computational simulations show strongly localised magnetic fields up to 700($\pm$100) MG in the high density regions of the plasma. Thus fluid hybrid models would be more accurate for detailed theoretical studies [41].

Fundamentals of the Experiment   A convenient way to study these fields is spectroscopy with radiation produced either inside the plasma or from an external source. The latter is rather difficult for visible and UV radiation because of the refraction at the steep density gradients at the plasma edges (see Figure 3.3). This improves for radiation with a shorter wavelength like x-rays. But the present performance of x-ray optics and sub-picosecond x-ray sources makes such experiments still very difficult. Hence an internal source of radiation, like high harmonics of the laser, seems to be more appropriate (see Subsection 3.3.1). Theoretical considerations and experimental findings suggest, that these harmonics are an ideal source for studying magnetic fields. Namely, they are a bright and quite localised source with presumably the same polarisation as the laser, radiating into a solid angle of 2π at VULCAN (see Subsection 3.3.2).

Observation of Magnetic Fields   If an electromagnetic wave propagates through a magnetised plasma, one can distinguish between parallel (Faraday effect) and perpendicular (Cotton-Mouton effect) propagation (see Subsection 3.4.3) with respect to the magnetic field. The latter is most important for our experiment, as the harmonics propagate from the centre of the laser–plasma interaction through the azimuthal magnetic field. However in this case the p-polarised component of the electromagnetic wave can only propagate if the magnetic field strength is below a certain level (x-wave cut-off), depending on the wavelength of the wave. This cut-off can be used to determine the field strength, even if the electron density is only known within one order of magnitude (see Subsection 3.4.4). Furthermore it is only complete if the magnetic field is perpendicular to the propagation direction of the wave. For wavelengths beyond the cut-offs one can determine the magnetic field strength from the components of the plasma's Müller matrix, if the polarisation state of the harmonics in front and behind the magnetised plasma region is known (see Subsection 3.4.6). In addition one has to know the extension of the magnetised plasma region and its electron density. Furthermore, one can distinguish between the Faraday and Cotton-Mouton effect, because the former scales with ω^{-2} whilst the latter scales
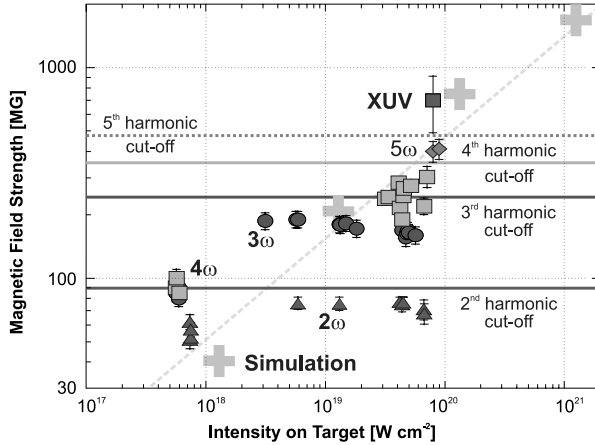
Figure 3.24: Overview of the observed magnetic field strengths versus laser-intensity during the experiment: the crosses are the field strength calculated from PIC simulations (see Subsection 3.2.2), the horizontal lines represent the x-wave cut-offs and the other points are based on the Müller matrix approach with VIS, UV, VUV and XUV polarimetry. It can be seen that the field strength grows exponentially with the laser intensity.

with ω^{-3}. If the cut-off frequency is *much* lower than the harmonic frequency, then one can calculate the magnetic field strength from the s^2/p^2-ratio.

Experimental Setup   An overview of the whole experimental setup is shown in Figure 3.9. To measure the x-wave cut-offs and the components of the Müller matrix two VUV / XUV polarimeters and three VIS / UV polarimeters were employed.

   VIS / UV Polarimeters   By setting up the VIS / UV polarimeters (see Figure 3.12) it was assured, that all angles of incidence onto the optical elements were kept below 20° to avoid an unnecessarily large phase-shift between the reflected s-polarised and p-polarised parts of the harmonic radiation. To calculate the Stokes parameters of the laser harmonics directly behind the plasma, the number of counts for each polarimeter channel was calculated (see Subsection 3.5.2.1) and then multiplied by the calibration matrix Eq. (3.49). The calibration matrix was determined by calibrating the instrument with a pulsed, highly linear polarised and frequency multiplied Nd:YAG laser (see Figure 3.9).

   Single-Shot VUV / XUV Polarimeters   The VUV / XUV polarimeters are shown in Figure 3.16 and have been employed for the first time in connection with a laser produced plasma. To derive the s^2/p^2-ratio directly behind the plasma the spectral traces have been integrated (see Subsection 3.5.3.1) and then the calibration equation Eq. (3.52) was used. The parameters of this calibration equation have been derived from tabulated measurements of the complex refraction index of gold [98, 186]. These calculated parameters roughly correspond with our own calibration measurements performed at the FORTH facility in Greece with laser produced gas harmonics.

Experimental Results   As already discussed above the magnetic field strength was determined with two independent methods: the x-wave cut-offs and the Müller matrix approach.

   X-Wave Cut-Offs   This is a very striking method for studying strong magnetic fields in a laser produced plasma, if the electron density is not so high, that the cut-off frequencies shift to lower frequencies (see Figure 3.8). The horizontal lines in Figure 3.24 represent the cut-off levels. In our experiment we repeatedly reproduced cut-offs for the 2nd, 3rd and 4th harmonic, but none of the 5th. As we can estimate, that the 4th harmonic propagates at least partially exclusively through plasma areas with an electron density

below $2 \cdot 10^{21}$ cm^{-3} (see Subsection 3.6.1.1), the peak magnetic field strength in our plasma must be larger than 350($\pm$60) MG. As we observed complete x-wave cut-offs of the 3$^{\text{rd}}$ and 4$^{\text{th}}$ harmonic, the Faraday effect can be of minor importance only and the observed magnetic field must be an azimuthal field indeed.

Müller Matrix Approach This method depends on deriving some components of the Müller matrix by measuring the Stokes parameters of the harmonic radiation behind the plasma. Hence it is limited to magnetic fields lower than the field strength that would produce an x-wave cut-off of the harmonic under consideration.

VIS / UV Polarimetry: The magnetic field strength calculated from a certain harmonic already becomes constant at laser pulse intensities much lower than the intensity needed to produce a magnetic field, cutting off the respective harmonic (see Figure 3.24). This is due to the approximations generally used to calculate the field strength (see Subsection 3.4.6). Consequently the calculated values underestimate the real peak magnetic field strength in general. If the field strength inside the plasma is much lower than the field needed to cut-off certain harmonics and the electron density is not too high, then one derives similar values for the field strength from each of these harmonics, as we found e.g. for the 3$^{\text{rd}}$ and 4$^{\text{th}}$ harmonic at intensities below 10^{18} W/cm^2. In contrast to that, the field strength derived from the 2$^{\text{nd}}$ harmonic is too low again, because the source size of this harmonic is presumably so large, that most radiation does not propagate through strongly magnetised areas. As the source size decreases and the critical electron density related to a certain harmonic grows with increasing harmonic order, it is not surprising, that we observed fields beyond 400 MG using the 5$^{\text{th}}$ harmonic (see Figure 3.4).

VUV / XUV Polarimetry: For sufficiently high VUV / XUV harmonics, it is possible to derive the field strength from the s^2/p^2-ratio (see Subsection 3.4.6.4). Analysing the measurements from the gracing incidence polarimeter (see Figure 3.9) we found a jump in the magnetic field strength between the 10$^{\text{th}}$ and 11$^{\text{th}}$ harmonics (see Figure 3.23). Assuming that the harmonics up to the 10$^{\text{th}}$ are mainly influenced by fields of at least 400($\pm$50) MG (see Subsection 3.6.1 and Subsection 3.6.2.2), then the harmonics from the 11$^{\text{th}}$ onwards should be influenced by fields not lower than 700($\pm$100) MG (compare Subsection 3.6.2.3). Propagation through a region with a particular density and high magnetic field cannot explain this jump, because the critical electron density between the 10$^{\text{th}}$ and 11$^{\text{th}}$ harmonics does not differ by more than 4 %. As the source size decreases with increasing harmonic order, it is much more likely, that for harmonics from the 11$^{\text{th}}$ onwards, all radiation propagates through a plasma area with a stronger and more localised magnetic field (see Figure 3.4). In addition the field strength for successive harmonics remained constant, which is an indication, that indeed the Cotton-Mouton effect determines the interaction of the harmonics and the magnetised plasma. Furthermore, the polarimeter set up close to normal incidence did not observe any magnetic fields, consistent with the PIC simulations in Figure 3.2.

Outlook   The double logarithmic plot in Figure 3.24 shows the observed magnetic field strength versus laser intensity. The crosses in this plot represent the field strength calculated with the PIC simulations described in Subsection 3.2.2. It is seen clearly that the calculated values grow exponentially with the laser intensity. The same increase of the field strength is supported by our experimental data (all other dots in the diagram). Obviously we have not been able to find any saturation of the magnetic field strength as proposed by Haines [68]. Hence the question, as to whether or not the magnetic field strength saturates, will remain open at least until detailed experimental studies can be performed with petawatt lasers, where one can expect fields beyond 1 GG. However the fields measured in our experiment already have a strength of several hundred megagauss, which is more than 10 times stronger than any magnetic field observed in a laser produced plasma so far. As this was the first experimental observation of such strong fields in a laser produced plasma, it is important to confirm our experimental findings with further experiments, based on alternative approaches as the Zeeman effect for example [141, 151].

Chapter 4
Summary and Outlook

In this work two important aspects of the interaction between an intensive sub-picosecond laser pulse and a dielectric solid have been studied. In the first major part the ultrafast ionisation and plasma formation at a dielectric surface was examined in detail. For this experiment moderate laser intensities around 10^{15} W/cm^2 with pulses as short as 60 fs have been used. One of the most striking results which we obtained was that the ionisation process can transform an initially transparent surface into an opaque plasma in less than 10 fs. Thus this mechanism is one of the fastest gates known, which gives rise to interesting applications as briefly discussed below. Furthermore we discovered that the decrease in transmissivity is much faster than the increase in reflectivity, which is due to the quickly increasing absorption of the laser beam inside the plasma.

The next major part of this work presents the first observation of magnetic fields beyond several 100 MG in the high density regions of a plasma produced at a dielectric solid with a femtosecond laser. For this experiment one of the strongest CPA lasers available was employed. Its 750 fs pulses were focused to intensities up to 10^{20} W/cm^2. A serious obstacle for measuring these magnetic fields is the strong refraction of an external electromagnetic probe beam in the entire VIS–XUV range at the edges of the plasma. We could overcome this problem by studying the polarisation properties of the laser harmonics produced inside the plasma itself. With this new approach we observed magnetic fields up to 400($\pm$60) MG with VIS / UV polarimetry. VUV / XUV polarimeter measurements, which we performed in addition, gave strong indications of fields beyond 700($\pm$100) MG. Supplementary summaries concerning the experimental procedures and more details about the scientific results are given in Section 2.5 for the ionisation experiment and in Section 3.7 for the magnetic field observation.

One exciting extension of the present ultrafast ionisation experiment is the use of an even shorter laser pulse with a duration of approximately 10 fs. In this case the ionisation process presumably becomes dependent on the absolute phase of the laser pulse, so that one might be able to study the influence of this absolute phase onto the ionisation process. This will be a challenging experiment, because most likely one will have to integrate over several laser pulses, so that absolute phase-locking between adjacent pulses is required [144]. The pump–probe setup (see Figure 2.9) used in the ionisation experiment could also be combined with the polarimeters employed in the magnetic field experiment to study the depolarisation of electromagnetic waves and the magnetic fields [139] in the under-dense regions of the plasma with high temporal resolution. For future studies of the magnetic field in the very high density region of the plasma x-ray polarimetry [143] will play an increasingly important role, because only x-rays can propagate through these high density areas of the plasma without being absorbed and refracted too much.

Furthermore, recent advances in the development of very high-power lasers [31] allow repetition rates of approximately 1 Hz, so that one can integrate over several laser shots and thus might be able to use an external x-ray probe beam. In addition to that, modern high resolution x-ray optics [40, 51] can enable the observation of the spatial distribution of the magnetic field inside the laser produced plasma [63].

Studying the magnetic fields inside the plasma is only a first step: in the present experiment we already observed very strong magnetic fields, which were only about one order of magnitude lower than the magnetic fields of the fast oscillating carrier frequency of the laser-pulse. As the upcoming generation of petawatt lasers allows even higher intensities and we did not find any saturation of the magnetic field strength so far, these lasers can presumably generate even stronger magnetic fields. Thus the magnetic pressure eventually reaches values at which the spherical symmetry of the hydrogen atoms deforms to cylindrical symmetry. In this case the atomic transitions are determined by the Landau quantisation [90], and one should observe a drastic change in the atomic line-emission spectra. By pre-compressing tiny spheres of matter with VULCAN's nanosecond beams to densities several orders of magnitude larger than solid density, one can even study extremely dense and strongly magnetised matter, which is similar to the surface of white dwarfs and neutron stars [150]. Hence these experiments could become key experiments in testing, improving and developing astrophysical models of compact cosmic objects. This will significantly contribute to a field of science known as laboratory astrophysics.

Appendix A
Mathematical Definitions and Equations

A.1 The Normalised Fourier Operator

From a mathematical point of view the relationship between the temporal and spectral representation of an optical signal is given by the Fourier transform. Unfortunately for historical reasons different definitions of this transform are widely used. Much worse, it can be quite difficult with some of these definitions to define the Fourier transform of even simple signals like an infinite and constant light wave. All these difficulties can be overcome by introducing the normalised Fourier operator, defined over a set of distributions. To avoid any confusion with other definitions, this appendix gives a short overview of this approach and lists the properties of the normalised Fourier operator.

A.1.1 Definitions

To define the *normalised Fourier operator* it is necessary to introduce the *normalised Fourier integral* first. In accordance with its common definition we write [26, 49, 188]:

Definition A.1 *Let* $f : \mathbb{R} \mapsto \mathbb{C}$ *be a Lebesgue-Integrable function of time (i.e.* $f \in \mathcal{L}_1(\mathbb{R}, \mathbb{C})$*), then the integral Eq. (A.1) exists and* $\widetilde{f}(\omega)$*, with the angular frequency* ω*, is called the* Fourier integral *of* $f(t)$:

$$\widetilde{f}(\omega) := \mathfrak{F}_{t \to \omega} f(t) := \frac{1}{\sqrt{2\pi}} \int_{-\infty}^{\infty} f(t) \, e^{+i\omega t} \, dt \qquad (A.1)$$

In general the inverse transformation of Eq. (A.1) does not exist. To ensure its existence $f(t)$ is required to be in $\mathcal{L}_1(\mathbb{R}, \mathbb{C}) \cap \mathcal{L}_2(\mathbb{R}, \mathbb{C})$, where $\mathcal{L}_2$ represents the space of Lebesgue square-integrable functions.

To define the Fourier transform of a distribution [49] we introduce *regular distributions* [56]:

Definition A.2 *Let be* $f \in \mathcal{L}_1(\mathbb{R}, \mathbb{C}) \cap \mathcal{L}_2(\mathbb{R}, \mathbb{C})$ *and let be* $\phi(t)$ *a test function (i.e. an infinitely differentiable function with compact support), then* F *is called a* regular distribution:

$$F\{\phi(t)\} := \int_{-\infty}^{\infty} f(t) \, \phi(t) \, dt \qquad : \forall \text{ test functions } \phi(t) \qquad (A.2)$$

Definition A.3 *The Fourier transform of* F *is given by:*

$$(\mathfrak{F}_{t \to \omega} F)\{\phi(t)\} := \int_{-\infty}^{\infty} \widetilde{f}(\omega) \, \phi(\omega) \, d\omega \qquad : \forall \text{ test-functions } \phi(t) \qquad (A.3)$$

$\mathfrak{F}_{t \to \omega}$ *is called the* normalised Fourier operator.

By using a series of regular distributions one can define the Fourier operator of an arbitrary *distribution* [56]:

Definition A.4 *Let* F_∞ *be a distribution and let* $\{F_n\}$ *be an arbitrary series of regular distributions, so that* F_n *converges uniformly against* F_∞, *then the Fourier transform of* F_∞ *is given by:*

$$(\mathfrak{F}_{t\to\omega}F_\infty)(\phi(t)) := \lim_{n\to\infty}\{\mathfrak{F}_{t\to\omega}F_n\}(\phi(t)) \quad : \forall \text{ test functions } \phi(t) \text{ and} \forall \{F_n\} \quad (A.4)$$

Furthermore, if the f_n *related to* F_n *converge against* $f_\infty : \mathbb{R} \mapsto \mathbb{C}$, *then* F_∞ *is the related distribution to* f_∞ *and* $\widetilde{F}_\infty$ *is the related Fourier transform.*

Due to Def. (A.2) and Def. (A.3) each signal $s \in \mathcal{L}_1(\mathbb{R}, \mathbb{C}) \cap \mathcal{L}_2(\mathbb{R}, \mathbb{C})$ and its Fourier transform can be represented as a distribution, so that one does not need to distinguish between the related distribution and the original signal. In addition, working with these distributions simplifies calculations considerably, because one can Fourier transform many distributions, whilst their appropriate physical signals cannot be Fourier transformed. An example of this is an infinite sinusoidal oscillation: its Fourier transform does not exist in general, but the Fourier transform of its related distribution is the non-regular δ-distribution.

A.1.2   Properties

Let be $a, b \in \mathbb{C}$ and let be f, g distributions. The definitions of operators used below are given in Appendix A.3.1.

A very basic property of the Fourier operator is its relation to the *parity operator*:

$$\mathfrak{F}^2 := \mathfrak{F}_{\omega\to t} \circ \mathfrak{F}_{t\to\omega} \equiv \mathfrak{P}_t \tag{A.5}$$

Thus the *inverse Fourier operator* $\mathfrak{F}_{t\to\omega}^{-1}$ is defined by:

$$\mathfrak{F}_{t\to\omega}^{-1} := \mathfrak{F}_{t\to\omega}^{-1} \circ \mathfrak{P}_t \circ \mathfrak{P}_t = \mathfrak{F}_{t\to\omega} \circ \mathfrak{P}_t \tag{A.6}$$

Another very fundamental property is the *linearity*:

$$\mathfrak{F}_{t\to\omega}\{a\,f(t) + b\,g(t)\} = a\,\mathfrak{F}_{t\to\omega}f(t) + b\,\mathfrak{F}_{t\to\omega}g(t) \tag{A.7}$$

More sophisticated is *Parseval's theorem*:

$$\mathfrak{F}_{t\to\omega}\,|h(t)|^2 = |\mathfrak{F}_{t\to\omega}h(t)|^2 \quad ; \quad h(t) \in \mathcal{L}_2(\mathbb{R}, \mathbb{C}) \tag{A.8}$$

The Fourier Transform of the *complex conjugate* $f^*(t)$ of $f(t)$ holds:

$$\mathfrak{F}_{t\to\omega}\{f(t)^*\} \equiv \left\{\mathfrak{F}_{t\to\omega}^{-1}f(t)\right\}^* \tag{A.9}$$

Furthermore the *translation theorem* states:

$$\mathfrak{F}_{t\to\omega}\{\mathfrak{T}_{t\rightsquigarrow a}f(t)\} = e^{ia\omega}\,\mathfrak{F}_{t\to\omega}f(t) \tag{A.10a}$$

$$\mathfrak{T}_{t\rightsquigarrow a}\{\mathfrak{F}_{t\to\omega}f(t)\} = \mathfrak{F}_{t\to\omega}\left\{e^{-iat}\,f(t)\right\} \tag{A.10b}$$

The *scaling theorem* is given by:

$$\mathfrak{F}_{t\to\omega}\left\{\mathfrak{S}_{t\updownarrow a}f(t)\right\} = \frac{1}{|a|}\,\mathfrak{F}_{t\to\omega/a}f(t) \tag{A.11a}$$

$$\mathfrak{S}_{\omega\updownarrow a}\left\{\mathfrak{F}_{t\to\omega}f(t)\right\} = \frac{1}{|a|}\,\mathfrak{F}_{t\to\omega}\left\{\mathfrak{S}_{t\updownarrow 1/a}f(t)\right\} \tag{A.11b}$$

Another prominent property of the Fourier operator is the *convolution theorem* (see Appendix A.2):

$$\mathfrak{F}_{t\to\omega}\left\{f(t) *_t g(t)\right\} = \sqrt{2\pi}\,\left(\mathfrak{F}_{t\to\omega}f(t)\right)\left(\mathfrak{F}_{t\to\omega}g(t)\right) \tag{A.12a}$$

$$\mathfrak{F}_{t\to\omega}\left\{f(t)\,g(t)\right\} = \frac{1}{\sqrt{2\pi}}\,\left(\mathfrak{F}_{t\to\omega}f(t)\right)*_\omega\left(\mathfrak{F}_{t\to\omega}g(t)\right) \tag{A.12b}$$

Equally important are the *derivation theorem*:

$$\mathfrak{F}_{t\to\omega}\left\{\mathfrak{D}_t f(t)\right\} = -i\omega\,\mathfrak{F}_{t\to\omega}f(t) \tag{A.13a}$$

$$\mathfrak{D}_\omega\left\{\mathfrak{F}_{t\to\omega}f(t)\right\} = \mathfrak{F}_{t\to\omega}\left\{it\,f(t)\right\} \tag{A.13b}$$

and the *integration theorem*:

$$\mathfrak{F}_{t\to\omega}\left\{\mathfrak{I}_t f(t)\right\} = \left(\frac{i}{\omega} + \pi\delta(\omega)\right)\mathfrak{F}_{t\to\omega}f(t) \tag{A.14a}$$

$$\mathfrak{I}_t\left\{\mathfrak{F}_{t\to\omega}f(t)\right\} = \mathfrak{F}_{t\to\omega}\left\{\left(\frac{-i}{t} + \pi\delta(t)\right)f(t)\right\} \tag{A.14b}$$

A.2 The Convolution Operator

A.2.1 Definition

In the time domain the gating of an optical signal is represented by multiplying the original signal with a gating function. As this multiplication becomes a convolution in the spectral domain it is useful to define a *convolution operator* for studying the gating process in the spectral domain. Similar to the definition of the Fourier operator one has to define the convolution of functions first:

Definition A.5 *Let* $f, g \in \mathcal{L}_1(\mathbb{R}, \mathbb{C})$ *be two functions, then the convolution* $*_t$ *is:*

$$f(t) *_t g(t) := \int_{-\infty}^{\infty} f(\tau)\,g(t-\tau)\,d\tau \tag{A.15}$$

Then the convolution operator of distributions is defined in a similar manner to the Fourier operator (see Appendix A.1).

A.2.2 Properties

Let be $a, b \in \mathbb{C}$ and let f, g, h be distributions. The definitions of operators used below are given in Appendix A.3.1.

The most fundamental properties of the convolution operator are its *symmetry*:

$$f(t) *_t g(t) = g(t) *_t f(t) \tag{A.16}$$

and its *linearity*

$$f(t) *_t [a\, g(t) + b\, h(t)] = a\, [f(t) *_t g(t)] + b\, [f(t) *_t h(t)] \tag{A.17}$$

The convolution operator and *parity* operator hold:

$$\mathfrak{P}_t\{f(t) *_t g(t)\} = (\mathfrak{P}_t\{f(t)\}) *_t (\mathfrak{P}_t\{g(t)\}) \tag{A.18}$$

and the *complex conjugate* holds:

$$\{f(t) *_t g(t)\}^* = f^*(t) *_t g^*(t) \tag{A.19}$$

The convolution operator and *Fourier operator* hold:

$$\mathfrak{F}_{t\to\omega}\{f(t) *_t g(t)\} = \sqrt{2\pi}\ (\mathfrak{F}_{t\to\omega}f(t))\ (\mathfrak{F}_{t\to\omega}g(t)) \tag{A.20a}$$

$$\mathfrak{F}_{t\to\omega}\{f(t)\, g(t)\} = \frac{1}{\sqrt{2\pi}}\ (\mathfrak{F}_{t\to\omega}f(t)) *_\omega (\mathfrak{F}_{t\to\omega}g(t)) \tag{A.20b}$$

The convolution operator and *derivation operator* hold:

$$\mathfrak{D}_t\{f(t) *_t g(t)\} = (\mathfrak{D}_t\{f(t)\}) *_t g(t) = f(t) *_t (\mathfrak{D}_t\{g(t)\}) \tag{A.21}$$

The convolution operator and *translation operator* hold:

$$\mathfrak{T}_{t\rightsquigarrow a}\{f(t) *_t g(t)\} = (\mathfrak{T}_{t\rightsquigarrow a}\{f(t)\}) *_t g(t) = f(t) *_t (\mathfrak{T}_{t\rightsquigarrow a}\{g(t)\}) \tag{A.22}$$

The convolution operator and *scaling operator* hold:

$$\mathfrak{S}_{t\updownarrow a}\{f(t) *_t g(t)\} = a\ (\mathfrak{S}_{t\updownarrow a}\{f(t)\}) *_t (\mathfrak{S}_{t\updownarrow a}\{g(t)\}) \tag{A.23}$$

A.3 Definitions and Properties of Operators, Distributions and Functions

This section lists some definitions and properties of various operators, distributions and functions used within this work. Most of them are not uniquely defined or they are rarely tabulated in the literature.

A.3.1 Definitions

A.3.1.1 Functions

We define the *error function* erf(t):

$$\mathrm{erf}(t) := \frac{2}{\sqrt{\pi}} \int_0^t \exp\left(-t^2\right)\ dt \tag{A.24}$$

and the *Heaviside function* H(t):

$$H(t) := \lim_{a\to\infty} \frac{1}{2}(1 + \mathrm{erf}(a\, t)) \tag{A.25}$$

A.3.1.2   Distributions

The *delta distribution* δ [49, 56] is given by:

$$
\begin{aligned}
\delta\{\varphi(t)\} &= \int_{-\infty}^{\infty} \delta(t)\,\varphi(t)\,dt \\
&:= \lim_{a\to\infty} \frac{a}{\sqrt{\pi}} \int_{-\infty}^{\infty} \exp\left(-(a\,t)^2\right)\,\varphi(t)\,dt \qquad : \forall \text{ test functions } \varphi(t)
\end{aligned}
\tag{A.26}
$$

Test functions are infinitely differentiable functions with compact support.

A.3.1.3   Operators

Always let $f : \mathbb{R} \mapsto \mathbb{C}$ be an appropriate function in the following.
The *parity operator*:

$$
\mathfrak{P}_t\{f(t)\} := f(-t)
\tag{A.27}
$$

The *translation operator* $\mathfrak{T}_{t\rightsquigarrow a}$ is defined by:

$$
\mathfrak{T}_{t\rightsquigarrow a}\{f(t)\} := f(t-a)
\tag{A.28}
$$

The *scaling operator* $\mathfrak{S}_{t\updownarrow a}$ is defined by:

$$
\mathfrak{S}_{t\updownarrow a}\{f(t)\} := f(a\,t)
\tag{A.29}
$$

The *integration operator* $\mathfrak{I}_t$ is defined by:

$$
\mathfrak{I}_t\{f(t)\} := \int_{\infty}^{t} f(\hat{t})\,d\hat{t}
\tag{A.30}
$$

The *derivation operator* is defined by: $^\S\mathfrak{D}_t$ is defined by:

$$
\mathfrak{D}_t\{f(t)\} := \lim_{\hat{t}\to t} \frac{f(\hat{t}) - f(t)}{\hat{t} - t}
\tag{A.31}
$$

Furthermore $\mathfrak{D}_t^{(m)}$ is the mth derivative.

A.3.2   Properties

A.3.2.1   Fourier Transforms

$$
\mathfrak{F}_{t\to\omega} \exp\left(-t^2\right) = \frac{1}{\sqrt{2}} \exp\left(-\frac{\omega^2}{4}\right)
\tag{A.32}
$$

$$
\mathfrak{F}_{t\to\omega} H(t) = \frac{1}{\sqrt{2\pi}} \left(\frac{i}{\omega} + \pi\,\delta(\omega)\right)
\tag{A.33}
$$

$$
\mathfrak{F}_{t\to\omega}\,\delta(t) = \frac{1}{\sqrt{2\pi}}
\tag{A.34}
$$

$$
\mathfrak{F}_{t\to\omega}\,\mathrm{erf}(t) = \sqrt{\frac{2}{\pi}} \left[\left(\frac{i}{\omega} + \pi\delta(\omega)\right)\exp\left(-\frac{\omega^2}{4}\right) - \sqrt{\pi}\delta(\omega)\right]
\tag{A.35}
$$

---

§The derivation operator of a distribution is defined analogous to the Fourier transform (see Appendix A.1).

$$\mathfrak{F}_{t\to\omega}\left\{\mathfrak{D}_t^{(m)}\,\delta(t)\right\} = \begin{cases} (-1)^{\frac{m}{2}}\,\omega^m & \text{if } m \text{ is even; } m \in \mathbb{N}, \\ (-1)^{\frac{m+1}{2}}\,i\,\omega^m & \text{if } m \text{ is odd; } m \in \mathbb{N}. \end{cases} \tag{A.36}$$

$$\mathfrak{F}_{t\to\omega}\left\{P(t)\right\} = \sqrt{2\pi}\,P\left(-i\,\mathfrak{D}_\omega\right)\,\delta(\omega) \tag{A.37}$$

where $P(t)$ represents a polynomial.

A.3.2.2   Derivatives

$$\mathfrak{D}_t\,H(t) = \delta(t) \tag{A.38}$$

$$\{\mathfrak{D}_t\,\delta(t)\}\phi(t) = \left[\frac{d}{dt}\phi(t)\right]_{t=0} \qquad : \forall \text{ test functions } \phi(t) \tag{A.39}$$

A.3.2.3   Convolutions

Let $f : \mathbb{R} \mapsto \mathbb{C}$ be a function, holding some very general constraints, then:

$$\delta(t)\} *_t f(t) = f(t) \tag{A.40}$$

$$\left[\frac{d}{dt}\delta(t)\right] *_t f(t) = \frac{d}{dt}f(t) \tag{A.41}$$

A.4   Gaussian Pulses

The *Gaussian pulse* is given by:

$$G_a(I_0, T_h, t) := I_0\,e^{-\left(\frac{2\sqrt{\ln 2}}{T_h}\,t\right)^2} \tag{A.42}$$

with the peak amplitude I_0 and the full width half maximum T_h.
The integral of $G_a(I_0, T_h, t)$ over $[-t_0; t_0]$ is given by

$$\int_{-t_0}^{t_0} G_a(I_0, T_h, t)\,dt = \sqrt{\frac{\pi}{4\ln 2}}\,\mathrm{erf}\left(\frac{2\sqrt{\ln 2}}{T_h}\,t_0\right)\,I_0 T_h \tag{A.43}$$

The integral of $G_a(I_0, T_h, t)$ over the FWHM T_h is given by:

$$E_{T_h}(I_0, T_h) := \int_{-T_h/2}^{T_h/2} G_a(I_0, T_h, t)\,dt = \sqrt{\frac{\pi}{4\ln 2}}\,\mathrm{erf}\left(\sqrt{\ln 2}\right)\,I_0 T_h \approx 0.8100\,I_0 T_h \tag{A.44}$$

The integral of $G_a(I_0, T_h, t)$ over $\mathbb{R}$ is given by:

$$E_\infty(I_0, T_h) = \int_{-\infty}^{\infty} G_a(I_0, T_h, t)\,dt := \sqrt{\frac{\pi}{4\ln 2}}\,I_0 T_h \approx 1.0645\,I_0 T_h \tag{A.45}$$

Thus the ratio of $E_{T_h}(I_0, T_h)$ to $E_\infty(I_0, T_h)$ is given by:

$$\frac{E_{T_h}(I_0, T_h)}{E_\infty(I_0, T_h)} = \mathrm{erf}\left(\sqrt{\ln 2}\right) \approx 0.7610 \tag{A.46}$$

In dealing with squared Gaussian pulses it is useful to note that:

$$\left(G_a(I_0, T_h, t)\right)^2 = G_a\left(I_0, \frac{T_h}{\sqrt{2}}, t\right) \tag{A.47}$$

The Fourier transform of a Gaussian pulse is:

$$\mathfrak{F}_{t \to \omega}\{G_a(I_0, T_h, t)\} = G_a\left(\frac{I_0 T_h}{\sqrt{8 \ln 2}}, \frac{8 \ln 2}{T_h}, \omega\right) \tag{A.48}$$

Appendix B

The Quasi Half Range Signal of a Gated Optical Pulse

In this Appendix it is shown that the convolution of any reasonable gating function and a complex quasi band-limited pulse is always a quasi half range signal. Basically this means that $s_f(\tau, \omega)$ from Eq. (2.11) is a quasi half range signal in any case. For showing this one has to define the quasi half range signals of a real physical signal.

B.1 Quasi Half Range Signals

B.1.1 Quasi Identical Signals

Sometimes it is convenient to use a signal slightly different from the original signal as this can simplify the algebra considerably. Thus a quantitative measure is needed to assess the deviation between them. Following ideas of Bedrosian [15], Rihaczek [135] and Nuttall [119] to use the relative energy difference between two signals $f_1, f_2, : \mathbb{R} \mapsto \mathbb{C}$ as a measure of their deviation, we define:

Definition B.1 *Let* $f_1, f_2, : \mathbb{R} \mapsto \mathbb{C}$ *be two signals, then* f_1 *and* f_2 *are called* quasi identical *signals, if*

$$\frac{\int \left| \widetilde{f_1}(\omega) - \widetilde{f_2}(\omega) \right|^2 \, d\omega}{\int \left| \widetilde{f_1}(\omega) + \widetilde{f_2}(\omega) \right|^2 \, d\omega} \equiv \frac{\int |f_1(\omega) - f_2(\omega)|^2 \, d\omega}{\int |f_1(\omega) + f_2(\omega)|^2 \, d\omega} < \epsilon \tag{B.1}$$

with the maximum permissible deviation $\epsilon \gtrsim 0$.

If this inequality holds, then f_1 and f_2 can be considered identical for all practical purpose. The identity between the time and frequency domain expressions hold because of Parseval's theorem Eq. (A.8).

An important *product theorem* of quasi identical signals is readily derived from this definition:

Theorem B.1 *Let* $f_1, f_2, g_1, g_2 : \mathbb{R} \mapsto \mathbb{C}$ *be arbitrary signals with* f_1, f_2 *and* g_1, g_2 *quasi identical in pairs, then* $(f_1 \, g_1)$ *and* $(f_2 \, g_2)$ *are quasi identical signals.*

B.1.2 Half Range Signals

As all physical signals $s(t)$ are real signals, i.e. $s : \mathbb{R} \mapsto \mathbb{R}$, their spectrum $\widetilde{s}(\omega) := \mathfrak{F}_{t \to \omega}\{s(t)\}$ shows a well known ordinate symmetry: The positive and negative frequencies are correlated via the *complex conjugate* *. Accordingly one can represent such a signal with the positive part of its spectrum solely. Hence, using the *Heaviside function* H, we define the *half range spectrum* $\widetilde{s^+}(\omega)$:

$$\widetilde{s^+}(\omega) := 2H(\omega)\mathfrak{F}_{t \to \omega}\{s(t)\} \tag{B.2}$$

The factor two rises from the conservation of energy, namely Parseval's theorem Eq. (A.8). In addition note, that the support $\sup(\widetilde{s^+}(\omega))$ of a half range spectrum is always a subset of $\mathbb{R}_0^+$.

The inverse Fourier transform of $\widetilde{s^+}(\omega)$ is a complex function called the *half range signal* $s^+(t)$ of $s(t)$. With some basic algebra one can show that:

$$s^+(t) := \mathfrak{F}_{\omega \to t}^{-1}\left\{\widetilde{s^+}(\omega)\right\} = s(t) + i\,\mathfrak{H}_t\left\{s(t)\right\} \tag{B.3}$$

with the *Hilbert transform*:

$$\mathfrak{H}_t\{s(t)\} := -\frac{1}{\pi}\int_{-\infty}^{\infty} \frac{s(\hat{t})}{t - \hat{t}}\,d\hat{t} \tag{B.4}$$

Working with half range signals is advantageous because a single-sided spectrum is more intuitive than a two-sided. In addition, dealing with vibrations is more convenient in a complex representation.

An important theorem about half range signals is the *product theorem*:

Theorem B.2 *Let* $f, g : \mathbb{R} \mapsto \mathbb{C}$ *be two arbitrary signals and let there exist* $\omega_a \in \mathbb{R}$, *so that* $\sup(\widetilde{f}(\omega)) \subseteq \{\omega \in \mathbb{R} | \omega \geq \omega_a\}$ *and* $\sup(\widetilde{g}(\omega)) \subseteq \{\omega \in \mathbb{R} | \omega \geq -\omega_a\}$, *then* $f(t)g(t)$ *is a half range signal.*

This is easily shown by using the convolution theorem of the Fourier transform and the constraints concerning the support of f and g

B.1.3   Quasi Half Range Signals

Unfortunately some important physical signals cannot be represented as a half range signal easily. A well known example of this is a Gaussian light pulse. Luckily a simple mathematical expression exists, which is quasi identical to its precise half range signal. Thus it is advantageous to introduce *quasi half range signals*:

Definition B.2 *An arbitrary signal* $s : \mathbb{R} \mapsto \mathbb{C}$ *is called a* quasi half range signals, *if its spectrum* $\widetilde{s}(\omega)$ *and the half range spectrum* $\widetilde{s}(\omega)\,H(\omega)$ *are quasi identical.*

Using Theorem B.1 one easily extended Theorem B.2 to quasi half range signals:

Theorem B.3 *Let* $f, g : \mathbb{R} \mapsto \mathbb{C}$ *be two arbitrary signals and let there exist* $\omega_a \in \mathbb{R}$, *so that* $\widetilde{f}(\omega)$, $\widetilde{f}(\omega)H(\omega - \omega_a)$ *and* $\widetilde{g}(\omega)$, $\widetilde{g}(\omega)H(\omega + \omega_a)$ *are quasi identical in pairs, then* $f(t)g(t)$ *is a quasi half range signal.*

Now this last theorem is applied to show that gated pulses are quasi half range signals in general.

B.2   Gated Optical Signals

B.2.1   Quasi Band-Limited Optical Signals

In complex notation any optical signal can be written as:

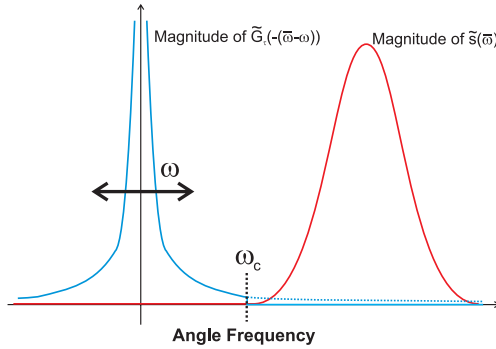$$s_c(t) = A(t)\,e^{i(\omega_0 t + \varphi(t))} \tag{B.5}$$

Figure B.1: Schematic spectrum $\widetilde{G}_\tau(\omega - \bar{\omega})$ of a gating function and an optical pulse $\widetilde{s_c}(\bar{\omega})$: it is seen clearly, that the two spectra do not overlap much for $\omega \leq 0$, if the gating function is shifted across the optical pulse.

$A(t)$ is called the envelope of the signal, ω_0 represents the angle frequency of the fast oscillating carrier frequency and $\varphi(t)$ is the phase modulation of ω_0. This signal is called a *quasi band-limited optical signal* if there exists a signal $s_{c,b} : \mathbb{R} \to \mathbb{C}$, so that $s_{c,b}(t)$ is quasi identical to $s_c(t)$ and $\max[\sup(\widetilde{s_{c,b}}(t))] - \min[\sup(\widetilde{s_{c,b}}(t))] < \omega_0$. This is true in general if $\frac{A'(t)}{A(t)} \ll \omega_0$ and $\varphi'(t) \ll \omega_0$ hold, whereby the apostrophe denotes the first derivative.

Even if Eq. (B.5) is quasi band-limited, it is not necessarily a half range signal as one can see by Fourier transforming $s_c(t)$ and assuming that $A(t)$ is a Gaussian. Regardless, if Eq. (B.5) is a quasi band-limited signal, it is easily shown with Def. (B.1) that there exists an $\omega_s \in \mathbb{R}^+$, so that the spectrum $\widetilde{s_c}(\omega)$ of $s_c(t)$ and $\widetilde{s_c}(\omega)H(\omega - \omega_s)$ are quasi identical signals (Compare Figure B.1). Consequently $s_c(t)$ is a quasi half range signal.

B.2.2   The Gating Function

Before we can discuss the convolution of a gating function and an optical pulse, we have to examine the spectral properties of an arbitrary gating function. We assume that the gating function $G_\tau : \mathbb{R} \mapsto \mathbb{C}$ is differentiable in terms of generalised functions and that the gate is triggered at a time τ. Then one can write with the derivative $G_\tau'(t)$:

$$\widetilde{G_\tau}(\omega) = \mathfrak{F}_{t\to\omega}\left\{\int_{-\infty}^{t} G_\tau'(T)\,dT\right\} = \mathfrak{F}_{t\to\omega}\left\{\int_{-\infty}^{\infty} H(-(T-t))G_\tau'(T)\,dT\right\} = \qquad (B.6)$$

$$\mathfrak{F}_{t\to\omega}\left\{G_\tau'(t) *_t H(t)\right\} = \sqrt{2\pi}\,\widetilde{H}(\omega)\,\widetilde{G_\tau'}(\omega) \qquad (B.7)$$

It is obvious, that all gating functions $G_\tau(t)$ approach a constant value for $t \to \pm\infty$ in such manner, that $\lim_{t\to\pm\infty} G_\tau'(t)$ converges against zero and that $\int |G_\tau'(t)|^2\,dt = \int |\widetilde{G_\tau'}(\omega)|^2\,d\omega$ exists and is finite. Thus there exists a constant $c \in \mathbb{R}^+$ for all $\omega_g \in \mathbb{R}^+$, so that $|\widetilde{G_\tau'}(\omega)| < c$ for all $\omega < \omega_g$. Consequently:

$$\int_{-\infty}^{-\omega_g} |\widetilde{G_\tau}(\omega)|^2\,d\omega \leq c^2 \int_{-\infty}^{-\omega_g} |\widetilde{H}(\omega)|^2\,d\omega = c^2 \int_{-\infty}^{-\omega_g} \frac{1}{\omega^2}\,d\omega \qquad (B.8)$$

With this equation and the definition Def. (B.1) it is straight forward to show, that the spectrum $\widetilde{G_\tau}(\omega)$ of $G_\tau(t)$ and $\widetilde{G_\tau}(\omega)H(\omega + \omega_g)$ are quasi identical signals.

B.2.3   The Gated Pulse

It was shown in the last two subsections, that the spectrum $\widetilde{s_c}(\omega)$ of all quasi band-limited optical pulses is quasi identical to $\widetilde{s_c}(\omega)H(\omega - \omega_s)$ and that the spectrum $\widetilde{G_\tau}(\omega)$ of an arbitrary gating function is quasi identical to $\widetilde{G_\tau}(\omega)H(\omega + \omega_g)$, whereby ω_s and ω_g

are real constants. Citing Theorem B.3 and choosing an appropriate common constant ω_c for ω_s and ω_g it becomes clear, that the gated optical pulse $s_c(t)\,G(t-\tau)$ is a quasi half range signal. This situation is depicted in Figure B.1 in the spectral domain. If one considers for instance a 30 fs pulse with 800 nm central wavelength and an error function like gating function with a transition time of 5 fs, then the relative deviation between the spectrum of the gated pulse and its quasi half range spectrum is much smaller than 10^{-10}.

Appendix C
Measuring the Polarisation of Light

One part of the experiment for measuring the magnetic field strength in a laser produced plasma (Chapter 3) is based on the measurement of polarisation changes. Thus a detailed understanding about measuring the polarisation state of an electromagnetic wave is vital for understanding the experiment. Hence this appendix gives a short introduction into the polarisation of light and explains the definition of Stokes parameters (see in addition [24, 72, 167]). Representing polarisation states in terms of Stokes parameters is hugely advantageous as they have a simple geometrical interpretation and can be measured easily.

C.1   The Polarisation of Electromagnetic Waves

The fundamental equations of electromagnetic phenomena are the the Maxwell equations [75, 105], which can be written as:

$$\nabla \times \vec{E}(\vec{r}, t) + \dot{\vec{B}}(\vec{r}, t) = 0 \tag{C.1a}$$

$$\nabla \times \vec{B}(\vec{r}, t) - c_0^{-2}\, \dot{\vec{E}}(\vec{r}, t) = \mu_0 \mathcal{J} \tag{C.1b}$$

$$\nabla \cdot \vec{E}(\vec{r}, t) = \frac{1}{\epsilon_0} \mathcal{Q} \tag{C.1c}$$

$$\nabla \cdot \vec{B}(\vec{r}, t) = 0 \tag{C.1d}$$

In general $\mathcal{Q}$ and $\mathcal{J}$ are differential operators incorporating charges, currents and the properties of the surrounding medium into the Maxwell equations. In the most simple case (i.e. in vacuum) $\mathcal{Q}$ and $\mathcal{J}$ equals zero. Admitting charges and currents $\mathcal{Q}$ and $\mathcal{J}$ represent the usual charge and current density. If the movement of charges and the flow of currents is determined by the fields $\vec{E}$ and $\vec{B}$ in addition, then the Maxwell equations Eq. (C.1) are called self-consistent. In this case $\mathcal{Q}$ and $\mathcal{J}$ can become differential operators depending on $\vec{E}$ and $\vec{B}$, too. This is usually true in the case of a plasma, where $\mathcal{Q}$ and $\mathcal{J}$ include properties like the shielding of charges and currents.

Nevertheless, as long as the the Maxwell equations remain linear equations, the time harmonic real vector wave is a solution of these equations and can be written in complex notation:

$$E_j(\vec{r}, t) := a_j(\vec{r}) e^{i(\omega t - g_j(\vec{r}))} \quad ; \quad a_j, g_j : \mathbb{R}^3 \mapsto \mathbb{R} \quad ; \quad j \in \{1, 2, 3\} \tag{C.2}$$
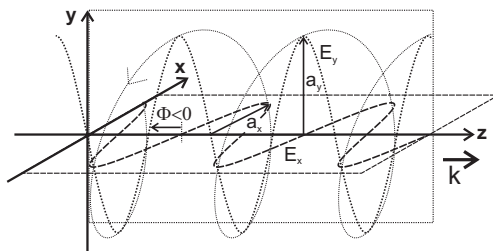

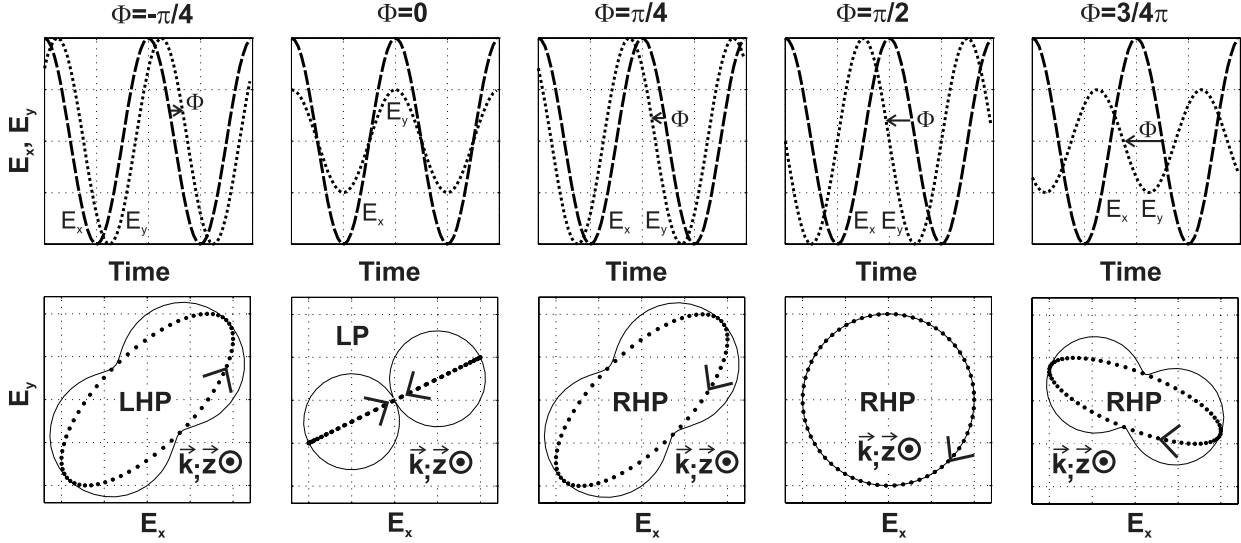Figure C.1: Sketch of a left handed electromagnetic wave propagating along the z-axis.

Figure C.2: Electric fields E_x (dashed line) and E_y (dotted line) for different sets of parameters a_x, a_y, Φ (see Eq. (C.3)) and their respective polarisation ellipses in the xy-plane. LHP denotes left handed polarisation, RHP right handed polarisation and LP linear polarisation. The arrows related to Φ denote the acceleration of E_y with respect to E_x. The thin continuous line is the square root of the angle dependent intensity behind a linear polariser.

Even more general solutions of Eq. (C.1) can be obtained by Fourier synthesis of different time harmonic vector waves. The local propagation direction of the wave's phase is given by the wave vector $\vec{k}(\vec{r})$. Furthermore it is important to note, that in anisotropic media the electric field vector $\vec{E}(\vec{r}, t)$ is in general no longer perpendicular to $\vec{k}(\vec{r})$. Anyhow its component in the k-direction is proportional to its component perpendicular to $\vec{k}(\vec{r})$, if the Maxwell equations stay linear. Thus one can introduce local Cartesian coordinates with the z-axis parallel to $\vec{k}(\vec{r})$ and fully represent the electric field $\vec{E}(\vec{r}, t)$ with its x- and y-component in this coordinate system. Then at a fixed point $\vec{r}_0$ in space a quasi band-limited electromagnetic wave (see Appendix B.2) is described by the two field components:

$$E_{x,r_0}(t) = a_x(t)\, e^{i\,(\omega(t)t + \Phi_x(t))} \tag{C.3a}$$

$$E_{y,r_0}(t) = a_y(t)\, e^{i\,(\omega(t)t + \Phi_y(t))} \tag{C.3b}$$

$a_x(t)$, $a_y(t)$, $\Phi_x(t)$, $\Phi_y(t)$ and $\omega(t)$ are real time-dependent functions. $a_x(t)$ and $a_y(t)$ are the amplitudes, $\Phi_x(t)$ and $\Phi_y(t)$ are the phases and $\omega(t)$ is called the angular frequency. The phase difference $\Phi(t) := \Phi_y(t) - \Phi_x(t)$ between the two waves is far more important than the absolute phases $\Phi_x(t)$ and $\Phi_y(t)$, because this difference mainly determines the polarisation properties.

For now assume $a_x(t)$, $a_y(t)$, $\Phi_x(t)$, $\Phi_y(t)$ and $\omega(t)$ to be constant, i.e. Eq. (C.3) is a strictly monochromatic wave. Such a wave is shown in Figure C.1. If one plots $E_{x,r_0}(t)$ and $E_{y,r_0}(t)$ for different sets of a_x, a_y and Φ in the xy-plane, then one obtains Figure C.2. The amplitudes a_x and a_y determine the smallest rectangle surrounding the polarisation ellipse (see Figure C.3), whilst the parameter Φ determines its precise shape: if Φ equals 0 or π, then the light is linear polarised and if Φ equals $\frac{-\pi}{2}$ or $\frac{\pi}{2}$, then it is
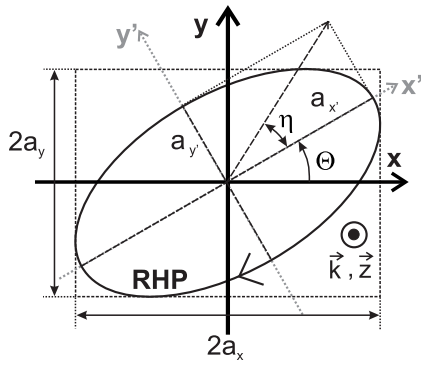
Figure C.3: The parameters η and Θ of an elliptically polarised wave. a_x, and a_y are the amplitudes of the wave along the x- and y-axis.
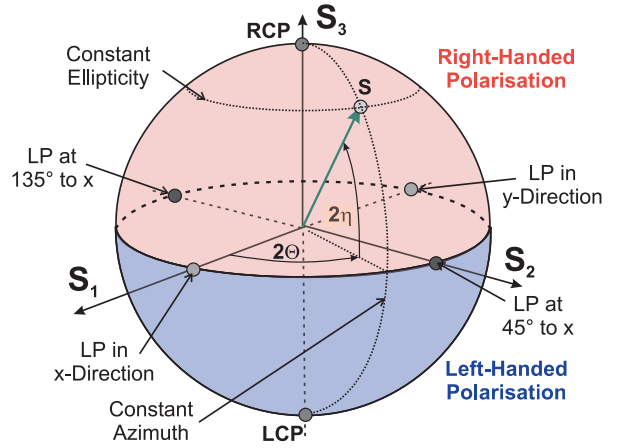
Figure C.4: The Poincaré Sphere: RCP denotes right circular polarised light and LCP left circular polarised light.

circular polarised. The sign of Φ determines the handiness of the electromagnetic wave. If the wave propagates out of the paper plane and Φ is positive, then its sense of rotation is clockwise and the wave has right handed polarisation (RHP). In other words: if Φ is negative, then the electric field vector's sense of rotation is counter-clockwise and the wave has left handed polarisation (LHP). If Φ is positive, then $\vec{E}_y$ is accelerated with respect to $\vec{E}_x$, otherwise it is retarded (see Figure C.1). Whilst $a_x(t)$ and $a_y(t)$ can be measured with a linear polariser (see Appendix D.3) quite easily, Φ is much more difficult to measure. For measuring all three quantities it is advantageous to introduce the Stokes parameters.

C.2   Stokes Parameters and Polarisation Measurements

C.2.1   The Reduced Set of Stokes Parameters and the Poincaré Sphere

From a geometrical point of view the polarisation state is characterised by the electric field vector's sense of rotation $\operatorname{sgn}\Phi$, by the polarisation ellipse's diameters of its major $2a_{x'}$ and minor $2a_{y'}$ principal axis and by the azimuth angle Θ (see Figure C.3). This angle is measured from the x-axis to the major principal axis of the ellipse, so that $\Theta \in [0°; 180°]$. Instead of using $\operatorname{sgn}\Phi$ and the diameters of the two principal axes, one can introduce an intensity I_0[§] and an ellipticity angle η:

$$I_0 := a_{x'}^2 + a_{y'}^2 \quad ; \quad I_0 \in [0; \infty] \tag{C.4a}$$

$$\tan\eta := \operatorname{sgn}\Phi \, \frac{a_{y'}}{a_{x'}} \quad ; \quad \eta \in [\text{-}45°; 45°] \tag{C.4b}$$

Consequently 2Θ and 2η can be regarded as the two tangential coordinates of a spherical coordinate system and the intensity I_0 as the radial coordinate. Thus the set $\{(I_0, 2\Theta, 2\eta)|, \Theta \in [0; \pi], \eta \in [-\frac{\pi}{4}; \frac{\pi}{4}]\}$ of spherical coordinates defines a sphere, called the Poincaré sphere (see Figure C.4): linear polarised states (LP) are located in the equatorial plane, whilst the right (RCP) and left (LCP) circular polarised states are located at the

[§]I_0 corresponds to $I_{E,pol}$ in Eq. (C.25)

north and south pole, respectively. Orbits on the Poincaré sphere with a constant lati-
tude represent polarisation states with a constant ellipticity, whilst orbits with a constant
longitude represent states with a constant azimuth angle.

The Cartesian representation of the spherical coordinate $(I_0, 2\eta, 2\Theta)$ is called the re-
duced set of Stokes parameters [24]:

$$\vec{S} = \begin{pmatrix} \bar{S}_1 \\ \bar{S}_2 \\ \bar{S}_3 \end{pmatrix} := I_0 \begin{pmatrix} \cos 2\eta \cos 2\Theta \\ \cos 2\eta \sin 2\Theta \\ \sin 2\eta \end{pmatrix} \overset{(\dagger)}{=} \begin{pmatrix} a_x^2 - a_y^2 \\ 2\,a_x\,a_y\,\cos\Phi \\ 2\,a_x\,a_y\,\sin\Phi \end{pmatrix} \overset{(\ddagger)}{=} \begin{pmatrix} E_x\,E_x^* - E_y\,E_y^* \\ E_x\,E_y^* + E_x^*\,E_y \\ i\,E_x^*\,E_y - i\,E_x\,E_y^* \end{pmatrix} \qquad (C.5)$$

It is quite tedious and technical to proof the equality $(\dagger)$. The details are given in [24]:
the starting point is to rotate the real part of Eq. (C.3) by an angle Θ and equate this
with the expression of an ellipse in the rotated coordinate system $O_{x'y'}$ from Figure C.3:

$$\begin{pmatrix} a_{x'}\cos(\omega t + \delta_0) \\ \pm a_{y'}\sin(\omega t + \delta_0) \end{pmatrix} = \begin{pmatrix} \cos(\Theta) & \sin(\Theta) \\ -\sin(\Theta) & \cos(\Theta) \end{pmatrix} \begin{pmatrix} a_x\cos(\omega t) \\ a_y\cos(\omega t + \Phi) \end{pmatrix}$$

where δ_0 is a constant phase. From this equation one can derive some auxiliary equations:

$$a_{x'}^2 + a_{y'}^2 = a_x^2 + a_y^2 \qquad\qquad \mp a_{x'}\,a_{y'} = a_x\,a_y\,\sin\Phi \qquad\qquad \tan 2\Theta = \frac{2\,a_x\,a_y}{a_x^2 - a_y^2}\cos\Phi$$
$$\text{(C.6a)} \qquad\qquad\qquad\qquad \text{(C.6b)} \qquad\qquad\qquad\qquad \text{(C.6c)}$$

With them and the trigonometric equation $\sin 2\eta = \frac{2\tan\eta}{1+\tan^2\eta}$ one finally proofs the equality
$(\dagger)$. The equality $(\ddagger)$ in Eq. (C.5) is derived directly from the definition of E_x and E_y in
Eq. (C.3).

Applying the definition Eq. (C.5), one can write down the reduced set of Stokes
parameters of the above mentioned states of linear and circular polarisation:

Reduced Set of Stokes Parameters of a Circular Polarised Electromagnetic Wave: In this case
the two principal axes are identical. Thus the angle Θ is of arbitrary size, whilst the
angle $\eta = \pm 45°$. Consequently:

$$\vec{S}_{\substack{RCP \\ LCP}} = \begin{pmatrix} \cos\frac{\pi}{2}\cos 2\Theta \\ \cos\frac{\pi}{2}\sin 2\Theta \\ \pm\sin\frac{\pi}{2} \end{pmatrix} = \begin{pmatrix} 0\,\cos 2\Theta \\ 0\,\sin 2\Theta \\ \pm 1 \end{pmatrix} = \begin{pmatrix} 0 \\ 0 \\ \pm 1 \end{pmatrix} \qquad (C.7)$$

Reduced Set of Stokes Parameters of a Linear Polarised Electromagnetic Wave: In this case
$\eta = 0°$ and Θ is fixed, defining the axis of polarisation. Thus one finds:

$$\vec{S}_\Theta = \begin{pmatrix} \cos 0 \cos 2\Theta \\ \cos 0 \sin 2\Theta \\ \sin 0 \end{pmatrix} = \begin{pmatrix} 1\,\cos 2\Theta \\ 1\,\sin 2\Theta \\ 0 \end{pmatrix} = \begin{pmatrix} \cos 2\Theta \\ \sin 2\Theta \\ 0 \end{pmatrix} \qquad (C.8)$$

C.2.2   Measuring the Reduced Set of Stokes Parameters

Deriving the Stokes parameters by directly measuring the fast vibrating electromagnetic
field proofs to be very difficult, as the response time of virtually all detectors is much
larger than the duration of this vibration. In contrast to that the averaged intensity

of the electromagnetic wave can be measured rather easy. In our case of laser plasma interactions with a lifetime of the plasma much shorter than the response time of the detector it is even more convenient to measure the pulse energy:

$$I_E := 2 \left\langle \Re\big(\vec{E}(t)\big) \cdot \Re\big(\vec{E}(t)\big) \right\rangle \stackrel{(\dagger)}{=} \left\langle \vec{E}(t) \cdot \vec{E}^*(t) \right\rangle = \int_{-\infty}^{\infty} \vec{E}(t) \cdot \vec{E}^*(t) \, dt \qquad (C.9)$$

where $\vec{E}(t)$ is the time-dependent complex half range signal of the electric field (see Appendix B.1.2). Note that the equality $(\dagger)$ only holds, if one can neglect the fast vibrating terms of $\Re\big(\vec{E}(t)\big) \cdot \Re\big(\vec{E}(t)\big)$. This is only possible, if the laser pulse comprises many oscillations, which is valid in our experiments.

For measuring the polarisation properties of light, one might be tempted to measure the polarisation ellipse directly, using a linear polariser set up at different angles α (see Appendix D.3). As can be seen from Figure C.2 the square root of this angle dependent energy does not correspond with the polarisation ellipse itself. Although one can determine the length and direction of the major and minor principal axis, it is impossible to determine the electric field vector's sense of rotation. To overcome this problem one has to introduce a phase retardation ϵ of e.g. the y-component in front of the polariser (see Appendix D.4). Then the measured energy of the electric field in the α-direction is given by [24]:

$$I_E(\alpha, \epsilon) = < E(t, \alpha, \epsilon) E^*(t, \alpha, \epsilon) > = < E_x(t) E_x^*(t) > \cos^2\alpha + < E_y(t) E_y^*(t) > \sin^2\alpha$$
$$+ \frac{\sin 2\alpha}{2} \left(< E_x(t) E_y^*(t) e^{-i\epsilon} > + < E_y(t) E_x^*(t) e^{i\epsilon} > \right) \qquad (C.10)$$

with $E(t, \alpha, \epsilon) := E_x(t) \cos\alpha + E_y(t) e^{i\epsilon} \sin\alpha$. Applying Eq. (C.10) one easily notes, that:

$$< E_x(t) E_x^*(t) > = I_E(\ 0°, 0) \qquad (C.11a)$$

$$< E_y(t) E_y^*(t) > = I_E(90°, 0) \qquad (C.11b)$$

$$< E_x(t) E_y^*(t) > = \tfrac{1}{2}\big(I_E(45°, 0) + I_E(135°, 0)\big) + \tfrac{i}{2}\big(I_E(45°, \pi/2) + I_E(135°, \pi/2)\big) \quad (C.11c)$$

$$< E_x^*(t) E_y(t) > = \tfrac{1}{2}\big(I_E(45°, 0) + I_E(135°, 0)\big) - \tfrac{i}{2}\big(I_E(45°, \pi/2) + I_E(135°, \pi/2)\big) \quad (C.11d)$$

Thus one can define measurable, averaged Stokes parameters in analogy to Eq. (C.5):

$$\vec{S}_{avg} := \begin{pmatrix} < E_x(t) E_x^*(t) > - < E_y(t) E_y^*(t) > \\ < E_x(t) E_y^*(t) > + < E_x^*(t) E_y(t) > \\ i < E_x^*(t) E_y(t) > -i < E_x(t) E_y^*(t) > \end{pmatrix} = \begin{pmatrix} < a_x(t)^2 > - < a_y(t)^2 > \\ 2 < a_x(t)\, a_y(t) \cos\Phi(t) > \\ 2 < a_x(t)\, a_y(t) \sin\Phi(t) > \end{pmatrix}$$
$$= \begin{pmatrix} I_E(\ 0°, 0) - I_E(\ 90°, 0) \\ I_E(45°, 0) + I_E(135°, 0) \\ I_E(45°, \pi/2) + I_E(135°, \pi/2) \end{pmatrix} \qquad (C.12)$$

If $a_x(t)$, $a_y(t)$ and $\Phi(t)$ from Eq. (C.3) are time-independent (this is true in particular, if $\vec{E}(t)$ is strictly monochromatic), then one can drop the averaging brackets and Eq. (C.12) is identical to Eq. (C.5). In the next paragraph we shall consider, what happens if

Eq. (C.12) is not strictly monochromatic.

C.2.3   The Four Stokes Parameters and the Polarisation of Light

To discuss the polarisation of light in the case of not strictly monochromatic light we extend the definition of Eq. (C.12) and introduce the full set of four Stokes parameters:

$$\vec{S} := \begin{pmatrix} S_0 \\ S_1 \\ S_2 \\ S_3 \end{pmatrix} = \begin{pmatrix} \langle E_x E_x^* \rangle + \langle E_y E_y^* \rangle \\ \langle E_x E_x^* \rangle - \langle E_y E_y^* \rangle \\ \langle E_x E_y^* \rangle + \langle E_x E_y^* \rangle^* \\ -i \left(\langle E_x E_y^* \rangle - \langle E_x E_y^* \rangle^* \right) \end{pmatrix} = \begin{pmatrix} \langle a_x^2 \rangle + \langle a_y^2 \rangle \\ \langle a_x^2 \rangle - \langle a_y^2 \rangle \\ 2 \langle a_x a_y \cos \Phi \rangle \\ 2 \langle a_x a_y \sin \Phi \rangle \end{pmatrix} \tag{C.13}$$

It is worth to note that S_0 is exactly the definition of the pulse energy from Eq. (C.9). A mathematically more advanced definition of the four Stokes parameters uses the Pauli spin matrices σ_i [99]:

$$S_j := \left\langle \vec{E}^T \sigma_j \vec{E}^* \right\rangle \quad ; \quad j \in \{0, 1, 2, 3\} \tag{C.14}$$

where $\vec{E}$ is limited to the x- and y-component of the electric field and $\vec{E}^T$ is the transposition of $\vec{E}$. The Pauli spin matrices σ_j are:

$$\sigma_0 = \begin{pmatrix} 1 & 0 \\ 0 & 1 \end{pmatrix} \quad \sigma_1 = \begin{pmatrix} 1 & 0 \\ 0 & -1 \end{pmatrix} \quad \sigma_2 = \begin{pmatrix} 0 & 1 \\ 1 & 0 \end{pmatrix} \quad \sigma_3 = \begin{pmatrix} 0 & i \\ -i & 0 \end{pmatrix} \tag{C.15}$$

As the Pauli spin matrices are a basis of $\mathbb{C}^2 \mapsto \mathbb{C}^2$, they can be used to represent the 2×2 propagation matrix of an electromagnetic wave in terms of Stokes parameters. Furthermore they are particularly useful for theoretical considerations.

A very important property of the Stokes parameters is a superposition theorem for N independent light waves $\vec{E}_1$, ..., $\vec{E}_N$ propagating in the same direction:

$$S_{ges,j} = \left\langle \vec{E}_{ges}^T \sigma_j \vec{E}_{ges}^* \right\rangle = \left\langle \left(\sum_{n=1}^N \vec{E}_n^T \right) \sigma_j \left(\sum_{m=1}^N \vec{E}_m^* \right) \right\rangle = \left\langle \sum_{n,m}^{[1;N]} \left(\vec{E}_n^T \sigma_j \vec{E}_m^* \right) \right\rangle$$

$$= \sum_{n=1}^N \left\langle \vec{E}_n^T \sigma_j \vec{E}_n^* \right\rangle + \sum_{n \neq m}^{[1;N]} \left\langle \vec{E}_n^T \sigma_j \vec{E}_m^* \right\rangle \overset{(\dagger)}{=} \sum_{n=1}^N S_{j,n} \tag{C.16}$$

with $j \in \{0, 1, 2, 3\}$. The equality $(\dagger)$ holds, because $< \vec{E}_n^T \sigma_j \vec{E}_m^* > = 0$ for independent fields $\vec{E}_n$ and $\vec{E}_m$, $n \neq m$. In particular harmonic waves

$$\vec{E}_{\omega_{\{m,n\}}}(t) := \vec{a}\left(\omega_{\{m,n\}}\right) e^{i \omega_{\{m,n\}} t} \quad ; \quad \vec{a}\left(\omega_{\{m,n\}}\right) : \mathbb{R} \to \mathbb{C}^2 \tag{C.17}$$

with $\omega_m \neq \omega_n$ are independent. Hence it is obvious how to extend the theorem Eq. (C.16) to an infinite number of harmonic waves:

$$S_{ges,j} = \left\langle \iint_{-\infty}^{\infty} \vec{a}^T\left(\omega_m\right) \sigma_j a^*\left(\omega_n\right) e^{i(\omega_m - \omega_n)t} \, d\omega_m \, d\omega_n \right\rangle = \int_{-\infty}^{\infty} S(\omega) \, d\omega \tag{C.18}$$
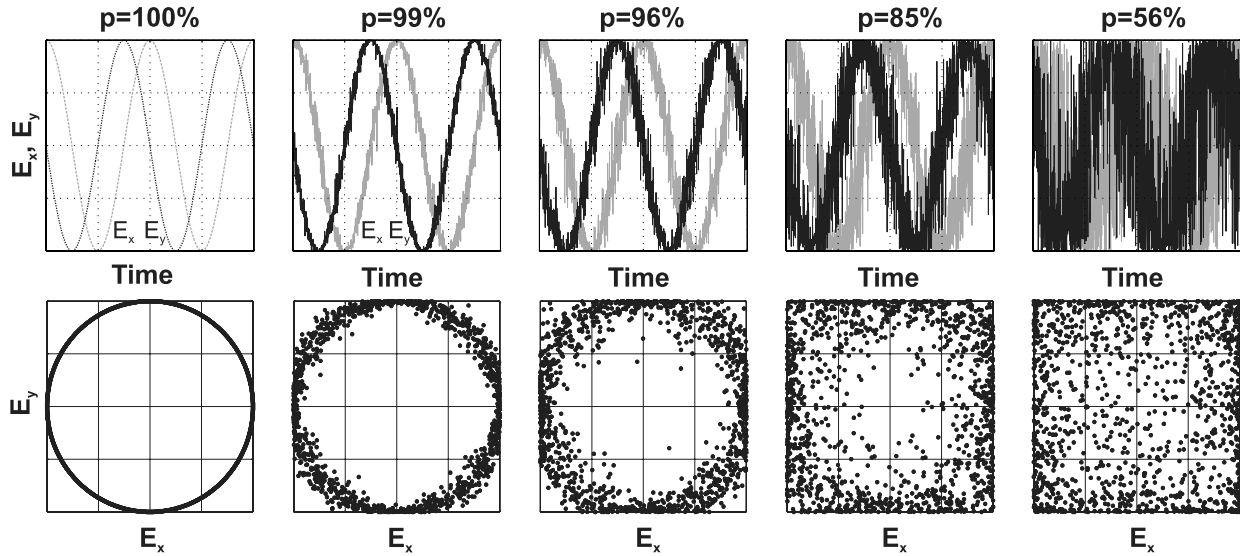
Figure C.5: The electric field (bright line: E_x, dark line: E_y) and its distribution in the xy-plane in the case of partially polarised light. It is clearly seen that with decreasing polarisation the original polarisation ellipse becomes more blurred.

Completely Unpolarised Light: Now we shall consider light for which the energy $I_E(\alpha, \epsilon)$ from Eq. (C.9) is constant for all α and ϵ. This requires that:

$$< E_x E_x^* > - < E_y E_y^*(t) > \qquad = < a_x^2 > - < a_y^2 > = 0$$
$$\wedge \; < E_x E_y^* > \qquad = < (a_x b_x) e^{-i\Phi} > = 0 \qquad \text{(C.19a)}$$

Using Eq. (C.13) and Eq. (C.9) one can show that this is equivalent to:

$$\vec{S}_{unpol}^T := (I_{E,unpol}, 0, 0, 0) \qquad \text{(C.19b)}$$

and to

$$S_1^2 + S_2^2 + S_3^2 = 0 \qquad \text{(C.19c)}$$

Light which holds any equality of Eq. (C.19) is called *completely unpolarised* light. This kind of light is commonly encountered in nature.

Completely Polarised Light: If the Stokes parameters hold:

$$\vec{S}_0 = \sqrt{S_1^2 + S_2^2 + S_3^2} \qquad \text{(C.20)}$$

then the light is called *completely polarised* and one can write:

$$\vec{S}_{pol}^T := \left(\sqrt{S_1^2 + S_2^2 + S_3^2}, S_1, S_2, S_3 \right) \qquad \text{(C.21)}$$

In this case S_0 is determined by the other three Stokes parameters, so that the reduced set of Stokes parameters already describes this kind of light completely. An example of polarised light is the radiation emitted from most lasers.

Partially Polarised Light: Light is called *partially polarised*, if

$$0 < \sqrt{S_1^2 + S_2^2 + S_3^2} < S_0 \qquad \text{(C.22)}$$

By using Eq. (C.16) it is obvious, that an arbitrary polarisation state $\vec{S}_{arb}$ can be represented by a unique decomposition into a polarised $\vec{S}_{pol}$ and an unpolarised $\vec{S}_{unpol}$ part. Thus any set of Stokes parameters can be written as:

$$\vec{S}_{arb} = \vec{S}_{pol} + \vec{S}_{unpol} = \begin{pmatrix} \sqrt{S_1^2 + S_2^2 + S_3^2} \\ S_1 \\ S_2 \\ S_3 \end{pmatrix} + \begin{pmatrix} I_{E,unpol} \\ 0 \\ 0 \\ 0 \end{pmatrix} \qquad \text{(C.23)}$$

Then the degree of polarisation is given by [24]:

$$P = \frac{I_{E,pol}}{I_{E,arb}} = \frac{\sqrt{S_1^2 + S_2^2 + S_3^2}^{\,\S}}{S_0} \qquad \text{(C.24)}$$

with

$$I_{E,arb} = I_{E,pol} + I_{E,unpol} \qquad \text{(C.25)}$$

In Figure C.5 it is shown, that the tip of the electric field vector does not describe a polarisation ellipse for partially polarised light. But one observes a probability distribution of the electric field vector in the E_x-E_y-plane. The width of this distribution increases with a decreasing degree of polarisation until the vectors are scattered over the whole plane in the case of unpolarised light. Hence the Stokes parameters can completely represent the state of polarisation.

---

§ $I_{E,pol}$ corresponds to I_0 in Eq. (C.4).

Appendix D
Müller Matrices of Optical Components

D.1 Definition of the Müller matrix and the Coherency Vector

If $\vec{S} \in \mathbb{R}^4$ are the Stokes parameters of an initial polarisation state and this state propagates through a polarisation altering system, then one obtains a final state $\vec{S}' \in \mathbb{R}^4$. Hence the transition from $\vec{S}$ to $\vec{S}'$ can be represented by a matrix $\mathsf{M} \in \mathbb{R}^4 \times \mathbb{R}^4$. This matrix is called the Müller matrix:

$$\vec{S}' := \mathsf{M}\,\vec{S} \quad ; \quad \vec{S}, \vec{S}' \in \mathbb{R}^4 \quad ; \quad \mathsf{M} \in \mathbb{R}^4 \times \mathbb{R}^4 \tag{D.1}$$

Calculating the Müller matrix of an optical system directly can be difficult, as the relationship between the optical properties of the system and the Stokes parameters is often more complicate than the relationship between the electric field and the optical properties. This difficulty can be overcome by introducing the coherency vector $\vec{\Gamma}$, which is easily calculated from the electric field vector $\vec{E}$:

$$\vec{\Gamma} := \begin{pmatrix} < E_x\, E_x^* > \\ < E_y\, E_y^* > \\ < E_x\, E_y^* > \\ < E_x^*\, E_y > \end{pmatrix} \tag{D.2}$$

With this vector one can write in analogy to Eq. (D.1):

$$\vec{\Gamma}' = \mathsf{M}_\Gamma \vec{\Gamma} \quad ; \quad \vec{\Gamma}, \vec{\Gamma}' \in \mathbb{R}^4 \quad ; \quad \mathsf{M}_\Gamma \in \mathbb{R}^4 \times \mathbb{R}^4 \tag{D.3}$$

with the coherency vector $\vec{\Gamma}$ in front and $\vec{\Gamma}'$ behind the optical system.

Luckily it is very simple to calculate the coherency vector $\vec{\Gamma}$ from the Stokes parameters $\vec{S}$ and vice versa:

$$\vec{\Gamma} = \mathsf{M}_c\,\vec{S} \tag{D.4}$$

with a transfer matrix M_c and its inverse M_c^{-1}:

$$\mathsf{M}_c = \frac{1}{2}\begin{pmatrix} 1 & 1 & 0 & 0 \\ 1 & -1 & 0 & 0 \\ 0 & 0 & 1 & i \\ 0 & 0 & 1 & -i \end{pmatrix} \quad \text{(D.5a)} \qquad \mathsf{M}_c^{-1} = \begin{pmatrix} 1 & 1 & 0 & 0 \\ 1 & -1 & 0 & 0 \\ 0 & 0 & 1 & 1 \\ 0 & 0 & -i & i \end{pmatrix} \quad \text{(D.5b)}$$

D.2 Rotation Matrix for the Stokes Parameters

Let $\vec{S}$ be the Stokes parameters in a coordinate system O_{xy} and let $\vec{S}'$ be the parameters of the same polarisation state in a coordinate system $O_{x'y'}$ rotated by an angle α with
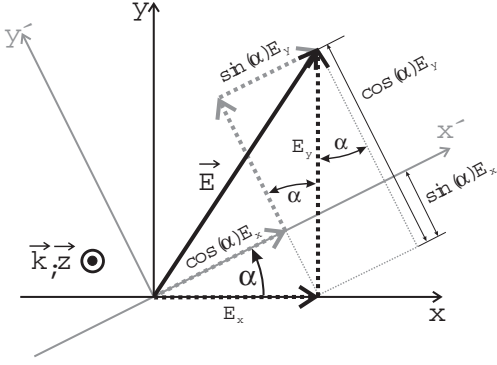
Figure D.1: Sketch of the coordinate systems O_{xy} and $O_{x'y'}$. The later is rotated by an angle α relative to the former.

respect to O_{xy} around the z-axis (see Figure D.1), then the Müller matrix $\mathsf{M}_{rot}(\alpha)$ transforming $\vec{S}$ into $\vec{S}'$ is:

$$\mathsf{M}_{rot}(\alpha) = \begin{pmatrix} 1 & 0 & 0 & 0 \\ 0 & \cos 2\alpha & \sin 2\alpha & 0 \\ 0 & -\sin 2\alpha & \cos 2\alpha & 0 \\ 0 & 0 & 0 & 1 \end{pmatrix} \qquad \mathsf{M}_{rot}^{-1}(\alpha) = \begin{pmatrix} 1 & 0 & 0 & 0 \\ 0 & \cos 2\alpha & -\sin 2\alpha & 0 \\ 0 & \sin 2\alpha & \cos 2\alpha & 0 \\ 0 & 0 & 0 & 1 \end{pmatrix}$$

$$\text{(D.6a)} \qquad\qquad\qquad\qquad\qquad\qquad\qquad\qquad \text{(D.6b)}$$

This is shown easily by calculating the coherency vector $\vec{\Gamma}'$ (see Eq. (D.2)) from the rotation-matrix of the electric field:

$$\begin{pmatrix} E_x' \\ E_y' \end{pmatrix} = \begin{pmatrix} \cos\alpha & \sin\alpha \\ -\sin\alpha & \cos\alpha \end{pmatrix} \begin{pmatrix} E_x \\ E_y \end{pmatrix} \tag{D.7}$$

With the addition theorems one immediately finds the rotation matrix $\mathsf{M}_{\Gamma_{rot}}(\alpha)$ of the coherency vector, i.e. $\Gamma' = \mathsf{M}_{\Gamma_{rot}}(\alpha)\Gamma$. Using Eq. (D.5) it is straight forward to calculate $\mathsf{M}_{rot}(\alpha) := \mathsf{M}_C^{-1}\mathsf{M}_\Gamma(\alpha)\mathsf{M}_C$.

D.3 Non-Ideal Linear Polarisers

Polarising axis set to $\alpha{=}0°$: If an electromagnetic wave propagates through a non-ideal linear polariser with its polarising axis (i.e. the direction of its highest transmission) parallel to the x-axis, then let $a \in [0,1]$ be its transmissivity parallel to the x-axis and let $b \in [0,1]$ be the transmissivity along the y-axis. Thus the electric fields in front ($\vec{E}$) and behind ($\vec{E}'$) the polariser are associated by the following equation:

$$\begin{pmatrix} E_x' \\ E_y' \end{pmatrix} = \begin{pmatrix} a & 0 \\ 0 & b \end{pmatrix} \begin{pmatrix} E_x \\ E_y \end{pmatrix} \quad ; \quad a, b \in [0,1] \tag{D.8}$$

With Eq. (D.8) it is simple to calculate the coherency vector $\Gamma' = \mathsf{M}_{\Gamma_{a,b}}(0°)\Gamma$ (see Eq. (D.2)). By using Eq. (D.5) it is straight forward again to calculate the respective Müller matrix:

$$\mathsf{M}_{a,b}(0°) = \begin{pmatrix} \frac{a^2+b^2}{2} & \frac{a^2-b^2}{2} & 0 & 0 \\ \frac{a^2-b^2}{2} & \frac{a^2+b^2}{2} & 0 & 0 \\ 0 & 0 & ab & 0 \\ 0 & 0 & 0 & ab \end{pmatrix} \qquad \mathsf{M}_{a,b}^{-1}(0°) = \frac{1}{(ab)^2} \begin{pmatrix} \frac{a^2+b^2}{2} & -\frac{a^2-b^2}{2} & 0 & 0 \\ -\frac{a^2-b^2}{2} & \frac{a^2+b^2}{2} & 0 & 0 \\ 0 & 0 & ab & 0 \\ 0 & 0 & 0 & ab \end{pmatrix}$$

$$\text{(D.9a)} \qquad\qquad\qquad\qquad\qquad\qquad\qquad\qquad\qquad \text{(D.9b)}$$

In the case of an ideal linear polariser with its polarising axis parallel to the x-axis the E_y-component of the electromagnetic wave is blocked completely (i.e. $b = 0$), whilst the E_x-component is transmitted entirely (i.e. $a = 1$).

If the spectrum of the electromagnetic wave is so wide, that a and b depend on the wavelength ω, then due to Eq. (C.16) the Stokes parameters behind the polariser are given by:

$$\vec{S}' \overset{\text{Eq. (C.18)}}{=} \int_{-\infty}^{\infty} \vec{S}'(\omega) \ d\omega = \int_{-\infty}^{\infty} M_{a(\omega),b(\omega)}(\alpha) \ \vec{S}(\omega) \ d\omega \tag{D.10}$$

Polarising axis set to an arbitrary angle α: If α is the angle from the x-axis to the polarising axis of the linear polariser, then the Müller matrix can be derived from Eq. (D.9) with the help of the rotation matrices from Eq. (D.6):

$$M_{a,b}(\alpha) = M_{\text{rot}}(-\alpha) M_{a,b}(0°) M_{\text{rot}}(\alpha)$$

$$= \begin{pmatrix} A & B\cos 2\alpha & B\sin 2\alpha & 0 \\ B\cos 2\alpha & A\cos^2 2\alpha + C\sin^2 2\alpha & D\sin 2\alpha \cos 2\alpha & 0 \\ B\sin 2\alpha & D\sin 2\alpha \cos 2\alpha & A\sin^2 2\alpha + C\cos^2 2\alpha & 0 \\ 0 & 0 & 0 & C \end{pmatrix} \tag{D.11a}$$

$$M_{a,b}^{-1}(\alpha) = M_{\text{rot}}(-\alpha) M_{a,b}^{-1}(0°) M_{\text{rot}}(\alpha)$$

$$= \frac{1}{C^2} \begin{pmatrix} A & -B\cos 2\alpha & -B\sin 2\alpha & 0 \\ -B\cos 2\alpha & A\cos^2 2\alpha + C\sin^2 2\alpha & D\sin 2\alpha \cos 2\alpha & 0 \\ -B\sin 2\alpha & D\sin 2\alpha \cos 2\alpha & A\sin^2 2\alpha + C\cos^2 2\alpha & 0 \\ 0 & 0 & 0 & C \end{pmatrix} \tag{D.11b}$$

with

$$A := \frac{a^2 + b^2}{2} \qquad B := \frac{a^2 - b^2}{2} \qquad C := ab \qquad D := \frac{(a - b)^2}{2} \qquad a > b \in [0, 1]$$

In addition to Eq. (D.9) there are three other cases, which can be important for building a polarimeter. These cases are derived from Eq. (D.11a):

Polarising axis set to α=45°:   With Eq. (D.11a) and α=45° one calculates the Müller matrix:

$$M_{a,b}(45°) = \begin{pmatrix} \frac{a^2+b^2}{2} & 0 & \frac{a^2-b^2}{2} & 0 \\ 0 & ab & 0 & 0 \\ \frac{a^2-b^2}{2} & 0 & \frac{a^2+b^2}{2} & 0 \\ 0 & 0 & 0 & ab \end{pmatrix} \tag{D.12}$$

Polarising axis set to $\alpha=90°$:   With Eq. (D.11a) and $\alpha=90°$ one calculates the Müller matrix:

$$\mathbf{M}_{a,b}(90°) = \begin{pmatrix} \frac{a^2+b^2}{2} & -\frac{a^2-b^2}{2} & 0 & 0 \\ -\frac{a^2-b^2}{2} & \frac{a^2+b^2}{2} & 0 & 0 \\ 0 & 0 & ab & 0 \\ 0 & 0 & 0 & ab \end{pmatrix} \tag{D.13}$$

Polarising axis set to $\alpha=135°$:   With Eq. (D.11a) and $\alpha=135°$ one calculates the Müller matrix:

$$\mathbf{M}_{a,b}(135°) = \begin{pmatrix} \frac{a^2+b^2}{2} & 0 & -\frac{a^2-b^2}{2} & 0 \\ 0 & ab & 0 & 0 \\ -\frac{a^2-b^2}{2} & 0 & \frac{a^2+b^2}{2} & 0 \\ 0 & 0 & 0 & ab \end{pmatrix} \tag{D.14}$$

D.4   Phase Shifting Devices with a Linear Anisotropy

Generally, phase shifting devices with a linear anisotropy have a prominent direction called the principal or optical axis. An arbitrarily polarised electromagnetic wave propagating through such a device is split into two characteristic waves: an *ordinary* one with its electric field *perpendicular* to the optical axis and an *extraordinary* one with its electric field vector *parallel* to the optical axis. As these two characteristic waves propagate with different phase velocities, they acquire a phase shift against each other, so that an incident linear polarised electromagnetic wave can become elliptically polarised (see Figure C.2), as its electric field vector splits into components parallel and perpendicular to the optical axis. In general these elements (commonly called wave plates) are thin discs of uniaxial crystals with their optical axis parallel to the surface of the plate. They are called zero order wave plates, if the acquired phase shift is in $[\pi, \pi]$.

D.4.1   Wave Plates with an Arbitrary Linear Phase Shift

Principal axis set to $\alpha=0°$:   Consider a wave plate with its optical axis parallel to the x-axis and an electromagnetic quasi monochromatic (i.e. spectral width $\Delta\omega \ll \omega$) wave propagating through the plate (i.e. along the z-axis). Furthermore assume that the phase of the wave's E_x-component is accelerated by Φ with respect to the E_y-component. Then the electric fields in front ($\vec{E}$) and behind ($\vec{E}'$) the wave plate are associated by the following equation:

$$\begin{pmatrix} E'_x \\ E'_y \end{pmatrix} = \begin{pmatrix} e^{i\Phi} & 0 \\ 0 & 1 \end{pmatrix} \begin{pmatrix} E_x \\ E_y \end{pmatrix} \quad ; \quad \Phi \in \mathbb{R} \tag{D.15}$$

Using Eq. (D.15) it is easy to calculate the coherency vector $\Gamma' = \mathbf{M}_{\Gamma_\Phi}(0°)\Gamma$ (see Eq. (D.2)). Then with Eq. (D.5) it is straight forward to calculate the respective Müller matrix:

$$\mathbf{M}_\Phi(0°) = \begin{pmatrix} 1 & 0 & 0 & 0 \\ 0 & 1 & 0 & 0 \\ 0 & 0 & \cos\Phi & -\sin\Phi \\ 0 & 0 & \sin\Phi & \cos\Phi \end{pmatrix} \tag{D.16}$$

If the wave is not quasi monochromatic, then the Stokes parameters behind the wave-plate are derived by using Eq. (C.16):

$$\vec{S}' \overset{\text{Eq. (C.18)}}{=} \int_{-\infty}^{\infty} \vec{S}'(\omega)\ d\omega = \int_{-\infty}^{\infty} \mathbf{M}_{\Phi(\omega)}(\alpha)\ \vec{S}(\omega)\ d\omega \tag{D.17}$$

Principal axis set to an arbitrary angle α: If α is the angle from the x-axis to the principal axis of the wave plate, then the Müller matrix can be derived from Eq. (D.16) with the help of the rotation matrices from Eq. (D.6):

$$\mathbf{M}_\Phi(\alpha) = \mathbf{M}_{\mathrm{rot}}(-\alpha)\mathbf{M}_\Phi(0°)\mathbf{M}_{\mathrm{rot}}(\alpha)$$

$$= \begin{pmatrix} 1 & 0 & 0 & 0 \\ 0 & \cos^2 2\alpha + \sin^2 2\alpha\cos\Phi & \sin 2\alpha\cos 2\alpha(1-\cos\Phi) & \sin 2\alpha\sin\Phi \\ 0 & \sin 2\alpha\cos 2\alpha(1-\cos\Phi) & \sin^2 2\alpha + \cos^2 2\alpha\cos\Phi & -\cos 2\alpha\sin\Phi \\ 0 & -\sin 2\alpha\sin\Phi & \cos 2\alpha\sin\Phi & \cos\Phi \end{pmatrix} \tag{D.18}$$

After deriving the general Müller matrix of a wave plate with an arbitrary phase shift Φ we discuss two special cases: the $\lambda/2$-wave plate and the $\lambda/4$-wave plate.

D.4.2 Half Wave Plates

The half wave plate introduces an additional phase shift of $\Phi = \pm\pi$ between E_x- and E_y-component. Again the angle from the x-axis to the principal axis of the wave plate is α. With Eq. (D.18) one calculates its Müller matrix:

$$\mathbf{M}_\pi(\alpha) = \begin{pmatrix} 1 & 0 & 0 & 0 \\ 0 & \cos 4\alpha & \sin 4\alpha & 0 \\ 0 & \sin 4\alpha & -\cos 4\alpha & 0 \\ 0 & 0 & 0 & -1 \end{pmatrix} \tag{D.19}$$

If the Stokes parameters $\vec{S}$ propagate through a half wave plate, then the resulting set of Stokes parameters $\vec{S}'$ is given by:

$$\vec{S}' := \mathbf{M}_\pi(\alpha)\vec{S} = \mathbf{M}_\pi(\alpha)I_0 \begin{pmatrix} 1 \\ \cos 2\eta\cos 2\Theta \\ \cos 2\eta\sin 2\Theta \\ \sin 2\eta \end{pmatrix} = I_0 \begin{pmatrix} 1 \\ \cos 2(-\eta)\cos 2(2\alpha-\Theta) \\ \cos 2(-\eta)\sin 2(2\alpha-\Theta) \\ \sin 2(-\eta) \end{pmatrix} \tag{D.20}$$

whereby two addition theorems have been used. Consequently for $\vec{S} \to \vec{S}'$:

$$\eta \to -\eta \qquad\qquad\qquad (D.21a)$$

$$\Theta \to -\Theta + 2\alpha \qquad\qquad\qquad (D.21b)$$

holds. In other words: if left circular polarised light (LCP) propagates through a half wave plate, then it becomes right circular polarised (RCP) and the other way round, independently of the angle α. On the other hand, if linear polarised light propagates through the wave plate, then it remains linear polarised, but its polarisation plane is rotated to $-\Theta + 2\alpha$.

D.4.3   Quarter Wave Plates

The quarter wave plate introduces an additional phase shift of $\Phi = \pm\pi/2$ between the E_x- and E_y-component. Again α is the angle from the x-axis to the principal axis of the wave plate.

Principal axis set to an arbitrary angle α: One easily calculates its Müller matrix, using Eq. (D.18):

$$M_{\pm\pi/2}(\alpha) = \begin{pmatrix} 1 & 0 & 0 & 0 \\ 0 & \cos^2 2\alpha & \sin 2\alpha \cos 2\alpha & \pm\sin 2\alpha \\ 0 & \sin 2\alpha \cos 2\alpha & \sin^2 2\alpha & \mp\cos 2\alpha \\ 0 & \mp\sin 2\alpha & \pm\cos 2\alpha & 0 \end{pmatrix} \qquad (D.22)$$

Principal axis set to α=0°:   With Eq. (D.22) and α=0° one calculates the Müller matrix:

$$M_{\pm\pi/2}(0°) = \begin{pmatrix} 1 & 0 & 0 & 0 \\ 0 & 1 & 0 & 0 \\ 0 & 0 & 0 & \mp 1 \\ 0 & 0 & \pm 1 & 0 \end{pmatrix} \qquad (D.23)$$

Principal axis set to α=45°:   With Eq. (D.22) and α=45° one calculates the Müller matrix:

$$M_{\pm\pi/2}(45°) = \begin{pmatrix} 1 & 0 & 0 & 0 \\ 0 & 0 & 0 & \pm 1 \\ 0 & 0 & 1 & 0 \\ 0 & \mp 1 & 0 & 0 \end{pmatrix} \qquad (D.24)$$

Principal axis set to α=90°:   With Eq. (D.22) and α=90° one calculates the Müller matrix:

$$M_{\pm\pi/2}(90°) = \begin{pmatrix} 1 & 0 & 0 & 0 \\ 0 & 1 & 0 & 0 \\ 0 & 0 & 0 & \pm 1 \\ 0 & 0 & \mp 1 & 0 \end{pmatrix} \qquad (D.25)$$

D.5 Phase Shifting Devices with a Circular Anisotropy

Phase shifting devices with a circular anisotropy are similar to phase shifting devices with a linear anisotropy. The only difference is that the two characteristic waves propagating with different velocities are not linear polarised any more, but left and right circular polarised. If E_{LCP} is a left circular polarised wave and E_{RCP} is a right circular polarised one, then

$$\begin{pmatrix} E'_{RCP} \\ E'_{LCP} \end{pmatrix} = k \begin{pmatrix} e^{i\Phi} & 0 \\ 0 & 1 \end{pmatrix} \begin{pmatrix} E_{RCP} \\ E_{LCP} \end{pmatrix} \quad ; \quad \Phi \in \mathbb{R} \tag{D.26}$$

holds (compare Eq. (D.15)). With the coordinate transformation:

$$\begin{pmatrix} E_x \\ E_y \end{pmatrix} = \underbrace{\begin{pmatrix} 1 & 1 \\ -i & i \end{pmatrix}}_{=:\ \mathbf{A}} \begin{pmatrix} E_{RCP} \\ E_{LCP} \end{pmatrix} \tag{D.27}$$

$$=: \mathbf{A} \tag{D.28}$$

one calculates:

$$\begin{pmatrix} E'_x \\ E'_y \end{pmatrix} = \mathbf{A}\,\mathbf{M}\,\mathbf{A}^{-1}\,\vec{E} = \frac{1}{2} \begin{pmatrix} e^{i\Phi} + 1 & i\left(e^{i\Phi} - 1\right) \\ -i\left(e^{i\Phi} - 1\right) & e^{i\Phi} + 1 \end{pmatrix} \begin{pmatrix} E_x \\ E_y \end{pmatrix} \tag{D.29}$$

Using Eq. (D.29) one derives the coherency vector $\Gamma' = \mathbf{M}_{\Gamma_{circ},\Phi}\,\Gamma$ (see Eq. (D.2)). Then with Eq. (D.5) it is straight forward to calculate the Müller matrix:

$$\mathbf{M}_{circ,\Phi} = \begin{pmatrix} 1 & 0 & 0 & 0 \\ 0 & \cos\Phi & -\sin\Phi & 0 \\ 0 & \sin\Phi & \cos\Phi & 0 \\ 0 & 0 & 0 & 1 \end{pmatrix} \tag{D.30}$$

If again the wave is not quasi monochromatic, then the Stokes parameters behind the wave-plate are given by:

$$\vec{S}' \overset{\text{Eq. (C.18)}}{=} \int_{-\infty}^{\infty} \vec{S}'(\omega)\ d\omega = \int_{-\infty}^{\infty} \mathbf{M}_{circ,\Phi(\omega)}\,\vec{S}(\omega)\ d\omega \tag{D.31}$$

Appendix E

Electromagnetic Waves in Magnetised Laser Produced Plasmas

There exists a huge variety of different wave phenomena in plasmas [29, 85, 161]. But for the recent experiment, measuring the azimuthal magnetic field in a laser produced plasma, mainly electromagnetic waves propagating through a magnetised plasma are important. To gain a quantitative understanding of how the magnetic field interacts with the electromagnetic wave, the first subsection of this Appendix gives a short introduction into the relevant theoretical plasma model. This model is used to derive the dielectric tensor and the wave equation, that describes the propagation of an electromagnetic wave through the magnetised plasma. A schematic overview of the whole derivation is shown in Figure 3.5 on page 40.

E.1 Basic Plasma Equations

To study the properties of a plasma one can start either with a microscopic or a macroscopic plasma model. Whilst in general the microscopic quantities are more difficult to measure than the macroscopic ones, from a theoretical point of view the microscopic model is the more fundamental one, as the macroscopic models can be derived from the former. Nevertheless, if it comes down to solve the resultant differential equations, approximations are necessary, sometimes reducing the microscopic model to a pure macroscopic one, as in our case. Starting with the microscopic description is still advantageous as this allows introducing more accurate approximations, if necessary.

In classical mechanics a many-particle system is fully described by the locations $\vec{x}_{\alpha_i}(t)$ and the velocities $\vec{v}_{\alpha_i}(t)$ of all particles α_i, where α is the particle species and i the particle number. Thus a microscopic system is completely specified by a set of equations called the particle position equations [85]:

$$N_\alpha(\vec{x}, \vec{v}, t) := \sum_{1 \leq i \leq \bar{N}_\alpha} \delta(\vec{x} - \vec{x}_{\alpha_i}(t))\, \delta(\vec{v} - \vec{v}_{\alpha_i}(t)) \equiv \sum_{1 \leq i \leq \bar{N}_\alpha} \delta(\vec{X} - \vec{X}_{\alpha_i}(t)) \qquad \text{(E.1)}$$

where the point-like particles are represented by the δ-distribution (see Eq. (A.26)). $\vec{X} := (\vec{x}, \vec{v})$ and $\bar{N}_\alpha$ is the total amount of particles from species α, i.e. the integral of Eq. (E.1) over the whole phase space. Note that $N_\alpha(\vec{x}, \vec{v}, t)$ implicitly depends on $\vec{X}_\alpha := (\vec{X}_{\alpha_1}, ..., \vec{X}_{\alpha_{\bar{N}_\alpha}})$. Combining Eq. (E.1) with the non-relativistic equation of motion of a single particle leads to an equation for the time development of the system, called the Klimontovich-Dupree equation [82]:

$$\frac{\partial N_\alpha(\vec{x}, \vec{v}, t)}{\partial t} + \vec{v} \cdot \frac{\partial N_\alpha(\vec{x}, \vec{v}, t)}{\partial \vec{x}} + \frac{q_\alpha}{m_\alpha} \left(\vec{E}^M + v \times \vec{B}^M \right)' \cdot \frac{\partial N_\alpha(\vec{x}, \vec{v}, t)}{\partial \vec{v}} = 0 \qquad \text{(E.2)}$$

with the charge q_α and the mass m_α of particle species α and the microscopic electric and magnetic field $\vec{E}^M$ and $\vec{B}^M$, respectively. The prime indicates that the fields due to the ith particle are omitted for calculating the forces pushing around this particle. Alternatively one can describe the system with the Liouville equation and the Hamilton function, which is more general from a theoretical point of view [153]. In any case the Maxwell equations are needed in addition to calculate the electric and magnetic field self-consistently. $\vec{E}^{ext}$ and $\vec{B}^{ext}$ represents the external electric and magnetic field:

$$\nabla \cdot \vec{E}^M = \frac{1}{\epsilon_0} \sum_\alpha q_\alpha \int N_\alpha(\vec{x}, \vec{v}, t) \, d\vec{v} + \nabla \cdot \vec{E}^{ext} \qquad (E.3a)$$

$$\nabla \times \vec{B}^M = \frac{1}{c_0^2} \frac{\partial}{\partial t} \vec{E}^M + \mu_0 \sum_\alpha q_\alpha \int \vec{v} \, N_\alpha(\vec{x}, \vec{v}, t) \, d\vec{v} + \nabla \times \vec{B}^{ext} \qquad (E.3b)$$

There are so many particles in a plasma that these seemingly simple equations are far too complicate for any practical purpose already. To simplify them one introduces the many-particle distribution function F_N, so that $F_N(\vec{X}_\alpha, \vec{X}_\beta, ..., t) \, d\vec{X}_\alpha \cdot d\vec{X}_\beta \cdots$ is the probability that at time t all particles have values around $\vec{X}_\alpha, \vec{X}_\beta, ...$ in the range of $d\vec{X}_\alpha, d\vec{X}_\beta, ...$ [85]. The function F_N can easily be reduced to the n-particle distribution function $f^{(n)}$ by integrating over all but n-variables. With an arbitrary function G, implicitly depending on $(\vec{X}_\alpha, \vec{X}_\beta, ...)$, and the definition

$$\left\langle G_{(\vec{X}_\alpha, \vec{X}_\beta, ...)}(\vec{x}, \vec{v}, t) \right\rangle := \int F_N(\vec{X}_\alpha, \vec{X}_\beta, ...) \, N_{(\vec{X}_\alpha, \vec{X}_\beta, ...)}(\vec{x}, \vec{v}, t) \, d\vec{X}_\alpha \cdot d\vec{X}_\beta \cdots \qquad (E.4)$$

it is simple to show, that $\langle N_\alpha(\vec{x}, \vec{v}, t) \rangle = \bar{n}_\alpha f_\alpha^{(1)}(\vec{x}, \vec{v}, t)$ holds. $\bar{n}_\alpha := \frac{N_\alpha}{V}$ is the average density of particle species α and V is the Volume of the system. Averaging Eq. (E.2) to Eq. (E.3b) with Eq. (E.4) gives:

$$\frac{\partial f_\alpha^{(1)}(\vec{x}, \vec{v}, t)}{\partial t} + \vec{v} \cdot \frac{\partial f_\alpha^{(1)}(\vec{x}, \vec{v}, t)}{\partial \vec{x}} + \frac{q_\alpha}{\bar{n}_\alpha m_\alpha} \left\langle \left(\vec{E}^M + \vec{v} \times \vec{B}^M \right)' \cdot \frac{\partial N_\alpha(\vec{x}, \vec{v}, t)}{\partial \vec{v}} \right\rangle = 0 \quad (E.5)$$

$$\nabla \cdot \vec{E} = \frac{1}{\epsilon_0} \sum_\alpha q_\alpha \bar{n}_\alpha \int f_\alpha^{(1)}(\vec{x}, \vec{v}, t) \, d\vec{v} + \nabla \cdot \vec{E}^{ext} \overset{Eq. (E.8)}{=} \frac{1}{\epsilon_0} \sum_\alpha q_\alpha n_\alpha + \nabla \cdot \vec{E}^{ext} \qquad (E.6a)$$

$$\nabla \times \vec{B} = \frac{1}{c_0^2} \frac{\partial}{\partial t} \vec{E} + \mu_0 \sum_\alpha q_\alpha \bar{n}_\alpha \int \vec{v} \, f_\alpha^{(1)}(\vec{x}, \vec{v}, t) \, d\vec{v} + \nabla \times \vec{B}^{ext}$$

$$\overset{Eq. (E.8)}{\underset{Eq. (E.9)}{=}} \nabla \cdot \frac{1}{c_0^2} \frac{\partial}{\partial t} \vec{E} + \mu_0 \sum_\alpha q_\alpha n_\alpha \vec{V}_\alpha + \nabla \times \vec{B}^{ext} \qquad (E.6b)$$

The triangular brackets in Eq. (E.5) can be expanded into a series of equations consisting of n-particle distribution functions $f^{(1)}, f^{(2)}, f^{(3)}, ...$ etc. Using the Mayer expansion [66, 106] $f^{(n)}$ can be written as a linear combination of products of one-particle distribution functions with additional cross-correlation terms $g^{(n)}$. The resultant scheme of hierarchical equations is called the BBGKY-hierarchy, as this was discovered by Bogolyubov

[20, 42], Born and Green [23], Kirkwood [79–81] and Yvon [190] independently. This infinite set of equations can be closed only by making a reasonable assumption for the higher order cross-correlation functions. In the most simple case one even neglects binary collisions (i.e. $g^{(n)} = 0$; $\forall\, n \geq 2$) obtaining the Vlasov equations. If $g^{(2)}$ is not zero, but all higher order cross-correlations are zero, one obtains the Landau approximation [153]. If interactions with three particles are partially included, then the approximation is called the Balescou-Lenard equation. For our purpose the Landau equation is sufficient. Using Eq. (E.5) one calculates:

$$\frac{\partial f_\alpha^{(1)}}{\partial t} + \vec{v} \cdot \frac{\partial f_\alpha^{(1)}}{\partial \vec{x}} + \frac{q_\alpha}{m_\alpha} \left(\vec{E} + \vec{v} \times \vec{B} \right) \cdot \frac{\partial f_\alpha^{(1)}}{\partial \vec{v}} = \left.\frac{\partial f_\alpha^{(1)}}{\partial t}\right|_C \tag{E.7}$$

where $\left.\frac{\partial f_\alpha^{(1)}}{\partial t}\right|_C$ is a symbolic expression representing the temporal change of $f_\alpha^{(1)}$ due to fast fluctuating microscopic inter-particle forces like collisions.

From Eq. (E.7) one can derive a pure macroscopic description of the plasma. But beforehand a few more definitions are needed:

The density of the particle species α is given by:

$$n_\alpha(\vec{x}, t) := \int \bar{n}_\alpha f_\alpha(\vec{x}, \vec{v}, t) \ d\vec{v} \,, \tag{E.8}$$

their average velocity is:

$$\vec{V}_\alpha(\vec{x}, t) := \frac{\bar{n}_\alpha}{n_\alpha(\vec{x}, t)} \int \vec{v}\, f_\alpha(\vec{x}, \vec{v}, t) \ d\vec{v} \,, \tag{E.9}$$

and the pressure tensor is:

$$\mathbf{P}_{\alpha,(i,j)}(\vec{x}, t) := \bar{n}_\alpha m_\alpha \int (\vec{v} - \vec{V}_\alpha)_{(i)} (\vec{v} - \vec{V}_\alpha)_{(j)}\, f_\alpha(\vec{x}, \vec{v}, t) \ d\vec{v} \tag{E.10}$$

By integrating Eq. (E.7) over the velocity space one obtains the continuity equation [85]:

$$\frac{\partial}{\partial t} n_\alpha + \nabla \cdot \left(n_\alpha \vec{V}_\alpha \right) = 0 \tag{E.11}$$

After multiplying Eq. (E.7) with the momentum $m_\alpha \vec{v}$, again integrating over the velocity space and applying Eq. (E.11), one obtains the momentum transfer equation [85]:

$$n_\alpha m_\alpha \left(\frac{\partial}{\partial t} + \vec{V}_\alpha \cdot \nabla \right) \vec{V}_\alpha - n_\alpha q_\alpha \left(\vec{E} + \vec{V}_\alpha \times \vec{B} \right) + \nabla \cdot \mathbf{P}_\alpha$$

$$= \bar{n}_\alpha m_\alpha \int \vec{v} \ \left.\frac{\partial f_\alpha}{\partial t}\right|_C \ d\vec{v} \approx n_\alpha m_\alpha \sum_\beta (\vec{V}_\beta - \vec{V}_\alpha) \langle \nu_{\alpha\beta} \rangle \tag{E.12}$$

with the mean collision frequency $\langle \nu_{\alpha\beta} \rangle$.

Our macroscopic description of the plasma is known as the fluid model and is made up of the continuity equation Eq. (E.11) and the momentum transfer equation Eq. (E.12) supplemented by the averaged Maxwell equations, in particular Eq. (E.6a) and Eq. (E.6b). Its macroscopic variables are the pressure, the density and the mean velocity of each species. Strictly speaking, in a fluid-plasma the electrons and each ionisation stage are

independent fluids. As we are interested in averaged quantities only and the ion mass is not much dependent on the ionisation stage, one can assume a single kind of ions with an averaged degree of ionisation, thus reducing the whole system to a two fluid system made up of electrons and one ion species, coupled through collision and Maxwell equations.

E.2   Small Amplitude Waves in a Magnetised Plasma

The fluid equations (Eq. (E.11), Eq. (E.12), Eq. (E.6a), Eq. (E.6b)) are still too complicate to be solved. Luckily, our focus is not on the plasma itself, but on an electromagnetic wave propagating through the plasma. Hence let the quantities $\vec{E}_0$, $\vec{B}_0$, $\vec{V}_{\alpha,0}$ and $n_{\alpha,0}$ be the solutions of the fluid equations in an unperturbed plasma. Then an electromagnetic small amplitude wave propagating through the plasma perturbs the above mentioned quantities only slightly, so that one can write:

$$y_{pert} = y_0 + y_1 \, e^{i\vec{k}\cdot\vec{x}} \, e^{-i\omega t} \tag{E.13}$$

where the index one marks the small perturbations and the index zero the unperturbed quantities. y can be any of the following quantities $n_\alpha, \vec{V}_\alpha, \vec{E}, \vec{B}$. Substituting these expressions into the fluid equations and neglecting second and higher order terms, e.g. $n_{\alpha,1}$, $\vec{V}_{\alpha,1}$, etc., simplifies the equations considerably. With the so called cold plasma assumption their complexity is reduced even more. This assumption requires, that

$$\sqrt{\frac{kT_e}{m_e}} \ll \frac{\omega}{k_\omega} \tag{E.14}$$

with the wave vector k_ω of the electromagnetic wave. This is particularly valid during the early phase of a laser produced plasma, because its thermal temperature is only a few electron volts in the beginning as briefly discussed in Subsection 2.2.2.

Consequently, $P_\alpha \approx 0$, $\left.\frac{\partial f_\alpha^{(1)}}{\partial t}\right|_C \approx 0$ and $\vec{V}_{\alpha,0} \approx 0$ hold. Note that $\vec{V}_{\alpha,0}$ is an averaged quantity, so that the oscillation of the electrons due to the laser pulse is averaged out. Furthermore Krall [85] mentions, that $P \approx 0\,\mathrm{Pa}$ is a particular good assumption, if strong magnetic fields are present. With these simplifications it is straight forward to calculate:
Continuity equation:

$$-i\omega n_{\alpha,1} + n_{\alpha,0}\,\vec{k}\cdot\vec{V}_{\alpha,1} = 0 \tag{E.15}$$

Momentum transfer equation:

$$-i\omega\vec{V}_{\alpha,1} = \frac{q_\alpha}{m_\alpha}\left(\vec{E}_1 + \vec{V}_{\alpha,1}\times\vec{B}_0\right) \tag{E.16}$$

Maxwell equations:

$$\vec{k}\times\vec{B}_1 = -\frac{\omega}{c_0^2}\vec{E}_1 - i\mu_0\sum_\alpha q_\alpha n_{\alpha,0}\,\vec{V}_{\alpha,1} \tag{E.17a}$$

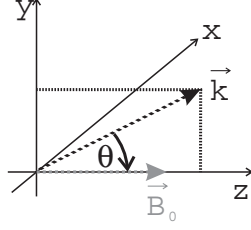$$\vec{k}\times\vec{E}_1 = \omega\,\vec{B}_1 \tag{E.17b}$$

Figure E.1: Direction of the magnetic field and of the electromagnetic wave propagating through the plasma.

Eq. (E.16) is a linear equation in $\vec{V}_{\alpha,1}$ and $\vec{E}_1$. Hence it can be written as:

$$q_\alpha n_\alpha \vec{V}_{\alpha,1} = \sigma_\alpha(\vec{B}_0)\, \vec{E}_1 \tag{E.18}$$

where $\sigma_\alpha(\vec{B}_0)$ is the conductivity tensor of the particle species α. Now it is simple to derive the wave equation from Eq. (E.17a) and Eq. (E.17b):

$$\vec{k} \times \vec{k} \times \vec{E}_1 = -\frac{\omega^2}{c_0^2}\left(1 + \frac{i}{\omega\epsilon_0}\sum_\alpha \sigma_\alpha(\vec{B}_0)\right)\vec{E}_1 = -\frac{\omega^2}{c_0^2}\epsilon_r(\vec{B}_0)\,\vec{E}_1 \tag{E.19}$$

This equation can be rewritten:

$$\left(\{\vec{k},\vec{k}\} - |\vec{k}|^2\mathbf{1} + \frac{\omega^2}{c_0^2}\epsilon_r(\vec{B}_0)\right)\cdot\vec{E}_1 = 0 \tag{E.20}$$

where $\mathbf{1}$ is the unit dyadic and $\{\vec{k},\vec{k}\}\vec{E}_1 := \vec{k}\,(\vec{k}\cdot\vec{E}_1)$.

By solving the linear equation Eq. (E.16) for $\vec{V}_{\alpha,1}$ and then substituting this result into Eq. (E.18), one obtains an equation which is again substituted into Eq. (E.19), leading to the equation of the dielectric tensor $\epsilon_r(\vec{B}_0)$. The straightforward but lengthy calculation is simplified much by assuming that $\vec{B}_0$ is parallel to the z-axis and that $\vec{k}$ lies in the yz-plane. Hence $\theta := \angle(\vec{B}_0, \vec{k})$ is the angle between the z-axis and the propagation direction $\vec{k}$ of the electromagnetic wave (see Figure E.1). Thus the dielectric tensor $\epsilon_r(\vec{B}_0)$ is given by:

$$\epsilon_r(\vec{B}_0) := \begin{pmatrix} \epsilon_1 & -i\epsilon_2 & 0 \\ +i\epsilon_2 & \epsilon_1 & 0 \\ 0 & 0 & \epsilon_3 \end{pmatrix} \tag{E.21}$$

In the case of a two fluid plasma, i.e. ions of the same species with an average ionisation and free electrons, one derives:

$$\epsilon_1 = 1 - \frac{\omega_{pe}^2}{\omega^2 - \omega_{ce}^2} - \frac{\omega_{pi}^2}{\omega^2 - \omega_{ci}^2} \qquad \approx 1 - \frac{\omega_{pe}^2}{\omega^2 - \omega_{ce}^2} \tag{E.22a}$$

$$\epsilon_2 = \frac{\omega_{ce}}{\omega}\frac{\omega_{pe}^2}{\omega^2 - \omega_{ce}^2} - \frac{\omega_{ci}}{\omega}\frac{\omega_{pi}^2}{\omega^2 - \omega_{ci}^2} \qquad \approx \frac{\omega_{ce}}{\omega}\frac{\omega_{pe}^2}{\omega^2 - \omega_{ce}^2} \tag{E.22b}$$

$$\epsilon_3 = 1 - \frac{\omega_{pe}^2}{\omega^2} - \frac{\omega_{pi}^2}{\omega^2} \qquad \approx 1 - \frac{\omega_{pe}^2}{\omega^2} \tag{E.22c}$$

where the cyclotron frequency of the electrons and ions is given by $\omega_{ce} := \frac{q_e}{m_e}|\vec{B}_0|$ and $\omega_{ci} := \frac{q_i}{m_i}|\vec{B}_0|$, respectively. In a similar manner the plasma frequency of the electrons and ions is given by $\omega_{pe} := \sqrt{\frac{q_e^2 n_e}{\epsilon_0 m_e}}$ and $\omega_{pi} := \sqrt{\frac{q_i^2 n_i}{\epsilon_0 m_i}}$, respectively. In many cases the middle part of Eq. (E.22) can be simplified by neglecting the influence of the ions,

resulting in the righthand side of Eq. (E.22). This is particularly true for magnetic fields below 3 GG and laser harmonics with a wavelength below 360 nm. Thus in the actual experiment the ions do not influence the interaction between the magnetic field and the harmonic radiation significantly. Hence, using the coordinate system from Figure E.1, Eq. (E.21) and the index of refraction $n := c_0 \frac{|\vec{k}|}{\omega}$, the wave equation Eq. (E.20) can be written as:

$$
\mathbf{A}\,\vec{E}_1 := \begin{pmatrix} n^2 - \epsilon_1 & i\epsilon_2 & 0 \\ -i\epsilon_2 & n^2\cos^2\theta - \epsilon_1 & -n^2\sin\theta\cos\theta \\ 0 & -n^2\sin\theta\cos\theta & n^2\sin^2\theta - \epsilon_3 \end{pmatrix} \begin{pmatrix} E_{1x} \\ E_{1y} \\ E_{1z} \end{pmatrix} = 0 \qquad (E.23)
$$

This matrix solution is represented by case B in Figure 3.5. Case A represents a far more general approach, in which Eq. (E.13) is replaced with

$$
y_{\text{pert}} = y_0 + y_1(\vec{x}, t) \qquad (E.24)
$$

to derive the wave equation. The huge drawback of this approach is that all calculations become more difficult. Finally, after a coordinate transformation to a system with its z-axis parallel to the propagation direction of the electromagnetic wave, the three component vector $\vec{E}$ can be reduced to the two components perpendicular to the z-direction. Then one can expand the remaining 2×2 differential matrix equation in terms of Pauli spin matrices. Applying the definition of the Stokes parameters by Pauli spin matrices (see Eq. (C.15)) one calculates the differential propagation equation in terms of Stokes parameters. This differential equation even describes dissipative propagation [87, 88]. If one can neglect damping, then this equation is reduced to:

$$
\frac{d\vec{S}}{dz} = \vec{\Omega}(z) \times \vec{S} \qquad (E.25)
$$

where $\vec{S}$ is a reduced set of Stokes parameters (see Eq. (C.5)). A closer look at Eq. (E.25) shows, that this differential equation describes an infinitesimal rotation around $\vec{\Omega}(z)$. Consequently one can visualise the solutions of Eq. (E.25) as circles on a Poincaré sphere (see Figure C.4). A more detailed discussion beyond the scope of this work is given in [10, 87, 88, 146].

Bibliography

[1] Acton Research. Vacuum monochromators. Homepage, 2004. URL http://www.acton-research.com.

[2] G. Agrawal. *Nonlinear Fiber Optics*. Academic Press, Inc., Boston, 1989.

[3] H. Ahlstrom. Laser fusion experiments, facilities and diagnostics at lawrence livermore national laboratory. *Appl. Opt.*, 20(11):1902(24), 1981.

[4] S. A.I. and W. Woyczyn'ski. *Distributions in the Physical and Engineering Sciences*. Birkhäuser, Boston, 1997.

[5] M. Ammosov, N. Delone, and V. Krainov. Tunnel ionization of complex atoms and of atomic ions in an alternating electromagnetic field. *Sov. Phys. – JETP*, 64(6):1191(4), 1986.

[6] Andor. CCD Cameras. Homepage, 2004. URL http://www.andor-tech.com.

[7] S. Augst, D. Strickland, D. Meyerhofer, S. Chin, and J. Eberly. Tunneling ionization of noble gases in a high-intensity laser field. *Phys. Rev. Lett.*, 63(20):2212(4), 1989.

[8] S. Augst, D. Meyerhofer, D. Strickland, and C. S.L. Laser ionization of noble gases by coulomb-barrier suppression. *J. Opt. Soc. Am. B*, 8(4):858(10), 1991.

[9] D. Auston and S. C.V. Picosecond ellipsometry of transient electron-hole pairs in germanium. *Phys. Rev. Lett.*, 32(20):1120(4), 1974.

[10] R. Azzam and B. N.M. *Ellipsometry and Polarized Light*. Elsevier, Amsterdam, 3rd edition, 1996.

[11] S. Backus, J. Peatross, M. Murnane, and H. Kapteyn. Ti:sapphire amplifier producing millijoule-level, 21 fs pulses at 1 kHz. *Opt. Lett.*, 20(19):2000(3), 1995.

[12] S. Backus, C. Dufee III, M. Murnane, and H. Kapteyn. High power ultrafast lasers. *Rev. Sci. Instr.*, 69(3):1207(17), 1998.

[13] P. Balcou, R. Haroutunian, S. Sebban, G. Grillon, A. Rousse, G. Mullot, J. Chamaret, G. Rey, A. Antonetti, D. Hulin, L. Roos, D. Descamps, M. Gaarde, A. L'Huillier, E. Constant, E. Mevel, V. der Linde D., A. Orisch, A. Tarasevitch, U. Teubner, D. Klöpfel, and W. Theobald. High-order-harmonic generation: towards laser-induced phase-matching control and relativistic effects. *Appl. Phys. B*, 74(6):509(7), 2002.

[14] J. Barth, R. Johnson, and M. Cardona. Spectroscopic ellipsometry in the 6–35 ev region. In E. Palik, editor, *Handbook of Optical Constants of Solids*, volume 2, chapter 10, page 213(34). Academic Press, Boston, 2 edition, 1998.

[15] E. Bedrosian. A product theorem for Hilbert transforms. *Proc. IEEE*, 51:868(2), 1963.

[16] F. Beg, A. Bell, A. Dangor, C. Danson, A. Fews, A. Glinsky, B. Hammel, P. Lee, P. Norreys, and M. Tatarakis. A study of picosecond laser-solid interactions up to 10^{19} W/cm^2. *Phys. Plas.*, 4(2):447(11), 1997.

[17] C. Birdsall and A. Langdon. *Plasma Physics via Computer Simulation*. The Adam Hilger Series on Plasma Physics. Adam Hilger, Bristol, Philadelphia, New York, 1991.

[18] A. Bishop. *Project Sherwood*. Addison-Wesley, Reading (Mass.), 1958.

[19] P. Blanc, P. Audbert, F. Fallies, J. Geindre, J. Gauthier, A. Dos Santos, A. Mysyrowicz, and A. Antonetti. Phase dynamics of reflected probe pulses from sub-100-fs laser-produced plasmas. *J. Opt. Soc. Am. B*, 13(1):118(7), 1996.

[20] N. Bogolyubov. *Problems of a Dynamical Theory in Statistical Physics*. State Technical Press, Moscow, 1946.

[21] M. Borghesi, A. MacKinnon, A. Bell, R. Gaillard, and O. Willi. Megagauss magnetic field generation and plasma jet formation on solid targets irradiated by an ultraintense picosecond laser pulse. *Phys. Rev. Lett.*, 81(1):112(4), 1998.

[22] M. Borghesi, A. MacKinnon, R. Gaillard, O. Willi, A. Pukhov, and J. Meyer-ter Vehn. Large quasistatic magnetic fields generated by relativistically intense laser pulse propagating in preionized plasma. *Phys. Rev. Lett.*, 80(23):5137(4), 1998.

[23] M. Born and H. Green. *A General Kinetic Theory of Liquids*. Cambridge University Press, Cambridge, London, 1949.

[24] M. Born and E. Wolf. *Principles of Optics*. Cambridge University Press, Cambridge, 7th (expanded) edition, 1999.

[25] R. Boyd. *Nonlinear Optics*. Academic Press, Amsterdam, 2nd edition, 2003.

[26] I. N. Bronstein and K. A. Semendjajew. *Taschenbuch der Mathematik*. Harry Thun, 5th edition, 2001.

[27] F. Brunel. Anomalous absorption of high intensity subpicosecond laser pulses. *Phys. Fluids*, 31(9):2714(6), 1988.

[28] S. Bulanov and N. Naumova. Interaction of an ultrashort, relativistically strong laser pulse with an overdense plasma. *Phys. Plas.*, 1(3):745(13), 1994.

[29] F. Chen. *Introduction to Plasma Physics and Controlled Fusion*, volume 1. Plenum Press, New York, London, 2nd edition, 1984.

[30] T. Claasen and W. Mecklenbrauker. The Wigner distribution — A tool for time frequency analysis; part III. *Philips J. Research*, 35(6):372(18), 1980.

[31] CLF – RAL. The Astra-Gemini Project. Homepage, 2004. URL http://www.clf.rl.ac.uk/Facilities/AstraWeb/AstraGeminiHome.htm.

[32] L. Cohen. Generalized phase-space distribution functions. *J Math. Phys.*, 7(5):781(5), 1966.

[33] L. Cohen. Time-frequency distributions – a review. *Proc. IEEE*, 77(7):941(41), 1989.

[34] Continuum. Minilight. Data Sheet, 2004. URL http://www.continuumlasers.com/resminilite.html.

[35] R. Craxton, R. McCrory, and J. Soures. Progress in laser fusion. *Sci. Am.*, 255(2):60(12), 1986.

[36] W. Crookes. On the illumination of lines of molecular pressure and the trajectory of molecules. *Phil. Mag.*, 5:135ff, 1879.

[37] C. Danson, L. Barzanti, A. Damerell, C. Edwards, S. Hancock, M. Hutchinson, M. Key, S. Luan, R. Mahadeo, I. Mercer, P. Norreys, D. Pepler, D. Rodkiss, I. Ross, M. Smith, R. Smith, P. Taday, W. Toner, K. Wigmore, T. Winstone, R. Wyatt, and F. Zhou. High contrast multi-terawatt pulse generation using chirped pulse amplification on the VULCAN laser facility. *Opt. Comm.*, 103(5,6):392(6), 1993.

[38] C. Danson, J. Collier, D. Neely, L. Barzanti, A. Damerell, C. Edwards, M. Hutchinson, M. Key, P. Norreys, D. Pepler, I. Ross, P. Taday, W. Toner, F. Trentelman, F. Walsh, T. Winstone, and W. R.W.W. Well characterised 10^{19} W/cm^2 operation of vulcan — an ultra-high power nd:glass laser. *J. Mod. Optics*, 45(8):1653(17), 1998.

[39] C. Danson, R. Allott, G. Booth, J. Collier, C. Edwards, P. Flintoff, S. Hawkes, M. Hutchinson, C. Hernandez-Gomez, J. Leach, D. Neely, P. Norreys, M. Notley, D. Pepler, I. Ross, J. Walczak, and T. Winstone. Generation of focused intensities of $5 \cdot 10^{19}$ W/cm^2. *Laser and Particle Beams*, 17(2):341(7), 1999.

[40] C. David, T. Weitkamp, B. Nohammer, and J. van der Veen. Diffractive and refractive x-ray optics for microanalysis applications. *Spect. Chim. Acta B*, 59(10–11):1505(6), 2004.

[41] J. Davies, A. Bell, and M. Tatarakis. Magnetic focusing and trapping of high-intensity laser-generated fast electrons at the rear of solid target. *Phys. Rev. E*, 59(5):6032(5), 1999.

[42] J. deBoer and G. Uhlenbeck, editors. *Studies in Statistical Mechanics*, volume 1, chapter Problems of a Dynamical Theory in Statistical Physics. North-Holland Publishing Co., Amsterdam, 1962.

[43] J. Diels and W. Rudolph. *Ultrashort Laser Pulse Phenomena*. Academic, San Diego (CA), 1996.

[44] K. Eidmann. Radiation transport and atomic physics modeling in high-energy-density laser-produced plasmas. *Laser-and-Particle-Beams*, 12(2):223(22), 1994.

[45] K. Eidmann, J. Meyer-ter Vehn, T. Schlegel, and S. Hüller. Hydrodynamic simulation of subpicosecond laser interaction with solid-density matter. *Phys. Rev. E*, 62(1):1202(13), 2000.

[46] F. Faisal and A. Becker. Double and multiple ionization of noble gas atoms in intense laser fields. *Comments At. Mol. Phys.*, 1(1):15(12), 1999.

[47] T. Feurer, A. Morak, I. Uschmann, C. Ziener, H. Schwoerer, C. Reich, P. Gibbon, E. Förster, and R. Sauerbrey. Femtosecond silicon K-α pulses from laser-produced plasmas. *Phys. Rev. E*, 65(1):016412(4), 2002.

[48] D. C. for Reflection Polarizers and A. in the vacuum ultraviolet. Hunter, w.r. *Appl. Opt.*, 17(8):1259(12), 1978.

[49] O. Forster. *Analysis 3 – Integralrechnung im $\mathbb{R}^n$ mit Anwendungen*. Vieweg, Braunschweig, 3rd edition, 1999.

[50] R. Freeman and P. Bucksbaum. Investigation of above-threshold ionization using subpicosecond laser pulses – topical review. *J. Phys. B: At. Mol. Opt. Phys.*, 24(2):325(23), 1991.

[51] E. Förster, K. Gäbel, and I. Uschmann. X-ray microscopy of laser-produced plasmas with the use of bent crystals. *Laser-and-Particle-Beams*, 9(1):135(14), 1991.

[52] D. Gabor. Theory of communication. *J. IEE: Radio and communication engineering*, 93,3:429(29), 1946.

[53] C. Gahn, G. Pretzler, A. Saemann, G. Tsakiris, K. Witte, D. Gassmann, T. Schatz, U. Schramm, P. Thirolf, and D. Habs. MeV gamma-ray yield from solid targets irradiated with fs-laser pulses. *Appl. Phys. Lett.*, 73(25):3662(4), 1998.

[54] K. G'al and S. Varr'o. Polarization properties of high harmonics generated on solid surfaces. *Opt. Comm.*, 198(4-6):419(13), 2001.

[55] M. Gavrila, editor. *Atoms in Intense Laser Fields*. Academic, Boston (MA), 1992.

[56] I. Gel'fand and G. E. Shilov. *Properties and Operations*, volume 1 of *Generalized Functions*. Academic Press, New York, 2nd edition, 1966.

[57] P. Gibbon. Efficient production of fast electrons from femtosecond laser interaction with solid targets. *Phys. Rev. Lett*, 73(5):664(4), 1994.

[58] P. Gibbon. *Short Pulse Laser Interactions With Matter: An Introduction*. Imperial College Press, London, 2004.

[59] P. Gibbon and E. Förster. Short-pulse laser-plasma interactions. *Plasma Physics and Controlled Fusion*, 38(6):769(25), 1996.

[60] D. Giulietti, L. Gizzi, A. Giulietti, A. Macchi, D. Teychenne, P. Chessa, A. Rousse, G. Cheriaux, J. Chambaret, and G. Darpentigny. Observation of solid-density laminar plasma transparency to intense 30 fs laser pulses. *Phys. Rev. Lett.*, 79(17), 1997.

[61] D. Gold, H. Nathel, P. Bolton, W. White, and L. Van-Woerkom. Prepulse suppression using a self-induced, ultrashort pulse plasma mirror. In H. Baldis, editor, *Short-Pulse*

High-Intensity Lasers and Applications, volume 1413 of *Proc. SPIE*, page 41(12). IEEE, 1991.

[62] A. Gopal. *Measurements of ultrastrong magnetic fields in laser produced plasmas*. PhD thesis, Imperial College, London (United Kingdom), 2004.

[63] A. Gopal, M. Tatarakis, A. Dangor, K. Krushelnick, and K. Cassou. Mapping of self-generated magnetic fields using harmonic polarimetry. In B. Wyborn, editor, *Central Laser Facility, Annual Report 2002/2003*, page 61(2). Library and Information Services, CCLRC, 2003.

[64] D. Gordon, W. Mori, and T. a. Antonsen. A ponderomotive guiding center particle-in-cell code for efficient modeling of laser-plasma interactions. *IEEE Trans. Plas. Sci.*, 28(4): 1224(9), 2000.

[65] K. Gröchenig. *Foundations of Time-Frequency Analysis*, chapter 10, page 203(12). Birkhäuser, Boston, Basel, Berlin, 2001.

[66] H. Green. Statistical thermodynamics of plasmas. *Nuclear Fusion*, 1(2):69(9), 1961.

[67] M. Gryzinski. Classical theory of atomic collisions. i. theory of inelastic collisions. *Phys. Rev.*, 138(2A):A336(23), 1965.

[68] M. Haines. Saturation mechanisms for the generated magnetic field in nonuniform laser-matter irradiation. *Phys. Rev. Lett.*, 78(2):254(4), 1997.

[69] *Silicon Photodiodes, Series S1336*. Hamamatsu, 2004. URL http://www.hpk.co.jp/eng/products/ssd/pdf/s1336_series_kspd1022e03.pdf.

[70] R. Hemker. *Particle-in-cell modeling of plasma-based accelerators in two and three dimensions*. PhD thesis, UCLA, 2000.

[71] M. Hooper and P. Osborne, editors. *Laser Plasma Interactions 5: Inertial Confinement Fusion*, volume 45 of *SUSSP Proceedings*, Edingburgh, Bristol, 1995. SUSSP and IOP Publishing.

[72] S. Huard. *Polarisation of Light*. J. Wiley and Sons, Chichester, 1997.

[73] T. Hughes. *Plasma and Laser Light*. Adam Hilger Ltd, Bristol, 1975.

[74] I. Hutchinson. *Principles of Plasma Diagnostics*. Cambridge University Press, Cambridge, 2nd edition, 2002.

[75] J. Jackson. *Classical Electrodynamics*. Wiley, New York, 3rd edition, 1999.

[76] JET. Joint european torus. Homepage, 2004. URL http://www.jet.efda.org.

[77] H. Kapteyn, M. Murnane, A. Szoke, and R. Falcone. Prepulse energy suppression for high-energy ultrashort pulses using self-induced plasma shuttering. *Opt. Lett.*, 16(7):490(3), 1991.

[78] L. Keldysh. Ionisation in the field of a strong electromagnetic wave. *Sov. Phys. – JETP*, 20(5):1307, 1965.

[79] J. Kirkwood. The statistical mechanical theory of transport processe I. General theory. *Journal of Chemical Physics*, 14(3):180(22), 1946.

[80] J. Kirkwood. Correction. *Journal of Chemical Physics*, 14(5):347(1), 1947.

[81] J. Kirkwood. The statistical mechanical theory of transport processe II. Transport in gases. *Journal of Chemical Physics*, 15(15):72(5), 1947.

[82] Y. Klimontovich. *The Statistical Theory of Non-Equilibrium Processes in a Plasma*, chapter 4. Pergamon Press, Oxford, 1967.

[83] J. Kmetec, J. Mackin, and J. Young. 0.5-TW, 125-fs Ti:sapphire laser. *Opt. Lett.*, 16(13): 1001(3), 1991.

[84] V. Korobkin and R. Serov. Investigation of magnetic field of a spark produced by focusing laser radiation. *JETP Lett.*, 4(3):70 ff, 1966.

[85] A. Krall and A. Trivelpiece. *Principles of Plasma Physics*. International Series in Pure and Applied Physics. McGraw-Hill, New York, 1973.

[86] W. Kruer. *The Physics of Laser Plasma Interactions*. Number 73 in Frontiers in physics. Addison-Wesley, Redwood City (Ca), 1988.

[87] H. Kubo and R. Nagata. Vector representaion of behavior of polarized light in a weakly inhomogeneous medium with birefringence and dichroism. *J. Opt. Soc. Am.*, 73(12):1719–1724, 1983.

[88] H. Kubo and R. Nagata. Vector representaion of behavior of polarized light in a weakly inhomogeneous medium with birefringence and dichroism. II. evolution of polarization states. *J. Opt. Soc. Am. A*, 2(1):30(5), 1985.

[89] Lab2. The virtual femtosecond laboratory. Homepage, 2004. URL http://www.lab2.de.

[90] D. Lai and E. Salpeter. Hydrogen phases on the surface of a strongly magnetized neutron star. *Astrophys. J.*, 491(1, pt. 1):270(16), 1997.

[91] Laser. List of huge lasers, 2004. URL http://members.rogers.com/biglasers.

[92] S. Le Blanc and R. Sauerbrey. Spectral, temporal, and spatial characteristics of plasma-induced spectral blue shifting and its application to femtosecond pulse measurement. *J. Opt. Soc. Am. B*, 13(1):72(17), 1996.

[93] K. Ledingham, I. Spencer, T. McCanny, R. Singhal, M. Santala, E. Clark, I. Watts, F. Beg, M. Zepf, K. Krushelnick, M. Tatarakis, A. Dangor, P. Norreys, R. Allott, D. Neely, R. Clark, A. Machacek, J. Wark, A. Cresswell, D. Sanderson, and J. Magill. Photonuclear physics when a multiterawatt laser pulse interacts with solid targets. *Phys. Rev. Lett.*, 84(5):899(4), 2000.

[94] R. Lehmberg and J. Stamper. Depolarization in laser probing of inhomogeneous magnetized plasmas. *Phys. Fluids*, 21(5):814(4), 1978.

[95] R. Lichters. *Relativistische Wechselwirkung intensiver kurzer Laserpulse mit überdichten Plasmen: Erzeugung hoher harmonischer*. PhD thesis, Max-Plank-Institut für Quantenoptik, 1997.

[96] R. Lichters, J. Meyer-ter Vehn, and A. Pukhov. Short-pulse laser harmonics from oscillating plasma surfaces driven at relativistic intensity. *Phys. Plas.*, 3(9):3425(13), 1996.

[97] J. Lindl. Development of the indirect-drive approach to inertial confinement fusion and the target physics basis for ignition and gain. *Phys. Plas.*, 2(11):3933(91), 1995.

[98] D. Lynch and W. Hunter. Comments on the optical constants of metals and an introduction to data for several metals. In E. Palik, editor, *Handbook of Optical Constants of Solids*, volume 1, chapter IV, page 286(10). Academic Press, Boston, 2 edition, 1998.

[99] W. MacMaster. Matrix representation of polarisation. *Rev. Mod. Phys.*, 33(1):8(17), 1961.

[100] T. Maiman. Stimulates optical radiation in ruby. *Nature*, 187(4736):493(2), 1960.

[101] P. Maine, D. Strickland, D. Bado, M. Pessot, , and G. Mourou. Generation of ultrahigh peak power by chirped pulse amplification. *IEEE J. Quant. Electron.*, 24(2):398(6), 1988.

[102] S. Mangles, C. Murphy, Z. Najmudin, A. Thomas, J. Collier, A. Dangor, E. Divall, P. Foster, J. Gallacher, C. Hooker, D. Jaroszynski, A. Langley, W. Mori, P. Norreys, F. Tsung, R. Viskup, B. Walton, and K. K. Monoenergetic beams of relativistic electrons from intense laser–plasma interactions. *Nature*, 431(7008):535(4), 2004.

[103] R. Mason and M. Tabak. Magnetic field-generation in high-intensity-laser-matter interactions. *Phys. Rev. Lett.*, 80(3):524(4), 1998.

[104] Mathworks. Matlab a numerical computing language. Homepage, 2004. URL http://www.mathworks.com.

[105] J. Maxwell. *A treatise on Electricity and Magnetism*, volume 1,2. Clarendon Press, Oxford, 3$^{\text{rd}}$ edition, 1891.

[106] J. Mayer and M. Mayer. *Statistical Mechanics of Fluids*. Wiley, New York, 1940.

[107] E. McLean, J. Stamper, C. Manka, H. Griem, D. Droemer, and B. Ripin. Observation of magnetic fields in laser-produced plasma using the Zeeman effect. *Phys. Fluids*, 27(5): 1327(9), 1984.

[108] S. McNaught, J. Knauer, and D. Meyerhofer. Photoelectron initial conditions for tunneling ionization in a linearily polarised laser. *Phys. Rev. A*, 58(2):1399(13), 1998.

[109] K. Michelmann. *Messung von Zeit-Frequenzverteilungen bei Femtosekunden-Laserpulsen*. PhD thesis, Friedrich-Schiller-Universität, Jena (Germany), 2002.

[110] K. Michelmann, U. Wagner, T. Feurer, U. Teubner, E. Förster, and R. Sauerbrey. Measurement of the page function of an ultrashort laser pulse. *Opt. Comm.*, 198(1-3):163(8), 2001.

[111] A. Michette. *Optical Systems for soft x-rays*. Plenum Press, New York, 1986.

[112] W. Morri. Plasmasimulation. Homepage, 2004. URL http://exodus.physics.ucla.edu.

[113] H. Mott-Smith. History of 'Plasmas'. *Nature*, 233:219(1), 1971.

[114] P. Mulser. Theory of short pulse interaction. In Hooper and Osborne [71], page 231(22).

[115] National Instruments. Labview a measurement and automation software. Homepage, 2004. URL http://www.labview.com.

[116] P. Norreys, M. Zepf, S. Moustaizis, A. Fews, J. Zhang, P. Lee, M. Bakarezos, C. Danson, A. Dyson, P. Gibbon, P. Loukakos, D. Neely, F. Walsh, J. Wark, and A. Dangor. Efficient extreme uv harmonics generated from picosecond laser pulse interactions with solid targets. *Phys. Rev. Lett.*, 76(11):1832–1835, 1996.

[117] P. Norreys, M. Santala, E. Clark, M. Zepf, I. Watts, F. Beg, K. Krushelnick, M. Tatarakis, X. Fang, P. Graham, T. McCanny, R. Singhal, K. Ledingham, A. Creswell, D. Sanderson, J. Magill, A. Machacek, J. Wark, R. Allott, B. Kennedy, and D. Neely. Observation of a highly directional γ-ray beam from ultrashort, ultraintense laser pulse interactions with solids. *Physics of Plasmas*, 6(5):2150(7), 1999.

[118] P. Norreys, R. Allot, R. Clarke, J. Collier, D. Neely, S. Rose, M. Zepf, M. Santala, A. Bell, K. Krushelnick, A. Dangor, N. Woolsey, E. R.G., H. Habara, T. Norimatsu, and R. Kodama. Experimental studies of the advanced fast igniter scheme. *Phy. Plas.*, 7(9):3721(6), 2000.

[119] A. Nuttall. On the quadrature approximation to the Hilbert transform of modulated signals. *Proc. IEEE*, 54(10):1458(2), 1966.

[120] C. of Materials for a vacuum-ultraviolet polarization analyser. Corti, g. and romoli, m. *Appl. Opt.*, 42(19):3950(7), 2003.

[121] P. Oonincx. *Mathematical signal analysis: Wavelets, Wigner distribution and a seismic application*. CWI, Amsterdam, 2000.

[122] A. Oppenheim and R. Schafer. *Zeitdiskrete Signalverarbeitung*. R. Oldenbourg Verlag, München, 3$^{\text{rd}}$ edition, 1999.

[123] C. Page. Instantaneous power spectra. *J. App. Phys*, 23(1):103(4), 1952.

[124] M. Perry and G. Mourou. Terawatt to petawatt subpicosecond lasers. *Science*, 264(5161): 917(7), 1994.

[125] M. Pessot, P. Maine, and G. Mourou. 1000 times expansion/compression of optical pulses for chirped pulse amplification. *Opt. Comm.*, 62(6):419(4), 1987.

[126] D. Phillion, R. Lerche, V. Rupert, R. Haas, and M. Boyle. Evidence for profile steepening in laser-irradiated plasmas. *Phys. Fluids*, 20(11):1892(8), 1977.

[127] Photonic Science. Darkstar, intensified 8 bit CCD camera. Homepage, 2004. URL http://www.photonic-science.co.uk.

[128] Proxitronic. Open MCPs. Homepage, 2004. URL http://www.proxitronic.de/prod/omcp/eos.htm.

[129] A. Pukhov and J. Meyer-ter Vehn. Laser hole boring into overdense plasma and relativistic electron currents for fast ignition of ICF targets. *Phys. Rev. Lett.*, 79(14):2686(4), 1997.

[130] S. Rae and K. Burnett. Possible production of cold plasma through optical-field-induced ionization. *Phys. Rev. A*, 46(4):2077(7), 1992.

[131] W. Raith, editor. *Vielteilchen Systeme*, volume 5 of *Bergmann Schäfer, Lehrbuch der Experimentalphysik*. Walter de Gruyter, Berlin, 1992.

[132] R. Ramis, R. Schmalz, and J. Meyer-ter Vehn. Multi – a computer code for one-dimensional multigroup radiation hydrodynamics. *Comp. Phys. Comm.*, 49(3):475(31), 1988.

[133] L. Rayleigh. On electrical vibrations and the constitution of the atom. *Phil. Mag.*, 11:117ff, 1906.

[134] J. Reintjes. Ultrafast imaging techniques in laser sources and applications. In A. Miller and D. Finlayson, editors, *Laser Sources and applications*, volume 47 of *SUSSP Proceedings*, page 331(37), Edingburgh, Bristol, 1996. SUSSP and IOP Publishing.

[135] A. Rihaczek. Hilbert transforms and complex representation of real signals. *Proc. IEEE*, 54(3):434(2), 1966.

[136] A. Rousse, C. Rischel, S. Fourmaux, I. Uschmann, S. Sebban, G. Grillon, P. Balcou, E. Förster, J. Geindre, P. Audebert, J. Gauthier, and D. Hulin. Non-thermal melting in semiconductors measured at femtosecond resolution. *Nature*, 410(6824):65(4), 2001.

[137] H. Ruhl and P. Mulser. Relativistic vlasov simulation of intense fs laser pulse-matter interaction. *Phys. Lett. A*, 205(5-6):388(5), 1995.

[138] A. Saemann and K. Eidmann. X-ray emission from metallic (Al) and dielectric (glass) targets irradiated by intense ultrashort laser pulses. *Appl. Phys. Lett.*, 73(10), 1998.

[139] A. Sandhu, A. Dharmadhikari, P. Rajeev, G. Kumar, S. Sengupta, A. Das, and P. Kaw. Laser-generated ultrashort multimegagauss magnetic pulses in plasmas. *Phys. Rev. Lett.*, 89(22):225002(4), 2002.

[140] M. Santala, M. Zepf, F. Beg, E. Clark, A. Dangor, K. Krushelnick, M. Tatarakis, I. Watts, K. Ledingham, T. McCanny, I. Spencer, A. Machacek, R. Allott, R. Clarke, and P. Norreys. Production of radioactive nuclides by energetic protons generated from intense laser-plasma interactions. *Appl. Phys. Lett.*, 78(1), 2001.

[141] M. Sarfaty, R. Shpitalnik, R. Arad, A. Weingarten, Y. Krasik, A. Fruschtman, and Y. Maron. Spectroscopic investigation of (ns) magnetic field penetration in a plasma. *Phys. Plas.*, 2 (6):2583(7), 1995.

[142] R. Sauerbrey, J. Fure, S. Le Blanc, B. van Wonterghem, U. Teubner, and F. Schäfer. Reflectivity of laser-produced plasmas generated by a high intensity ultrashort pulse. *Phys. Plas.*, 1(5):1635(8), 1994.

[143] F. Schäfer, H. Mertins, A. Gaupp, W. Gudat, M. Mertin, I. Pack, F. Schmolla, S. Di Fonzo, G. Soullie, W. Jark, R. Walker, X. Le Cann, R. Nyholm, and M. Eriksson. Soft-x-ray polarimeter with multilayer optics: complete analysis of the polarization state of light. *Appl. Opt.*, 38(19):4074(15), 1999.

[144] M. Schätzel, F. Lindner, G. Paulus, H. Walther, E. Goulielmakis, A. Baltuska, M. Lezius, and F. Krausz. Long-term stabilization of the carrier-envelope phase of few-cycle laser pulses. *Appl. Phys. B*, 79(8):1021(5), 2004.

[145] H. Schwoerer, F. Ewald, R. Sauerbrey, J. Galy, J. Magill, V. Rondinella, R. Schenkel, and T. Butz. Fission of actinides using a tabletop laser. *Euro. Phys. Lett.*, 66(1):47(6), 2003.

[146] S. Segre. A review of plasma polarimetry – theory and methods. *Plasma Phys. Control. Fusion*, 41(2):R57(44), 1999.

[147] J. Seidel and B. Wende. *Kernfusionsplasmen*, chapter 2.13, page 193(29). Volume 5 of , Raith [131], 1992.

[148] J. Seidel and B. Wende. Pinch-Gleichung, Bennett-Gleichung. In Raith [131], chapter 2.12.2.3, page 192(2).

[149] C. Shanks, R. Yen, and C. Hirlimann. Time-resolved reflectivity measurements of femtosecond-optical-pulse-induced phase transitions in silicon. *Phys. Rev. Lett.*, 50(6): 454(4), 1983.

[150] S. Shapiro and S. Teukolsky. *Black Holes, White Dwarfs and Neutron Stars. The Physics of Compact Objects*. Wiley-Interscience, New York, 1983.

[151] R. Shpitalnik, A. Weingarten, K. Gomberoff, Y. Krasik, and Y. Maron. Observation of two dimensional magnetic field evolution in a plasma opening switch. *Phys. Plas.*, 5(3):792(7), 1998.

[152] K. Sokolowski-Tinten, C. Blome, C. Dietrich, A. Tarasevitch, M. Horn-von Hoegen, D. von-der Linde, A. Cavalleri, J. Squier, and M. Kammler. Femtosecond X-ray measurement of ultrafast melting and large acoustic transients. *Phys. Rev. Lett*, 87(22):257011(4), 2001.

[153] K. Spatschek. *Theoretische Plasmaphysik*. Teubner Studienbücher. B.G. Teubner Stuttgart, Stuttgart, 1990.

[154] Spectra Physics. *Tsunami femtosecond oszillator*. Spectra Physics, 2004. URL http://www.spectra-physics.com/eThermo/CMA/PDFs/Product/productPDF_21208.pdf.

[155] D. Spencer, P. Kean, and W. Sibbett. 60-fsec pulse generation from a self-mode-locked Ti:sapphire laser. *Opt. Lett.*, 16(1):42(3), 1991.

[156] L. Spitzer. *Physics of Fully Ionised Gases*. Wiley Interscience, New York, 1962.

[157] J. Stampa. Review on spontaneous magnetic fields in laser-produced plasmas: Phenomena and measurements. *Laser and Particle Beams*, 9(4):841(22), 1991.

[158] J. Stampa, K. Papadopoulos, R. Sudan, S. Dean, E. McLean, and J. Dawson. Spontaneous magnetic fields in laser-produced plasmas. *Phys. Rev. Lett.*, 26(17):1012(4), 1971.

[159] L. Stamper and B. Ripin. Faraday-rotation measurements of megagauss magnetic fields in laser-produced plasmas. *Phys. Rev. Lett.*, 34(3):138(4), 1975.

[160] R. Stephens, R. Snavely, Y. Aglitskiy, F. Amiranoff, C. Andersen, D. Batani, S. Baton, T. Cowan, R. Freeman, T. Hall, S. Hatchett, J. Hill, M. Key, J. King, J. Koch, M. Koenig, A. MacKinnon, K. Lancaster, E. Martinolli, P. Norreys, E. Perelli-Cippo, M. Le Gloahec, C. Rousseaux, J. Santos, and F. Scianitti. K-alpha fluorescence measurement of relativistic electron transport in the context of fast ignition. *Phys. Rev. E*, 69(6):066414(7), 2004.

[161] T. Stix. *Waves in Plasmas*. American Institute of Physics, New York, 1992.

[162] G. Stobrawa. *Aufbau und Anwendung eines hochauflösenden Impulsformers zur Kontrolle ultrakurzer Laserpulse*. PhD thesis, Friedrich-Schiller-Universität, Jena (Germany), 2003.

[163] D. Strickland and G. Mourou. Compression of amplified chirped optical pulses. *Opt. Comm.*, 56(3):219(4), 1985.

[164] D. Strickland and G. Mourou. Compression of amplified chirped optical pulses. *Opt. Comm.*, 55(6):447(3), 1985.

[165] R. Sudan. Mechanisms for the generation of 10^9 G magnetic fields in the interaction of ultraintense short laser pulse with an overdense plasma target. *Phys. Rev. Lett.*, 70(20): 3075(4), 1993.

[166] A. Sullivan, H. Hamster, H. Kapteyn, S. Gordon, W. White, H. Nathel, R. Blair, and R. Falcone. Multiterawatt, 100-fs laser. *Opt. Lett.*, 16(18):1406(3), 1991.

[167] Y. Svirko and V. Zheludev. *Polarisation of Light in Nonlinear Optics*. J. Wiley and Son, Chichester, 1998.

[168] M. Tabak, J. Hammer, M. Glinsky, W. Kruer, S. Wilks, J. Woodworth, E. Campbell, M. Perry, and R. Mason. Ignition and high gain with ultrapowerful lasers. *Phy. Plas.*, 1 (5):1626(9), 1994.

[169] A. Tarasevitch, A. Orisch, D. von der Linde, P. Balcou, G. Rey, J. Chambaret, U. Teubner, D. Klopfel, and W. Theobald. Generation of high-order spatially coherent harmonics from solid targets by femtosecond laser pulses. *Phys. Rev. A*, 62(2):023816(6), 2000.

[170] A. Tarasevitch, C. Dietrich, and D. von der Linde. Plasma mirror distortions and parametric instabilities induced by high intensity femtosecond pulses on solid targets. In M. Lantano, editor, *Superstrong Fields in Plasmas: Second International Conference on Superstrong Fields in Plasmas*, volume 611 of *AIP Conf. Proc.*, page 294(6), Melville (NY.), 2002. AIP.

[171] M. Tatarakis, I. Watts, F. Beg, E. Clark, A. Dangor, A. Gopal, M. Haines, P. Norreys, U. Wagner, M. Wei, M. Zepf, and K. Krushelnick. Measuring huge magnetic fields. *Nature*, 415(3):280(1), 2002.

[172] U. Teubner and E. Förster. Physik lasererzeugter Plasmen. Vorlesungsskript, Friedrich-Schiller-Universität, Jena (Germany), 1997.

[173] U. Teubner, J. Bergmann, B. van Wonterghem, F. Schäfer, and R. Sauerbrey. Angle-dependent x-ray emission and resonance absorption in a laser-produced plasma generated by a high intensity ultrashort pulse. *Phys. Rev. Lett.*, 70(6):794(4), 1993.

[174] U. Teubner, U. Wagner, and E. Förster. Sub-10 fs gating of optical pulses. *J. Phys. B: At. Mol. Opt. Phys.*, 34(15):2993(10), 2001.

[175] U. Teubner, G. Pretzler, K. Eidmann, E. Förster, and K. Witte. Anomalies in high order harmonic generation at relativistic intensities. *Phys. Rev A.*, 67(1):013816(11), 2003.

[176] U. Teubner, K. Eidmann, U. Wagner, U. Andiel, F. Pisani, G. D. Tsakiris, K. Witte, J. Meyer-ter Vehn, T. Schlegel, and E. Förster. Harmonic emission from the rear side of thin overdense foils irradiated with intense ultrashort laser pulses. *Phys. Rev. Lett.*, 92 (18):185001(4), 2004.

[177] L. Tonks and I. Langmuire. Oscillations in ionized gases. *Phys. Rev.*, 33(2):195(17), 1906.

[178] R. Trebino, K. DeLong, D. Fittinghoff, J. Sweetser, M. Krumbugel, B. Richman, and D. Kane. Measuring ultrashort laser pulses in the time-frequency domain using frequency-resolved optical gating. *Rev. Sci. Inst.*, 68(9):3277(19), 1997.

[179] J. Ville. Theórie et applications de la notation de signal analytique. *Cables et Transmission*, 2:61(14), 1948.

[180] D. von der Linde. Ultrashort interactions in solids. In W. Kaiser and D. Auston, editors, *Ultrashort Laser Pulses, Generation and Application*, volume 60 of *Topics in Applied Physics*, chapter 4.4, page 113(70). Springer, Berlin, 2nd edition, 1993.

[181] D. von der Linde. Breakdown threshold and plasma formation in femtosecond laser-solid interaction. *J. Opt. Soc. Am. B*, 13(1):216(7), 1996.

[182] D. von der Linde. Generation of high order optical harmonics from solid surfaces. *Appl. Phys. B*, 68(3):315(5), 1999.

[183] D. von der Linde and K. Rz'azewski. High-order optical harmonic generation from solid surfaces. *Appl. Phys. B*, 63(5):499(8), 1996.

[184] B. Vu, R. Lee, O. Landen, D. Price, J. Bonlie, and S. R.E. Temporally and radially-resolved optical measurements of solid density plasma reflectivities and transmissivities. *J. Quant. Spect. Rad. Trans.*, 54(1-2):413(6), 1995.

[185] I. Watts, M. Zepf, M. Clark, E.L. Tatarakis, K. Krushelnick, A. Dangor, R. Allot, R. Clarke, D. Neely, and P. Norreys. Dynamics of the critical surface in high-intensity laser-solid

interactions: Modulation of the XUV harmonic spectra. *Phys. Rev. Lett.*, 88(15):155001(4), 2002.

[186] J. H. Weaver, C. Krafka, D. W. Lynch, and E. Koch. Optical properties of metals. II. Noble metals, Aluminum, Scandium, Yttrium, the Lanthanides and the Actinides (0.1$\lesssim$ hν $\lesssim$500 eV). *Physik-Daten*, 18(2):1(269), 1981.

[187] C. Weißmantel and C. Hamann. *Grundlagen der Festkörperphysik*, chapter 9.1–9.2, page 571(21). Johann Ambrosius Barth Verlag, Heidelberg, 4$^{\text{th}}$ edition, 1995.

[188] E. Weisstein. Fourier transform, 1999. URL `http://mathworld.wolfram.com/FourierTransform.html`.

[189] S. Wilks, K. W.L., M. Tabak, and A. Langdon. Absorption of ultra-intense laser pulses. *Phys. Rev. Lett.*, 69(9):1383(4), 1992.

[190] J. Yvon. *La théorie des fluides et d'état: actualités scientifiques et industrielle*. Herman et Cie, Paris, 1935.

[191] M. Zepf, G. Tsakiris, G. Pretzler, D. Chambers, P. Norreys, U. Andiel, A. Dangor, K. Eidmann, C. Gahn, A. Machacek, J. Wark, and K. Witte. Role of the plasma scale length in the harmonic generation from solid targets. *Phys. Rev. E*, 58(5):R5253(4), 1998.

Curriculum Vitae

Ulrich Hilmar Wagner

Date of Birth: 28. November 1972

Education

1979 - 1983   Primary school: Gerhart-Hauptmann-Schule, Wanfried.

1983 - 1989   Grammar school: Friedrich-Wilhelm-Schule, Eschwege.

1989 - 1992   Sixth form college: Oberstufengymnasium, Eschwege.

1992   A-level examination.

Academic Education

1992 - 1997   University education in Physics: Georg-August-Universität, Göttingen

1997   Diploma Degree in Physics. Diploma thesis: Ultradünne Flüssigkeits-
                 strahlen als Targets zur Erzeugung laserinduzierter Plasmaquellen.

Since 1998   PHD student of Prof. E. Förster, X-ray optics group of the IOQ at the
                 Friedrich-Schiller University in Jena.

2000-2001   Marie-Curie PHD fellow at the CLF of the Rutherford-Appleton-
                 Laboratory, Great Britain.

2002-2003   EU research fellow at the CNR in Pisa, Italy.

Since 2004   Scientist at Diamond Light Sources Ltd.

2004   PHD thesis: Sub-Picosecond Laser Plasma Experiments on Dielectric
                 Solids: Ultrafast Ionisation and Observation of Megagauss Magnetic
                 Fields.

Acknowledgement

I would like to say a very sincere thank you very much to all, who have supported me in writing this thesis.

Primarily, I would like to thank Prof. Dr. Förster and Dr. U. Teubner for all their advice, support and encouragement in writing this thesis and for the freedom to explore my own ideas. Not less, I would like to acknowledge Dr. P. Norreys and Prof. Dr. K. Krushelnick for the great opportunity to stay at the Rutherford-Appleton-Laboratory for one year as a EU funded Marie-Curie PHD student and for the exciting research I was involved in.

In this context I would like to say thank you very much to my dear colleagues M. Tatarakis, F. Beg, A. Gopal and S. Mangles from Imperial College, with whom I spend numerous days and evenings together in the laboratory, working hard, discussing a lot, but nevertheless having a good time and learning much about Indian food and culture.

I also owe thanks to Dr. Roger Evans for his advice about theoretical aspects of the laser–plasma interaction and for the PIC simulations, performed with the OSIRIS code developed in Prof. W.B. Mori's group at the University of California in Los Angeles.

A warm thank you to all the people running the laser, operating the target area, preparing the targets, designing and building the scientific instruments. In particular I would like to thank: C. Hernandez-Gomez, S. Hawkes, C. Danson, R. Allot, R.J. Clarke, M. Poulter and D. Neely.

In addition I would like to acknowledge A. Brown and R. Tubb, who have been working hard to sort out all the administrative troubles with setting me up as the first Marie-Curie PHD student at the Rutherford-Appleton-Laboratories.

I would like to acknowledge T. Feurer, G. Stobrawa, R. Netz for operating and characterising the kHz-fs-laser in Jena and D. Klöpfel for his self-devoting technical assistance. Without their help the plasma switch experiment would not have been possible. In particular I would like to thank Prof. Dr. Sauerbrey for granting access to the laser-systems in Jena.

During my moving between Germany, Britain and France I have been sharing accommodation with some people who became good friends, enduring my sometimes rarely being at home and having not much time for anything else despite science. Thank you very much A. Gamst, A. Naumann, J. Streicher, F. Freudenberg and D. Trautwein.

I am very grateful to all friends, who have been encouraging me through the long struggle for scientific knowledge, who have been forbearing with my mood and my sometimes being negligent of them. Among them are: T. Schubach, E. Vincovik, A. Drutkowski, H. and C. Kauhaus, A. Lotz, P. and T. Weichelt, A. Möller, R. Bär and J. Gintrowski.

And last but not least I owe thanks to my parents and my brother, who always have encouraged me to keep on studying and writing.